5-2015

Characterization of Nano-Porous Si-Cu Composites to Enhance Lubricant Retention Impacting the Tribological Properties of Sliding Surfaces

Julius Sheldon Morehead
University of Arkansas, Fayetteville

Characterization of Nano-Porous Si-Cu Composites to Enhance Lubricant Retention Impacting the Tribological Properties of Sliding Surfaces

Characterization of Nano-Porous Si-Cu Composites to Enhance Lubricant Retention Impacting the Tribological Properties of Sliding Surfaces

A dissertation submitted in partial fulfillment
of the requirements for the degree of
Doctor of Philosophy in Mechanical Engineering

By

Julius Sheldon Morehead
University of Arkansas
Bachelor of Science in Mechanical Engineering, 2009
Master of Science in Mechanical Engineering, 2011

May 2015
University of Arkansas

This dissertation is approved for recommendation to the Graduate Council.

Dr. Hameed Naseem
Dissertation Director

Dr. Uchechukwu Wejinya
Committee Member

Dr. Rick Couvillion
Committee Member

Dr. Po-Hao Huang
Committee Member

Dr. Darrin Nutter
Committee Member

Abstract

As the expectations for modern machinery's tribological and thermal performances continue to rise, the retention of lubricant on the contact surfaces of their sliding components becomes an increasingly important issue. Friction and wear cause heat-related failures which lead to catastrophic damage to machinery. Evaporation of a lubricant's volatile constituents as well as lubricant migration leads not only to a reduction in lubricant quantity but also in its quality, thus facilitating component failures. In order to enhance component reliability, the surface should incorporate features that actively retain lubricants. The unique properties of nano-porous topographies such as their high surface area-to-volume ratio indicate they hold great potential to address these lubrication issues.

Thermodynamics-based numerical models of smooth and nano-porous Si-Cu composite topographies were developed to predict the trends of lubricant retention. Photolithographic processes as well as physical etching and thin film deposition tools were utilized to fabricate smooth and patterned Si-Cu composite sample types. The nano-porous topographies incorporated various nano-pore geometries for determination of the optimum conditions for lubricant retention. Amorphous Si film was deposited on the samples using chemical vapor deposition which served as a surface chemistry modification to examine the film's potential to enhance lubricant retention. Lubricant retention tests were performed using a custom-fabricated apparatus for evaporating lubricant from the sample types. Finally, the model's predictions of lubricant retention trends were compared to actual testing results to examine the validity of those predictions.

The predictions of the models were supported by the evaporation testing data obtained from the samples. It was found that surface nano-pores having the proper geometry, in combination with

the dehydrogenated amorphous Si surface chemistry, could significantly enhance retention above the one micrometer fluid film thickness typically formed between interacting surfaces of machine components undergoing relative motion. The surface features show potential to prevent many types of mechanical failures, reduce maintenance costs, and achieve higher energy efficiency.

Acknowledgments

There are so many people whom I need to thank for making this dissertation possible. Thank you, first of all, Dr. Naseem for your many efforts on my behalf, academically. Please know that you are appreciated for helping me transition to your research group, for your trust in my abilities, and for the many conversations we had. It was your continued concern and encouragement that helped me to endure when things became difficult. To Dr. Wejinya, I am truly appreciative of your guidance in my academic pursuits (and 2 theses) during the past several years. We all need a "center" in our lives, a true advocate when we feel besieged or uncertain as to the way to go. You have been there for me, and I truly thank you for this. To Dr. Couvillion, you have been there for me academically and for 3 theses, and your outstanding recommendations were instrumental to my obtaining the fellowships that supported my research. To you I say, "Thank you, thank you, thank you". Thank you also Drs. Huang and Nutter for responding to my call to serve on my dissertation committees. During our conversations together, your experience and frank input was informative and greatly appreciated. Thank you, Dr. Fisher Yu, for the use of the FTIR equipment in your lab and Dr. Ben Conley for training me.

There are several people related to HiDEC that I need to thank for lending their help to accomplish my research. Thank you Dr. Shannon Davis, Kyle Cook, Dr. Ang, Jeff Knox, and the rest of the HiDEC and ENRC staff for your work and generosity that helped me arrive at this point. Without your dedication to students like myself who needed a "hand up", I doubt that I would have been able to finish this research. My appreciation also goes to the team at Georgia Tech: Hang Chen, Paul Joseph, Traci Warren, Charlie Turgeon, and Purnima Sharma. You all moved mountains for me to do research at your impressive facility. To the awesomely talented

staff at Data Electronic Services, Herculano Murillo and Juan Jimenez, you guys are my heroes. Thank you for undertaking the herculean task of performing the electroless and electrolytic Cu depositions. A special thanks to Mourad Benamara and the staff at the Electron Optics Facility for lending your expertise and knowledge that helped me obtain the SEM, EDX, and TEM images used in the dissertation. Thank you mechanical engineering staff (especially Laura Dumontier and Ben Fleming) and professors, and electrical engineering staff who kindly provided me the educational support I needed. Your efforts resulted in a quality education that has served me well on 4 internships, and I am sure will help me in my future endeavors. Last, but not least, I wish to express special appreciation to my friend, Thomas Carter, whose financial help, guidance, and extensive network of people were crucial to my surviving this momentous undertaking.

Dedication

Reaching this stage in my academic career has taken 11 long years. This endeavor has been challenging, fear-inspiring at times, exhilarating, and represents for me a truly awesome achievement. A feat such as this was not easy, but it was made possible because of some very special people in my life. This dissertation is posthumously dedicated to my sister, Terry Morehead-Davis and my father, Thelma Morehead, whose entrepreneurial spirit and determination in the face of tremendous obstacles had a profound influence in my life. To my mother, Elrie Morehead: much love and appreciation for always loving and encouraging me no matter the circumstances in life in which I found myself. To my sisters, Thelma and Jacqueline, and brothers, Frederick and Stevie; thank you all for being there for me. Thank you Destinee, my loving niece, for the fun we had when you were younger and for the inspiration you give to me now. Thinking about those times helps me smile when I take life and myself too seriously. To all my extended family and friends, thank you all for your kind words and encouragement that kept me focused on this monumental task.

Table of Contents

Publications Citation

1. Morehead, J., and Zou, M., “Superhydrophilic Surface on Cu Substrate to Enhance Lubricant Retention”, *Journal of Adhesion Science and Technology Special Issue: Superhydrophilic Surfaces*, Vol. 28, No. 8-9, pp. 833-842, 2014 (online 2012).

List of Figures

List of Tables

CHAPTER 1

INTRODUCTION

1.1 Introduction

From the beginning of recorded history, machinery has been synonymous with the presence of mankind. The inclined plane, lever, pulley, wheel, axle, and screw are examples of simple machines known to exist several thousand years ago. Although the sophistication of modern machinery has escalated in response to events stemming from the airplane, railroad, automobile-driven industrial age [1], two world wars of the twentieth century, and the computer age, the fact is even the most complex machines are assemblies of simpler machines and basic moving components. The number of moving components in existence allows seemingly endless permutations of machines which, in turn, spur greater need for machines. After all, it usually takes machines to manufacture other machines. One thing that the machines of old and newer designs have in common is the need to address friction, wear, and lubrication [2].

1.2 Tribological Loss Statistics

It is estimated that the financial loss due to friction and wear are 1% to 1.4% of an industrialized country's gross national product [3]. The losses, the author asserts, stems from a culture characterized by a lack of awareness of the effects of tribology. Tribology is defined as the study of friction, wear, and lubrication of interacting surfaces in relative motion [4]. The lack of tribology research by industry, educational development by academic institutions, and implementation of tribology in design has led to avoidable loss of financial resources and human lives through failed products. There is more to consider than the thermal energy recovery which is the typical focus of energy savings. Another source estimates that the direct and consequential

annual loss to industries due to friction and wear is in the billions [5]. The well-known Jost report provides a comprehensive breakout of the losses by industry and the potential savings that would result from a minimal investment in the area of tribology [6].

1.3 Importance of Lubricant Retention

The annual production of motors, engines, and machine bearings that rely on lubrication numbers in the billions. Liquid lubrication is a prominent method of addressing tribological issues in these assemblies. Liquid lubricants simultaneously provide four critical functions for moving machine components. They (1) reduce friction and wear, (2) provide cooling to dissipate heat, (3) protect the components from corrosion, and (4) cleanse the contacting surfaces of debris. The amount of success a lubricant has in accomplishing these tasks is related to the ability of the system to provide lubricant to the proper location, in the quantity required, and for the duration it is needed—in other words, lubricant retention.

The reduction in lubricant quantity and deterioration of lubricant quality, over time, can lead to machine component failures. The evaporation of lubricant can cause both of these scenarios to co-exist. Some possible solutions for these situations are to incorporate methods that enhance the retention of lubricant by reducing the evaporated amount of the lubricant's volatile constituents. This continues to be a challenge as borne out by the tribology statistics related to friction, wear, and corrosion expressed in section 1.2.

1.4 Potential of Nano-Porous Surfaces to Solve Tribological Issues

The development of better lubricants and its retention between rolling and sliding surfaces has been a topic of consideration for several centuries [7]. The retention of lubricant to the vicinity of moving components became especially important during the industrial age when lubricants other than grease were needed and operating conditions put never-before-seen demands on the

lubricants and moving components [8]. Also, the infamous oil patches left by early automobiles put pressure on manufacturers to improve lubricant retention to transform the image of the automobile into a more socially acceptable means of transportation. Fast forwarding to modern times, there is still a considerable need for improving lubricant retention.

Various macro-scale geometric surface features have been implemented throughout history to address the problems that arose as a result of lubricant loss. These efforts became more pronounced during the 20th century. Research interest in surface engineering to address the tribological issues of sliding surfaces peaked in the late-1990s. Nonetheless, a few researchers continued to develop novel methods of creating micro-scale features on the surface of machine components to reduce friction and wear [9][10][11][12]. About the same time that lubricant retention research peaked, research in surface engineering to affect the wetting behavior of materials gained momentum.

A number of researchers interested in surface wetting were already engineering micro-scale features to affect wetting behavior, but some began investigating material properties on the nano-scale principally to address stiction and adhesion issues of micro-electromechanical systems or MEMS [13][14][15][16]. Inspiration was drawn from the unique behaviors of surfaces which were observed in nature such as the lotus leaf plant, beetle's wings, water strider's legs, and gecko lizard feet, to name a few [17][18]. The field now known as bio-mimetics includes the study of nature's surfaces to advance scientific knowledge.

Important insights into the properties of nano-materials were gained and these began to find their way into applications like sliding machine components that were affected by friction and wear [19]. Rather than adopting the traditional surface feature engineering approaches, however, the majority of current research is focused on developing nano-material products that modify the

lubricant's chemistry to make machine surfaces more slippery. Molybdenum disulfide (MoS_2), lead (Pb), and graphite are types of additives investigated and used extensively in modern machinery's lubricants [20]. Other methods employ surface coatings or lubricant additives like polytetrafluoroethylene (PTFE) to combat friction and wear [21]. The inclusion of these single-purpose products increases the already bloated list of additives and production expenses that lubricants have these days. Curing the symptoms affecting sliding surfaces by prescribing more additives is likened to the practice of some medical doctors who prescribe pills to treat every ailment encountered by a patient. In the end, the additives do little to enhance the retention of lubricants on the surface, and a number of performance claims of these miracle products have been debunked by the Federal Trade Commission.

An area in tribological research that is largely overlooked by many is nano-porous surface engineering. The potential of nano-porous surfaces to help alleviate these issues and others impacting sliding machine components is summarized:

- The appropriate nano-porous geometry may enhance the retention of lubricant by reducing evaporation
- Nano-pores can allow more storage for improving lubricant retention due to their high surface area-to-volume ratio
- Nano-pores may reduce the accumulation of varnish and charred residue on the surface during thermal degradation of lubricants
- Nano-porous surfaces might allow greater control to address problems such as seal and bearing lubricant leakage that could not be solved using micro-texturing techniques
- Nano-porous surfaces might reduce friction and wear
- Nano-porous topographies may reduce the use of additives in lubricants

The proposed research in chapters 3 - 8 will investigate the potential of nano-porous surfaces to enhance the retention of lubricant that impacts the tribological properties of sliding surfaces. The interest in these particular topographies had its beginning from the author's earlier research, a work that flourished in content to become a journal article that was included in a special journal publication for superhydrophilic surfaces. The work is cited in the publications citation

page following the Table of Contents. An explanation for including the journal article in this dissertation is offered in section 1.5.

1.5 Inclusion of Journal Paper in the Dissertation

The impetus for including the journal paper entitled, "Superhydrophilic Surfaces on Cu Substrate to Enhance Lubricant Retention" is it served as an inspiration for pursuing the current research on lubricant retention behavior of nano-porous topographies. In this paper, relatively smooth surfaces consisting of as-received Cu were compared to micro-textured and combination micro/nano-textured Cu surfaces for determination of the effect of topographies to enhance lubricant retention. The micro-texturing was done by sandblasting the surface of as-received Cu samples for several durations. Nano-texturing was performed using aluminum-induced crystallization (AIC) of amorphous silicon (a-Si). The parameters affecting the crystallization behavior such as the temperature and duration of annealing were used to create various nano-topographies. Copper and a-Si film are the materials used in the proposed research for this dissertation and these, therefore, have a direct connection to the research in the journal paper.

In the research for the journal paper, the topography's attraction to liquid was tested using surface energy measurements carried out by means of a video-based technique known as contact angle measurements. Water and mineral oil were used as wetting agents for testing the relative surface energy of the topographies. Investigations were done to determine the most hydrophilic (water-attracting) surface. Once the most hydrophilic (superhydrophilic) surface was found, the task was to determine if there was a link between the superhydrophilic surface and lubricant retention by comparing water contact angles (WCA) with those of mineral oil referred to as oil contact angles (OCA). A dynamic (spinning) method was employed to explore correlations between the hydrophilicity of all of the surfaces and lubricant retention. It was surmised that if

certain features and properties of the topographies could be identified as contributors to the retention enhancement of the lubricant, a link existed between superhydrophilic surfaces and lubricant retention.

The results proved that the superhydrophilic surface, which was the combination micro/nano-textured surface, had better lubricant retention capabilities than the independent micro-textured and smooth topographies. The superiority of the micro/nano-textured surface was due to the presence of textures that provided a physical barrier against lubricant displacement during dynamic testing, provided convenient storage facilities between the nano-textures that enhanced the retention capabilities of the surface, and enhanced the energy of the surface by providing a chemistry that was not only favorable to the retention of lubricant, but the roughness of the surface chemistry treatment contributed extraordinary surface area to the topography whose capillarity was enhanced more so than a surface without the nano-texture's roughness. The journal paper's connection to the current research is the common goal of enhancing the retention of lubricant on the surface of nano-topographies.

Another connection of the previous work to the proposed research is the successful topographies had a combination of micro- and nano-porous features. There were particles, but especially, voids and pores that defined the structure of these topographies. For example, the average nano-particle size was 500 nm or 0.5 μm in diameter, nano-void (lateral space between particles) size was about 0.5 μm, and embedded nano-pores in the a-Si film located within the void space of the nano-topography had even smaller diameters. The void size was incorporated in the topographies of the current research. Additionally, the nano-topographies were produced from a-Si film having a thickness of 250 nm, the same as used in the proposed research for smooth and nano-porous topographies.

All of the aforementioned features were important to isolate and investigate their individual contribution to the success of nano-topographies to enhance lubricant retention. The problem is the micro/nano-texture generation process, though successful, did not facilitate easy isolation of the features. As an example, the annealing process which created the nano-topography was inextricably linked to the feature's number and size. In other words, there was no way to unlink the size of the nano-particles with the number of them. The size always grew with the number because as more particles were formed, they would coalesce together to form larger particles. Then, larger particles progressively yielded fewer particles as the annealing process continued.

Fabrication process limitations, too, prevented an in-situ observation of the nano-particle growth so that it was difficult to know the conditions when all of the particles achieved the same size and control the number of them. The random sizes and orientations of the micro-textured surface underneath the nano-topography added to the complexity of the lubricant-surface interaction. Imagine, now, the task of trying to use these irreplicable surfaces for precise characterization of their behavior.

A way was found to utilize the knowledge gained from the research reported in the journal paper and photolithography-based MEMS fabrication techniques to produce nano-porous topographies that had controllable features and characterizability. Micro/nano-porous topographies could now be fabricated and replicated for research purposes. The possibilities of isolating and investigating the topography's features and properties and exploring their connection to lubricant retention are motivation for the research paper presented in chapter 2.

CHAPTER 2

SUPERHYDROPHILIC SURFACE ON Cu SUBSTRATE TO ENHANCE LUBRICANT RETENTION

Julius Morehead and Min Zou*

Mechanical Engineering Department, University of Arkansas

Fayetteville, AR 72701

---

* To whom correspondence should be addressed. Tel: (479) 575-6671, Fax: (479) 575-6982, E-mail: mzou@uark.edu.

Abstract

The loss of lubricant from the surfaces of critical machine parts often leads to friction and heat-related failures which can cause catastrophic damage to machinery. In this study, the effect of micro- and nano-texturing on lubricant retention was investigated. Micro-textures were produced by sandblasting Cu substrates, while nano-textures were created by aluminum-induced crystallization of amorphous silicon. The topography and the wettability of the textured surfaces were characterized by means of scanning electron microscopy and a video-based optical contact angle measuring system, respectively. The lubricant retention on the textured surfaces was investigated using a dynamic method. It was found that superhydrophilic surfaces created by the combined micro- and nano-texturing technique can significantly enhance the lubricant retention on Cu substrates.

Keywords: aluminum-induced crystallization, amorphous silicon, superhydrophilicity, lubricant retention, and Cu substrate.

2.1. Introduction

Lubricants are necessary for the proper functioning of machinery. They are an important part of the total lubrication system—the "lifeblood" of all rotating machinery. Lubricants reduce friction between parts in contact, dissipate heat to maintain suitable operating temperatures of machinery, and protect critical parts from dust and corrosion. To accomplish these tasks effectively, though, lubricants must have sufficient retention time [1].

Various macro-scale techniques have been developed to retain lubricants on a surface. For example, oil-laden felt pads and splash lubrication reservoirs are used for holding lubricants in devices [1][2]. Mechanical barriers created via surface machining and sintering have also been implemented as a means of enhancing lubricant retention on surfaces [3][4].

In the last decade, surface micro-texturing techniques to enhance general lubricant retention have received increasing attention. The application of reactive ion etching to bearings made from silicon carbide was studied by Wang and coworkers to investigate the effect of micro-pits on the loading capacity of water-lubricated thrust bearings [5][6][7]. Laser surface texturing has been investigated to create micro-topographies that produced enhancements in lubricant retention on mechanical face seal surfaces [8][9][10]. Along the same lines, a lubrication technique identified as micro-plasto hydrodynamic lubrication (MPHL) was used to achieve enhanced lubricant permeability between workpiece asperities and contacting tools during sheet metal forming [11].

It is well known that nanostructures possess high surface area-to-volume ratios. Higher surface areas are the result of increased surface roughness. According to Wenzel’s model [12], surface roughness, together with the hydrophilic properties of a surface, may lead to a superhydrophilic

surface. Superhydrophilic surfaces may increase the surface's affinity to lubricant, and possibly, enhance lubricant retention.

Although it is well known that surface texturing can significantly alter the wettability of a surface, no report has been found on the effect of surface wettability, particularly superhydrophilicity, on lubricant retention. Since Cu is widely used in machinery bearings [13] and seal assemblies, it was selected in this study as the substrate for generating superhydrophilic surfaces and investigating the relationship between the wettability of Cu substrates and oil retention.

The creation of superhydrophilic surfaces on Cu substrate is a relatively new area of research. Superhydrophilic $Cu(OH)_2$ nanowires were produced by a solution-immersion process using aqueous sodium hydroxide and potassium persulfate on the surface of an immersed Cu plate [14]. Similarly, membrane formations featuring nano-belts and "stick bundles" were types of nanosurfaces created from the modification of $Cu(OH)_2$ [15]. Superhydrophilic surfaces were also created by exposing TiO_2 deposited on Cu to ultraviolet light [16][17]. The irradiated Cu produced highly-wetting surfaces for improvement in critical heat flux related to pool and nucleate boiling. Other superhydrophilic nanostructures were formed on the surface of Cu foil by galvanic cell corrosion using aqueous phosphoric acid droplets [18]. However, these techniques for generating superhydrophilic surfaces do not provide separate control of the surface topography at both the micro- and nano-scales, which could be important for lubricant retention.

In this study, sandblasting (SB) and aluminum-induced crystallization (AIC) of amorphous silicon (a-Si) were used to create both micro- and combined micro/nano-textured hydrophilic and

superhydrophilic surfaces on Cu substrates. AIC of a-Si technique has been developed by Zou et al. to generate micro/nano-textured, superhydrophilic surfaces on glass and stainless steel substrates for potential applications such as anti-fogging, self-cleaning surfaces, and oil transportation [19][20]. This is the first time it is combined with the SB technique for generating micro/nano-textured surfaces on Cu substrates for lubricant retention study.

2.2. Experimental Details

Cu samples measuring 13 mm wide x 25 mm long x 0.82 mm thick were cut from a Cu sheet (product no. 9821K31, McMaster-Carr, Elmhurst, IL) and used as substrates in the study. Four groups of samples were created. The samples in groups A, B, C, and D were: as-received, smooth Cu substrates (AR); samples micro-textured by sandblasting (SB); samples nano-textured by AIC (AIC); and samples micro- and nano-textured by combining sandblasting with AIC (SB/AIC), respectively.

The samples from group B were micro-textured using sandblasting medium with an average particle size of 165 μm. Blasting pressure and distance between the sandblasting gun tip and samples were 240 kPa and 203 mm, respectively. During sandblasting, the stream of blasting medium was swept vertically across the sample surfaces. Sandblasting duration was varied from 1 s to 10 s in 3 s increments. After sandblasting, group B samples were cleaned ultrasonically using acetone for 20 min duration, followed by isopropyl alcohol for the same duration to remove any organic contaminants and sandblasting remnants from the sample surfaces, and finally rinsed with de-ionized water to remove the isopropyl alcohol residue.

Characterization of the samples was carried out next. A profilometer (Dektak 3030, Sloan Technology Corporation, Santa Barbara, CA) was used to characterize the roughness of the

sample surfaces. A 20 μN scanning force and 2 mm long scan length were used to trace the surface profile of the SB micro-topography. Three average depth readings were recorded for each sample. A scanning electron microscope (SEM) (FEI/Philips XL30 ESEM, Hillsboro, Oregon), was employed to characterize the topography of the samples. All SEM micrographs were taken at a 45° angle. The wettability of the samples was characterized by a water contact angle (WCA) measurement system (OCA 15, DataPhysics Instruments GmbH, Filderstadt, Germany) using the sessile drop method. De-ionized water droplets having a volume of 3 μL were dispensed onto each sample through a syringe at a rate of 1 μL/s and recorded by a video-based recording system. Three WCA measurements were taken on each sample to evaluate the uniformity of the samples. The same characterization procedure as used for WCAs was used to obtain oil contact angle (OCA) measurements to examine the relationship between the hydrophilicity and oil affinity of AR, SB, and SB/AIC topographies.

Samples in group C were used to investigate the effect of AIC of a-Si for enhancing the wettability of Cu substrates. A 250 nm thick a-Si film was deposited on the AR samples using plasma enhanced chemical vapor deposition (PECVD). The PECVD system was operated at a RF power of 20 W, substrate temperature of 250°C, chamber pressure of 133 Pa, and SiH_4 flow rate of 85 sccm. After a-Si deposition, the samples were placed in a thermal evaporator for depositing a film of Al about 530 nm thick onto the Cu/a-Si substrates. The settings chosen for evaporator operation were a base pressure of 3.4E-04 Pa and 4 nm/s deposition rate. The samples were allowed to cool in the evacuated chamber for 10 min duration.

Following Al deposition, group C samples were annealed at various conditions for investigating the impact of annealing on the wettability of the samples. The annealing temperatures used were

650°C, 750°C, and 850°C, while the annealing durations were 5 s and 10 s. After annealing, the samples were submersed in a solution of Al etchant, type D (Transene Company, Inc., Danvers, MA) at 50°C for a minimum of 10 min duration to remove excess Al. Thorough rinsing with de-ionized water removed the chemical residue left behind by the etching process. The samples were then dried using N_2.

Once the effects of sandblasting and AIC of a-Si on surface wettability were investigated, attention turned to combining the results of both texturing techniques. The most hydrophilic result from the SB and AIC samples was used to produce a combined micro/nano-textured surface that exhibited surface wettability characteristics superior to either technique separately. Micro-textures were first produced on the samples in group D by sandblasting, and then nano-textures were created on the micro-textured surfaces using the AIC of a-Si technique to produce superhydrophilic surfaces for studying the relationship between superhydrophilicity and lubricant retention.

The oil retention capability of AR, SB, and SB/AIC samples was investigated using a dynamic method that included the following steps: (1) measuring the weights of all samples; (2) dispensing a known amount of oil onto the samples; (3) placing the samples on a spin coater; (4) spinning the samples for a predetermined speed and duration; and (5) measuring the weights of all samples again after spinning. Subtracting the final weights from the initial weights of the samples gave the weight of oil lost during spinning and thus provided information about oil retention.

More specifically, the samples were first weighed using a digital scale (Adventurer Pro AV64C, Ohaus Corporation, Pine Brook, NJ). Next, a syringe was used to dispense 50 µL (0.04 g) of

mineral oil onto each sample. To ensure uniform distribution of oil, a spin coater (KW-4A, Chemat Technology, Inc., Northridge, CA) was used at a low spin speed of 500 rpm for 9 s to spread the oil across the surface of the samples. Afterward, the spin speed was increased to displace the oil for lubricant retention testing. Nine spin speeds, starting at 1000 rpm, were used. The spin speeds were increased by 800 rpm increments until reaching 7200 rpm. The duration at each spin speed was 105 s. After each spin test was completed, the samples were weighed again using the digital scale.

2.3. Results and Discussion

Figure 1 shows SEM micrographs taken from an AR sample and an SB sample at a 45° oblique angle. Figures 1 (a) and (b) were taken at a magnification of 500x, while Figures 1 (c) and (d) were taken at a magnification of 5000x. Figures 1 (a) and (c) show that the surface of the AR sample is relatively smooth, except for the presence of grooves. Profilometry measurements reveal that the average groove depth of AR Cu is 72 nm. It is believed that these grooves were created by the manufacturer during surface polishing. Figures 1 (b) and (d) illustrate the roughness of the SB micro-topography. The sizes of the craters created by sandblasting typically ranged from a few μm to over 20 μm. Profilometry measurements taken from sandblasted samples of this study showed randomized peak-to-valley distances ranging between 2 and 18.2 μm.

Figure 2 shows the relationship between the WCAs of the SB samples and the SB duration. Initially, the WCA decreased with SB duration until 4 s; it then increased for longer SB duration up to 7 s before flattening out at 10 s. This WCA changing trend with the SB duration correlates well with the changing trend of the average depth of the surface topography created by

sandblasting. Nine profilometry measurements each for the 1 s, 4 s, 7 s, and 10 s sandblasting durations were averaged to obtain average depths of 2.5, 5.5, 4.8, and 5.1 μm, respectively. The average depth created by sandblasting increased first with increasing sandblasting duration and then decreased, and finally reached a stable value. Figure 2 reveals that sandblasting Cu substrate for 4 s resulted in the lowest WCA (61°) of the SB samples, which corresponded to the largest value for average depth of 5.5 μm.

The SEM micrograph shown in Figure 3 was taken from a sample surface in group C. The nano-sized random structures are Si crystallites produced by AIC of a-Si on AR Cu substrates. The structures uniformly covered the Cu substrate. Detailed analyses of these Si crystallites can be found in our previous publications [21][22][23].

Crystallization of a-Si, and the resulting topography and wettability of Cu substrate, is strongly affected by the annealing temperature and duration. To achieve the best wettability, the effects of annealing temperature and duration on WCAs were investigated. Figure 4 shows the result. In the figure, there are six columns which show the annealing temperatures used to create the AIC nano-topographies used in the study. The first two columns relate to 650°C, the middle two columns correspond to 750°C, and the last two columns are 850°C. The annealing durations at each temperature were 5 s and 10 s. It is clear that the WCAs of the samples annealed at 650°C and the one annealed at 750°C/5 s are much larger than the samples annealed at 750°C/10 s, 850°C/5 s, and 850°C/10 s. Although 750°C/10 s and 850°C/5 s annealing conditions produced similar WCAs, the 750°C/10 s condition was selected because of its lower energy input for generating nano-structures on SB Cu surfaces to produce combined micro- and nano-textures for further studies.

Based on the WCA results from SB (Fig. 2) and AIC (Fig. 4) samples, the 4 s sandblasting duration and 750°C/10 s annealing condition were selected to produce micro/nano-textures for the investigation of lubricant retention. An SEM micrograph demonstrating the combined micro- and nano-scale surface topography is shown in Figure 5. In the figure, the large random structures were created by sandblasting, while the small, lighter-colored structures are Si crystallites produced by AIC of a-Si.

The WCA results for AR, SB, and AIC samples were 87°, 61°, and 40°, respectively. The reduction of the WCA of the SB sample compared to the AR sample can be easily explained by Wenzel's model which suggests that surface roughness can enhance the hydrophilicity of a hydrophilic surface [12]. Similarly, the small WCA of the AIC sample was due to the hydrophilic nature of Si and the roughness of the nano-textures enhancing the hydrophilicity of the surface. The WCA of the micro/nano-textured SB/AIC sample was very small as manifested by the extremely rapid spreading of the water droplets on the surface. This is, again, because the Si nano-textures are more hydrophilic. They also have small radii of curvature which can generate strong capillary interactions between water and the nano-textures thus enhancing the hydrophilicity. In addition, nano-textures provide increased roughness on top of the SB micro-topography, which according to Wenzel's model, will further enhance the hydrophilicity.

The superhydrophilicity of the SB/AIC sample was verified by video images taken of water droplets as they were brought into contact with the surface. A 25 frames/s rate was selected to appropriately monitor the spreading rate of a 3 μL droplet dispensed onto the micro/nano-topographies. The frames were advanced sequentially, and WCAs were noted. At frame 6 or about 0.2 s after the droplet contacted the surface, the droplet had disappeared completely into

the textured surface, resulting in a WCA of 1°. The video image, taken at 0.2 s after dispensing, is shown in Figure 6.

Figure 7 shows video images of OCAs taken on AR, SB, and SB/AIC samples as a 3 µL oil droplet was dispensed onto each surface. The OCAs of the AR, SB, and SB/AIC samples are 29°, 19°, and 5°, respectively, which indicate that the highest oil spreading occurred on the micro/nano-textured, superhydrophilic SB/AIC sample (WCA of 1°), followed by the micro-textured, hydrophilic SB sample (WCA of 61°), and then the relatively smooth, AR sample with the least hydrophilicity (WCA of 87°). Figures 7 (a), (b), and (c) insets show photographs of AR, SB, and SB/AIC samples, respectively, 1 min after depositing 50 µL of oil on the surfaces of the samples. Visually, it is clear that the oil droplet remained confined in a small area after deposition on the AR sample, while oil spread out much more on the SB sample, covering the majority of the surface. The oil on the SB/AIC sample spread over the entire textured part of the surface. It should be noted that the two edges of the SB/AIC sample were not textured because they were covered by a tape to hold the sample during the texturing processes. Consequently, the oil droplet was not able to spread to these edges due to the lower oil affinity of the unprocessed portion of the surface.

To quantitatively evaluate the effects of surface texturing on oil retention, a dynamic test method was used. The hypothesis is that the viscous and cohesive intermolecular forces of the oil and the surface's capillary force, combined with the restraining force provided by the physical barriers of the SB craters and nano-textures, would oppose the oil-dispersing centrifugal force generated during spinning [24]. The results are presented in Figure 8 which shows the

relationship between retained oil weight and spin speed of AR, SB, and SB/AIC topographies after spinning the samples for 105 s.

It can be observed from Figure 8 that at low spin speed (1000 rpm), the retained oil weight is nearly the same for the 3 samples. This means that surface texturing does not have a significant impact on oil retention at low speed. The retained oil weights of all samples quickly decreased in a similar manner with the increase in spin speed up to 1800 rpm. However, for spin speeds higher than 1800 rpm, the trends of oil retention diverge. The oil retention of the AR sample continued to decrease rapidly with the increase in spin speed to 7200 rpm, while the oil retention of the SB and SB/AIC samples decreased slowly with the increase in spin speed up to 3400 rpm. At 4200 rpm and higher speed, however, the retained oil weights of SB and SB/AIC samples differed significantly. The oil weight retained on the SB/AIC sample was more than that on the SB sample in the 4200 - 7200 rpm speed range. The rate of oil loss was slightly faster on the SB sample in this range. At the spin speed of 7200 rpm, the weights of the oil on the sample surfaces were 0.3 mg, 1.0 mg, and 1.4 mg for the AR, SB, and SB/AIC samples, respectively, which indicate that the oil retention of the SB/AIC sample is about 1.5 times that of the SB sample and 5 times that of the AR sample.

The retention results of Figure 8 can be understood as follows: after dispensing oil onto the SB and SB/AIC samples, a portion of the oil filled the valleys, while the excess oil remained on the top of the samples out of contact with the textures and thus was easily spun off. Therefore, at low spin speeds, AR, SB, and SB/AIC samples exhibited similar trends. At higher spin speeds, the oil in the valleys of the SB and SB/AIC samples was more difficult to displace than the oil floating on top of the AR samples. The effect of micro-texturing clearly played an important

role in oil retention. More importantly, the application of nano-textures combined with micro-textures enhanced lubricant spreading and retention because of the increased affinity of the surface to oil. Nano-textures also increased the retention of the oil due to the textures themselves providing barriers against lubricant displacement. Therefore, the micro/nano-textured, superhydrophilic surface significantly enhanced oil retention compared to the micro-textured, SB sample.

2.4. Conclusions

Surface wettability of three different topographies and the effects of surface texturing on lubricant retention were studied. It was found that sandblasting changed AR Cu surfaces to hydrophilic ones by creating micro-textured surfaces, while the combination of sandblasting and AIC of a-Si produced micro/nano-textured topographies resulting in superhydrophilic surfaces. Compared to smooth, AR Cu substrates, micro/nano-textured, superhydrophilic surfaces significantly enhanced oil retention on the Cu samples. At the spin speed of 7200 rpm, the oil retained on the SB/AIC samples is about 5 times that of the oil retained on smooth, AR Cu samples.

Acknowledgments

We thank the US National Science Foundation (NSF) for its support under grants CMS-0600642 and CMS-0645040. We also thank Dr. Andrew Wang from Ocean NanoTech, LLC, and the Electron Optics Facility (EOF) of the University of Arkansas for equipment use.

References

1. Weber, H., “Not Just Simply Pumps”, *International Paper World*, No. 4, pp. 10-11, 2009.

2. Hafner, E., “Bearing Down on Lubrication-Part 2”, *Power Transmission Design*, Vol. 22, No. 7, pp. 51-53 1979.

3. Lim, S., and Seah, W., “Design and Manufacture of Long Life PM Bearings”, *Journal of Materials Processing Technology*, Vol. 23, pp. 97-105, 1990.

4. Mohler, J., “Porous Sleeve Bearings”, *Plant Engineering*, Vol. 32, No. 23, pp. 147-150, 1978.

5. Wang, X., Kato, K., and Adachi, K., “The Lubrication Effect of Micro-Pits on Parallel Sliding Faces of SiC in Water”, *Tribology Transactions*, Vol. 45, No. 3, pp. 294-301, 2002.

6. Wang, X., K. Kato, K., and Adachi, K., "Loads Carrying Capacity Map for the Surface Texture Design of SiC Thrust Bearing Sliding in Water", *Tribology International*, Vol. 36, No. 3, pp. 189-197 2003.

7. X. Wang, K. Adachi, K. Otsuka, and K. Kato, "Optimization of the Surface Texture for Silicon Carbide Sliding in Water", *Applied Surface Science*, Vol. 253, No. 3, pp. 1282-1286, 2006.

8. Yu, X., et al., "Experimental Investigation on Friction Performance of Mechanical Seals with a Laser-Textured Seal Face", *Anonymous Trans Tech Publications Ltd*, Vols. 532-533 pp. 81-84, 2006.

9. Etsion, I., Kligerman, Y., and Halperin, G., "Analytical and Experimental Investigation of Laser-Textured Mechanical Seal Faces", *Tribology Transactions*, Vol. 42, No. 3, pp. 511-516, 1999.

10. X. Peng, et al., "Effects of Dimple Geometric Parameters on the Performance of a Laser-Textured Mechanical Seal," *Key Engineering Materials*, Vols. 373-374, pp. 766-769, 2008.

11. Nilsson, M., et al., “Strategic Surface Topographies for Enhanced Lubrication in Sheet Forming of Stainless Steel”,*International Journal of Surface Science and Engineering*, Vol. 4**,** No. 1, pp. 68-79, 2010.

12. Wenzel, R., “Resistance of Solid Surfaces to Wetting by Water”, *Industrial and Engineering Chemistry,*Vol. 28, No. 988, pp. 7426–7431, 1936.

13. Unlü, B., Investigation of Tribological and Mechanical Properties of Metal Bearings”, *Bulletin of Material Science*, Vol. 32, 451–457, 2009.

14. Pan, Q., Jin, H., and Wang, H., “Fabrication of Superhydrophobic Surfaces on Interconnected $Cu(OH)_2$ Nanowires via Solution-Immersion”, *Nanotechnology*, Vol. 18, pp. 355605-355608, 2007.

15. Tang, K., et al., “Fabrication of Superhydrophilic Cu_2O and CuO Membranes”, Journal of Membrane Science, Vol. 286, pp. 279-284, 2006.

16. Takata, Y., et al., “Pool Boiling on a Superhydrophilic Surface”, *Journal of Energy Research*, Vol. 27, No. 2, pp. 111-119, 2003.

17. Qui, Y., and Liu, Z., “Nucleate Boiling on the Superhydrophilic Surface with a Small Water Impingement Jet”, *Journal of Heat* Transfer, Vol. 51, Nos. 7-8, pp. 1683-1690, 2008.

18. Wu, X., and Shi, G., “Fabrication of a Lotus-Like Micro-Nanoscale Binary Structured Surface and Wettability Modulation from Superhydrophilic to Superhydrophobic”, *Nanotechnology*, Vol. 16, pp. 2056-2060, 2005.

19. Kollias, K., and Wang, H., “Production of a Superhydrophilic Surface by Aluminum-Induced Crystallization of Amorphous Silicon”, *Nanotechnology*, Vol. 19, pp. 465304-465310, 2008.

20. Wang, H., Zou, M., and Wei, R., "Superhydrophilic Textured-Surfaces on Stainless Steel Substrates”, *Thin Solid Films*, Vol. 518, No. 5, pp. 1571-1574, 2009.

21. Nair, R., and Zou, M., “Surface-Nano-Texturing by Aluminum-Induced Crystallization of Amorphous Silicon”, *Surface & Coatings Technology*, Vol. 203, Nos. 5-7, pp. 675-9, 2008.

22. Zou, M., et al., “Self-Assembly of Si Nanoparticles Produced by Aluminum-Induced Crystallization of Amorphous Silicon Film”, *Electrochemical and Solid-State Letters*, Vol. 10, No. 2, pp. K1-K9, 2007.

23. Zou, M., Cai, L., and Dorey, S., “Self-Assembly of Aluminum-Induced Silicon Nanowires”, *Electrochemical and Solid-State Letters*, Vol. 9, No. 4, pp. G133-G135, 2006.

24. Emslie, A., Bonner, F., and Peck, L., “Flow of a Viscous Liquid on a Rotating Disk”, *Journal of Applied Physics*, Vol. 29, pp. 858-862, 1958.

Figures

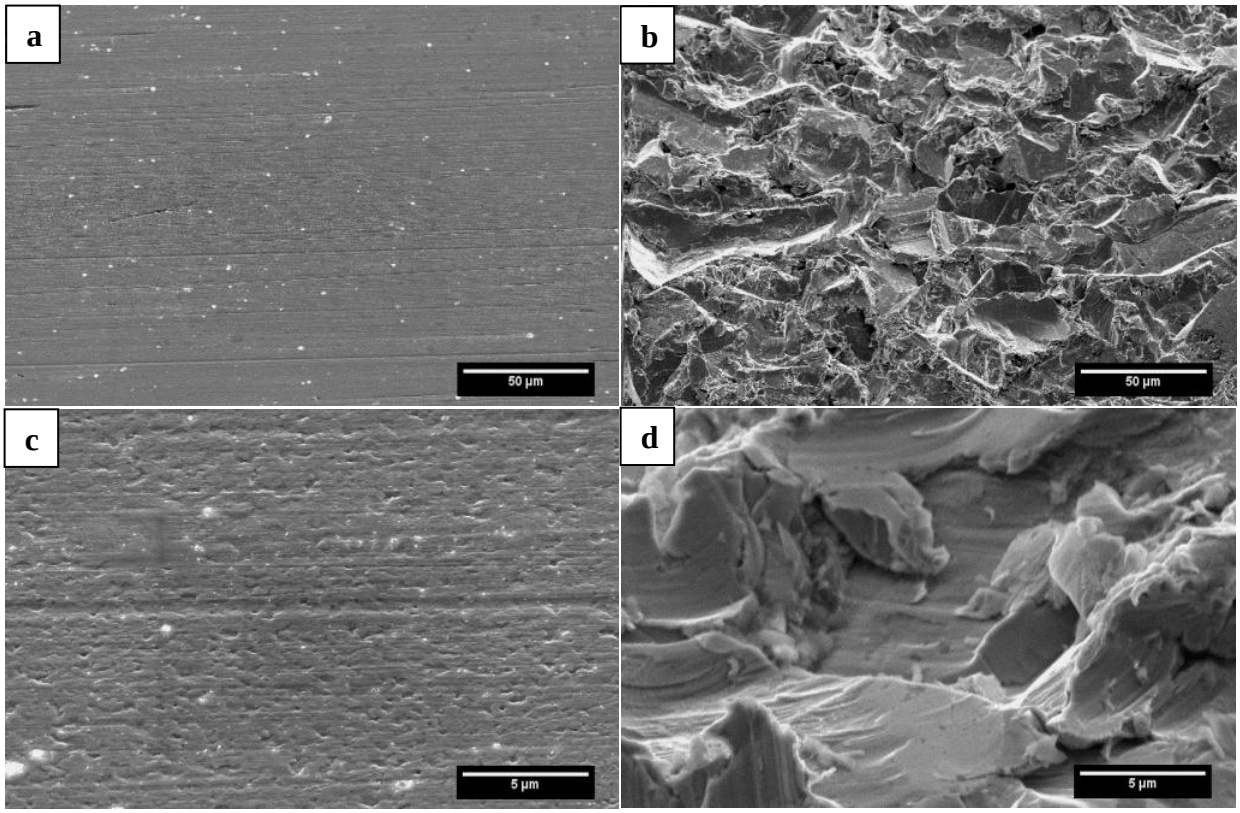

Figure 2.1a - d. SEM micrographs taken on an AR sample and an SB sample. (a) AR sample and (b) SB sample at 500x magnification. (c) AR sample and (d) SB sample at 5000x magnification (*Images by the author*).

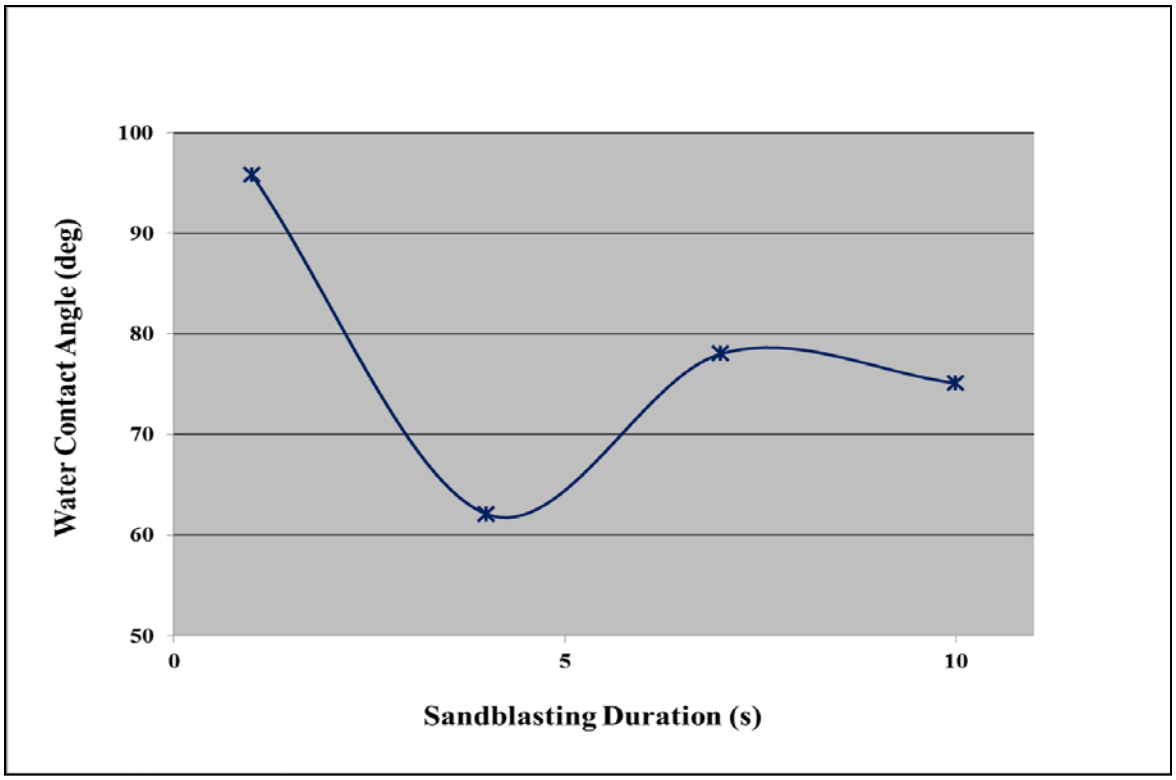

Figure 2.2. The effect of sandblasting duration on the water contact angle of a sandblasted surface. The most hydrophilic behavior of sandblasted samples occurs at 4 s duration (*Image by the author*).

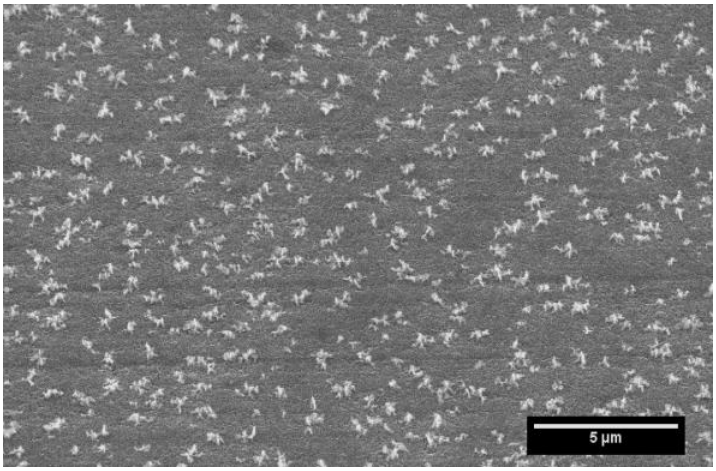

Figure 2.3. Nano-structures produced on AR Cu by AIC of a-Si technique (*Image by the author*).

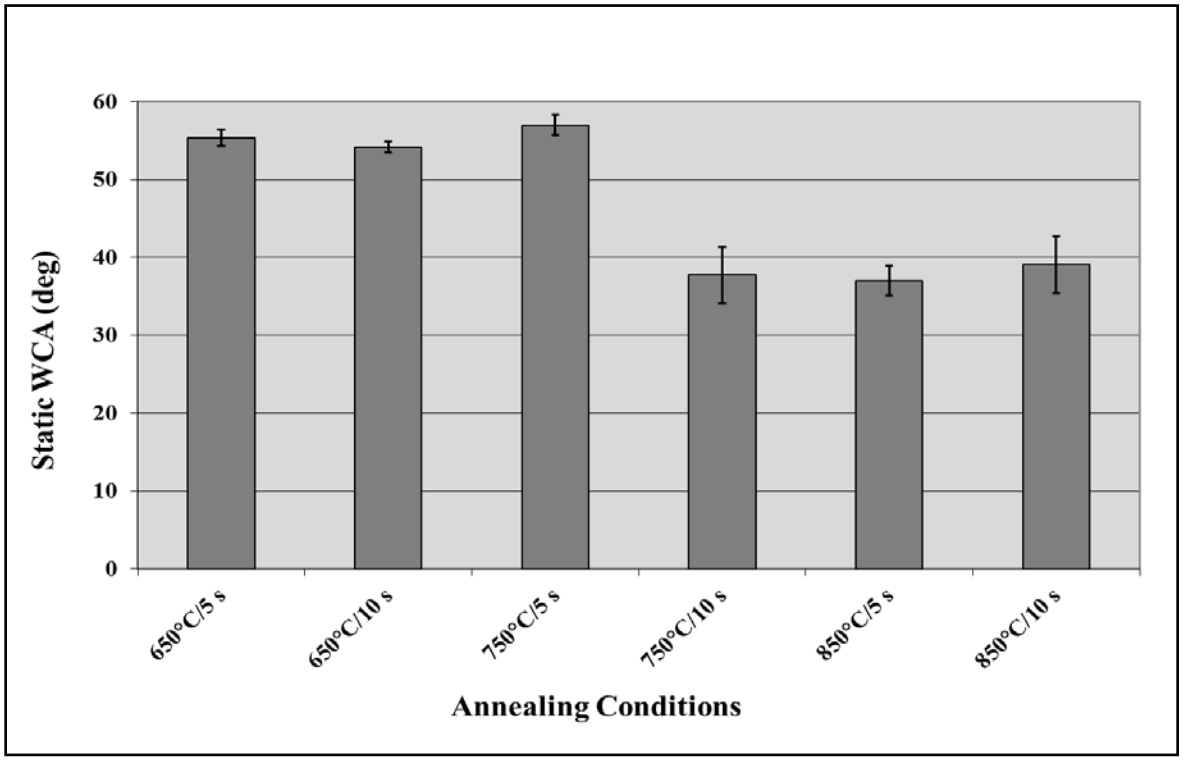

Figure 2.4. The effect of AIC of a-Si annealing conditions on the static water contact angle. The optimum hydrophilic surface with the lowest annealing temperature occurred at 750°C/10 s (*Image by the author*).

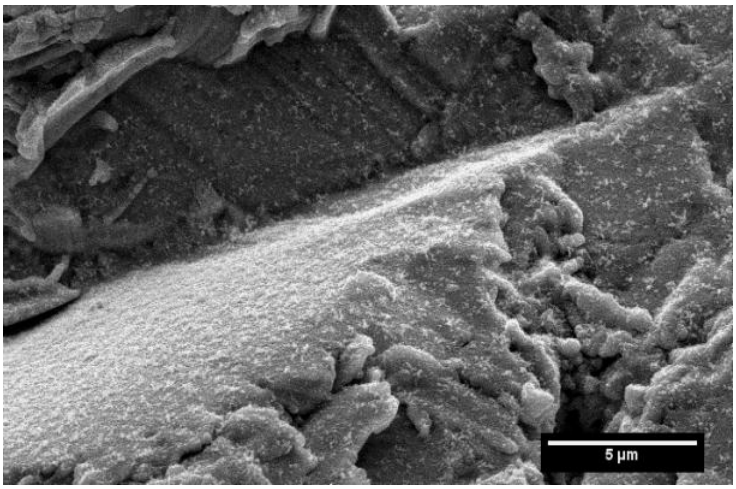

Figure 2.5. SEM micrograph of a surface produced by combining SB and AIC of a-Si texturing techniques. Nano-texture coverage remained uniform despite the random surface orientation (*Image by the author*).

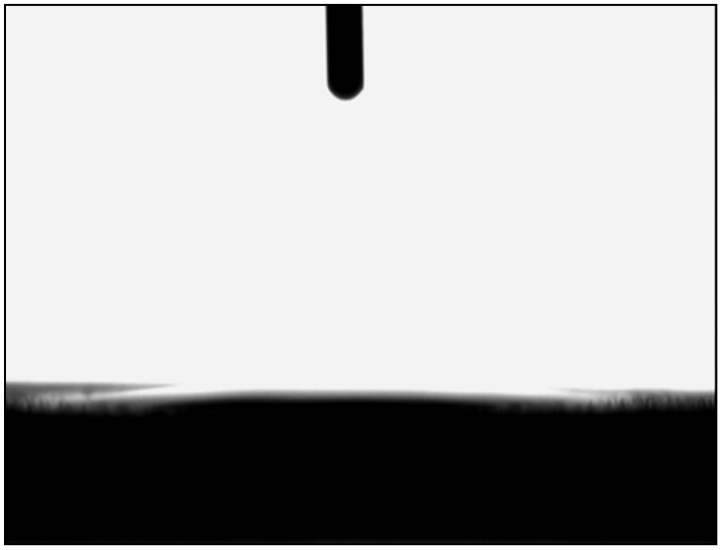

Figure 2.6. Video image of a 3 µL water droplet dispensed on the micro/nano-textured, superhydrophilic surface. The image was taken at 0.2 s after dispensing, and the WCA is about 1° (*Image by the author*).

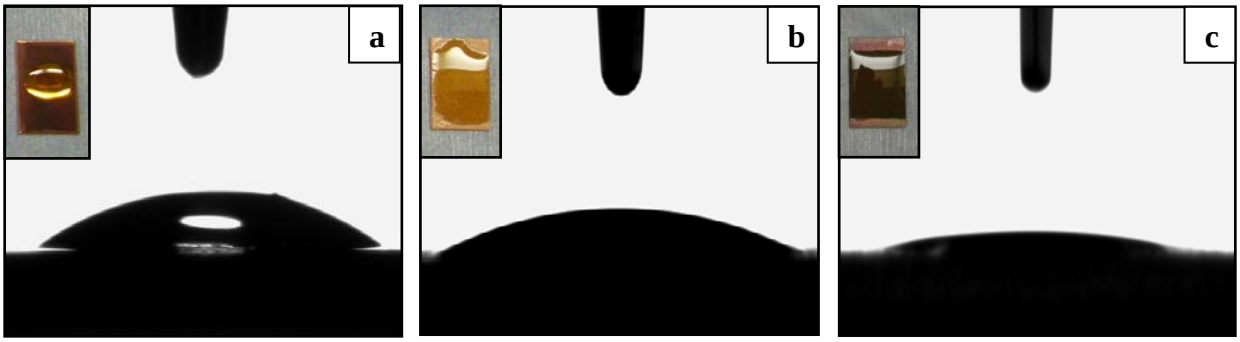

Figure 2.7. Video images of oil contact angles (OCAs) for (a) AR, (b) SB, and (c) SB/AIC samples. OCAs on AR, SB, and SB/AIC samples stabilized at 29°, 19°, and 5°, respectively. The inset photographs show AR, SB, and SB/AIC samples 1 min after deposition of 50 µL of oil on them (*Images by the author*).

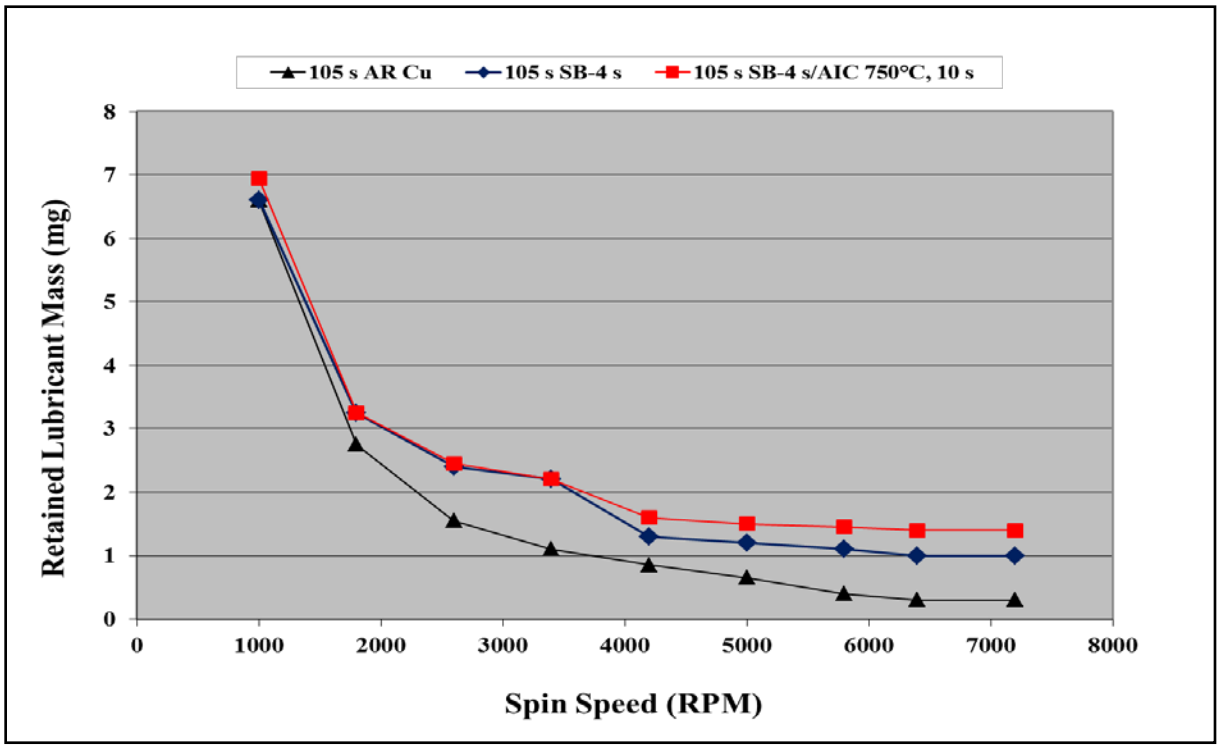

Figure 2.8. Comparisons of the retained lubricant mass on the AR Cu, SB, and SB/AIC samples as a function of spin speed. The samples were spun for 105 s duration at each of the nine spin speeds. At 7200 rpm, the SB/AIC sample retained about 1.5 times the oil of SB and 5 times the oil of AR Cu samples (*Image by the author*).

CHAPTER 3

BACKGROUND AND APPLICATIONS

3.1 Scope of Background and Applications

The task of reviewing a subject as broad as lubricated moving machine components is clearly difficult. Therefore, it was necessary to restrict the scope of the review to a manageable level. Since the research objective was to produce a novel method for enhancing the retention of lubricants that affect the tribological properties of sliding and conformal (fitted-together) surfaces, the focus of the review should certainly include these types of surfaces. Limiting the review to these machine components seemed, in the beginning to be manageable, but even this classification of moving components was too extensive to discuss in a satisfactory manner. To resolve this conundrum, a few paragraphs will discuss the omitted types of sliding and conformal surfaces and the reasons for doing so. Afterward, a clearer, more focused review theme will emerge.

Machine components known as rolling element assemblies include ball, tapered, and needle bearing, as well as gears. These assemblies are used to support the rotation of shafts or parts rotating on stationary shafts. They perform a combination of sliding, rolling, and surface deformation that result in lubrication known as elasto-hydrodynamic lubrication. Even though sliding friction occurs during the assembly's operation, and this would ordinarily be of interest for the friction reduction methods proposed in the author's research, these assemblies are omitted from the review. The sliding occurs at points where the two surfaces meet (formally known as Hertzian contact). This means the assemblies are close to their minimum friction values already, so nothing tangible would result from incorporating nano-pores on their surfaces. Besides, it has

been shown that adding porous topographies to Hertzian-contact types of surfaces like rolling elements and gear teeth initiates fracturing and leads to premature failure of the components.

Other bearing assemblies will be omitted as well. Hydrostatic bearings rely upon externally-pressurized lubricant to flow between the contact surfaces of static or stationary bearings and the rotating component. The high pressure flow provides surface separation for friction reduction and exceptional load support, even without the rotation of the parts. While it is acknowledged that the surfaces are both sliding and conformal, the external pressure is an integral part of the operation of the bearing system, making the addition of nano-porous topographies for enhancing lubricant retention unnecessary.

Porous metallic bearings and bushings are very popular types of sliding, conformal surfaces which are manufactured using powder metallurgy or drilling techniques to create pores for the containment of lubricant. Either solid or liquid lubricant can be used in these components. Graphite, molybdenum disulfide (MoS_2), lead (Pb), and polytetrafluoroethylene (PTFE) are products frequently amalgamated into porous bearings for situations where dry lubrication is desired. Solid-lubricated porous bearings, however, are not considered good prospects for the current research because they are not plagued by the evaporation and migration issues that liquid-lubricated ones may encounter. Further, porous bearings do not need nano-porous topographies since the entire bearing body is purposely designed as a reservoir for the retention of liquid lubricants.

The focus of this review will, instead, be limited to sliding, conformal surfaces that depend upon fluid-film lubrication for the generation of hydrodynamic pressure. Sleeve-like and squeeze film bearings and bushings which support camshafts, piston wrist pins, crankshaft and turbocharger shaft journals, in addition to sliding seal mechanisms such as mechanical face seals and engine

cylinder rings and liners are widely-used machine components that depend upon hydrodynamic lubrication [22][23]. They could benefit from nano-porous topographies to reduce friction and the catastrophic damage that might occur when their sliding components operate during starved lubricant conditions.

3.2 Hydrodynamic Lubrication Regimes Explained

Sliding, conformal machine surfaces which depend upon hydrodynamic lubrication for their operation encounter three lubrication regimes. The regimes are denoted as boundary, mixed, and full-film [23]. These are illustrated on a graph known as the Stribeck curve similar to the one shown in Figure 3.1 [24]. The graph shows the dimensionless coefficient of friction (COF) on the vertical axis and the Sommerfeld number on the horizontal axis. The figure is a generalized representation of the Stribeck curve, so the numerical values are omitted. The Sommerfeld number is a product of the lubricant's viscosity and the sliding surface's rotational speed divided by the external load per-projected-area (or pressure) on the surfaces. The radial clearance ratio normally appears as a constant in the Sommerfeld number. It is computed using the shaft radius and clearance between the shaft and sleeve-like bearing of a specific application, but it is not included in the figure for simplicity.

Below are the conditions which should be understood when using the Stribeck curve to describe the behavior of sliding machine components that rely upon hydrodynamic lubrication:

1. The '*x*', '*y*', and '*z*' axes directions are horizontal, vertical, and into the page, respectively.
2. The flow is fully-developed and laminar, i.e., there is no flow in the '*y*' or '*z*' direction.
3. The lubricant obeys Newton's laws of viscous flow.
4. The lubricant is incompressible.
5. The viscosity of the lubricant is constant throughout the film.
6. The lubricant velocity is dependent on the '*y*' coordinate only.
7. The curvature of the sliding surface can be ignored.
8. The film pressure is constant in the '*y*' and '*z*' directions, and depends only upon '*x*'.
9. The inertial effects of the lubricant are neglected.

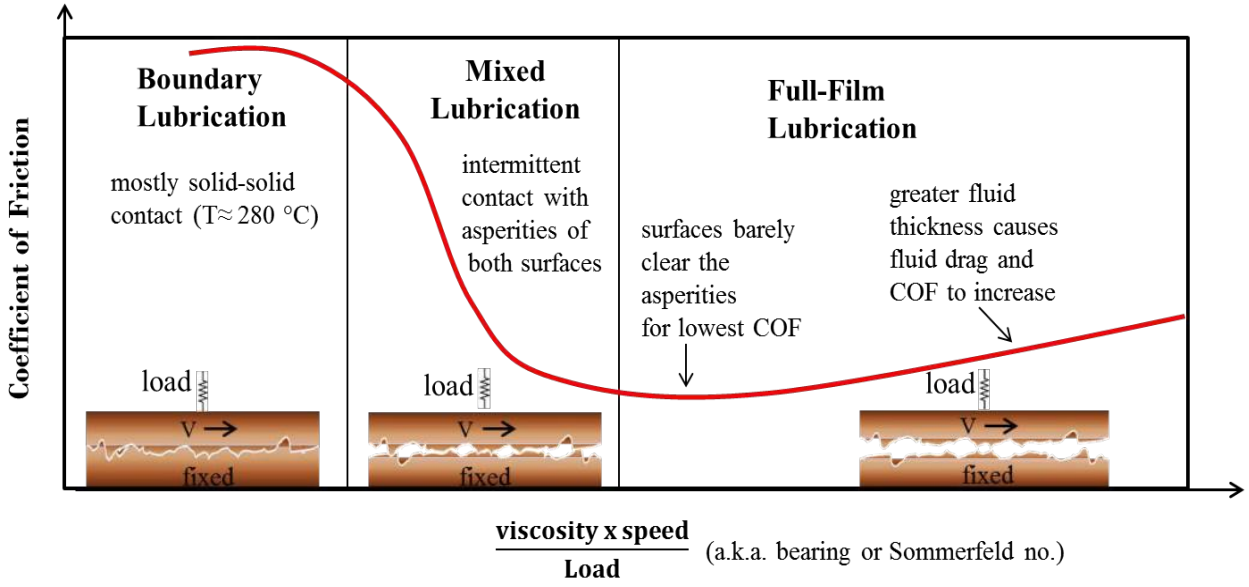

Figure 3.1. The Stribeck curve showing the boundary, mixed, and full-film lubrication regimes encountered by sliding, conformal surfaces. The inset images illustrate the gradual opening force resulting from the hydrodynamic pressure of the lubricant (*Image from the author*).

Included in the graph of Figure 3.1 are inset images of two surfaces in relative motion. The movable surface is shown as the top surface having a velocity, *V*, as it moves to the right. Attached to the moving surface is an external load represented by a spring. The spring imposes a closing force on the sliding assembly. It opposes the hydrodynamic opening pressure of the lubricant to limit the leakage of fluid in the case of mechanical seals, or it mimics the load placed on rotating shafts such as those found on crankshaft journal bearings.

The stationary surface is described as *fixed*, meaning it has no velocity. The velocity of the sliding surface, as illustrated in the figure, starts from zero at the extreme left on the horizontal axis and increases in magnitude toward the right. At some point during the velocity increase, an ideal velocity is obtained that is sufficient to generate hydrodynamic pressure to separate the surfaces

The COF is shown to be at its maximum value at the beginning of the surface's movement because the asperities of both surfaces are in direct contact. As the velocity gradually increases, the hydrodynamic effect causes the asperities on the two surfaces to incur decreasing contact until they no longer touch. This condition allows the minimum COF value to be achieved. Further increase of the velocity of the moving surface causes the lubricant's thickness to rise higher than the amount required for clearing the asperities. In response, the COF value slowly increases again due to the additional sliding friction of the thicker lubricant's layers.

Now, a closer look between the sliding surfaces of Figure 3.1 will allow a better understanding of how the lubricant and surfaces interact to generate hydrodynamic pressure. As the movable surface proceeds from standstill, the movable surface and the stationary one experience solid contact. This defines the boundary lubrication regime of the Stribeck curve. As the moving surface drags fluid between the surfaces owing to the no-slip phenomenon, the lubricant's presence reduces the COF and permits the film's rising thickness to create a small gap between the surfaces. The surfaces are now in the mixed lubrication state, so named because partial contact remains between the asperities on both surfaces despite the presence of lubricant.

An illustration of the hydrodynamic effect is shown in Figure 3.2. Note that actual sliding surfaces are not perfectly flat, and in fact resemble the converging gap shown. The law of conservation of mass states that the entering fluid mass must equal the exiting mass. However, as the lubricant enters from the left through the wider opening and exits through the smaller area on the right, the lubricant attempts to accelerate but is restrained by the two surface's velocities. As a consequence, the fluid develops hydrodynamic pressure [25]. The pressure's profile is drawn above the stationary surface in the figure.

A Newtonian fluid located between two parallel plates in which one is a moving surface develops shearing stress in direct proportion to the velocity of the plate surface [26]. This results in the linear behavior of the velocity profile of the fluid as demonstrated by the dotted lines extending from the stationary surface to the movable one of Figure 3.2. Observe that the velocity profiles of the entering and exiting lubricant no longer exhibit the linear behavior of Newtonian fluids because of the effect of non-parallel surfaces. Due to amassing hydrodynamic pressure, the entrance profile retracts parabolically in opposition to the incoming fluid while the exit profile distends in the direction of the exiting fluid. To equalize the pressure, the gap between the surfaces must widen, resulting in their separation. The surfaces can then achieve the final lubricating regime, full-film lubrication.

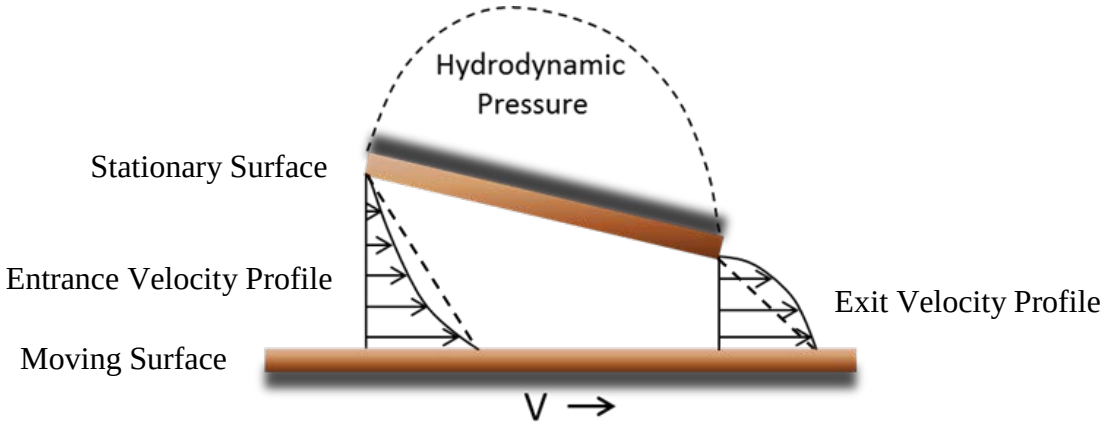

Figure 3.2. An illustration of lubrication occurring between the surfaces of sliding, conformal machine components. Forcing lubricant into a converging gap creates hydrodynamic pressure which separates the surfaces (*Image from the author*).

The Stribeck curve of Figure 3.1 shows a sliding, conformal component's normal progression through the lubrication regimes. Normal behavior is not ensured, though, if there is insufficient lubricant between the surfaces; neither is it ensured if the moving surface experiences a substantial decrease in velocity, a temperature rise decreases the viscosity, or an increase in the

external load occurs. Either of these changes, if allowed to continue unaddressed, leads to excessive friction, wear, and eventual failure of the machine component.

3.3 Applications of Textured Topographies

The problems related to sliding surfaces have no shortage of techniques designed to combat them. One approach was to design the contacting surfaces of sliding parts to be as smooth and flat as possible since designers could examine the microstructural roughness of the surface. The thinking of surface engineers at the time was rough surfaces hindered the smooth sliding operation of bearings. Admittedly, the flatness contributed to a more stable lubricant film between the surfaces. However, the fatal flaw in this approach was ultra-smooth, flat surface topographies can fail to generate sufficient hydrodynamic pressure to separate the surfaces under a load [27][28]. Sliding surfaces typically need about 1 μm lubricant thickness and the roughness to produce the hydrodynamic effect for adequate load support and to avoid severe wear during operation [29].

A different approach has been to use favorable geometric designs to steer lubricant toward the locations where it is needed. Macro-scale techniques such as spiraled grooves, cross-hatching, and stepped surfaces have all been used to create the conditions required for long component life [30]. A recent method that is a modified version of porous topographies is dimpling. This micro-texturing technique is likened to the texturing deployed on golf balls. Shot peening, sandblasting, and indentation tools are used to physically impact the surface to produce the dimples. A more sophisticated technique involves using a laser to ablate the material's surface [31][32][33]. The latter comes closer in practice to producing well-defined and arrayed porous features.

Laser surface texturing, or LST, has been used by various researchers to create micro-porous surfaces on seals and bearings to address friction, wear, and lubrication issues of sliding surfaces for nearly 15 years. The technique has been effective for reducing these tribological issues to some degree, but others persist. Additionally, the technique creates certain negative effects on the bulk material beneath the pores such as heat stress related cracking that could become a problem that threatens the integrity of the bearing or seal structure [32][33][34][35]. Perhaps the solution lies in developing a nano-texturing approach to more fully address the tribological issues of sliding surfaces.

3.4 Defining the Problem

Sliding machine components can encounter many lubrication problems. Numerous applications are lacking effective retention strategies, fail to control lubricant leakage, cannot deal properly with lubricant degradation products, and are not designed with the surface chemistry in mind to optimize lubricant retention. Tribological issues such as friction and wear are symptoms typically linked to these problems, and over time, the problems lead to catastrophic equipment damage. Discussed in sections 3.4.1 – 3.4.7 are specific problems encountered by sliding machine components and some possible solutions to them offered by the author's research.

3.4.1 Increased Tribological and Thermal Expectations

Modern machinery is not immune from the relentless pressure to minimize its size to save space, materials, and money. This directly affects the machine manufacturer's procurement and marketing decisions, as well as its profitability. The pressure placed on manufacturers to economize also comes from consumers who expect machines to perform to higher standards and cost less money [3]. As a consequence, the performance expectations of the machinery and lubricants used in them has risen.

Nowadays, machines and the moving components they employ are expected to run faster and hotter [36]. In order for machine manufacturers to meet theirs and the consumer's economic and performance goals, gear casings are built smaller and lubricant cooling is treated as an optional add-on, if available at all. Yet, the lubricants and the components are expected to last longer and require less maintenance under these conditions. For sliding machine components then, the retention of lubricant on the contact surfaces is a very important criterion.

3.4.2 Lack of Effective Retention Strategies Result in Lubricant Loss

If liquid-lubricated machinery is idle for any period of time, gravity causes the fluid to migrate. An example is the engines of automobiles. As soon as the engine is shut off, oil that protects the sliding parts from friction and wear drains to the bottom and collects in the drain pan. When this happens, the parts are starved of lubricant. After starting the engine, the oil pump must transport oil to the top of the engine quickly to lubricate those parts. Durability tests done on automobile engines operated with no lubricant proved that they last only seconds before seizing. Therefore, the retention of lubricant between the surfaces of sliding machine components is vital to their long-term durability.

Considering that sliding parts will encounter starved lubricant conditions twice during each start and stop cycle, it is easy to see how surface wear is accelerated and catastrophic damage can occur. Amusingly, some lubricant manufacturers invented "magnetic" lubricant products like Castrol's Magnetec™ that were attractive toward metal surfaces. They achieved this feat by changing the molecular chemistry of the oil from a non-polar nature to a polar one. The idea seemed promising on paper, but the products were ultimately removed from production because the lubricant attracted another polar molecule—water.

Nano-porous topographies, on the other hand, have the potential to help retain and replenish lubricant on the surfaces to avoid starved lubricant conditions during idling. These topographies may buy valuable time, allowing repairs to take place before major damage occurs.

3.4.3 Non-Textured Surfaces Cannot Store Excess Lubricant

Non-textured surfaces, in general, can do little to enhance lubricant retention unless physical barriers are used to contain the lubricant [30][37]. It is on these surfaces that the small size of nano-scale features can be used to great advantage. For example if the diameter of a nano-pore is 1 nm, and each pore touches an adjacent pore, and these pores form a rectangular array which has an area of 1 mm^2, there could be 10^{12} nano-pores fitted into this space.

Now, consider the case of a nano-pore that has a diameter and a depth of 1 nm each. The available surface area for the attachment of lubricant molecules is 3.14 times that of a flat surface of the same material with the same diameter. Assuming the diameter remains constant at 1 nm, each additional nanometer of depth acts as a multiplier, providing 3.14 times more surface area to the nano-pore. From a strictly geometric standpoint, the potential of nano-porous surfaces to enhance lubricant retention is very promising.

Storing excess lubricant is an efficient way to control the operating temperatures of sliding components. The concept is similar to the method that engine builders utilize for ridding the lubrication system of heat. Large heat sinks such as oil and transmission pans become heat exchangers which conduct heat away to an unobjectionable place. Nano-porous topographies can provide additional surface area that serves the same purpose as pans.

Whenever the nano-topography is accompanied by a material like Cu that has a thermal conductivity of nearly 400 W/m·K, the benefits are too good to ignore. The best part is the nano-topography does not interfere with the dynamic flow of the lubricant driven between sliding

surfaces. The convective heat transfer caused by the driven fluid can supplement conduction heat transfer to control the temperature of sliding components.

3.4.4 Need to Improve Lubricant Leakage Control

Problems persist in applications like mechanical face seals despite the improvement in friction and wear reductions that were gained using micro-texturing techniques. One problem for these popular sliding machine components is the hydrodynamic pressure generated between the seal's faces. Assuming the operating temperature and external load remains constant, the seal's rotation speed increases from idling and produces pressure in a thin film of lubricant located between the faces. The pressure creates a gap for separation of the faces. In reality, though, the speed, temperature-dependent viscosity, and load are all variables that can change over time.

Some clearance is necessary to reduce the friction and wear as the seal's rotating face spins near the stationary one, but excessive clearance provides a convenient place for lubricant leakage to occur. Full- and partial-face micro-texturing techniques have addressed some issues, but excessive lubricant leakage continues [38][39][40]. Nano-porous surface texturing on the faces have the potential to further reduce friction and wear beyond micro-textured surfaces while simultaneously increasing the retention of lubricant by allowing greater control of the seal's opening pressure [41].

3.4.5 Accumulation of Varnish and Charring During Thermal Degradation

The natural behavior of a heated lubricant is it becomes less viscous, thinner. Special additives called viscosity improvers are needed to prevent the temperature from reducing the viscosity too much during machine operation. However, when lubricant temperatures are raised to extremes beyond its stable operating limit, varnishing or polymerization becomes an issue.

Polymerization occurs when the lubricant's volatile constituents are driven off by higher-than-normal operating temperatures. The physical characteristics of this unwanted condition are the thickening of the lubricant and subsequent varnish accumulation on the surface of moving components. At the least, the flow of lubricant to machine components is inhibited due to the thickening, and this leads to damage from a lack of lubrication. Components affected by polymerization are rarely serviceable because the material forms an insoluble coating on the surface. The coating also acts as an insulator for trapping heat and provides a lodging place for abrasive machine debris that erodes sliding surfaces.

Degradation that goes beyond the polymerization of lubricant is known as charring. This type of degradation is seen in high temperature applications such as aero-derivative gas turbines and liquid oxygen turbopumps where the lubricant can come into direct contact with metal surfaces having localized temperatures as high as 800K [29]. Hydrogen molecules of the lubricant's hydrocarbon chain are preferentially oxidized over carbon during this stage of lubricant degradation, leaving carbon behind as a residue [42]. A possible solution for diminishing varnishing and charring is to incorporate nano-porous topographies which can act as debris traps for these products, therefore creating a contact surface mostly free from their accumulation.

3.4.6 Lubricant Properties Change During the Evaporation of Lubricant

The need to reduce friction and wear's effects on moving components in which greater demands were being placed stimulated early research in the area of lubricant quality. The attention given to quality nowadays underscores its continued relevance in modern times. It is well known that lubricant quality degrades for a variety of reasons, but thermally-induced evaporation and chemical breakdown of its constituents are primary ones. Evaporation causes an irreversible change in phase by converting a portion of the lubricant's mass from liquid to vapor form.

Evaporation of a lubricant's volatile constituents not only leads to a reduction in the lubricant's quantity, it also affects the chemical composition and quality of the original formulation. Formation of hydroxyls (OH-), carbonyls (C=0), carboxylic acids (C=O-OH), along with carbon and oxides are aided by the environment present during the normal operation of machinery [43][44]. These harmful compounds have been found to increase in concentration as lubricant degrades. Their formation can be accelerated by abnormal conditions like excessive temperatures and infrequent service intervals. Changes in lubricant properties such as color, acid content, density, and viscosity occur as a result [44].

Just as evaporation of lubricant is a problem affecting the formation of these harmful species, so are electro-chemical reactions between the surface and lubricant. Research has shown that static discharges are generated as the lubricant flows over the surface of metals [45]. These discharges are believed to be the catalysts for the chemical reactions leading to lubricant degradation. If hot spots such as the places where moving metal surfaces make contact are included, then the potential of creating these harmful species increases even more.

Chemically-modified nano-porous topographies might provide a solution to the degradation of lubricant caused by evaporation if the topographies are effective in raising the activation energy of the harmful chemical components of the lubricant. The basic idea is to make the formation of the harmful species more difficult in the region of the surface contact. Also, incorporating a surface chemistry that interrupts static electricity discharge by forming a protective barrier on the nano-porous surfaces could inhibit the formation of these species.

3.4.7 Surface Chemistry Needs to be Improved to Help Lubricant Retention

The addition of a surface chemistry that attracts the molecules of lubricants has the potential to bring even greater benefits beyond the geometric argument for nano-pores by itself [46]. A

favorable surface chemistry can increase the capillary effect. The need to consider such modifications is buoyed by these facts: (1) not all machine surfaces are naturally receptive to lubricants [47], and (2) further increasing the retention of lubricants can provide greater performance during extraordinary dynamic and thermodynamic stresses.

The choice of material for a surface chemistry would logically take advantage of the abundance of C available from the saturated hydrocarbon chains of the lubricant to form stronger intermolecular attractions than van der Waal forces [48]. In the same manner, lubricants that have unsaturated C chains (known as olefins) might take advantage of such a surface chemistry. Nano-pores not only provide a storage location for the lubricant, the surface chemistry—together with the geometry of the pore, can amplify the interfacial force of the surface and lubricant, therefore enhancing its retention.

3.5 Lubrication Issues of Cu

Copper is an attractive research material because it is widely available, versatile, and has properties useful for many applications where heavy loads, corrosion, high temperatures, and abrasion are issues of concern. There are several alloys of Cu that also enjoy wide use in demanding applications. Beryllium copper (alloy C17200) contains 98% Cu and up to 2% Be. It is used in pump shafts, rock bit bearings and bushings, wear plates, marine hardware, racing engine valve seats, and mechanical face seals [49]. Aerospace bronze (alloy C96900) is 84% Cu, 15.5% Ni, 0.3% Mn, 0.1% Nb, 0.5% Fe, and 0.02% Pb. This alloy is used in bearings and bushings in landing gears and cargo doors, wheel and brake components, wing and tail actuators, and hydraulic pump components. Naval brass (alloy C46400) is a high strength, corrosion resistant alloy containing, nominally, 60% Cu, 0.8% Sn, and 39.2% Zn. This versatile alloy of Cu is used for bushings, light-duty bearings, marine hardware, and propeller shafts.

Because Cu and its alloys are used in many demanding machine applications, the components containing Cu are affected by similar lubrication problems as other metals [50]. Wear, discoloration, fretting, flaking and cracking, smearing, scuffing, and seizing are common problems that relate to the failure to retain lubricant in the proper location, in the right quantity, and for the duration it is needed. Manufacturers of some Cu machine components have responded in a limited way by incorporating macro-scale features to function as barriers and pores for the retention of lubricant. Three notable organizations that have embraced the benefits that Cu has to offer are the Copper Development Association, CLI-Industrial, and NBM Metals Company. The porous features may be stamped inserts fitted to the curvature of the component or drilled holes through the component body. These actions are a step in the right direction, but more could be done to address the retention issues of Cu on the nano-scale.

3.5.1 Nano-Texturing on Cu

The predominant method of nano-texturing Cu is wet chemical etching because it is a fast and simple technique that only requires a minor investment in processing facilities and time [51][52]. The two chemical solutions frequently used are ferric chloride ($FeCl_3$) and ammonium persulfate, or APS ($[NH4]_2S_2O_8$), in which the Cu can be dipped. Although the method successfully creates nano-textures on the surface, the etchant is dependent upon the location of the grain boundaries and microstructural defects of Cu which it attacks [53]. Therefore it is not a controllable nano-texturing technique. The results of wet etching done on 99.9 wt. % Cu (alloy C11000) is shown in Figures 3.3a and b.

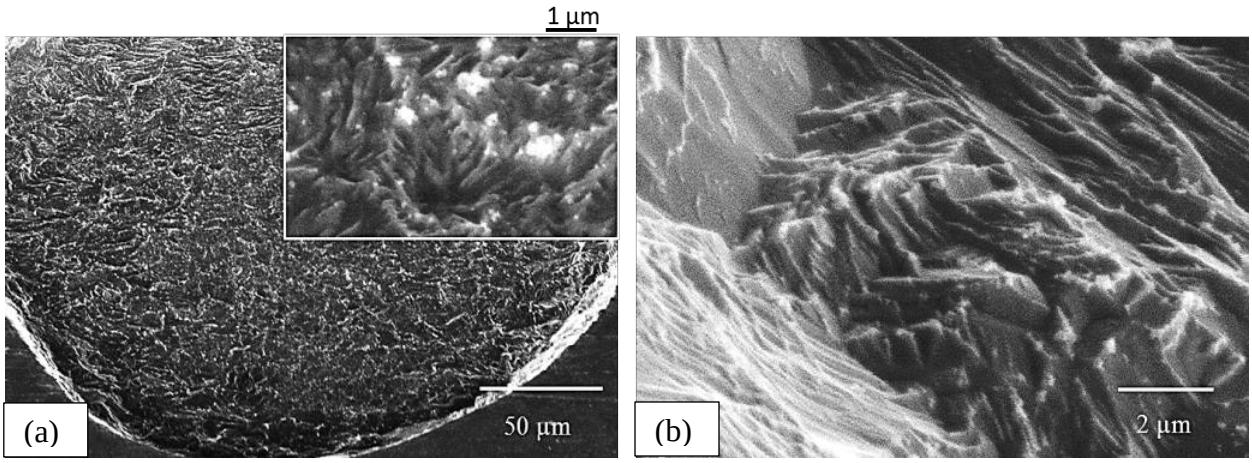

Figures 3.3a and b. Images of a pore created on the surface of Cu using APS etchant. (a) The inset shows the rough and uncharacterizable pore surface, and (b) demonstrates the face-centered cubic 1-1-1 planes of Cu (*Images from the author*).

The surface features were formed by depositing photoresist on the surface of Cu samples and overlaying a photolithographic mask to pattern the photoresist. The patterning was done by UV exposure and chemically developing the photoresist thereby creating a cylindrical opening in the photoresist to allow the etchant to reach the surface of Cu. A thorough explanation of the pattern transfer process is provided in sections 4.2.1 - 4.2.3. The samples were immersed in a 100% APS solution at 50 ˚C for 5 min to produce the pores.

Wet chemical etching exposed the very rough surface of Cu such as the sharp peaks highlighted in the inset image of Figure 3.3a. These features are not easily characterized and even more difficult to replicate for research purposes. In addition, wet etching creates hemispherical pore geometries due to the tendency of the etching solution to preferentially etch all crystallographic planes of Cu except face-centered cubic (1-1-1). The planes form pores with sloped sidewalls similar to those in Figure 3.3b. Hemispherical pore shapes have been shown in actual mechanical face seal testing to cause hydrodynamic pressure cancellation [54], even though numerical simulations of these shapes have predicted them to be quite effective in generating

pressure. A solution allowing the creation and study of these important surface features of Cu is offered using composite materials.

3.5.2 What are Composites?

Composites are defined as materials made from two or more constituent materials with significantly different physical or chemical properties that, when combined, produces a new material with characteristics different from the individual components. Composites are unique in that the components which comprise them maintain their distinct properties, yet they can modify the behavior of the structure they are a part of. The structure may be laminated or sandwiched layers of bonded materials, a matrix formed by bonding the strips of different materials, or a mixture of particles or fibers of materials immersed in a bonding agent, absent a chemical reaction.

It is important to understand the bonding of composite materials used in the author's research. For example, studies have been done to understand the inter-diffusion of the atoms of Si-Cu composites which form species called silicides [55][56][57]. Much has been learned of their alloying behavior at the bulk and nano-scale levels. Over time, Cu atoms will migrate into the c-Si wafer on which it is deposited. To facilitate a bonding mechanism and prevent the diffusion (disappearance) of Cu during the testing of Si-Cu composites of this research, a 50 nm thick film of Ti was deposited as a diffusion barrier before sputtering the Cu film. The c-Si formed a covalent bond to Ti, and Cu formed a metal-to-metal bond to Ti thus eliminating film adhesion issues that plagued Si-Cu composites.

Other material bonding behavior such as the bonding of hydrogenated a-Si (a-Si:H) film to Cu was of interest, too. A 250 nm thick a-Si film was deposited on Cu substrate to serve as a surface chemistry modification during preliminary testing. Al film having a thickness of 500 nm

was deposited on the a-Si:H film to facilitate the crystallization of a-Si. Figure 3.4 shows a high resolution transmission electron microscope (HRTEM) image of Al and a-Si:H films deposited on Cu substrate.

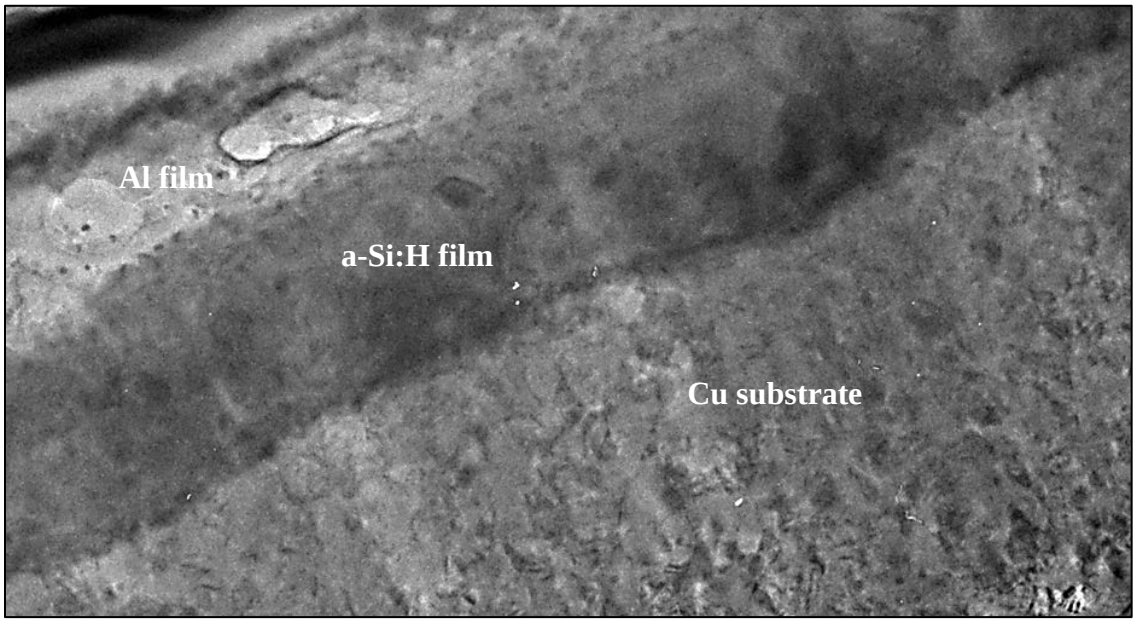

Figure 3.4. The HRTEM image of the film stack that was used to perform preliminary tests for lubricant retention. A conformal a-Si:H film contributed to a strong mechanical bond and good adhesion (*Image from the author*).

The a-Si:H film thickness is 250 nm, the same as proposed for use in the current research. Of interest is the conformal behavior of the film to the substrate suggesting, at the minimum, that a bond formed between the rough surface of Cu and a-Si:H film. The a-Si:H film and Cu substrate formed a 3-dimensional interlocking composite that, in the beginning, was strictly mechanical in nature. It is surmised that heating the samples to 850°C for 10 s to crystallize the a-Si:H film actually improved the adhesion of a-Si:H film to Cu substrate by enabling interdiffusion between the materials. This is indicated by the elemental composition of the profile in Figure 3.5.

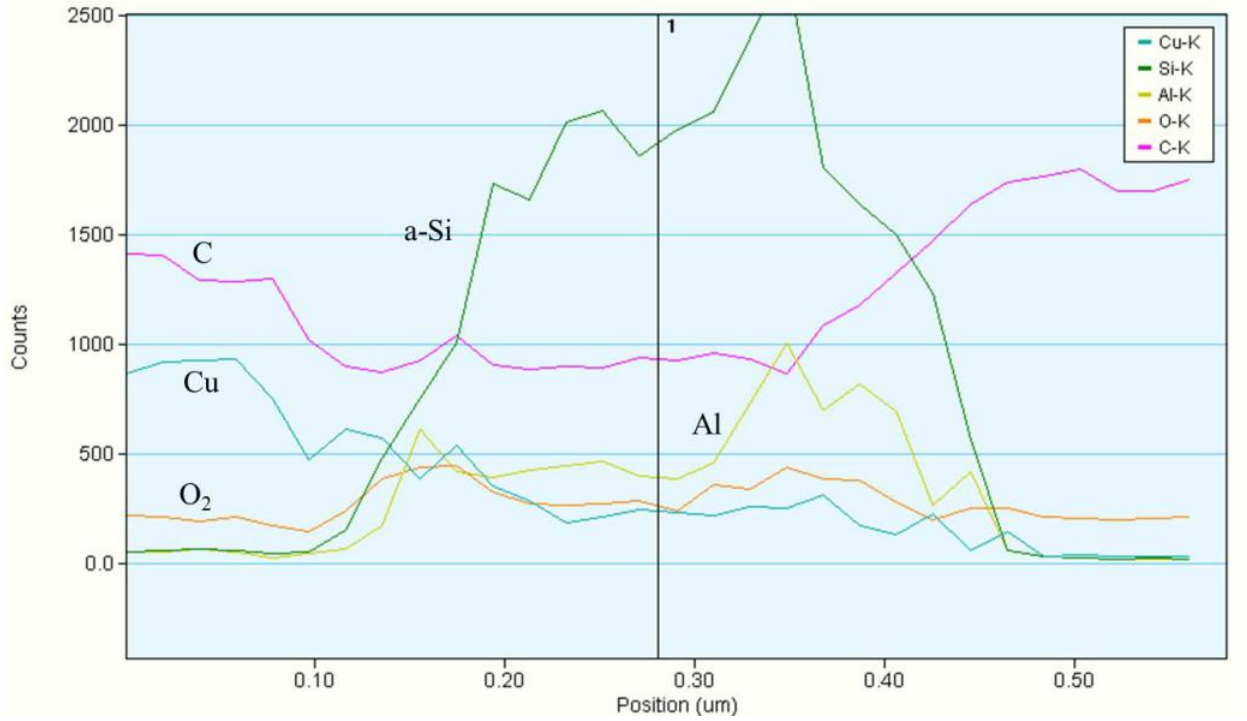

Figure 3.5. The elemental composition of the film stack in Figure 3.4 was captured using HRTEM. The graph shows the presence of Cu along with a-Si:H film between the 0.1 µm and 0.47 µm positions of the cross-section thickness, suggesting that interdiffusion of a-Si:H film and Cu occurred to enhance the adhesion of a-Si:H film to Cu substrate (*Image from the author*).

For the proposed research, preliminary smooth Si-Cu composite wafers were tested to investigate the adhesions of Cu film to c-Si wafers and a-Si:H film to Cu film. The result was the bond between the two films and the substrate was substantial enough to endure the 30,000 rpm dicing process in which the composite wafers were cut into sample-size pieces. Also, the samples showed no evidence of delamination before or after the heating phase of the preliminary lubricant retention testing, therefore indicating good adhesion throughout the fabrication processes and testing. As was done for the a-Si:H film on Cu substrate , the Si-Cu composites will have a 250 nm thick layer of a-Si:H film deposited on the Cu film for retention testing.

3.5.2.1 Composites of c-Si and Cu and its Alloys

The use of Cu composites has grown because of their exceptional heat transfer abilities and the wide availability of Cu. These characteristics make Cu composites favorable prospects to address tribological issues such as friction and heat dissipation. A number of researchers have investigated the tribological behavior of Cu composites for the reduction of friction and wear under dry sliding conditions. Cu-SiO_2, Cu-graphite, Cu-SiC, and Cu-TiC are a few examples of Cu-based composites [58][59][60][61]. Si has also been used for improving the castability of copper-zinc alloys, as well as contributing significantly to the alloy's strength for lubricated sliding surfaces [62]. Although silicon brasses are not common bearing alloys, they do have favorable bearing characteristics at moderately high speeds. They are amenable to machining, higher in strength than standard Sn bearing alloys, and are particularly effective as bearing materials against hardened shafts.

3.5.3 Why Use Composites?

The discussion of composites is appropriate at this juncture because of the failure of wet chemical etching techniques to allow the replication and characterization of prospective surface features of Cu which could facilitate lubricant retention. A new method, based on composites, was formulated to alleviate the difficulties. The method involves producing cylindrically-shaped pores in Si-Cu composites by dry etching pores in c-Si substrate and overlaying the patterned c-Si with Cu and a-Si:H films [63]. The patterned c-Si wafers serve as a form and support for the Cu and a-Si:H films which are deposited on them afterward. Figures 3.6a and b show the results from early experiments using c-Si wafers to understand the various parameters for producing controllable pore dimensions. They are used here as an illustration of the research approach and a demonstration of the possibilities of creating nano-porous topographies.

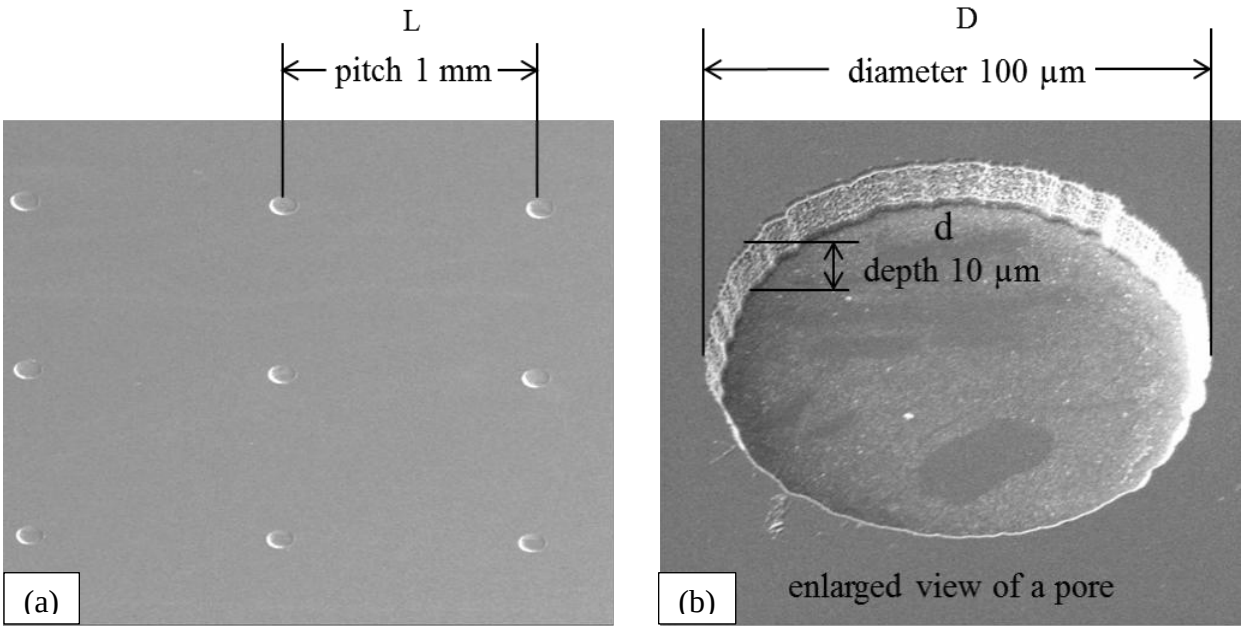

Figures 3.6a and b. Examples of pores etched in 640 µm thick, (1-0-0) oriented c-Si wafer substrate. (a) Well-defined and precisely-located pore arrays and (b) excellent dimensional control and smoothness were achieved, opening the possibility for creating similar features on the nano-scale (*Images from the author*).

The etched pores in (1-0-0) c-Si wafers were easily replicated as demonstrated by the uniform array in Figure 3.6a. The pitch, defined as the center to center distance between adjacent pores, was 1 mm as designed. Although there were some sidewall ripples, the diameter of the pores were uniform as well.

Most interesting was the fact that the depth of the pores, like the one shown in Figure 3.6b, was controllable and uniform. At any depth, the bottom of the pore was as flat as the outermost surface. This outcome is vastly superior to the uncharacterizable geometry of the pore in Figure 3.3 that was wet etched. The preciseness of the dimensions allow an accurate comparison of important parameters such as aspect ratio, pore density, and area ratio used in evaluating the

lubricant retention potential, leakage rate, lubricant film stiffness, friction torque, etc., of sliding machine components having porous topographies such as mechanical face seals.

The research approach is unconventional but can be very successful if the purpose is to create Si-Cu composites for studying the effect of large-scale arrayed, nano-porous surfaces on the retention of lubricant [64]. Section 3.5.2.1 provided abundant evidence that the pairing of c-Si with Cu and its alloys was an effective way to improve the tribological properties of sliding, conformal surfaces. The research proposed by the author merely extends the present use of these materials to a never-before-imagined scale that can lead to many groundbreaking discoveries. Not to be overlooked is the fact that the knowledge gained from the nano-pore's effects on lubricant retention can be readily applied to other bearing and seal materials of ones' preference.

3.5.3.1 Statistical Quantities (AFM Results) of Si-Cu Composites

A qualitative investigation of the roughness of both surfaces was done using scanning electron microscopy (SEM). The decision to use c-Si wafers as a substrate material is further justified when it is recognized that the surface on which the nano-pores are created should be as smooth as possible to accurately evaluate the nano-porous topography's effect on lubricant retention, free of the influence of Cu's microstructure.

Prime-grade, 125 mm diameter, (1-0-0) oriented wafers were used, allowing the flattest and most defect-free c-Si surface possible. For a roughness comparison, as-received (AR), mirror-finished Cu which had the flattest surface of its kind available commercially, was used to test the validity of using c-Si wafers as substrates. The results are shown in Figures 3.7a and b.

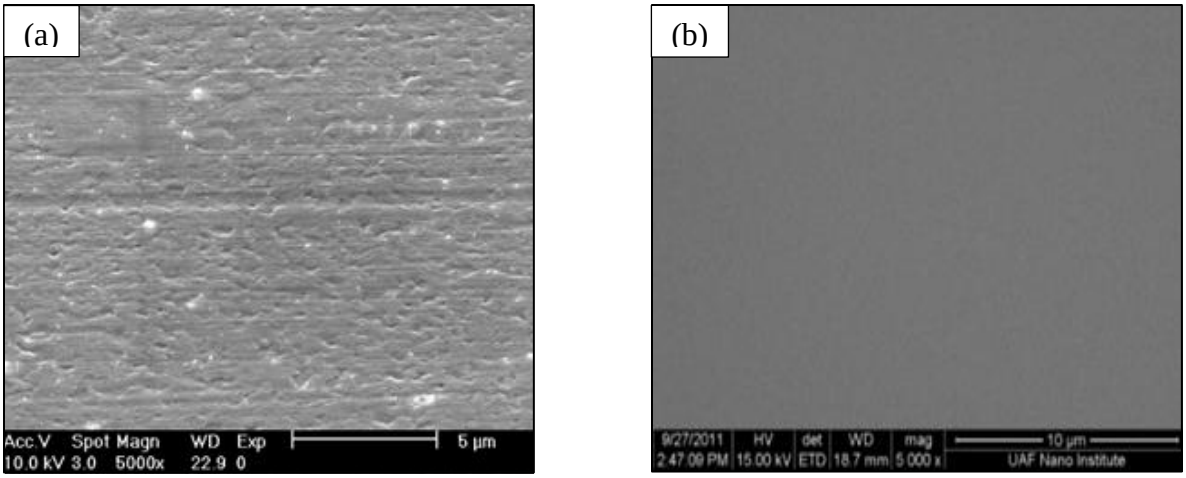

Figure 3.7a and b. SEM micrographs of (a) 800 µm thick mirror-finished AR Cu and (b) 640 µm thick smooth, polished (1-0-0) c-Si wafer captured at 5k magnification. The surface microstructure of Cu consisted of grooves and pits which would clearly make isolating the effects of nano-pores more difficult (*Images from the author*).

Examination of the microstructural features on the surface of AR Cu in Figure 3.7a shows it is rougher in appearance than the c-Si wafer substrate in Figure 3.7b. A more rigorous test of surface roughness was done by depositing a thin, sputtered Cu film on the wafer substrate and comparing the roughness of the Si-Cu composite to AR Cu. The deposition was performed using the Varian 3180 (Palo Alto, CA, USA) sputtering tool available at the High Density Electronics Center (HiDEC). A film thickness of 2 µm was produced on 640 µm thick, 125 mm diameter, polished, (1-0-0) c-Si wafers, which were the same ones used for the pore etching experiments.

Samples from the Si-Cu composite wafers were created by dicing the wafers into 12.7 mm x 25.4 mm pieces. The same size AR Cu samples were made from a bulk sheet via water jet cutting to cause minimal effect on the surface flatness. An Agilent 5500 (Santa Clara, CA, USA) atomic force microscope (AFM) was used in tapping mode to obtain various roughness measurements from both types of surfaces. Figures 3.8a and b show the optical and quantitative results of the scans.

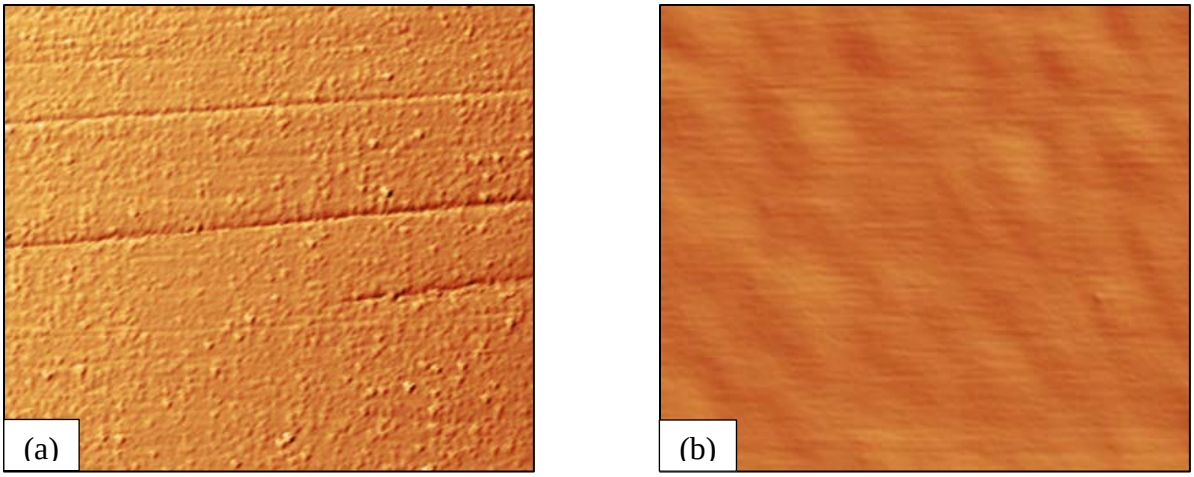

Selected area: 60.0 × 60.0 µm
Maximum: 561.8 nm
Median: 257.4 nm
Ra: 67.0 nm
Rms: 80.3 nm

Selected area: 5.00 × 5.00 µm
Maximum: 32.40 nm
Median: 15.93 nm
Ra: 5.59 nm
Rms: 6.83 nm

Figures 3.8a and b. AFM images of Cu topographies acquired using the tapping mode. (a) Scan of AR Cu substrate and (b) scan of Si-Cu composite surface. The roughness measurements of AR Cu are 15 times larger than the composite surface (*Images from the author*).

A quantitative comparison of the scans for both surfaces in Figures 3.8a and b indicates the AR Cu substrate is 15 times larger than the Si-Cu surface, as confirmed by the maximum, median, Ra, and Rms roughness measurements. The composite surface undoubtedly was aided by the smooth polishing process of c-Si wafers. The conclusion is c-Si is the better surface for creating nano-porous topographies that are unaffected by microstructural surface features like those of AR Cu.

The roles that c-Si wafers play are essentially to serve as forms for the pores and supports for the Cu films and lubricants used during testing. It should be remembered that the goal of the research is to quantify the potential for lubricant retention enhancement that nano-porous topographies alone can provide. However, AR Cu as well as other bearing and seal materials, although rough, can still benefit by adding nano-pores to their surfaces.

3.5.3.2 Potential Thermal Testing Concerns for Si-Cu Composites

Some points of concern that need to be addressed are: (1) should Si-Cu composites be used for lubricant retention testing, and (2) are the heating conditions that the lubricated samples will be exposed to during testing valid? The objection may be raised that the composite surfaces do not adequately represent real-world applications and environments encountered by topographies of sliding, conformal surfaces. Although section 3.5.2.1 discussed the concerns to some extent, brief responses are put forth in the following paragraph.

The goal in mind for enhancing the retention of lubricant is to use nano-porous surfaces to reduce the evaporation of lubricant under a wide range of temperatures. The heating conditions chosen are in good agreement with those encountered in actual practice [65]. In order to determine the effectiveness of the nano-pores, the evaporation test conditions performed on lubricated Si-Cu nano-porous surfaces will also be done on lubricated smooth Si-Cu surfaces which have the same film order and thicknesses. The only difference in the Si-Cu topographies will be the pores themselves, and not the composition of the materials. As long as the testing conditions are faithfully replicated, the approach allows a direct correlation of the effects of the topographies on the retention of lubricant. Consequently, there is no reason for concern that the results will be non-representative of actual thermal conditions.

3.6 Research Overview

In light of the preliminary work done by the author to produce large scale, controllable, micro-scale porous surfaces on Si-Cu composites, the focus can now be shifted to creating nano-porous topographies for lubricant retention testing. Sections 3.6.1 – 3.6.3.4 discusses the ways the proposed research differs from other approaches and presents an overview of the research plan, including the objectives related to designing, fabricating, and modeling of nano-pores. Also

discussed are the objectives associated with Fourier transform infrared spectroscopy (FTIR) for characterizing the a-Si:H film used as a surface chemisty modification.

3.6.1 How is My Research Different?

A significant amount of time has elapsed since the ground-breaking micro-scale surface engineering work of Etsion, Peng, Adachi, Wang, and other luminaries in the past 2 decades [38][40][66][67]. Their research mainly paved the way for advancement in wear and friction reduction of sliding surfaces which were the objectives at that time. Nano-science during that period was in its infancy, so there was only limited knowledge of the behavior of materials on the nano-scale. As a result, little effort was put forth to implement nano-texturing techniques on the surface of machine components.

Fast-forwarding to the present, there has accumulated a vast body of work related to material behavior on the nano-scale that now allows greater possibilities to not only improve friction and wear reduction further, but also to enhance the retention of lubricants. The work herein explores the lubricant retention opportunities using nano-porous topographies. This fresh approach represents a significant change from the long-standing micro-scale techniques developed by other researchers. Although the use of porous arrays are not new, and they have been reported and even implemented on sliding components such as mechanical face seals, they have not been produced on the nano-scale, and certainly not for enhancing the lubricant retention of Cu, its alloys, or its composites.

The proposed research differs from traditional approaches in other definitive ways. In addition to the new scale and the composite materials to be researched, the investigation of the nano-topography's potential for evaporation reduction is performed using medium hydrocarbon-based oil as the lubricant. Medium hydrocarbons are those that reside within the 22.3 to 30.2 API

gravity index (source: Petroleum Communication Foundation/Canadian Centre for Energy Information). This is a significant departure from the typical studies that use lubricants such as water, dodecane, and hexadecane whose evaporation rate is linear over time and accumulate little or no residue during heating [68]. Research of water evaporation under very restricted conditions garnered the attention of a number of groups that studied droplet dynamics [69][70]. A few researchers delved into volatile droplet simulations and experiments with oil-in-water emulsions as they pertain to evaporation, but the results are confined to very tiny specimens [71]. Medium and heavy hydrocarbons like oil are inherently more difficult to study because of the myriad chemical and physical changes taking place in the lubricant as it is heated. These changes are in addition to the polymerized residue that remains after evaporation has ceased. The relationships of these complex, interrelated processes are shown in Figure 3.9.

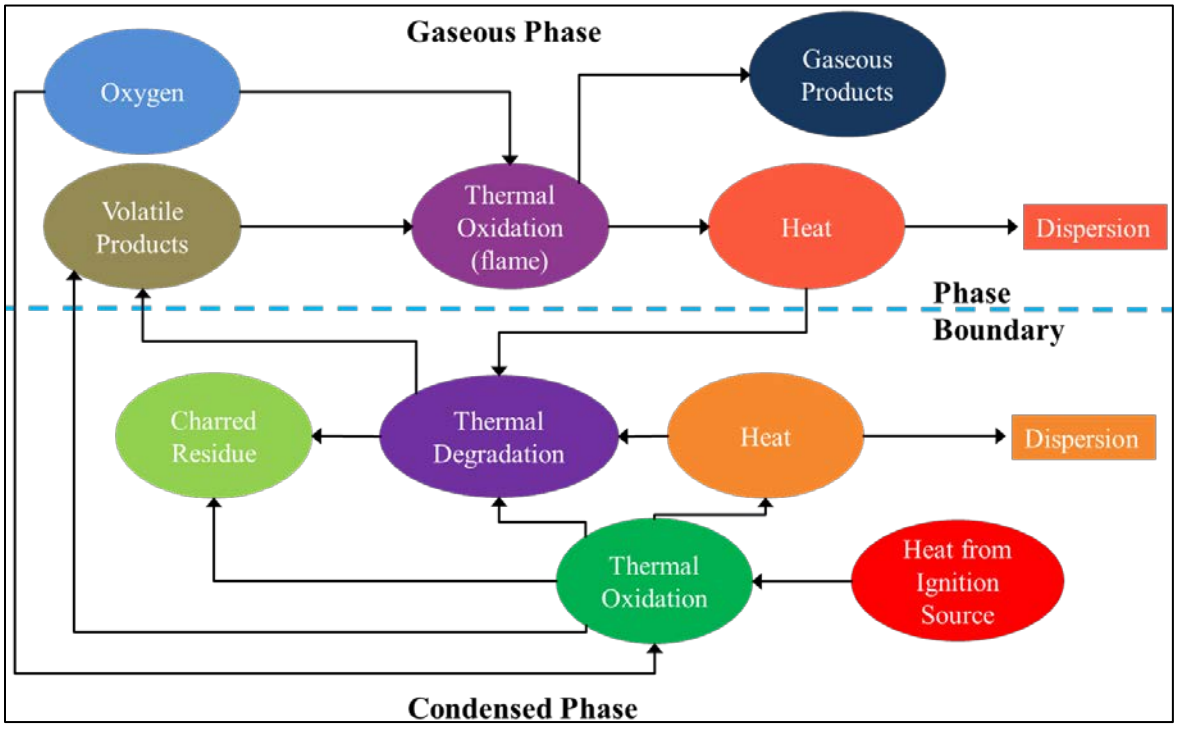

Figure 3.9. The combustion process of a heavy liquid fuel (*Image from the author*).

There are many interrelated processes that affect the combustion of lubricants as the figure clearly shows. The one that is of interest for the proposed research is volatile products. The process flow of Figure 3.9 illustrates the challenges that make it difficult to accurately control, much less predict the creation of volatile products of a heavy fuel such as oil. The development of volatile products depends on thermal degradation and oxidation of the lubricant. The volatile products occurring in the gaseous phase of combustion are of interest because they are directly associated with evaporation.

Volatile products are emitted as the oil's lighter constituents such as solvents and aromatics evaporate during heating, leaving the oil's base components behind. If the evaporation of the volatile constituents can be reduced, the lubricant can retain its original chemical formulation and lubricating properties longer. Nano-porous topographies may provide these solutions.

3.6.2 The Potential of Si-Cu Composites to Enhance Lubricant Retention

It has been elaborated in sections 3.4.2 - 3.4.7 the potential benefits to be gained from incorporating nano-porous topographies on the surface of sliding, conformal machine components. In section 3.5.3, the creation of Si-Cu composites were proposed as a means of producing the nano-topographies for lubricant retention enhancement. Further, section 3.6.1 identified evaporation as a contributor to the migration of the lubricant's lighter constituents which affects its amount and quality. Now, a brief plan for testing the potential of Si-Cu composites to reduce lubricant evaporation is given in sections 3.6.2.1 - 3.6.2.4.

3.6.2.1 Fabricating Topographies Using Photolithography

The reasons for using c-Si wafers as substrates have been presented. The wafers will be used to create ultra-smooth and nano-porous Si-Cu composites for lubricant retention testing. The fabrication of the topographies will require the use of photolithographic techniques meticulously

developed during the creation of smooth and porous micro-scale topographies as a proof of concept. The techniques included determining the thickness parameters for the photoresist and applying it to the wafers, creating masks, exposing and developing the photoresist, dry etching the pores, and depositing Cu and a-Si:H films. In addition to controlling the variables of the materials used in the fabrication process, the machines needed for each step had their own parameters to manipulate for achieving good results. These are explained in greater detail in Chapter 4 Experimental Details.

3.6.2.2 Rationale for Testing Nano-Pores

The reason for creating nano-pores is to use them to enhance the retention of lubricant on the surface of sliding machine components. To accomplish this task, nano-pores exhibiting various geometries will be tested to determine the most effective ones for achieving the optimum retention of lubricant. There are several variables that could affect the outcome: the pore diameter, the pore depth, the capillary force of the surface, the intermolecular force of the lubricant, the temperature of the lubricant, etc. With the optimum retention objective in mind, a strategy has been developed to systematically test the geometric variables and the effect of enhancing the surface energy via chemical modification.

Scientific knowledge that the pore diameter affects the capillary force of porous surfaces would suggest, on the one hand, selecting the smallest possible pore diameter. Smaller diameters may amplify the interfacial force between the lubricant and the pore surface to retain more lubricant. On the other hand, conventional knowledge leads one to believe larger pore diameters should be incorporated into the topographies. Larger pores can hold more oil and improve the lubricity of the surface, even though they may cause a reduction in the strength of the interfacial force.

The same analysis might be applicable to the pore depth. Is it better to have a shallow pore, but use a wider diameter for maximum lubricant retention or should a narrow, yet deep pore be used in its place? How does the depth of the pore impact the ability of the lubricant to reduce evaporation or provide lubricant replenishment to a surface undergoing evaporation? These conundrums are why different pore diameters and depths will be needed to find the best conditions for lubricant retention. Therefore, tests for capillarity will focus on keeping the pores at a constant diameter while allowing the depth to change. Three depths will be tested. The data collected from the testing should produce a retention hierarchy that could be useful for a wide variety of engineering applications.

After performing the tests for capillarity and most effective geometry, the same tests could be undertaken with a new variable in hand—the surface's energy as it is affected by chemical modification. The surfaces of smooth and nano-porous Si-Cu composites will be deposited with a-Si:H film, a material proven in earlier research to be effective for enhancing the surface energy of Cu and stainless steel [46][72]. Then, testing of the Si-Cu/a-Si:H composites can allow a comparison of the effect of the surface energy on lubricant retention.

In the earlier research, water and mineral oil were tested on smooth and micro-textured AR Cu topographies that incorporated a nano-texture produced by crystallizing a-Si:H film on them [73]. The nano-textured topographies were shown to cause greater attraction of fluid to both types of surfaces, even under dynamic testing. But characterization of the topographies was problematic due to the irregular shapes and orientations of the crystals. The difference in approach for the proposed research will be the use of a non-crystallized a-Si:H film on the smooth and nano-porous topographies to allow characterization and modeling.

3.6.2.3 Models to Predict the Lubricant Retention of Si-Cu Composite Surfaces

Modeling of the smooth and nano-porous topographies and their effect on lubricant retention are prime objectives of the research. The apparatus described in section 4.5, which will be used for thermally evaporating the lubricated samples, was fabricated to follow the American Society of Testing Materials (ASTM) standards set forth for testing lubricant evaporation. Thermal resistance networks which are based on the geometry, material properties of the Si-Cu composites, and the testing apparatus design will be modeled to account for the conduction, convection, and radiation heat transfers to the lubricant during evaporation.

A combination of analytical evaluation and empirical testing will be employed to deal with the lubricant evaporation process. Data will be collected to assess the effects of thermal evaporation on the lubricant's mass. By developing geometric and thermodynamic models, lubricant retention testing of new nano-porous topographies by trial and error can be significantly reduced. Simulations using computers may allow customization of nano-porous topographies to meet specific lubrication requirements for future applications.

3.6.2.4 FTIR Investigation of the a-Si:H Surface Chemistry Effect on Lubricant Retention

Another outcome that is of particular interest in the proposed research is investigating the quantity of the lubricant before and after changing the surface chemistry. Analysis of the chemical composition of the a-Si:H film is done using FTIR. FTIR is a useful tool for determining the H composition of a-Si:H films. If the FTIR spectra of c-Si wafers (the background spectra) is known and the combined spectra of as-deposited a-Si:H film and c-Si wafers are obtained, then the background spectra can be subtracted from any subsequent spectra collected to render data that describes the a-Si:H surface chemistry composition. Of interest for this method of testing is the concentration of the mono- and poly-hydride species formed during

the a-Si:H film deposition process. For example, a higher H concentration indicates more sites for potentially enhancing the retention of lubricant. The tests using FTIR are explained in section 7.2.2.

3.7 Motivation

Enhancing the lubricant retention capability of sliding, conformal machine components is the motivation for undertaking this research. A successful outcome of the work is expected to broadly impact the economic and performance potential of the machines, industries, and societies which rely upon them. Various benefits to be reaped from the research are enumerated in sections 3.7.1 – 3.7.5.

3.7.1 Preserving the Characteristics of the Lubricant

According to the ASTM standard D972-91, the evaporation of the lubricant's volatile components adversely affects its original performance characteristics. The use of nano-porous topographies might help accomplish the important task of preserving the lubricant's characteristics in two ways. First, nano-pores could enhance the retention of the lubricant by controlling its migration from the location where it is needed. The nano-pores can act as storage facilities whose geometry can be engineered to enhance the surface energy of the substrate that the lubricant rests on, thereby reducing evaporation. They can also serve as cooling reservoirs for reducing the temperature of the lubricant.

Second, the evaporation of lubricant can be further reduced by incorporating a surface treatment that retards the formation of the harmful chemical species that lead to thermal breakdown of the lubricant. If hot spots on the surfaces of machine components are known, then lubricant could be directed to them via the enhanced surface capillary action provided by the treatment to suppress the build-up of heat before it leads to evaporation of the lubricant. The treatment, together with

the nano-pore geometry, may help provide an effective solution to the problem of preserving the lubricant's original characteristics.

3.7.2 Improving Equipment Reliability

Catastrophic equipment failures are often linked to the loss of lubricant from the surface of critical machine components. Lubricant loss leads to excessive temperatures caused by friction. In response to the excessive temperatures, a portion of the lubricant evaporates, leaving behind a thicker and heavier mass. In a self-sustaining pattern, poor circulation of the thicker lubricant perpetuates friction, wear, and overheating. In the final stages, the part is coated in a thick, insoluble varnish before it seizes completely. The random, unpredictable nature of these failures is cause for serious concern because they are directly linked to equipment durability and reliability.

Numbered below are some applications whose reliability can benefit from reducing lubricant evaporation. The ways nano-porous surfaces can benefit the application are indicated by letters adjacent to the numbers:

1. Bearing and Seals.
a. Controls outgassing, migration, and liquid flashing to vapor for more reliable operation.
b. Reduces friction and wear.
2. Lubrication systems cooling effectiveness.
a. Prevents oil migration.
3. Spindle-type hard drive motors.
a. Controls lubricant loss due to outgassing.
4. Oil loss models.
a. Helps anticipate the effects of evaporation on lubricant quality and machine components.
5. Expensive turbo vacuum pumps.
a. Provides lubricant migration control.

Improving equipment reliability is a worthwhile goal of any research related to machine components. Nano-porous topographies can potentially improve the reliability of components by relocating the polymerized lubricant to an un-objectionable location such as the bottom of the

pores away from the sliding surfaces. Preliminary evaporation testing results suggest less polymerization occurs in the presence of nano-porous topographies. The answer may lie in the geometry of the pores, the enhanced interfacial forces of the surface, or elsewhere. The prospects of using these surface features for lubricant retention, polymer mitigation, and debris traps are very promising. Alternatively, the nano-pores can be used to locally resupply lubricant to the areas on the surface that need replenishing because of lubricant loss. The equipment's sliding components can last longer during starved lubricant conditions, therefore reducing the extent of catastrophic failures.

3.7.3 Reducing Maintenance and Operating Costs

Maintenance of machine components is an important function that can extend the life of equipment. Unfortunately, it incurs a cost that affects the profitability of its owners. Ultimately, the maintenance costs are transferred to the consumers via cost increases for the products that are made using the machinery. The other option is to delay maintenance until the components fail. This is often a more risky and costly strategy in the end. Not only would the cost of new components have to be included, the downtime related to the repair or replacement of the machine components can be astronomical if the machine affects the productivity of other operations [6].

When lubricant fails to remain in the location, amount, and duration needed to be effective, the result is higher operating costs. Nano-porous topographies have the potential to improve the quality and retention of lubricant on sliding, conformal surfaces. This may allow longer intervals between servicing which reduces maintenance costs. Nano-pores reduce the surface contact between the sliding components for friction and wear reduction which makes the components

more reliable. The improved reliability of the components lowers operating costs by reducing the likelihood that the components fail prematurely.

An additional benefit nano-porous topographies may provide is the reduction of lubricant additives in some types of machinery. Eliminating the need for so many additives will help lower the processing cost of lubricants. For example, modern lubricants are packaged with additives to combat thermal breakdown, high pressure, and viscosity reduction. They contain anti-friction, anti-wear, and anti-foaming agents, along with detergents. Nano-pores are inherently useful for reducing friction and wear because they can reduce the surface contact between sliding components. Reducing the thermal breakdown of lubricants by creating nano-porous topographies for controlling evaporation is a direct goal of this research for sliding machine components.

3.7.4 Reducing the Emission of Volatile Products

It is estimated that heavy oils lose about 5% of their volume because of evaporation in the first few days of a spill [74]. Petroleum evaporation from storage tanks, too, account for hundreds of thousands of tons of product polluting the environment every year. These situations have raised the public's consciousness of the need to stop harming the environment. As a consequence, today's machinery must be engineered to not only perform their designated tasks effectively and economically, the negative effects of the machine's operation on the environment must be minimized. Governmental agencies and consumers alike are demanding environmentally-conscious engineering solutions for the products being produced. This includes reducing the pollution of the environment by volatile emissions such as the vapors created during evaporation of machinery lubricants.

Nano-porous topographies might be used to reduce the evaporation of lubricant between sliding, conformal surfaces such as mechanical face seals by allowing a smaller seal clearance opening during operation. A smaller seal clearance decreases the amount of liquid lubricant that leaks to the environment. As an extra benefit, the presence of nano-pores can be used to retain more lubricant for better component cooling to reduce the likelihood of lubricant evaporation. If nano-pores are used in conjunction with oleophilic-oleophobic surface chemistry modifications, zones could be created that allow lubricant between the sliding surfaces, yet prevent the escape of lubricant beyond the seal's contact surfaces.

3.7.5 Decreasing the Risks to Health

The issues pertaining to the air quality in workplace buildings such as sick building syndrome (SBS) has spawned a revolution in building design and function. Terms such as green, sustainability, renewable, L.E.E.D™ certified, and smoke-free are frequently used as assessments of the environment within buildings and their impact on the broader environment, in general. Along with this increased scrutiny is a focus on eliminating workplace health hazards as set out in standards such as OSHA 3430-04 Indoor Air Quality in Commercial and Institutional Buildings. Stricter emissions regulations that govern exposure to hazards are the result of studies which show a building's environment are the cause of various illnesses related to SBS that affect worker productivity and healthcare costs. Clearly, reducing the evaporation of lubricants should be at the heart of efforts to make the workplace environment safer.

The reduction of lubricant evaporation for the previously-stated reasons, as well as the protection of health, are motivations for carrying out this research. Whereas the other reasons given are related to machine components or the environment, the protection of health is more personal in nature. Nano-porous topographies might contribute to a reduction in the emission of lubricant

vapors for cleaner operating machinery, thus supporting a healthier work environment and workers as well. There may also be financial incentives provided which are similar to those for renewable and sustainable energy solutions, but at the least, healthy workers require less sick time and businesses incur lower health insurance costs that can help improve their bottom line.

3.8 Organization of the Dissertation

The dissertation is organized into 8 chapters. Chapter 1 is the introduction that outlines the scope and goals of the research. Chapter 2 is a reproduction of the research paper that was the motivation for investigating the retention of lubricants using nano-porous surfaces. Chapter 3 provides background understanding and motivation for the research. Chapter 4 gives an explanation of the experimental details which includes the procedures for fabrication of the topographies and testing apparatus, and testing criteria for lubricant retention. Chapter 5 consists of the thermophysical properties and surface chemistry analyses that provide numerical models for the theoretical evaluation of the topographies. The models double as a comparison tool against the actual lubricant retention results reported in chapter 7.

Chapter 6 is devoted to the characterization of materials, topographies of the samples, and validation of the presence of lubricant in the pores. The SEM imaging results and other sample characterization techniques are included. Chapter 7 contains the results and discussions of lubricant retention testing. The effects of pore geometry, capillarity, surface chemistry modification, and other results will be presented. Conclusions of the research are explained in chapter 8 where comparisons and contrasts are made with respect to the anticipated and actual outcomes of the research. The chapter also includes a preview of future research possibilities to be gleaned from the current work.

CHAPTER 4

EXPERIMENTAL DETAILS

4.1 Overview of Experimental Details

The experimental details section will discuss the creation of smooth samples and the nano-pore fabrication process, including the preparatory wafer processing steps, materials used during fabrication, and rationale for the pore design. Theory and operation of the principal technologies used in the fabrication process are discussed. The evaporation testing apparatus' construction and operation are explained. The testing criteria for the evaporation of lubricant will be explained as well.

4.1.1 Physical and Chemical Properties of c-Si Wafers

The c-Si wafers used for fabricating the testing samples were obtained from Mitsubishi Silicon America (Part Number 034544). The wafers were specified as single crystal Si (c-Si), prime grade, single side polished, 125 mm diameter, 640 μm thickness, (1-0-0) orientation, p-type, boron-doped, and resistivity between 5 and 30 Ω-cm.

The wafers underwent cleaning to remove dust, organic contaminants, and oxidation that may have accumulated on the surface during storage and handling. Spin rinsing and drying, or SRD, was the standard procedure for eliminating contaminants and the chemical residue of processes from the wafer surface. The SRD machine, shown in Figure 4.1, is a SemiTool model ST-270D (Applied Materials, Inc., Santa Clara, CA, USA), programmed to perform a deionized water spray rinse for 2 min while spinning the wafers at 1500 rpm. The wafers then entered a drying phase for 4 min n which N_2 vapor was injected into the spin chamber. The wafers spin at 2500

rpm while drying to provide a residue-free surface when completed. The wafers were ready for photoresist coating.

Figure 4.1. The SemiTool spin rinse and drying tool was used to remove contaminants from the surface of c-Si wafers (*Image from the author*).

4.2 Preview of c-Si Wafer Processing for Creating Nano-Pores

Perhaps at this point would be a good opportunity to provide a preview of the upcoming sections that explain processes such as photoresist coating, exposing, and developing, the etching steps, and extensive c-Si wafer cleaning procedures. There were many nuances to the processes described in this section that must go unmentioned to reserve attention for the most critical process steps. Figure 4.2 outlines the 5 principle steps that are required to produce nano-pores in c-Si wafers.

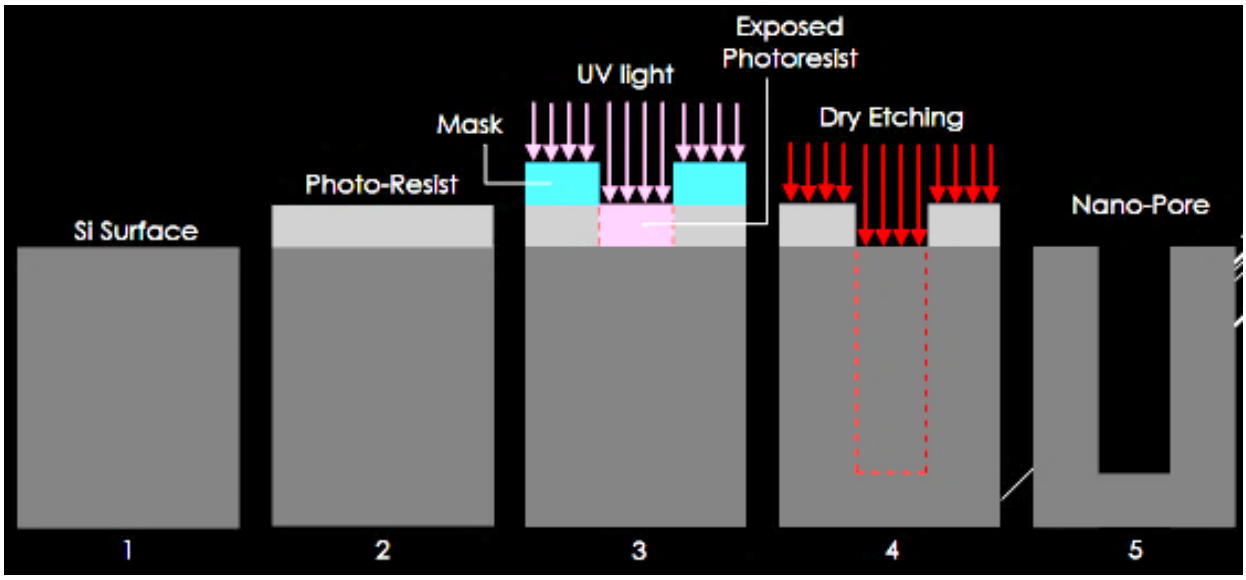

Figure 4.2. The key process steps for creating nano-pores are outlined in the illustration (*Image from the author*).

Numbers are located in the figure below each significant operation for creating the nano-pores. The steps are: (1) preparation of the c-Si wafers for photoresist coating, (2) application of the photoresist, (3) aligning the mask over the wafers and exposing and developing the photoresist, (4) using deep reactive ion etching (DRIE) as a technique to etch the nano-pores into the wafers, and (5) removing the remnants of the photoresist to prepare the etched wafers for subsequent thin film depositions. Sections 4.2.1 - 4.2.7 contains details for each of these steps.

4.2.1 Photoresist Coating on c-Si Wafers

After SRD, the wafers were prepared for photoresist coating. Before applying photoresist on c-Si wafers, it was imperative that the wafers were dehydrated and treated with an adhesion promoter. The wafers were loaded into a steel cassette and placed in the vacuum oven. The vacuum oven is manufactured by Yield Engineering Systems (Livermore, CA, USA) and is shown in Figure 4.3. Dehydration was performed in the vacuum oven set to 150°C temperature and 1 Torr vacuum pressure.

Figure 4.3. The vacuum oven was used for dehydration and application of adhesion promoter on the wafers. The room lighting was yellow to prevent premature exposure of the photoresist before photolithographic processing was done (*Image from the author*).

Following dehydration, the oven dispensed hexamethyldisilazane (HMDS) adhesion promoter in vapor form into the heating compartment to coat the wafers. The promoter primed the wafers so that the photoresist adhered better and distributed evenly. The wafers remained in the compartment for 30 min. The wafers were removed from the oven and allowed to cool to the room temperature of 21°C. Alternatively, the adhesion promoter was applied as a liquid sprayed directly on the surface of the wafer using a rinsing bottle while the wafer was rotated at 2500 rpm for 20 s using a spin coater. The wafers were ready for spin coating of the photoresist.

The photoresist was AZ-4330 manufactured by AZ Electronic Materials (Luxembourg). This photoresist was chosen because of its ready availability, good spreading characteristics, and favorable tone. The tone determined how the photoresist reacted to ultraviolet (UV) light during

exposure. Negative-toned photoresist cross-linked or hardened when it was exposed to UV light, and positive-toned photoresist softened. As a result, the photolithographic mask must be designed with the desired pattern and photoresist tone in mind. The choice of positive tone was made to take advantage of the geometric characteristics of the mask which will be discussed in detail in section 4.2.2.

The spin coater was the G3P-8 model (Specialty Coating Systems, Indianapolis, IN, USA). A single wafer was mounted on the spin coater's chuck as seen in Figure 4.4. The chuck was designed to hold the wafer securely in place during spinning by enabling vacuum to exist between the wafer's bottom and the area of the chuck inside of the rubber seal.

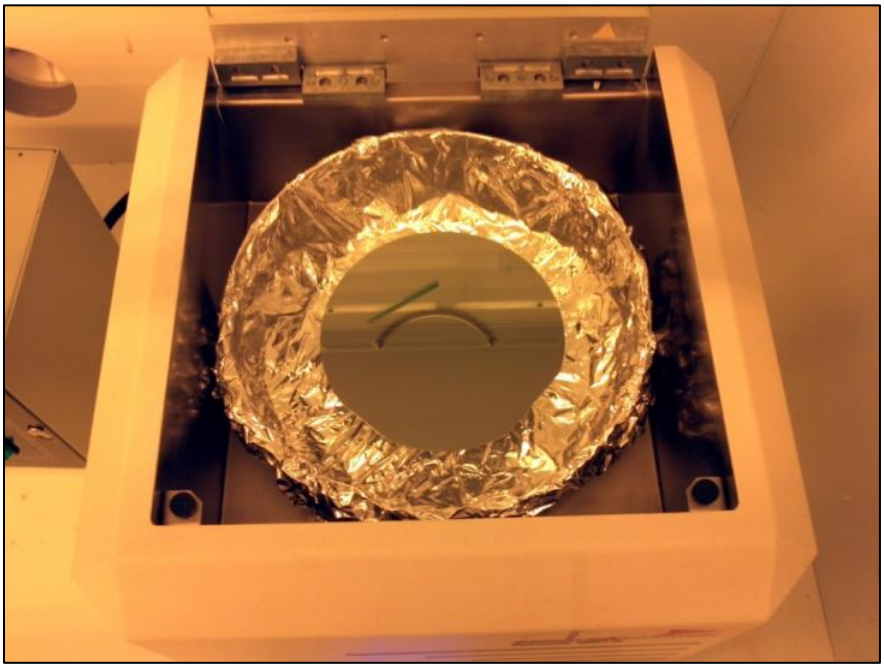

Figure 4.4. The G3P-8 spin coater was used to distribute photoresist across the wafers (*Image from the author*).

The spin coater recipe programming was vital to ensuring a sufficiently thick and evenly distributed coating of photoresist was achieved on the wafer. The proper thickness was governed by the needs of the etching method. The photoresist must be thick enough to withstand the deep

reactive ion etching technique that created the nano-pores at a sufficient depth into the wafers while protecting the areas surrounding the pores from damage. The thickness was controlled by the spin speed (higher rpm for thinner layers, slower rpm for thicker layers) and the properties of the photoresist such as its viscosity, molecular weight, and polymer and solvent concentrations. The thickness can be approximated using the photoresist manufacturer's suggestions as a starting point, but ultimately, the task involved repeated applications and thickness measurements.

The spin coater recipe for creating the nano-pores is provided in Table 4.1. The *step* parameter indicated the progress of the spin coater as it advanced through the recipe. The *ramp* parameter was the time duration allotted for the spin coater to achieve its rotational speed for each step. The rotational *speed* of the wafer is given in rpm. *Dwell* defined the time duration allotted for the individual steps, whether or not there was rotational speed. As examples, step *1* had a 2 s dwell and no speed associated with the step, whereas step *5* was allotted 60 s and had a spin speed of 2500 rpm. The remaining parameters (*dispense* and *time*) controlled an external supply of N_2 that was injected into the spin coater for a length of time during purging.

Table 4.1. The spin coater recipe for the application of photoresist.

Step #	Ramp (s)	Speed (rpm)	Dwell (s)	Dispense	Time (s)	Task
0	0	0	0	4	0.1	Home
1	0	0	2	n/a	n/a	Coat
2	0.5	500	2	n/a	n/a	Spread
3	0.5	1000	2	n/a	n/a	Coverage
4	0.5	500	2	n/a	n/a	Settle
5	2	2500	60	n/a	n/a	Final Spin
6	0.5	200	10	n/a	n/a	Slow Down
7	0	0	0	0	0	Stop

The recipe has steps which transitioned the wafers through the various phases of the photoresist application process. Steps *0* and *1* allowed the opportunity to dispense the photoresist on the wafers. A half dollar-sized portion of photoresist was placed near the wafer's center. Steps *2* and *3* were slow and medium rotation speeds, respectively, for distribution and coverage of the photoresist across the wafers. Step *4* allowed the photoresist to settle on the wafers and step *5* allowed the ramp-up of the machine to the highest spin speed in which the photoresist was thinned to its objective height. This speed yielded about a 4 µm thick layer of AZ-4330 photoresist as measured using the Dektak 3030 surface profilometer (Sloan Technology Corporation, Santa Barbara, CA, USA) shown in Figure 4.5. Step *6* dwell countdown began the speed ramp down. The coated part was removed from the machine after step *7* ended.

Figure 4.5. The Dektak 3030 surface profilometer was used to measure the photoresist, Cu, and a-Si:H film thicknesses throughout the photolithographic and thin film deposition processes (*Image from the author*).

The photoresist-coated wafers were soft-baked using hot and cold plates to remove the remaining solvent and residual film stress from the photoresist. Baking was also done to promote better photoresist adhesion to the wafers. A gradual step-down of the temperatures prevented the wafers from cracking. Cracking can occur during rapid cooling of the wafers which now had a material on the surface with a different coefficient of thermal expansion than c-Si. The Eaton coater plates are shown in Figure 4.6. The wafers were placed on the hot plate set to 110°C for 2 min. The wafers were transferred to the cold plate set at 45°C for 1 min. The soft-baked photoresist was ready for exposing and developing.

Figure 4.6. The hot (left) and cold (right) plates were used to drive solvents away, reduce stress, and promote adhesion of the photoresist (*Image from the author*).

4.2.2 Masks

The photolithographic mask, or simply a "mask", is a geometric template or stencil designed to allow patterns to be transferred to photoresist-coated wafers. The mask's function was as the name implied which was to prevent unwanted exposure of the photoresist on certain parts of the wafers, yet allow exposure on the area where it was desired. The features of interest for this research were cylindrically-shaped nano-pores of various diameters and depths. Throughout this dissertation, the description "patterned" wafers and samples refer collectively to the porous structures created using photolithographic techniques. The pattern required to produce the nano-pores were circles arranged in a rectangular array such as the ones shown in Figure 4.7.

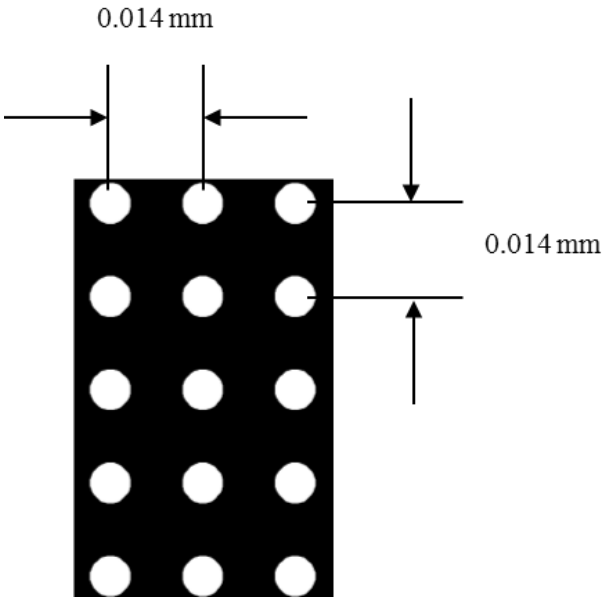

Figure 4.7. Rectangular-shaped arrays of circles having different diameters, yet the same pitch, were created for the nano-pore mask (*Image from the author*).

Forethought must be given to several features related to the mask such as how many nano-pores were desired, what should be their diameter and pitch, how many arrays of nano-pores were needed, what was the overall sample size desired, what processing supplies and materials were available for use, and was the processing equipment adequate for generating the required feature

sizes? In order to produce the mask, images of the c-Si wafer and arrays were designed using Autodesk's AutoCAD™ 2013 software. An outline of a c-Si wafer was drawn and the arrays were optimally spaced to have the largest number of samples sized 12.7 mm x 25.4 mm possible from a 125 mm diameter wafer. The mask was arranged so that four rows, each containing multiple arrays, could be placed on one wafer. Counting from the top of the wafer outline, rows 1 and 4 contained 6 arrays each and rows 2 and 3 had 8 each. This is illustrated in Figure 4.8.

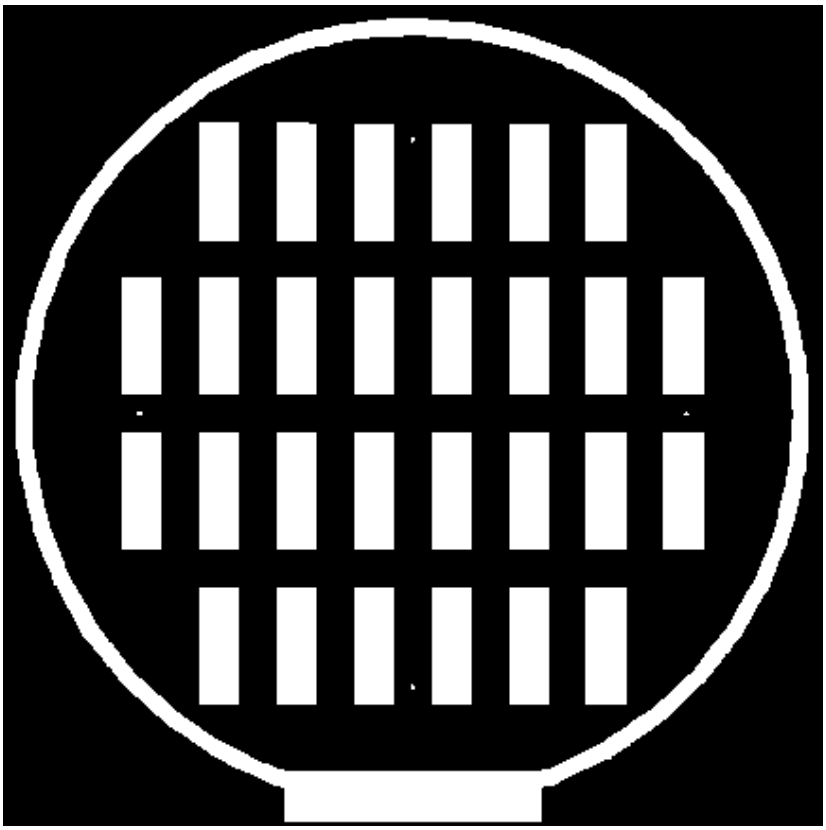

Figure 4.8. The mask contains the wafer outline and rows of rectangular-shaped arrays. The array shown in Figure 4.7 is located within the white spaces of the rows (*Image from the author*).

The mask was purposely designed so that each row yielded multiple samples. Each row had rectangular arrays of circles having a fixed diameter for creating the nano-pores. For row 1, the diameter of the circles in the rectangular arrays was 7.5 µm, row 2 was 6 µm, row 3 was 6.5 µm, and row 4 was 9.5 µm. It should be explained that the pores etched in the c-Si wafers were not

nano-pores at the outset, but they will become nano-pores when Cu and a-Si:H films are overlaid on the wafers. Creating various sizes and depths of nano-pores will allow for testing the effects of geometry and capillarity of the nano-pores on lubricant retention.

A fixed number of circles were designed for each array, even though each row of arrays had different diameter circles. To arrive at the number of circles for each array, consider that the pitch for the circles in the $-x$ and $-y$ directions is 0.014 mm as shown in Figure 4.7. The width of the rectangular array is 6.35 mm and its length is 19.05 mm. Dividing each dimension of the array by the pitch gives the number of circles that occupy the width and the length of the array. The calculations result in 453 circles for the width and 1360 for the length. Simple multiplication of the width times the length revealed there were 616,080 circles in each array.

The number of nano-pores planned for use in each array seems staggering, but the rationale is based on numbers extricated from the successful results of prior nano-surface engineering research [46]. That research yielded a plethora of features such as nano-particles, -voids, and -pores that combined to enhance the attraction of the nano-topography to water and oil. The flaws in the earlier research were the nano-topographies' random feature size and orientation made replicating the same topography for research and characterization difficult. However, it was observed that the void space and particle size of the most successful nano-topographies had an approximate size of 0.5 μm which is of interest in the current research.

The mask dimensions and properties were sent to Photo Sciences, Inc. (Torrence, CA, USA) for manufacture. The mask was specified as dark field, clear features, soft contact, chrome side down, and mounted on 15.24 cm x 15.24 cm soda lime glass. The feature size was assured by the company to be accurate for line widths larger than 3 μm. Upon receipt of the mask, close

examination of the features under a microscope confirmed the quality of the product met the standards for the intended research.

4.2.3 Exposing and Developing the Wafers

Exposing and developing the photoresist on the wafers was required to transfer the image of the arrays of circles to the c-Si wafer surface. The system at the Georgia Institute of Technology's Marcus Inorganic Building cleanroom facility is the MA-6 mask aligner (Karl Suss, Waterbury, VT, USA). Each wafer was placed on the machine's chuck, the mask was located over the wafer, and the left-right-forward-back-theta alignments were performed. An alignment gap of 60 µm between the wafer and mask was chosen for soft contact and good image transfer. The mask aligner system is shown in Figure 4.9.

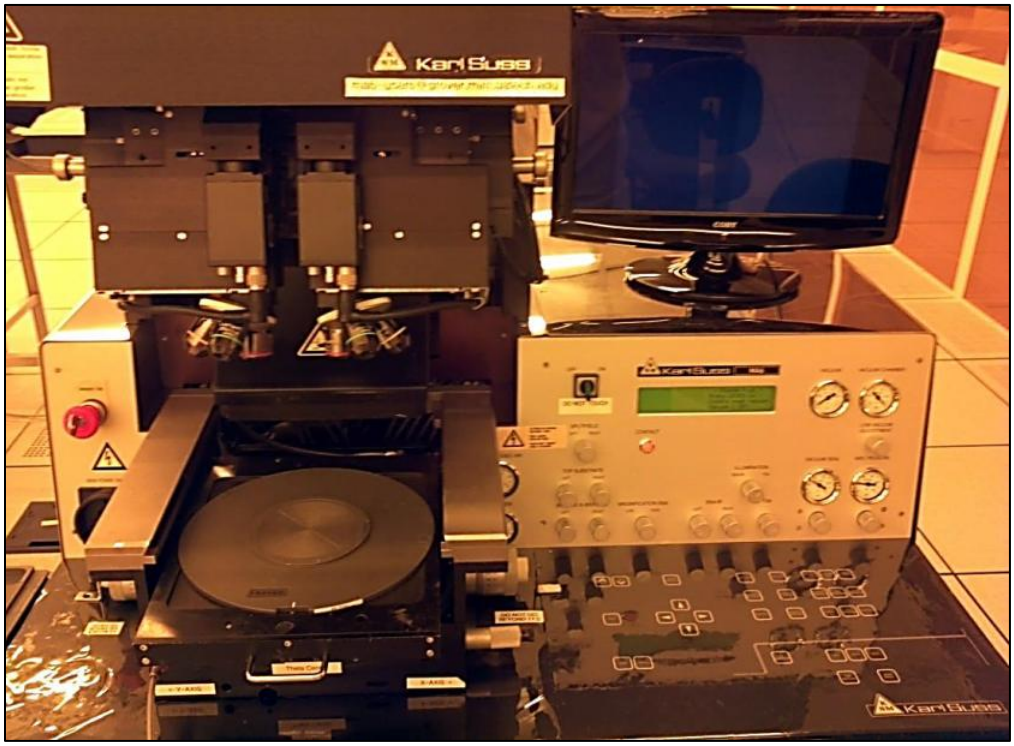

Figure 4.9. A mask aligner was used to align the wafer and mask and expose the photoresist (*Image from the author*).

The exposure system used a 350 W mercury lamp that generated UV light for exposing the photoresist. The UV lamp's optics was moved into position above the mask when the user initiated UV exposure. UV radiation caused a chemical reaction in the sensitizer of the photoresist that was in direct view of the clear features of the mask—the features were circles in this case for the creating nano-pores. The radiation induced the solubility of the exposed positive-toned photoresist so that when it was developed, the photoresist dissolved away. The amount of radiant energy or dose required was 60 mJ/cm^2-µm. The radiant energy value, the intended thickness of the photoresist (4 µm), and the radiation intensity allowed calculation of the exposure duration,

$$\text{exposure duration} = \frac{\text{energy flux} * \text{thickness}}{\text{intensity}} = \frac{60\ \frac{\text{mJ}}{\text{cm}^2 \cdot \mu\text{m}} * 4\ \mu\text{m}}{11.5 \frac{\text{mW}}{\text{cm}^2}} = 20.9\text{s} \quad \text{Equation (4.1)}$$

After exposure of the photoresist, the wafers were loaded into a cassette and immersed in a tank of tetramethylammonium hydroxide (TMAH) developer solution sold under the name Microposit MF-319 (Rohm and Haas Electronic Materials LLC, Marlborough, MA). The developer was used at 21°C room temperature and full strength (2.4% TMAH, 95% H_2O) as received. A sequence of soaking and swirling the wafers in the solution was carried out in 15 s intervals for 2 min. The wafers were cleansed of the developer using DI water dump rinsing for 3 cycles and SRD and inspected under a microscope for evidence of satisfactory transfer of the array pattern to the c-Si substrate.

Once cleaning was completed, the wafers underwent hard-baking. This type of baking is identical to the soft baking described in section 4.2.1, except the hot plate temperature was increased to 120°C and the wafers remained on it for 90 s. Hard baking cured the photoresist,

improved its selectivity, removed any remaining solvent, and facilitated good adhesion. The selectivity of the photoresist was determined by the ratio of the number of etch cycles completed per micron of photoresist removed. The ratio was about 100:1. Achieving the best adhesion possible produces well-defined edges of the nano-pores when they were etched into the wafers, which was the next step.

4.2.4 Theory and Operation of the Inductively-Coupled Plasma Tool for c-Si Etching

The Surface Technology Systems (STS) inductively-coupled plasma (ICP) tool was used to etch nano-pores into the surface of c-Si wafers. The STS ICP is a complementary metal oxide semiconductor (CMOS)-compatible tool used for integrated MEMS-CMOS processes. The tool is effective for narrow (<10 μm in width), high aspect-ratio trench etching (or DRIE) in c-Si and silicon-on-insulator (SOI) wafers. The tool is shown in Figure 4.10.

Figure 4.10. The STS ICP tool was used to etch pores in c-Si wafers (*Image from the author*).

There are two chambers in the STS-ICP system, a load lock and a process chamber, that are separated by a pneumatically-controlled isolation valve. After venting and opening the load lock to atmospheric pressure, a single process wafer was placed on the robotic arm that has a tray configured for holding them. The load lock was closed and pumped down to 25 mTorr. The wafer was transferred from the load lock into the process chamber by the robotic arm. The process chamber had a 2.5E-06 mTorr base pressure during the transfer to minimize contaminants and protect users from hazardous etch by-products that would back-stream into the load lock were it not for the lower process chamber pressure. During processing, the chamber was maintained at 94 mTorr. Standard 125 mm diameter wafers were processed in the system.

There were 2 RF power sources to separately control the properties of the plasma and platen voltage bias. The first was a 1000 W power supply inductively coupled to the gas in the process chamber. Induction occurred by locating a coil outside of the plasma chamber so that the magnetic field penetrated the chamber wall. The power supply generated high frequency magnetic fields which oscillated gas atoms into frenzy. The results were broken SF_6 molecular bonds and the transitioning of gas molecules from a higher energy state to a lower one, therefore emitting photons which produced the glow characteristic of the plasma state. The plasma ionized the SF_6 etch gas molecules to form F^+ ions and neutrals (radicals).

The plasma contained a high density of radicals and F^+ ions with only a small voltage potential between the plasma and the wafer surface. An additional 500 W power supply induced a negative voltage potential between the platen and the plasma as does a traditional RIE system. The advantage of the separate RF sources was the plasma density and the wafer substrate bias voltage could be independently controlled. Another benefit of the separation was it allowed etch by-products to escape more readily from deep trenches for improved etch quality. A model of

the plasma chamber is shown in Figure 4.11 for illustrating the creation of radicals and ions during the etch step.

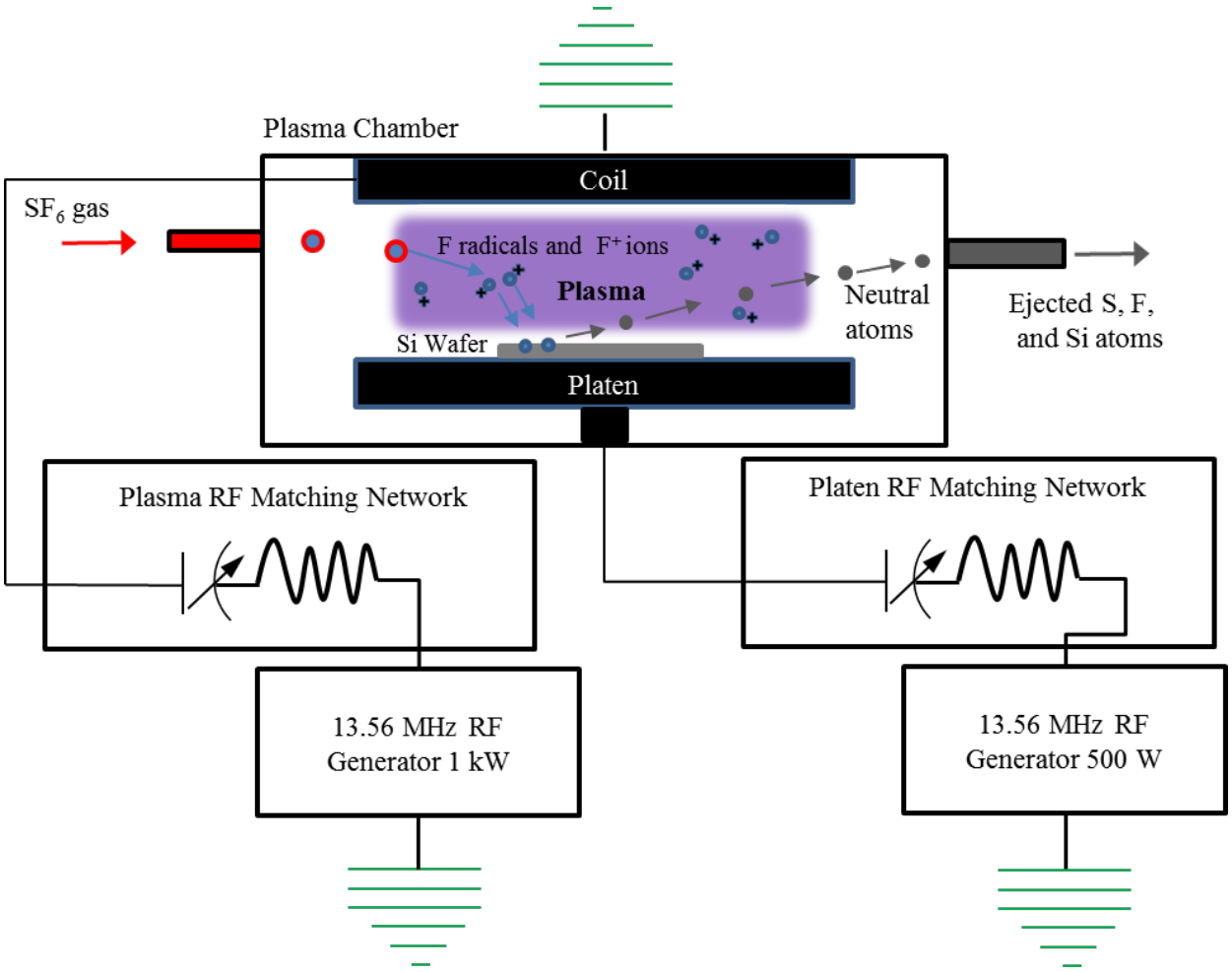

Figure 4.11. The model of the STS ICP system (*Image from the author*).

Radicals are atoms and molecules having partially-filled valence electron shells, whereas ions are species of atoms that do not have an equal number of protons and electrons. Atoms with a reduced electron count are called cations. The radicals are neutral in charge, yet they are in a very reactive state chemically. They reach the etch site via momentum of the flowing gas (diffusion) rather than by electrical attraction like cations. The radicals provided a localized chemical etch inside the pore to contribute to desorption of the c-Si substrate. The platen was

negatively biased so that the cations were attracted toward the wafer located on the platen. The amount of voltage bias, in effect, controlled the bombardment energy of the cations.

During passivation, octafluorocyclobutane (C_4F_8) gas was decomposed into CF_2 polymer molecules by the plasma. The platen power was deactivated during passivation because ions were not essential to creating the polymer. The polymer used the plasma for molecule cross-linking, similar to exposing positive-toned photoresist described in section 4.2.1. The cross-linked polymer protected the previously etched portion of the sidewalls of the nano-pores from further undercutting during subsequent etch cycles.

The momentum possessed by the F^+ ions drawn toward the wafer was used for etching through the passivation polymer layer at the bottom of the nano-pore. On impact, their kinetic energy was converted into heat. The platen on which the wafer rested employed a mechanically-clamped, backside He cooled chuck that was temperature controlled with a CFT-75 (Neslab, Newington, NH, USA) chilled water circulator set to 35°C. Backside He cooling prevented the wafer from deforming or cracking due to heat build-up caused by the plasma, bombardment of ions, and chemical reactions of the radicals on its surface. The impacting atoms, unused components of the gas molecules, and Si atoms desorbed from the surface passed unrestrained through the plasma and out of the chamber exhaust.

The APC angle parameter in the recipe was important because it fixed the exhaust valve position and worked in tandem with the gas input pressure to automatically control the total process pressure. The APC angle simultaneously controlled the rate of the exhaust gases leaving the chamber. Proper setting of the APC angle was critical for producing etch uniformity across the wafer. The process dry pump, Ebara A10S (Ideal Vacuum Products., Albuquerque, NM, USA), carried the by-products away which were then removed by the HiDEC scrubber system.

Having described the theory of operation, the actual etching of wafers could proceed. Before etching pores into c-Si wafers, however, it was important to clean the process chamber of residual etching by-products because the system supported several users. To facilitate the cleaning process, thermally-oxidized c-Si wafers were made using the Bruce oxidation furnace. An oxidized wafer was loaded into the STS ICP tool's process chamber. The cleaning recipe used O_2 gas in combination with high RF power and the oxidized wafer to perform oxygen cleaning. The RF power was used to create plasma that reduced O_2 gas into O^+ ions and O radicals which became highly chemically reactive as they encountered the remaining atoms of etching by-products. More in-depth information explaining the functions of RF power, the parameters for ICP systems, and the operation sequence of the tool are provided in later paragraphs of this section that deal with the etching and passivation steps. The initial cleaning process took 2 h to complete. Shorter 15 min cleanings were done as necessary during continuous wafer processing to maintain chamber cleanliness. The parameters of the cleaning program are given in Table 4.2.

Table 4.2. The recipe parameters for O_2 chamber cleaning.

Coil Power	**Platen Power**	**O_2 Gas Flow Rate**	**APC Angle**
800 W	30 W	49 sccm	78°

A chamber conditioning program was used prior to DRIE processing of the wafers as well. Chamber conditioning was necessary to ensure that any remnants of the cleaning process were rendered ineffective in terms of affecting the etching and passivation quality. It was also a safeguard against contamination of the chamber and wafer due to back-streaming F atoms from the vacuum turbopump's lubricant. Preferably, the lubricant will remain in place and in liquid form unless the chamber pressure drops below the value of its vapor pressure and causes F atom

back-streaming. Low pressures were necessary if the chamber was to be rid of air molecules and contaminants, so there was a conundrum. Conditioning the chamber solved the conundrum by using sulfur hexafluoride (SF_6) etching gas to produce a SF_x capping layer that trapped the remnants of the O_2 cleaning and back-streamed F atoms underneath it. The conditioning process took 0.5 h to complete. The recipe parameters are given in Table 4.3.

Table 4.3. The recipe parameters for SF_6 chamber conditioning.

Coil Power	**Platen Power**	**SF_6 Gas Flow Rate**	**APC Angle**
700 W	20 W	49 sccm	50°

The alternating technique for anisotropically etching high-aspect ratio features (up to 30:1) into c-Si and SOI wafers is referred to as the Bosch process [75]. The etch recipe was programmed for alternating cycles of etching and passivation via the parameter switching function in the menu of the user software interface. Sulfur hexafluoride + O_2 and C_4F_8, respectively, were the gases used during an etch-passivation cycle. Once the necessary parameters for the plasma were set, the etch depth was controlled by the durations of etching and passivation steps and number of etch-passivation cycles. The durations of each etch and passivation step programmed in the recipe were 12 s and 7 s, respectively.

Test wafers were sacrificed to obtain the number of etch-passivation cycles per micron of depth to eliminate inconsistencies in the depth between different sessions. Interpolation was then employed to estimate the number of cycles required to etch the desired depth for the processed wafer. If the plasma was stable, that is to say, if the full RF power of the plasma was available for the processes, the depth could be accurate within 0.1 μm of the projected value. The gas flow rates, RF etch and passivation (E/P) powers and vacuum throttling valve position (APC) are the

primary parameters determined by the user to achieve the intended etch profile. The recipes for the current research are provided in Table 4.4.

Table 4.4. The recipe parameters for etching pores.

Recipe No	SF_6 Flow Rate (sccm)	C_4F_8 Flow Rate (sccm)	O_2 Flow Rate (sccm)	Platen Power (E/P) (W)	Coil Power E/P (W)	APC Angle
1	130	95	13	12 / 0	650 / 650	62°
2	130	95	13	13 / 0	650 / 650	61°
3	130	95	13	14 / 0	650 / 650	60°
4	130	95	13	15 / 0	650 / 650	59°
5	130	95	13	16 / 0	650 / 650	58°

The differences in the recipes are subtle, yet important. The platen power gradually increases in magnitude while the APC angle decreases as the recipes proceed. Decreasing APC angles opens the vacuum throttling valve to facilitate greater process gas elimination which aids the removal of desorbed etch by-products from the deep pores. Higher platen power improves the etch capabilities of the ions (and radicals) as the pores become progressively deeper. Further challenges loomed such as determining the number of cycles needed and the finding the critical point at which the current recipe in the etch process lost its effectiveness. These challenges were overcome using various etch schemes.

The 25, 50, and 75 µm pore depths required extensive etching trials and SEM characterizations to arrive at the number of E/P cycles to create them. In addition, the number of cycles affected the two diameters, 6 and 6.5 µm, in different ways. Wider pores garnered more of the ions and radicals from the plasma so they etched at a faster rate than smaller pores having higher aspect ratios. To circumvent this issue, the ideal depths for the 6.5 µm diameter pore arrays were etched first. These were covered with several micrometers of photoresist and baked dry for 4

min at 120°C. The E/P process was resumed a few more cycles for the 6 µm diameter pore arrays until they became the same depth as the 6.5 µm diameter pore arrays. The number of cycles used to create the 3 depths for the two pore diameters along with the recipe identification numbers are presented in Tables 4.5 - 4.7.

Table 4.5. The DRIE parameters used to create 25 µm deep pores for 6 and 6.5 µm diameters.

Pore Diameter (µm)	E/P Cycle No.	Recipe No.
6.5	0 – 25	1
	26 – 35	2
6	36 – 38	2

Table 4.6. The DRIE parameters used to create 50 µm deep pores for 6 and 6.5 µm diameters.

Pore Diameter (µm)	E/P Cycle No.	Recipe No.
6.5	0 – 25	1
	26 – 50	2
	51 – 70	3
6	71 – 75	3

Table 4.7. The DRIE parameters used to create 75 µm deep pores for 6 and 6.5 µm diameters.

Pore Diameter (µm)	E/P Cycle No.	Recipe No.
6.5	0 – 25	1
	26 – 50	2
	51 – 75	3
	76 – 100	4
	101 – 120	5
6	121 – 125	5

A total of 18 c-Si wafers were etched which included 6 wafers for each of the 3 pore depths. The 18 etched wafers had the two pore diameters incorporated in rows 2 and 3 as explained in section 4.2.2. An image of an etched wafer is shown in Figure 4.12.

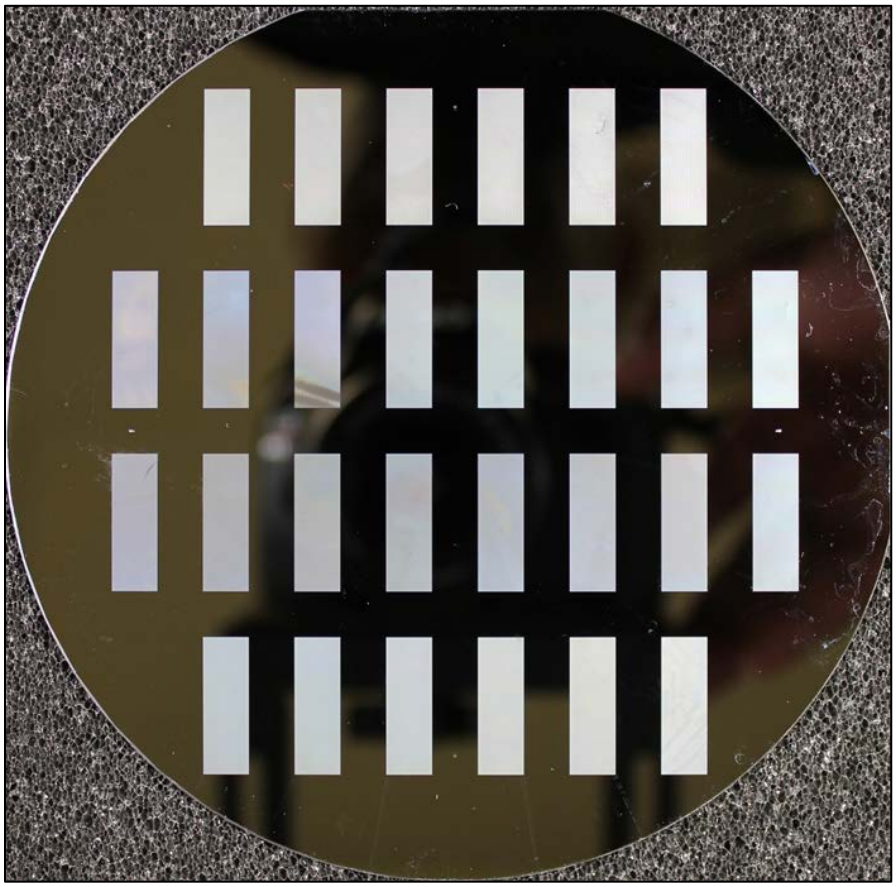

Figure 4.12. A c-Si wafer after pores were etched using the STS-ICP tool (*Image from the author*).

After removing the wafers from the STS ICP tool, the by-product of the passivation step, CF_2 polymer, was removed from the etched nano-pores. The positive-toned photoresist removal product, PRS 1000 (Baker, Phillipsburg, NJ, USA) was used for this purpose. The solution was placed in a vat that provided bubbling and heat to enhance the removal of the polymer. The wafers were lowered into the solution for 20 min at 90°C, after which they underwent DI water dump rinsing for 3 cycles and SRD.

As a precautionary step, the wafers were stripped of any remaining photoresist using UV exposure and plasma cleaning. The UV exposure was similar to the steps in section 4.2.3, except the mask was a blank 15.24 cm x 15.24 cm piece of soda lime glass and the duration of exposure was three times (a total of 64 s) the original exposure duration for the nano-pore mask. The wafers were placed in TMAH developer which dissolved most of the remaining photoresist. Now, the wafers were rinsed in acetone, IPA, and DI water, followed by SRD. Following their inspection, the wafers underwent plasma cleaning.

The wafers were cleaned using O_2 plasma produced by the system shown in Figure 4.13. It was a preventive measure in the event the developing process left some photoresist behind. Plasma cleaning was also used as a surface de-hazing step before sputtering Cu on the wafer.

Figure 4.13. The plasma etching system was used for cleaning the wafers of photoresist remnants (*Image from the author*).

The APE 110 plasma etching system (Mark IV LFE Corporation, Clinton, MA, USA) uses O_2 plasma, high RF power, high pressure, and a heated compartment to remove implanted photoresist (scum) from the wafers. In plasma cleaning, a RF electric field breaks down the non-reactive O_2 gas molecules into reactive monatomic O radicals. The highly reactive radicals break down the organic polymers in the photoresist to form gaseous products of CO and CO_2, along with H_2O vapor that are pumped away. Etching was performed at a power of 200 W for 10 min. The chamber pressure was 0.4 Torr and the O_2 flow rate was 80 sccm. The cleaning process was repeated until all photoresist was removed.

Removing the photoresist and CF_2 passivation polymer revealed the irregularities in the nano-pore shape. Each etch step during DRIE created "corrugations" resembling ripples along the pore's sidewall and extending to the pore's bottom [76]. The corrugations occurred due to the isotropic nature of SF_6 plasma etching. The isotropy resulted in a slight undercut of the masked area of the photoresist before the CF_2 polymer passivation had been applied. These are shown in Figure 4.14.

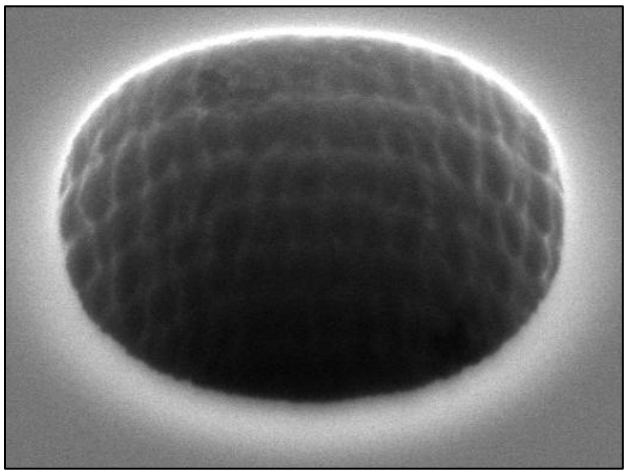

Figure 4.14. SEM micrograph of corrugations. Corrugations are ripple patterns formed along the wall during etching of the pores into c-Si wafers. The image was captured at 10k magnification (*Image from the author*).

4.3 Preview of Thin Film Depositions

Thin films are deposited films of materials whose layers are 1 nm to several micrometers thick. Compared to thick film or bulk materials, thin films exhibit a number of good qualities. They have low roughness and porosity as well as high purity and geometric accuracy that make them suitable for MEMS and nano-electromechanical systems (NEMS) materials. Thin films were used in this research as prospective materials to enhance the retention of lubricants for improving the tribological properties of sliding machine surfaces, preserve the lubricant's original quantity, and reduce the emission of the lubricant's volatile products to the environment. It was necessary to examine many of the tribological properties of materials benefiting from lubricant retention at the micro- and nano-scales. This is where the qualities of thin films were used to best advantage. There were three thin films used in the process for creating smooth Si-Cu samples. These are illustrated on a smooth topography in Figure 4.15.

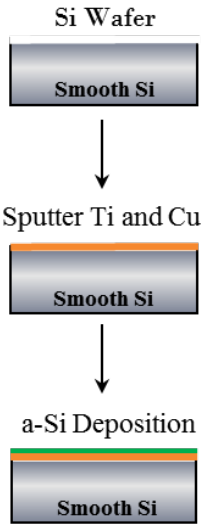

Figure 4.15. The process flow for c-Si wafers undergoing thin film depositions of Ti, Cu, and a-Si:H. The sputtering process was used for smooth topographies only (*Image from the author*).

The first two films, Ti and Cu, were produced using the sputter deposition technique. The third film, a-Si:H, was produced using the plasma enhanced chemical vapor deposition (PECVD)

technique. Sections 4.3.1 - 4.3.3 discusses the theory and operation of the tools for the deposition techniques. The parameters that were determined by experimentation to produce the thin films are given also. Section 4.3.4 is a discussion of the wafer dicing operation that created the samples for lubricant retention testing.

4.3.1 Theory and Operation of the Sputtering Tool for Ti and Cu Film Depositions

The Ti and Cu films used in the fabrication of the samples for testing was produced by the Varian 3180 sputtering tool (Varian, Palo Alto, CA, USA). The machine is based on DC magnetron sputtering, an approach widely used in industry to deposit conductive materials such as metals on glass, c-Si, plastic, etc. Magnetron sputtering, in general, is a type of physical vapor deposition technique in which a target material in the machine is vaporized and deposited on a nearby substrate to create a thin film. The technique offers higher ionization rates and less electron damage to the target material than traditional sputter deposition techniques. A model of a sputtering chamber is presented in Figure 4.16 to illustrate the theory of its operation.

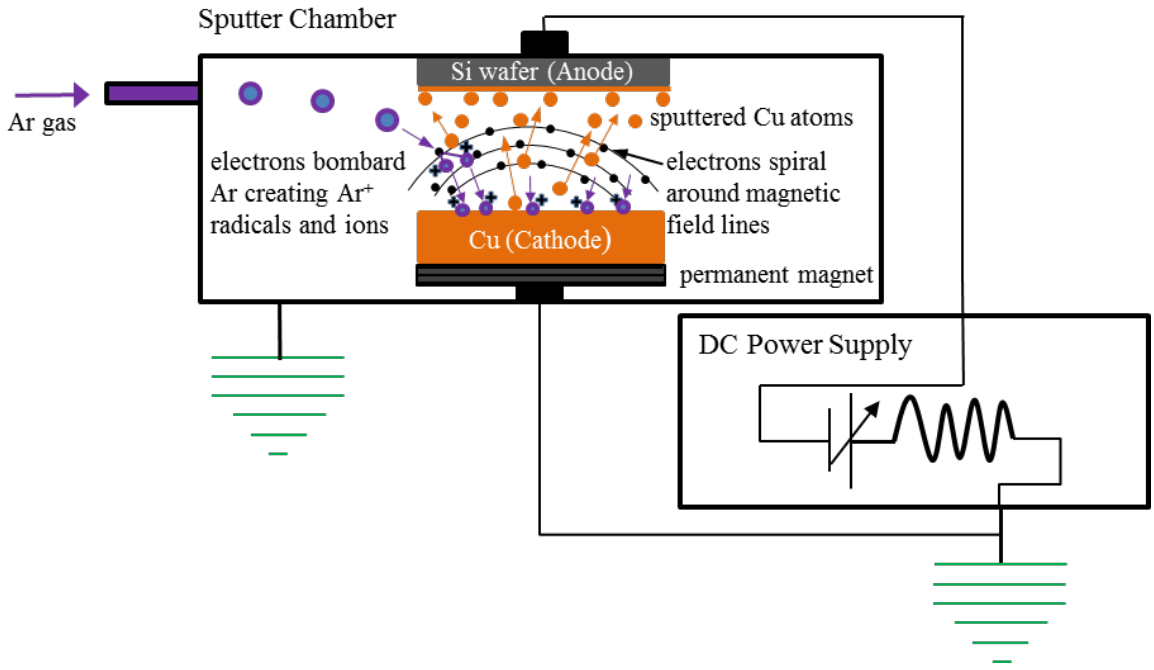

Figure 4.16. A model of a DC magnetron sputtering system (*Image from the author*).

The magnetron sputtering process created nanometer-accurate film height and uniform film coverage on wafer surfaces, while it allowed for more variety in the target material and control of the properties of the resulting film. The Ar sputtering gas was chosen because it is inert. The target used a permanent magnet to stabilize the ionic charge of the gas so that magnetron sputtering can be conducted at lower chamber and gas pressures. More information is provided in the following paragraph on the role of the magnets. The gas pressure can be as low as 0.5 mTorr. Ar gas pressure was used to control the deposition rate of the sputtering process because it moderated the mean free path of the source atoms moving toward and collecting on the wafer.

Sputtering sources (targets) often employ strong electric and magnetic fields. The electric field was produced by the source power supply. Its main purpose was to attract the cations created by the plasma toward the target. The permanent magnet was located behind the target to control the free electrons in the plasma. It protected the target material from electron contact by creating a field that kept the electrons restrained and trapped above the target material where they could not harm it. Keeping the plasma close to the target aided the deposition rate of the sputtering process because the distance to impact was kept to a minimum. The magnet rotated via its attachment to the gun motor to facilitate homogeneous plasma and avoid hot spots in the sputtering chamber.

Furthermore, the magnet increased the likelihood that the electrons ionized the Ar gas atoms. Electrons follow helical paths around the magnetic field lines due to the influence of concurrent magnetic and electric fields which were orthogonal to each other. As a result, more ionizing collisions with gaseous neutrals happened near the target surface than would otherwise occur. An additional benefit of the magnet was its magnetic field lines were curved, so the paths of the electrons in the chamber were extended through the stream of gas, resulting in improved ionization rates and decreased time duration for completion of the film's deposition. As the

target material was depleted, an annular erosion profile developed on the surface of the target in response to the shape of the magnetic field. The DC sputtering tool in Figure 4.17 was used to sputter metal films on wafers in the HiDEC facility.

Figure 4.17. The Varian 3180 sputtering system used in the deposition of Ti, Cu, and Al films (*Image from the author*).

The tool processes up to 25 125 mm diameter wafers in sequence when loaded into a cassette. There are 3 stations containing metal sources, an RF etch station, and a load lock where wafers entered the machine for transfer to the etching and sputtering stations. The stations were located in a circular arrangement and in a specific order to facilitate traditional wafer processing steps. The order was: (1) load lock, (2) RF etching, and (3) Ti, (4) Cu, and (5) Al targets. However, the film deposition order could be programmed independently of the station order to allow a variety of possibilities for creating custom composite film structures. The RF etch step, often included for cleaning and roughening Si wafers before sputtering metal, was omitted in favor of

O_2 plasma ashing described in section 4.2.4. Since Cu was the principle film to be sputtered on the wafer surface in this research, the discussion of the sputtering process hereafter is based on it. A c-Si wafer sputtered with Ti and Cu is shown in Figure 4.18.

Figure 4.18. C-Si wafers were sputtered with 50 nm Ti and 2.5 and 2.75 µm Cu thicknesses. Good film coverage and uniformity was achieved (*Image from the author*).

The thickness of the sputtered metal was dependent on settings for process deposition power, rate, and duration. The parameters were determined through experiments. It should be pointed out that Cu atoms do not adhere permanently to the surface of c-Si wafers due to their migration into the wafer. Ti, however, provided a barrier as well as an excellent bonding material between c-Si and Cu. A 50 nm thick Ti film was sputtered onto the wafers first, followed by the Cu film

with thicknesses of approximately 2.5 and 2.75 µm for building composite film layers on smooth samples.

To create the Ti and Cu films, Ar cations created by the plasma bombarded the Ti and Cu targets which had a negative voltage potential. The deposition power parameter which set the voltage potential was programmed in the sputtering recipe. It determined the percentage of the 12 kW available from the power supply to control bombardment strength. During bombardment, high densities of Ti and Cu atoms were ejected from the targets, generating a vapor or spray of the respective films. The ejected Ti and Cu atoms are charge neutral and as such are uninhibited by the plasma's magnetic and electric fields, though they do compete for space with incoming neutral Ar atoms in the chamber. The c-Si wafer was located nearby on the anode of the sputter chamber to enable the collection of Ti and Cu atoms into films on its surface. The parameters for the metal depositions are shown in Table 4.8.

Table 4.8. The sputtering system parameters for depositing Ti and Cu films on c-Si wafers.

Metal Type	Power (W)	Total Power (W)	Total Power (%)	Deposition Rate (Å/s)	Deposition Thickness (Å)	Deposition Duration (s)
Ti	2500	12000	21	50	500	10
Cu	3000	12000	25	181	25000	140.1
Cu	3000	12000	25	181	27500	148.7

4.3.2 Theory of Electroless Cu Film Deposition

A problem encountered in the deposition of Cu film on porous topographies was the inability of the sputtered Cu film to penetrate uniformly to the full depth of the 50 and 75 µm pores. Examination of the pore profiles using SEM micrographs revealed the depth of Cu film was limited to about 25 µm, regardless of the amount of Cu film accumulating on the surface

surrounding the pores. Another concern was related to the diameter of the pore being relatively unaffected by the thickness of the sputtered Cu film. The idea was to use the Cu film deposition to reduce the diameter of the pores, in the case of the smallest pore of 6 μm, to 1 μm by depositing 2.5 μm thick Cu film on the pore wall and the surface surrounding each pore. Experiments were done to determine the thickness of Cu film required for reducing the pore diameter. The target diameter required a 15 μm thick Cu film on the surface in order to achieve it. Even though the diameter was achieved, the depth limitation of 25 μm remained the flaw in the sputtering approach.

A hybrid approach utilizing sputtered, electroless, and electrolytic deposition techniques was incorporated to address the problems of Cu film penetration into the deep pores and non-uniform accumulation occurring inside and outside of the pore. Electrolytic deposition is not discussed here. Electroless Cu uniquely provided a solution to the problem of obtaining a smooth, uniform film inside of the pores. Electroless plating uses a reduction/oxidation reaction to deposit metal on an object without an electric current. It employs a constant metal ion concentration to bathe the plating object, resulting in uniform metal deposits along edges, inside holes, and over irregularly shaped objects which are difficult to plate evenly. Electroless plating is also used to deposit a conductive surface on a nonconductive object to allow it to be electroplated. The drawback to the technique, though, is its complicated chemical set-up and maintenance.

Electroless plating is a non-electrolytic process. Therefore, the deposition of a starter film of metal was required. For the author's work, two starter films were utilized: one for the surface and another for inside the pores. A 100 nm thick Ti film was sputtered on the surface of the patterned c-Si wafers using the CVC DC sputtering tool located in the Petit Organic Cleanroom at the Georgia Institute of Technology. This film was necessary because the wafers contained a

polished finish which prevented the adsorption of the typical colloidal starter films used in electroless Cu deposition. The sputtered Ti film also served as an electrochemical bridge to facilitate seamless interaction of electroless and electrolytic Cu deposition inside the pores and it enhanced array-to-array Cu film thickness uniformity during the electrolytic process. Electrolytic Cu deposition was necessary to achieve the final 2.5 and 2.75 μm thicknesses because electroless Cu was restricted to 1 μm. The surface surrounding the pore opening would have a slightly thicker film due to the 100 nm sputtered Ti, but the enhancement in array uniformity made the trade-off worthwhile.

The second starter film, a Pd-Sn colloid, was essential to facilitate electroless Cu deposition inside of the pores. A catalyst solution was introduced first so that the Pd-Sn colloid particles would be adsorbed on the non-conductive surface of the c-Si pore wall when lowered into it. The Pd-Sn colloid was prepared by mixing $PdCl_2$ with an excess of $SnCl_2$ in HCl solutions in a vat. Through the reduction of Pd^{2+} ions to Pd^0 by $SnCl_2$ via the redox reaction, $Pd^{2+} + Sn^{2+} \rightarrow Pd + Sn^{4+}$, a solution was produced that contained Pd particles surrounded by a Sn (IV) sheath. Once adsorbed, a chemical accelerator was used to expose the Pd by partially removing the Sn sheath thus changing the ratio of Pd to Sn.

The colloid particle cluster diameter is between 40 and 70 nm and consists of 20 to 100 particles per cluster. The Pd-exposed colloidal particle nuclei diameters are typically from 1 nm to 5 nm. The specimen was then submersed in a $CuCl_2$ salt bath for the deposition of Cu on the Pd-rich substrate. The author contemplated undertaking the electroless and electrolytic Cu processes, but it was decided in the end to allow the specialists at Data Electronic Services perform them. The collective results of the sputtered, electroless, and electrolytic processes on c-Si wafers are shown in Figures 4.19a - c.

(a)

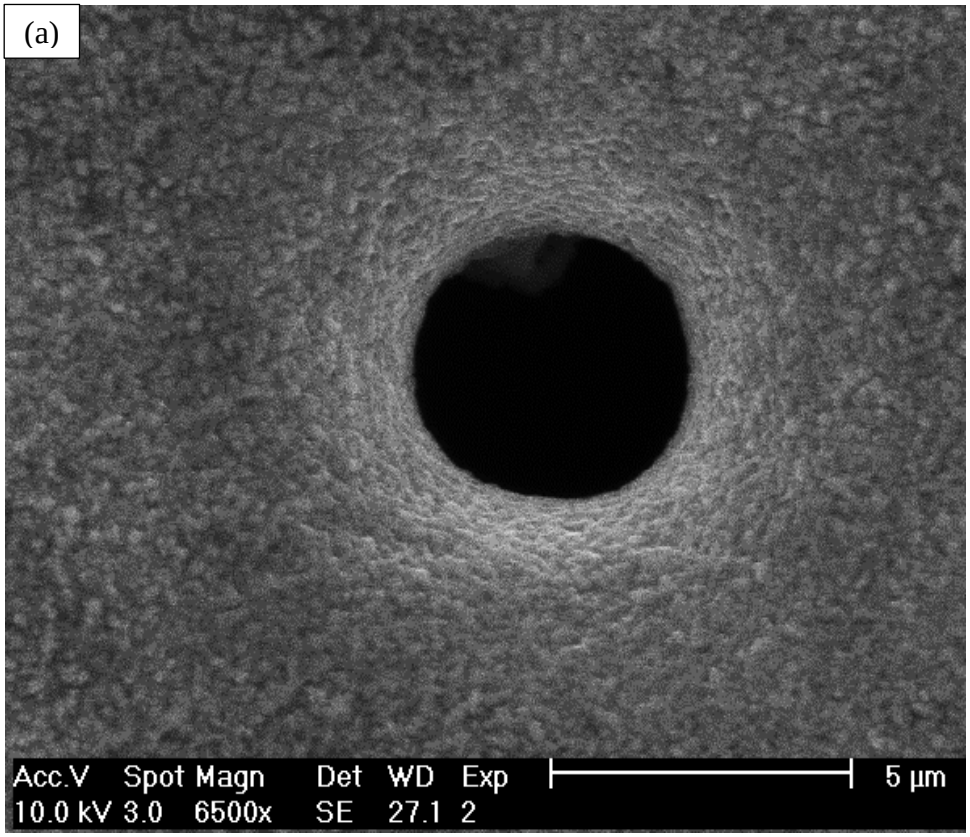
Acc.V Spot Magn Det WD Exp
10.0 kV 3.0 6500x SE 27.1 2
5 µm

(b)

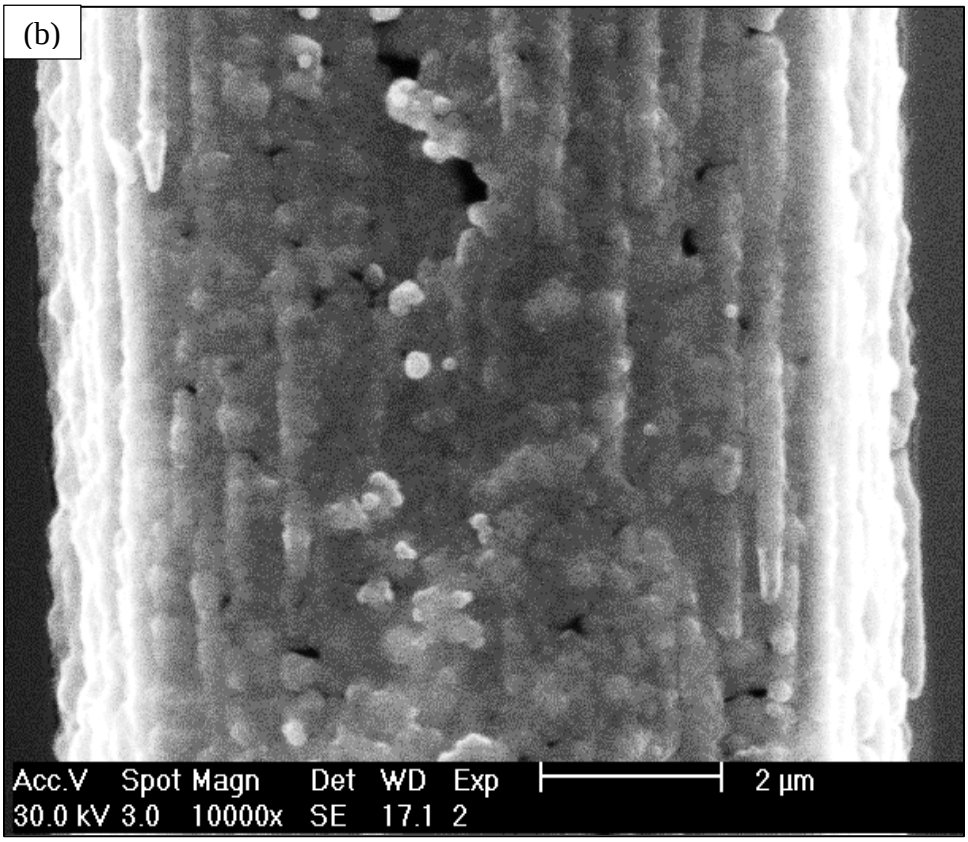
Acc.V Spot Magn Det WD Exp
30.0 kV 3.0 10000x SE 17.1 2
2 µm

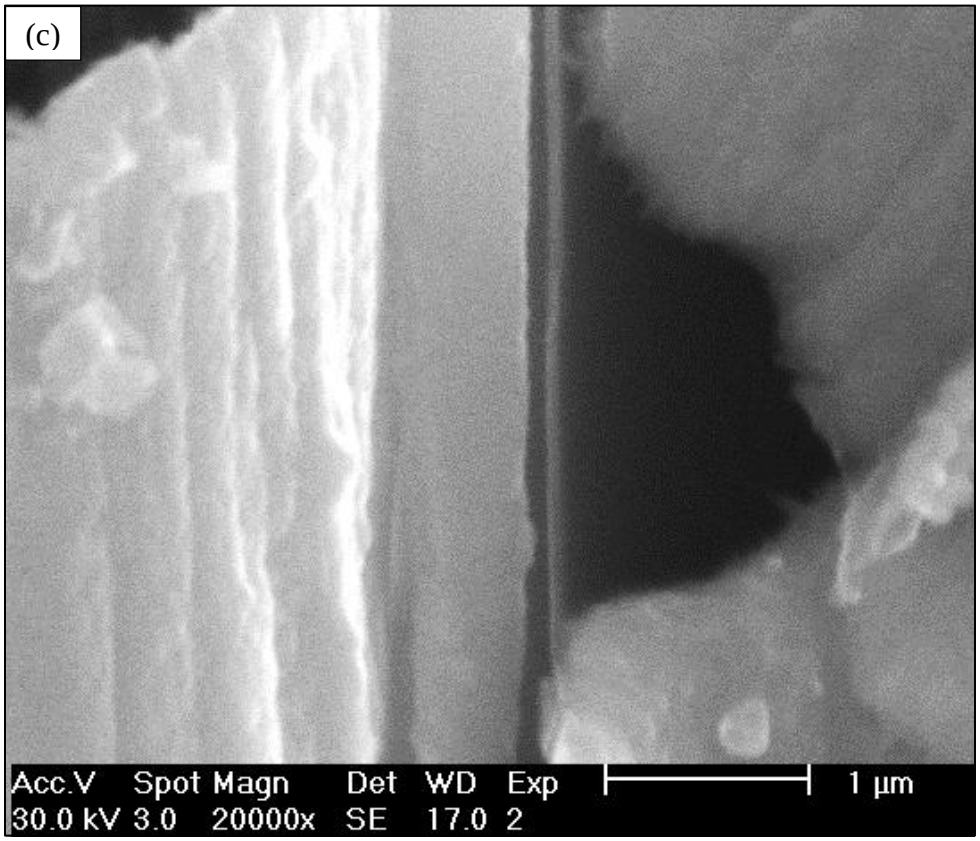

Figs. 4.19a - c. SEM micrographs of (a) the pore opening, (b) the outer wall, and (c) the inner wall. The pores were constructed from c-Si overlaid with Sn-Pd colloid, electroless, and electrolytic Cu depositions. The combined processes produced good conformity to the physical irregularities along the outer pore wall, yet achieved relatively smooth, uniform surfaces on the inner pore wall (*Images from the author*).

4.3.3 Theory and Operation of the PECVD Tool for a-Si:H Film Deposition

The plasma enhanced chemical vapor deposition (PECVD) tool used for applying thin films is the SLR 730 (Plasma-Therm, Pfäffikon, CH). The tool offers uniform sidewall coverage of the deposited film on high aspect ratio features such as pores. The tool is shown in Figure 4.20.

Figure 4.20. The Plasma-Therm PECVD tool was used to deposit a-Si:H films (*Image from the author*).

The system uses O_2, N_2O, and silane (SiH_4) gases to create silicon oxides (SiO_2), silicon nitrides (Si_xNi_x), and a-Si:H films on wafers, respectively. The first two film types are used during MEMS fabrication processes for dielectric layers, surface machining building materials, etch stops, and sacrificial layers. The third film type has a following among researchers interested in photovoltaic-related applications. The particular interest in the tool for this research was to create a-Si:H films to modify the surface chemistry of the nano-pores for lubricant retention enhancement. The a-Si:H film features SiH_x bonds [77] which offer attractive opportunities for intermolecular bonding between the atoms of a-Si film and those of hydrocarbon-based lubricants.

The process chamber configuration is referred to as the capacitive-coupled or parallel plate design. The design features a plate (anode) affixed to the top of the chamber and another plate (electrode) on the bottom as shown in Figure 4.21.

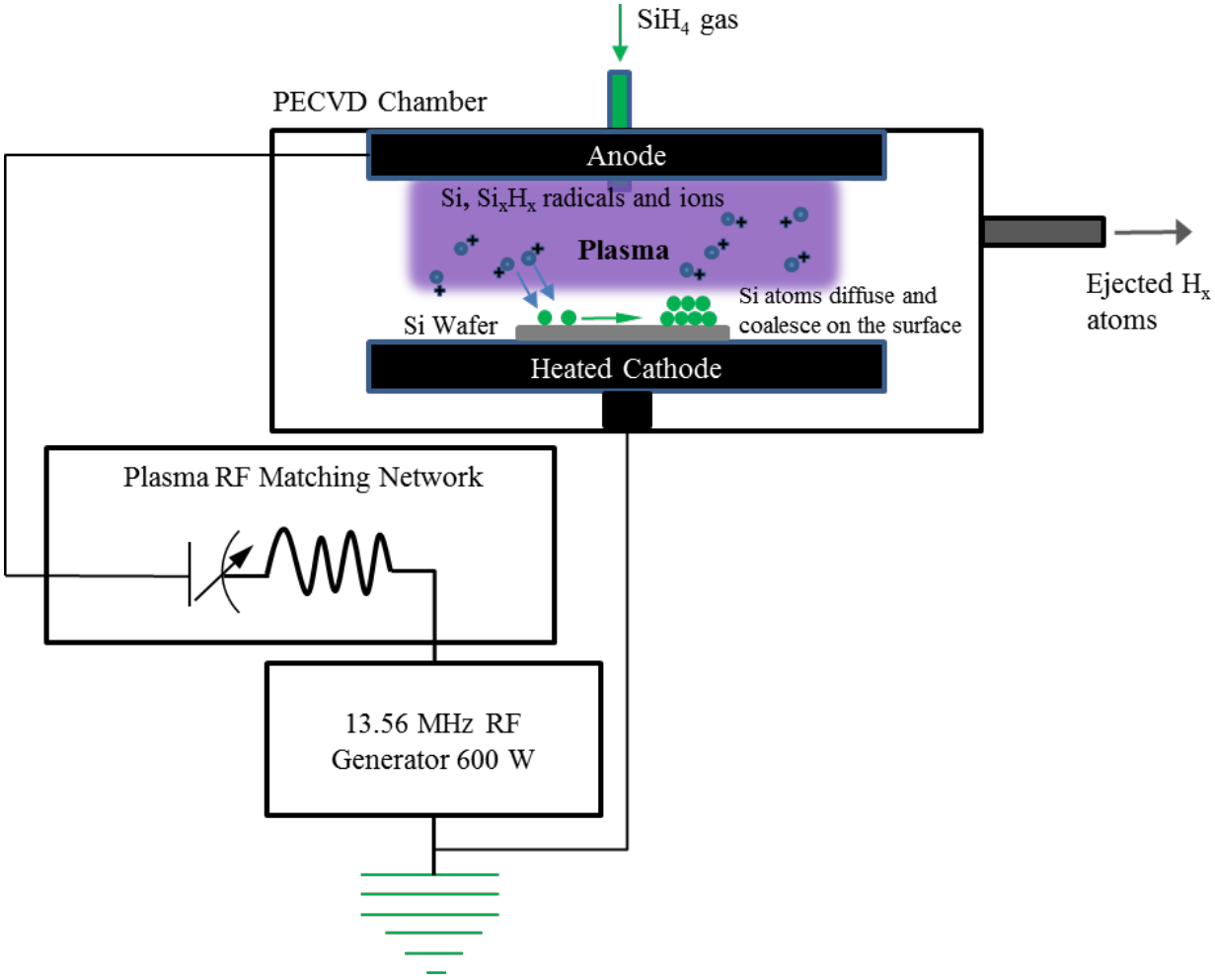

Figure 4.21. The parallel plate design of the PECVD chamber generates Si and SiH_x cations and radicals (*Image from the author*).

The theory of the PECVD system is similar to other plasma-based tools discussed thus far. The load lock chamber was vented to atmospheric pressure using N_2 gas to allow for loading 3 wafers onto the transfer tray. After loading the wafers, the chamber was pumped down to 100 mTorr. The process chamber pressure was maintained to 10 mTorr to ensure the by-products from

previous processing do not enter the load lock, to control the mean free path of the bombarding ions and molecules, and to enhance the purity of the deposited film. A robotic arm transferred the tray into the process chamber through an isolation valve located between the chambers.

The wafers were placed on the grounded bottom electrode (cathode). From that point and until the purging of the chamber at the end of processing, the chamber pressure was maintained at 900 mTorr using a process pressure controller. The pressure affected the mean free path of the cations and radicals as they journeyed toward the wafer surface and determined whether the deposition products polymerized in the gas phase or on the substrate where it was desired. If the pressure was too low, the deposited film exhibited a columnar morphology with higher defect densities as seen with physical vapor deposition methods [78]. The wafers and cathode were preheated to 250°C amid a 450 sccm flow of N_2 purge gas. Heating the substrate improved the deposited film's adhesion, uniformity, and density, in addition to decreasing the occurrence of pin holes.

Once the chamber conditions for deposition were met, N_2 flow was terminated. Silane was injected into the chamber at 85 sccm (without RF power) to stabilize the gas concentration in preparation for the plasma. It was important to select the correct gas flow because it determined the residency time of the gas in the process chamber. After 30 s SiH_4 flow duration, the RF power was activated while the gas continued to flow. The power used for producing a-Si:H film was 20 W at 13.56 MHz frequency. The SiH_x and Si cations produced in the plasma were attracted toward the wafers due to the presence of the grounded cathode on which the wafer was placed. RF power controlled the ion bombardment strength. The bombardment strength was used to manipulate the deposited film's properties (density, stress, sidewall coverage), unlike DRIE in which ion bombardment affected the anisotropy of the etch process.

The reaction created by the plasma is represented in simple form by

$$SiH_4 \rightarrow Si + 2H_2 \qquad \text{Equation (4.2)}$$

In actuality, the plasma electrons decomposed SiH_4 into Si cations and neutrals (radicals) and various radicalized molecules of SiH_x. The Si and SiH_x radicals were neutrally charged and so were unaffected by the electric field between the anode and cathode. Although electrically neutral, radicals are highly chemically reactive molecules and were the precursors formed in the plasma. They diffused toward the wafers as a result of the momentum of the flowing gas, and to a large extent, they determined the deposition rate of the film. The gas, which possessed a low sticking coefficient, delivered these molecules to the wafer surface to take part in surface chemical reactions with other adsorbed precursor molecules. The surface reactions between Si atoms resulted in the release of the by-product, H_2, which was evacuated by the vacuum system. The molecular composition and intermolecular reactions to form a-Si:H film are discussed in greater detail in section 7.2.1.

The growth of the film was therefore controlled by the rate of the reactions occurring on the wafer surface and not the flux of the impinging molecules. If the reactions were produced in the plasma rather than on the wafer surface, the products would be evacuated along with the exhausted H_2 molecules. Once the precursors were deposited on the wafers, the heated cathode served as a catalyst for the reactions and provided high mobility energy to the SiH_3 molecules diffusing and coalescing on the surface. High mobility molecules produce a smooth, conformal film, in contrast to the low mobility ones that can occur due to high sticking coefficients. Low mobility molecules result in a columnar film morphology that resembles vertical striations of a-Si:H film with a high void volume between them.

The deposition thickness was determined by the reaction rate of the products arriving at the wafer surface. Studies were done to determine the proper deposition rate for achieving the highest film quality and controlled thickness without introducing film stresses detrimental to the adhesion of a-Si:H film to the substrate. The deposition rate is 100 nm per 4 min and 42 s process duration when using the parameters listed in Table 4.9.

Table 4.9. An overview of the process parameters used to deposit 250 nm thick a-Si:H films.

Steps	SiH_4 Flow (sccm)	N_2 Flow (sccm)	Pressure (mTorr)	Power (W)	Duration (min:s)
Preheat	0	450	900	0	5:00
Stability	85	0	900	0	0:30
Deposition	85	0	900	20	11:45
Purge	0	0	100	0	2:00
Evacuation	0	0	10	0	1:10
End	0	0	10	0	0:10

The wafers were removed from the PECVD system and allowed to cool to room temperature. A deposition thickness of 250 nm was achieved for coverage of smooth and nano-porous Si-Cu composite surfaces. The wafers exhibited a purple hue that was characteristic of a-Si:H film deposited to this depth. Wafers sometimes exhibited blue/green hues, but this was not evidence of a film defect. Figure 4.22 shows a smooth Si-Cu wafer after a-Si:H film deposition. The film exhibited good adhesion and uniform coverage. The wafers were placed in storage boxes and kept under normal laboratory conditions until ready for further processing. The a-Si:H film surface was known to develop an oxide film that reached its saturation thickness in 2 days. SRD cleaning was used to remove the oxide before proceeding to the other processing steps.

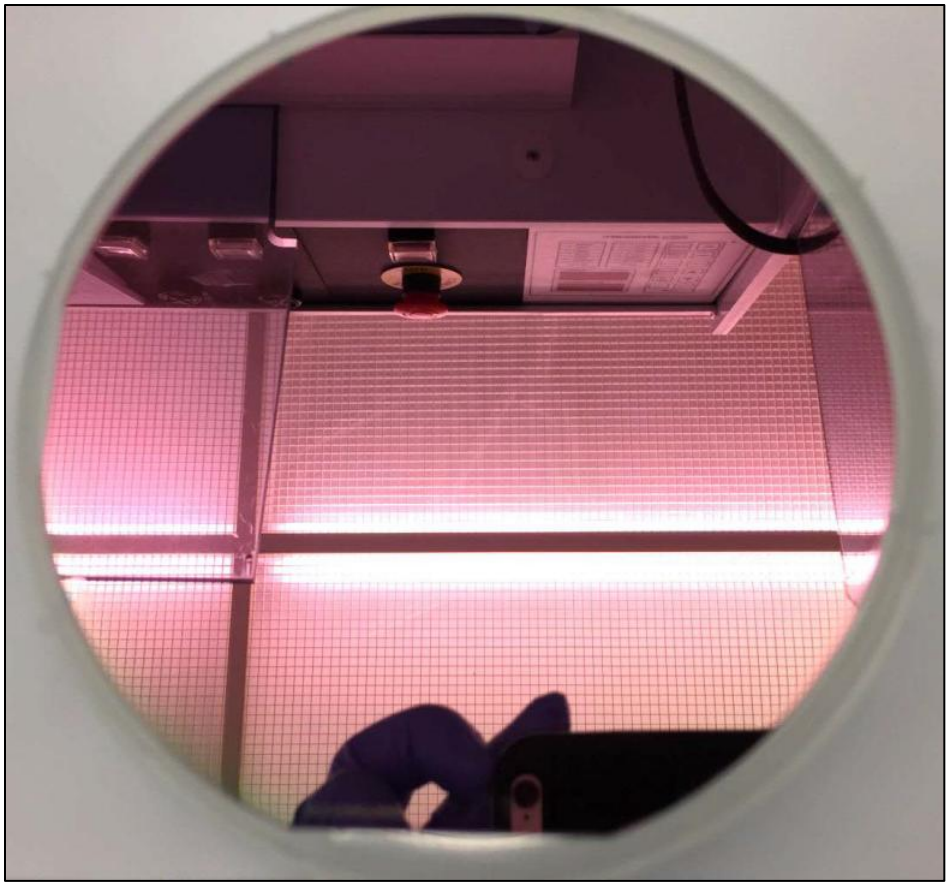

Figure 4.22. The substrate is a smooth Si-Cu wafer. The purple hue is indicative of 250 nm thick a-Si:H film deposited on Cu film (*Image from the author*).

4.3.4 Creating Samples from Wafers Using the Dicing Saw

The processed wafers passed the patterning, developing, deep reactive ion etching, and cleaning stages, as well as Cu and a-Si:H film depositions and were ready for dicing. As a protective measure to ensure the control wafers having Cu film were not exposed to the cooling water used by the dicing saw blade and therefore allow an opportunity to cause oxidation, the wafers were coated with AZ-4330 photoresist. After placing each wafer onto the tape and mounting ring using the model DFM-M150 plastic film mounter (Disco Abrasive Systems, Ltd, Japan), a single wafer was placed into position on the 928-10 Plus (Kulicke & Soffa, Yokneam Elite, Israel) dicing machine shown in Figure 4.23.

Figure 4.23. Image of the dicing saw used to cut samples from c-Si wafers for testing (*Image from the author*).

Before dicing the wafer, a blade height check and theta alignment were performed to ensure the targeted wafer features and desired cutting path were aligned with the cutting blade as it traveled across the wafer. Coordinates for the –*x* and –*y* cut indices (25.4 mm and 12.7 mm, respectively), 0.6761 mm wafer and tape thickness, 0.6001 mm cut depth, 0.0760 mm tape thickness, 2.54 mm/s entry speed, 5.40 mm/s cutting speed, 30,000 rpm spindle speed, and circular wafer diameter (125 mm) were then programmed to automate the dicing process. Precise dicing dimensions were important to maintain the size uniformity of the samples. Each

wafer yielded 28 samples sized 12.7 mm x 25.4 mm. A diced wafer and sample are shown in Figures 4.24a and b.

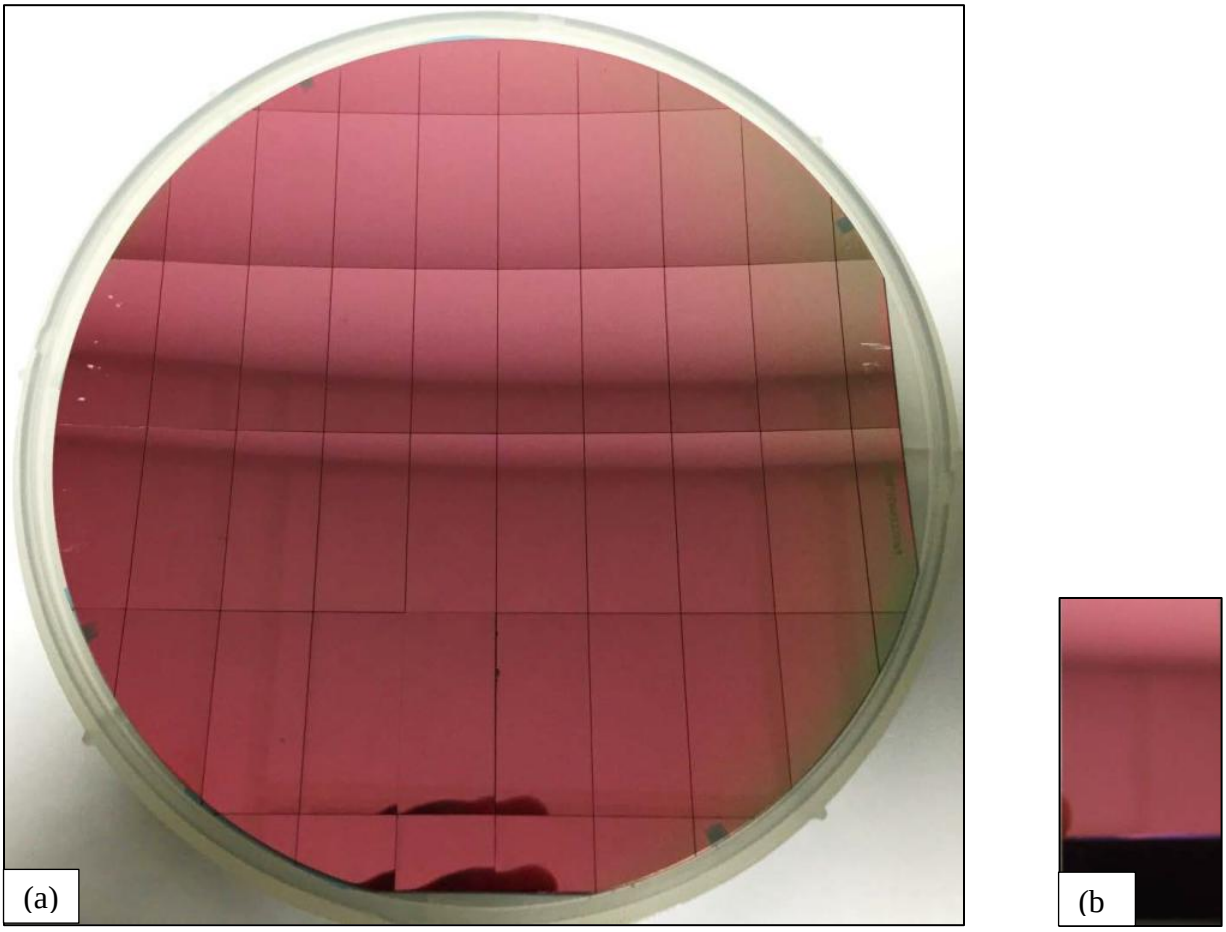

Figures 4.24a and b. Examples of (a) diced Si-Cu wafer and (b) test sample from the wafer. The image was taken after the application of 250 nm thick a-Si:H film (*Images from the author*).

The samples were demounted from the dicing tape that was applied to the back of the wafers to hold the diced samples together until ready for separation. The model 4800 demounting machine (Semiconductor Equipment Corp, Moorpark, CA, USA) uses a combination of vacuum pressure and heat to de-bond the adhesive of the tape from the samples. The samples contained wafer fragments and debris from the dicing process. Cleaning the samples of the saw's contaminated cooling water was in order also. The samples were pre-washed under a spray of DI water using

moderate pressure, followed by dump rinse cleaning for 3 cycles using the caustics wet bench in HiDEC.

The samples underwent a further cleaning process that consisted of placing them in a fixture that allowed them to be lowered vertically-oriented into a solution of acetone in a beaker. They were then washed ultrasonically for 20 min. Dump rinsing the samples followed the acetone cleaning to remove the acetone remnants from the surface. A beaker of IPA was prepared and the samples, fixture, and beaker were placed once again in the ultrasonic bath and cleaned for 20 min. The samples were removed from the IPA and placed into the dump rinse a final time to remove the IPA residue. Once dump rinsing was completed, the samples were individually dried using a spray of N_2 vapor and they were placed in storage containers under normal lab conditions until ready for further processing.

An Adventurer Pro AV64C digital scale (Ohaus Corporation, Pine Brook, NJ, USA) was used to measure the sample's tare mass. The scale has an accuracy of 0.1 ± 0.05 mg. After recording the tare mass and assigning an identification number for the 216 samples used in evaporation testing, the next steps were to apply the lubricant and remove the air from it and the pores. This is explained in section 4.4.

4.4 Application of Testing Lubricant on the Samples

Successful application of the lubricant and testing using thermal evaporation were cornerstones in the effort to determine whether enhanced retention of lubricant was ultimately achieved in the author's work. A description of the testing lubricant is provided in section 4.4.1, a detailed discussion of common issues encountered when porous topographies are used in conjunction with liquids is done in section 4.4.2, the method for determining the lubricant mass is explained in section 4.4.3, and the description of the evaporation testing apparatus is given in section 4.5.

4.4.1 Description of the Lubricant

A mineral-based lubricant was applied to the samples for evaporation testing. The oil brand was 3-N-One™ Multi-Purpose Oil, distributed by WD-40 Company, Inc (San Diego, CA, USA). The mineral oil was specified as hydrotreated heavy naphthenic petroleum distillate (distillates have an initial boiling point >100°C), boiling point >287.8°C, 23.31 cSt viscosity at 37.8°C, 0.866 - 0.923 relative density, and 151.7°C flash point. The naphthenic description of the lubricant identified it as a member of the cycloalkanes which were characterized by single-bonded C atoms arranged into ring structures, and each C atom was bonded to two H atoms. Their chemical formulation was described by C_nH_{2n} similar to alkenes; however, the lubricant itself was a complex mix of these ringed (cyclic) hydrocarbons. During testing, carbon monoxide, sulfur oxides, aldehydes, and other petroleum decomposition products may occur if there was incomplete combustion. Oxides of nitrogen, phosphorus, calcium, copper, magnesium, sodium, and hydrogen sulfide may also be present in various concentrations. The lubricant's chemical abstract service (CAS) number is 64742-52-5.

4.4.2 Air Evacuation from the Pores and Lubricant Using Ultrasound and Vacuum Chamber Apparatus

Some problems that may affect the evaporation of lubricant from the samples were the presence of air bubbles and pockets. During normal handling of the container of lubricant and the application of lubricant onto the sample surface, it accumulated air bubbles. This was unavoidable. Another source of concern was the air that existed inside the nano-pores before the lubricant was applied to the sample surface. After the lubricant was applied, it essentially enveloped the air therefore trapping some between the pore surface and lubricant. The reduction

of heat transfer by the presence of this air could affect evaporation even more. An illustration of the intrusion of air into the lubricant and pore is shown in Figure 4.25.

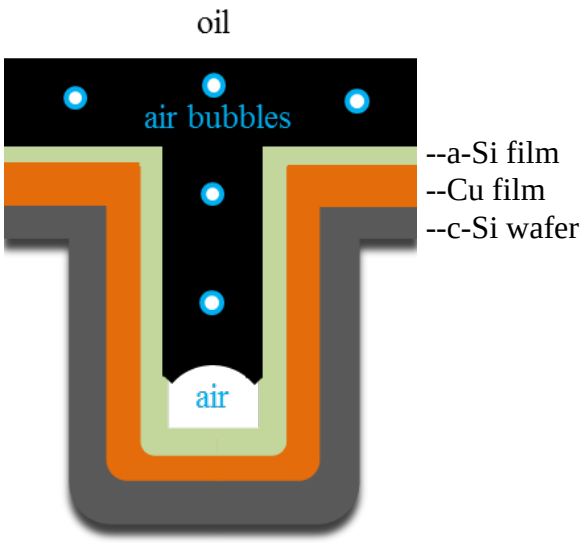

Figure 4.25. Illustration of air entrapped within the lubricant and pore (*Image from the author*).

Air entrapment was an issue that had the potential to affect the evaporation data of smooth and nano-porous surfaces alike. When accounting for the 300 and 400°C temperature range of air during evaporation testing at atmospheric pressure, air has a mass density that is between 0.06158 and 0.05243 kg/m^3 [26], so its mass was ignored during the calculation of the lubricant amount to be applied on the samples. More importantly, the thermal conductivity of air varies between 0.04418 and 0.05015 W/m-K during the full temperature range of testing, which meant it was a very poor conductor of heat. It was this property that might have an effect on the amount of heat transferred from the samples to the lubricant. The amount of heat transferred, in turn, affects the amount of lubricant evaporated. Figure 4.26 further illustrates some possible effects of air on the filling of the pores.

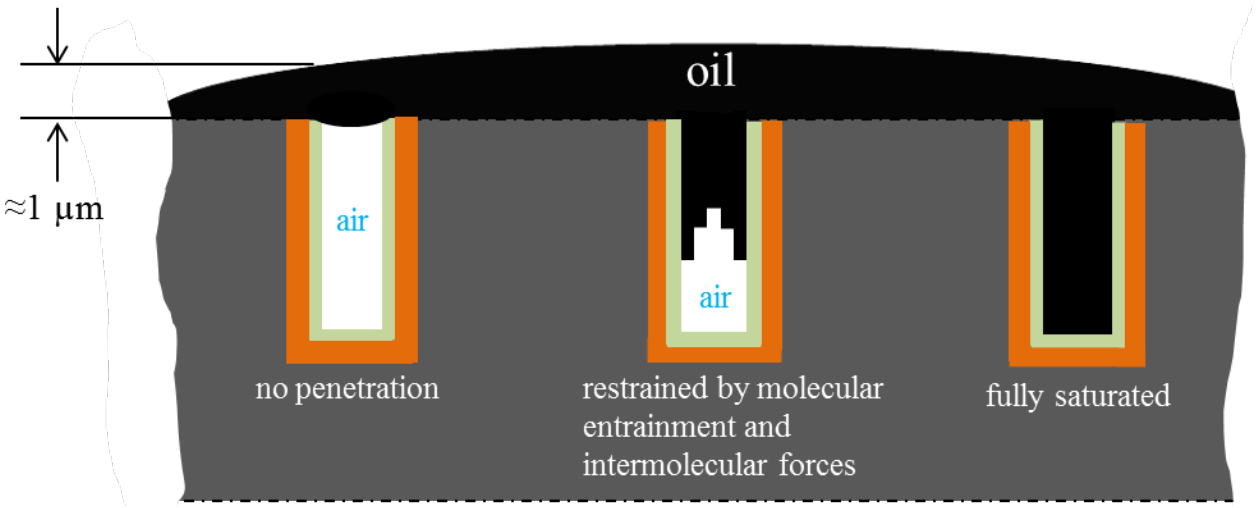

Figure 4.26. The lack of penetration of lubricant into the pores might affect the evaporation of lubricant from the nano-porous topographies (*Image from the author*).

Figure 4.26 shows two undesirable conditions that arise when air exists between the pore surface and lubricant. The first pore (on the left) in the illustration demonstrates a condition known as "tenting" of the lubricant across the opening of the pore. This occurs when the lubricant's molecules possess greater intermolecular attraction forces than does the pore surface toward the lubricant. The lubricant is not pulled downward into the pore to permit its filling. This phenomenon is more of a concern for the control samples which have Cu film as a layer in contact with the oil. The surface of Cu is less oleophilic than a-Si:H film [46]. Alternatively, tenting can occur when the diameter of the pore is small such as the case with nano-pores. The lubricant molecules build a bridge or tent across the pore opening, therefore preventing lubricant penetration into the pore. Air inside of the pore can cause the lubricant to encounter even greater resistance to pore filling.

The middle pore in the illustration shows the result of a pore being partially filled. The lubricant can penetrate the pore to some extent because of the capillary attraction of the pore surface to the lubricant. The penetration is governed by the strength of the bonding between the lubricant and

pore surface molecules as well as the intermolecular bonding strength of oil molecules. The molecules accumulate near the pore opening to inhibit further penetration of oil. The air trapped at the bottom of the pore also acts as a restraint to limit the complete filling of the pore. Unless there is some external assistance, the pocket of air cannot simply migrate through the lubricant because of the higher viscosity of the lubricant. Even worse, during lubricant evaporation the entrapped air is further immobilized as the surrounding lubricant polymerizes into a thick varnish.

The third pore illustrates the ideal situation because it permits full contact between the lubricant and pore surface. The pore is fully saturated with lubricant, enabling it to achieve the maximum heat transfer possible for evaporation. In order to avoid the pitfalls of the first and second pore conditions, it was prudent to evacuate the air from the lubricant and pores before testing began. This was accomplished by submersing the samples in a beaker of lubricant for 48 h and degassing them using the ultrasonic feature of a sonicator for 1 h.

The sonication apparatus, model 5510 (Branson, Danbury CT, USA), beaker of lubricant, and sample holder are shown in Figures 4.27a - c. The apparatus accomplished degassing by creating ultrasonic pressure waves that caused the air bubbles in the lubricant to align horizontally and coalesce. The coalescing bubbles formed larger bubbles and consequently larger surface areas which caused the air bubbles to rise toward the liquid surface where they were released. Degassing also removed the bubbles trapped between the sample surface and liquid to promote filling of the pores. After degassing, the samples were removed from the beaker and sample holder. Excess lubricant was removed from the samples using absorbent cleanroom wipes. Any remnant of oil film residing on the back of the samples was removed using a cleanroom wipe dipped in acetone.

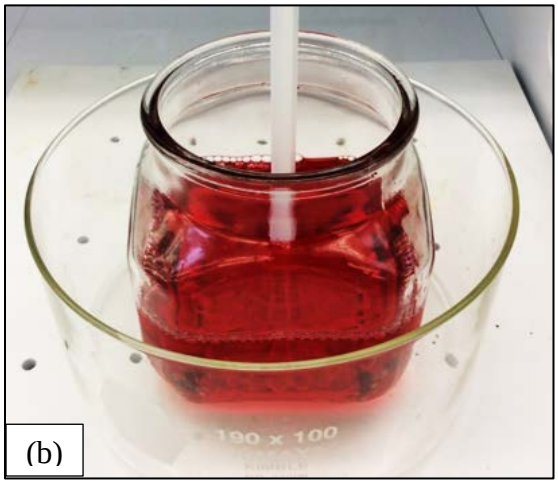

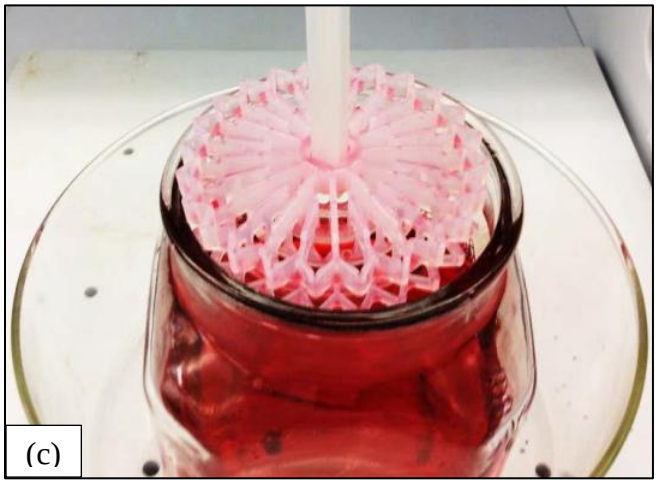

Figures 4.27a - c. (a) Degassing apparatus, (b) beaker of lubricant, and (c) sample holder used to degas the lubricant and pores in the samples (*Images from the author*).

The combination of degassing by ultrasound and vacuum is promoted as a better method of removing entrapped air from liquids and surfaces than ultrasound alone. A mechanical vacuum pump and chamber was procured from HiDEC. The samples were placed inside the chamber in flat orientation and kept under vacuum for 4 h. Figure 4.28 shows the vacuum chamber and pump used for this purpose.

Figure 4.28. The vacuum chamber and pump used to remove trapped air from the samples (*Image from the author*).

The vacuum pump was the Leybold-Heraeus model D16B (Leybold Vacuum, Export, PA, USA). It was capable of achieving 10 mTorr vacuum pressure. The pump's vacuum pressure was important because the testing lubricant can only tolerate pressures above 7.5 mTorr. Allowing the pressure to decrease below 7.5 mTorr was undesirable because it reduces the original amount of oil deposited on the samples for evaporation testing. Likewise, pressures below 0.1 mTorr would cause oil back-streaming in which the vacuum pump's own oil would vaporize and travel backward in direction and deposit on the sample's surface, thus affecting the pre-test amount of oil. To prevent both conditions from occurring, the pressure was monitored using a Televac II thermistor vacuum gauge (The Fredricks Co., Huntingdon Valley, PA, USA).

Another possible benefit of using the vacuum chamber and pump apparatus was the rigid piping connecting the chamber to the pump transmitted mechanical vibration. After the oil-laden samples were placed inside, the vibration of the chamber induced vibration of the lubricant on the sample surface. The vibration might weaken the intermolecular forces of molecules and allow surface forces to dominate and therefore aid the penetration of lubricant into the pores.

4.4.3 Determination of Proper Lubricant Mass for Retention Testing

After degassing the samples, the amount of lubricant required for testing must be attained. The total amount of oil was determined by calculating the volume of a pore, then adding the volumes of all pores and finally, adding the volume of oil that would reside on top of the patterned area of the sample if it was deposited to a depth of 1 µm. The 1 µm depth was derived from the knowledge that the clearance between bearing surfaces during operation is typically this depth. For smooth samples, an equivalent amount of lubricant was deposited over the same sized test area, meaning the total mass was the same as if pores were on the surface. This allowed a favorable comparison of smooth versus nano-porous sample's effect on lubricant evaporation. The sample testing area is illustrated in Figure 4.29.

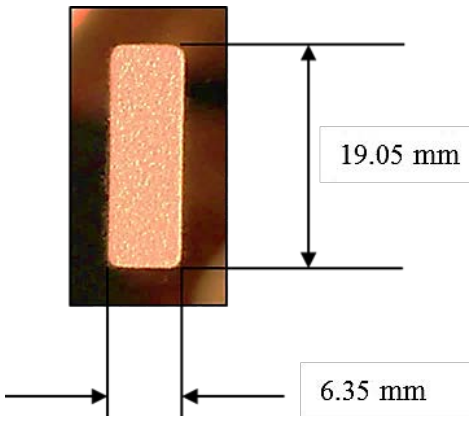

Figure 4.29. Example of the centrally-located testing area created on nano-porous samples to hold lubricant (*Image from the author*).

Figure 4.29 shows the dimensions of the test area on each sample to be 6.35 mm x 19.05 mm or 121 mm^2. Using the 1 µm depth as a reference, the volume of oil on top of the nano-pores was 0.1210 mm^3 or 120967500 μm^3. This area was assumed the same for each sample, regardless if the sample was patterned by nano-pores or smooth.

For nano-porous samples, the volume of each pore (there were 616,080 pores) was calculated using the formula,

$$\text{Pore Volume} = \pi \cdot \frac{\text{Si Pore Diameter}^2}{4} \cdot \text{Length} \qquad \text{Equation (4.3)}$$

The length of the pore is represented as *L* and the diameter is *D* as shown in Figure 4.30. Note that the diameter of the original pore opening in c-Si was used in equation (4.3). The volume of oil located on the testing area plus the volume for all pores (V_{Pores}) became the total volume (V_{Total}). The V_{Total} amount was converted into total mass (M_{Total}). The oil's density is 904.97 kg/m^3. The formula for the mass of the lubricant is given in equation (4.4) by,

$$M_{Total} = \text{Oil Density} \cdot V_{Total} \qquad \text{Equation (4.4)}$$

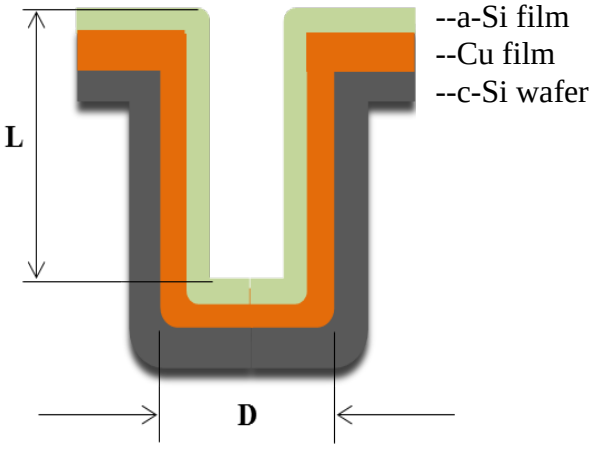

Figure 4.30. The dimensional representations *L* and *D* were used in the calculation of lubricant volume (*Image from the author*).

The sample's tare mass, which was recorded before degassing, became important in the ensuing calculations for lubricant mass to be applied on each sample. A veterinarian-grade syringe and needle was purchased from a local farming supply store. The syringe and needle was used to dispense the calculated mass that corresponded to the chosen pore diameter and depth plus the amount residing on top of the test area for each sample. The syringe and needle was the best method available for achieving a dispensing accuracy of 0.1 mg. The amount to be deposited was typically small because lubricant was already on the sample as a consequence of degassing. The lubricant's mass was adjusted while the sample remained on the scale. The calculated amounts are shown in Table 4.10. For convenience, the M_{Total} amounts were rounded to the nearest 0.1 mg during deposition. Further clarification is provided in the Appendix.

Table 4.10. Values for M_{Total} calculated for oil deposition on smooth and nano-porous samples.

Oil Amt	**6 µm dia, 25 µm D**	**6 µm dia, 50 µm D**	**6 µm dia, 75 µm D**	**6.5 µm dia, 25 µm D**	**6.5 µm dia, 50 µm D**	**6.5 µm dia, 75 µm D**
$\mathbf{V_{Pores}}$ **$(\mu m)^3$**	435481290	870962581	130644387	511085681	102217136	153325704
$\mathbf{V_{Total}}$ **$(\mu m)^3$**	556448791	991930081	142741137	632053181	114313886	165422454
***$\mathbf{M_{Total}}$ (mg)**	0.50356949	0.89766697	1.29176447	0.57198917	1.03450638	1.49702359

*Slight dimensional variations existed from sample to sample. Note that the 6 and 6.5 µm diameters were used in the calculations for M_{Total} so that extra lubricant was added to the samples before testing to ensure they were sufficiently covered.

4.5 Evaporation Testing Apparatus

The American Society for Testing and Materials (ASTM) created testing criteria that provided a method of calculating evaporation losses of lubricants such as oil and grease (ASTM D-972-91 and D-2595-90, respectively). The standards cover test apparatus construction, testing temperatures and duration for oil and grease lubricants, and methods of data acquisition.

Although the standard's primary focus was the evaporation of lubricant from a cup and not the substrate on which the lubricant rested, some of the criteria were used, nonetheless, during the testing of smooth and nano-porous Si-Cu composites to investigate lubricant evaporation.

The completed testing apparatus is shown in Figures 4.31a and b. House air having a temperature between 15.5 and 29.4°C was supplied to a pressure regulator that reduced the air pressure to 172.4 kPa. The air was routed via 6.35 mm high-pressure plastic tubing into a drier canister containing silica gel desiccant material. The dried air left the canister and flowed through a Millipak 100 particulate filter designed to remove impurities as small as 0.22 µm diameter. A second pressure regulator that was more sensitive to the test requirements further reduced the air pressure to 48.2 kPa. The dried, filtered, and pressure-regulated house air entered a Dwyer flow meter (Part Number RMB-50-SSV) where it was metered to deliver 120.1 l/h as specified by the ASTM standards for lubricant evaporation testing. The metered air entered the preheater where it was heated to the selected evaporation testing temperature.

(a)

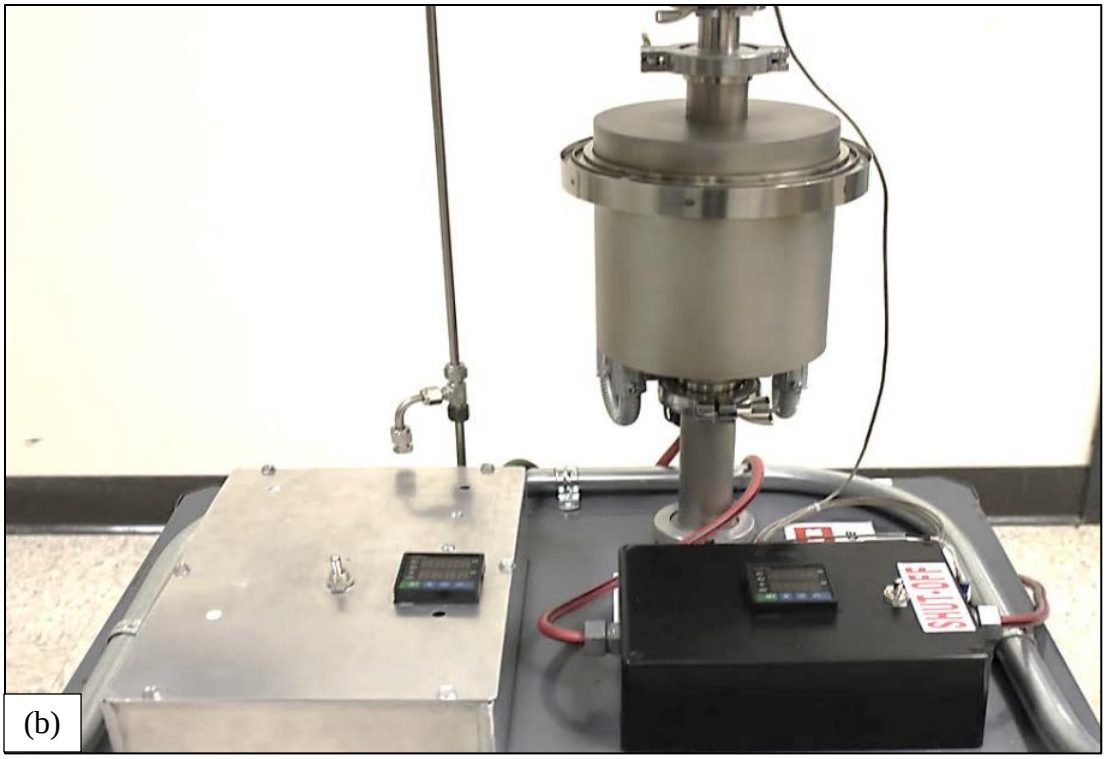

Figures 4.31a and b. The evaporation testing apparatus consisting of (a) filtering and regulating devices, and (b) preheater, controllers, and test chamber (*Images from the author*).

A custom built tube-style air preheater was located external to the test chamber. Its construction consisted of a thin-walled, hollow aluminum box having dimensions of 20.3 cm wide x 30.5 cm long x 7.62 cm high. The box housed the Vulcan Thunderbolt, 120 V, 550 W cartridge heater (Part Number TB6214A) and tube, Fotek 60 A solid state heater relay (Part Number SSR-60-DA), and ColdfusionX proportional integral differential (PID) switch (Part Number JLD612) for controlling relay and cartridge heater temperature.

The heater tube was fabricated using a stock 2.54 cm diameter x 15.24 cm long black steel schedule 40 nipple. Black steel fittings were also purchased from a local hardware store as needed to permit the 1.588 cm diameter x 10.16 cm long cartridge heater to be concentrically-mounted into the nipple. A 2.54 cm x 2.54 cm x 2.54 cm black steel tee was attached to the tube

assembly to allow treated house air to be routed over the heater surface and permit an exit for the heater wires. The heater tube assembly was wrapped in 7.62 cm thick alumina insulation to improve its efficiency and protect the surrounding components from high temperature. The heated air, under positive pressure, exited the preheater via 6.35 mm stainless steel tubing. The preheater PID controller's thermocouple was inserted in-line and downstream of the preheater tube assembly. The thermocouple monitored the outgoing air to ensure it achieved the proper temperature during testing. A rendering of the completed testing apparatus is shown in Figure 4.32.

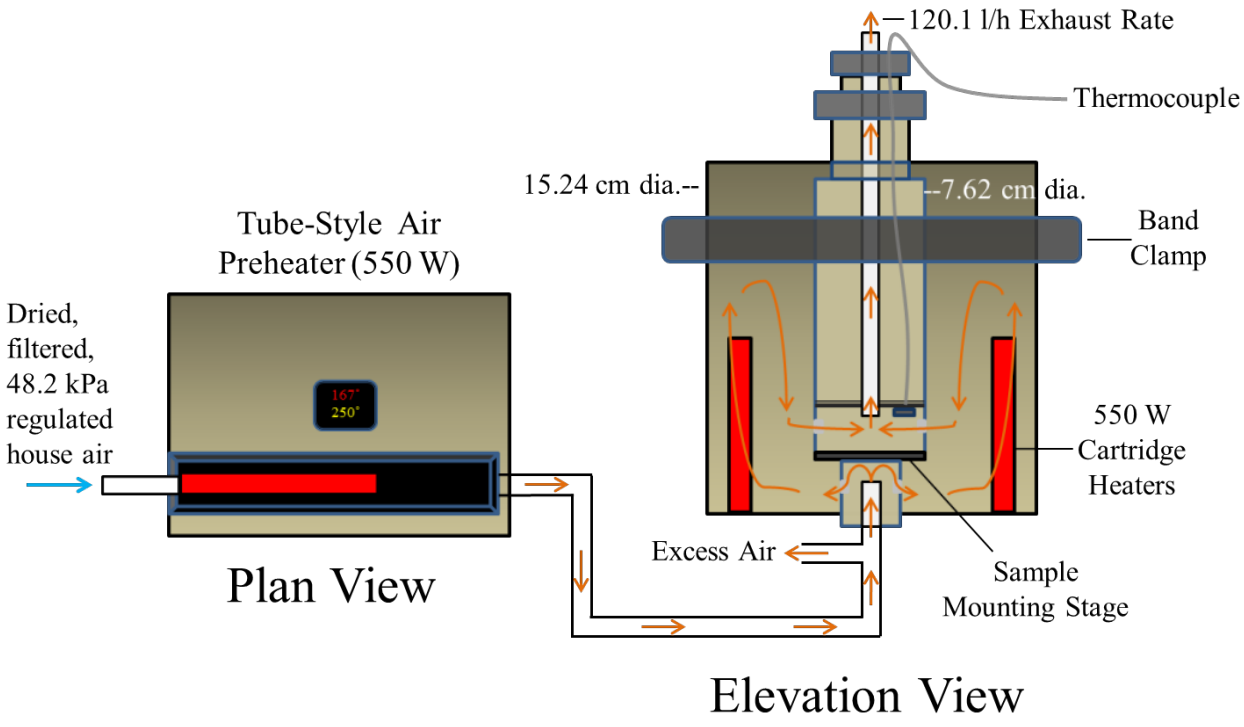

Figure 4.32. A schematic for the lubricant evaporation testing apparatus showing the air's route through it (*Image from the author*).

A plan view of the tube-style air preheater illustrates the location of its key components which are the tube preheater and controller. An elevation view of the test chamber shows its key components, the heaters and test compartment, as well as the air routing scheme. The chambers

were constructed using two-piece, ISO quick flange style oil trap assemblies employed on mechanical vacuum pumps. The chamber design consisted of a 15.24 cm diameter x 22.9 cm high stainless steel outer chamber brazed to a coaxially-aligned 7.62 cm diameter stainless steel inner chamber of similar height. The thickness of all chamber walls is 3.18 mm. Air from the preheater entered the testing chamber through 6.35 mm stainless steel tubing which terminated in a compartment below the sample mounting stage of the inner chamber. The preheated air provided conduction heating to the samples for lubricant evaporation testing.

The air exited the compartment underneath the sample mounting stage through two 3.18 mm diameter, diametrically-opposed holes and entered the area between the inner and outer chamber walls to be reheated. Reheating was necessary due to the loss of heat by conduction through the sample stage and the outer chamber wall. The heat was replenished by two diametrically-located 550 W cartridge heaters which were the same style used in the preheater. The high wattage ensured the apparatus could pre-condition the chambers thoroughly before evaporation testing, facilitate a rapid return to the test temperature after the chamber was opened for sample loading, and assured the apparatus could achieve the full range of evaporation testing temperatures (300 to 400°C). The relay and heaters were controlled by the same style PID controller used for the preheater, but the relay was the higher-ampacity Fotek 90 solid state model (Part Number SSR-90-DA). The dual heater's controller and relay were housed separately in a Radio Shack project enclosure (Part Number 270-1809). All electrical components were installed, wired, and operated according to the manufacturer's recommendations.

After reheating, the air entered two 3.18 mm diameter, diametrically-opposed holes in the section of the inner chamber wall leading to the test compartment. The air provided convection heating for the samples during lubricant evaporation testing. The holes allowed parallel air flow across

the top of oil-laden samples placed on the sample stage located within the test compartment. The sample stage was designed to hold 3 samples sized 12.7 mm x 25.4 mm. The dual heater's PID controller thermocouple was mounted inside the test compartment. It monitored the air temperature produced by the cartridge heaters to ensure the samples were exposed to the proper testing temperature.

During testing, the volatile lighter constituents of the oil evaporated first, leaving behind an increasingly viscous film. Smoke and vapors, or effluent, exited the test compartment via a 6.35 mm diameter stainless steel eduction tube. Although the air left the compartment under positive pressure, the eduction tube was also connected to the negatively-pressurized house ventilation system as a safety precaution against flammable vapor accumulation. An overview of the criteria for the apparatus and tests is provided in Table 4.11.

Table 4.11. The criteria overview for the testing apparatus and lubricant evaporation tests.

1. The device is constructed from type 304 stainless steel
2. Flow meters and filters deliver dust-free air between 15.5 and 29.4°C to the preheater.
3. The test chamber must be pre-conditioned by operating its heaters at the test temperature for 1 h.
4. Assure the apparatus returns to the testing temperature after loading the samples.
5. Testing temperatures are 300, 350, and 400°C (±1°).
6. Effluent exits the apparatus at 120.1 l/h.
7. Tests are performed in 5 min increments for all test temperatures.
8. After testing, cool the samples to room temperature and measure the mass to the nearest 0.1 mg.

CHAPTER 5

THERMOPHYSICAL AND FOURIER TRANSFORM INFRARED MODELING

5.1 Thermophysical and FTIR Modeling of Smooth and Nano-Porous Topographies

The benefits of creating topographies using photolithography are the processes allow precise control of the features and characterization of the topographies without the ambiguity associated with randomly ordered topographies. The ability to physically characterize the topographies is important because it provides a critical link to understanding how changes made in the design affect the testing results. Smooth and nano-porous topographies' characterizability also lends itself to thermodynamics-based numerical modeling. These methods are noteworthy because they go beyond simple qualitative analysis to provide quantitative measures of the performance of nano-topographies. The numerical models are representations of what may occur under ideal conditions which is why they are called models. Their value is they can be used as standards to compare with the actual results.

Modeling of the topographies using heat transfer equations is discussed in sections 5.1.1 - 5.1.4. The constituent equations, material-specific properties, and parameters for these modes of heat transfer are explained. Section 5.2 presents Fourier Transform Infrared (FTIR) spectroscopy as an analytical technique to determine the number of H atoms. This approach might establish a correlation between the changes in pore geometry, the change in the number of available bonding sites, and the subsequent amount of lubricant retained.

5.1.1 Conduction Heating of Smooth and Nano-Porous Si-Cu Topographies

Heat transfer, simply stated, is the transfer of thermal energy from one medium, system, or location to another as a result of a temperature difference. Conduction is a mode of heat transfer

in which heat is transferred through a solid. The solids used for fabricating the test samples are c-Si wafers, thin films of Cu and a-Si:H, and liquid lubricant. It is recognized that the latter material is initially a liquid which is usually accounted for during convection heat transfer, but its classification as a solid stems from the fact that the fluid is not flowing along the sample's surface as required for the lubricant to transfer heat by convection.

Figures 5.1 and 5.2 will show all of the modes of heat transfer concurrently to conserve space. However, the mode under consideration is conduction. The source of conduction heat is represented by arrows pointing upward in direction, indicating the heat is flowing toward the interior of the sample. Conduction heat for the samples was supplied by the sample mounting stage that was heated to the testing temperature using the testing apparatus' preheater. The sample stage was construed as a wall that delivered a constant temperature to the samples laid in flat orientation. The transfer of heat was driven by the temperature difference between the wall and the cooler inner parts of the sample. There were negligible temperature gradients encountered in the left, right, front, and back directions constituting the sides of the sample, so there was negligible heat transferred in these directions. Fourier's law of heat conduction for one-dimensional heat transfer was permissible in this case and was given by,

$$\mathrm{Q_{Conductance}} = -\mathrm{kA}\frac{\mathrm{dT}}{\mathrm{dy}} \qquad \text{Equation (5.1)}$$

The symbol *Q* represents the heat transferred (W), *k* is the thermal conductivity of the material (W/μm·°C), *A* is the cross-sectional area (μm^2) of the material normal to the direction of heat transfer, and the temperature gradient *dT/dy* (°C/μm) is the temperature difference as a function of the material's thickness, considering that the vertical direction is represented by *y*. Rewriting Fourier's equation allowed a simplified expression that used the total thermal resistance, R_T, of

the constituent materials and the temperature difference between the lower interior of the sample and upper interior of the lubricant to calculate the heat transferred. Fourier's equation became,

$$Q_{\text{Conductance}} = \frac{T_{\text{lower interior}} - T_{\text{upper interior}}}{R_T} \qquad \text{Equation (5.2)}$$

and the thermal resistance was calculated using,

$$R_T = \frac{t}{kA} \qquad \text{Equation (5.3)}$$

where R_T is equal to the thickness of the material, t, divided by the product of the cross-sectional area, A, and thermal conductivity, k. In the research on Si-Cu composites, the conduction heat encountered multiple layers of different materials. A thermal resistance network was modeled to achieve total resistance values for smooth and nano-porous topographies.

Images of nano-porous and smooth topographies are shown in Figures 5.1 and 5.2, respectively. The color legends in Figures 5.1 and 5.2 denote the materials used to fabricate the composites. The thermal resistance network for the nano-porous topography was expected to be the more complicated of the two because of the film structure of the pore and the use of segments. The resistance network of the nano-pore was created using an image of a pore which was partitioned and numbered as illustrated in Figure 5.1. It should be understood that the illustration represents one half of a nano-pore in order to simplify the resistance network as much as possible. There were 10 segments partitioned as shown so that each segment had the same cross-sectional area throughout the segment while remaining part of a specific material of the composite. The conduction heat approached the *c-Si* segment from the bottom, traveled through that material, and entered the bottom of the segments located above it. The heat progressed toward the top surface of the lubricant.

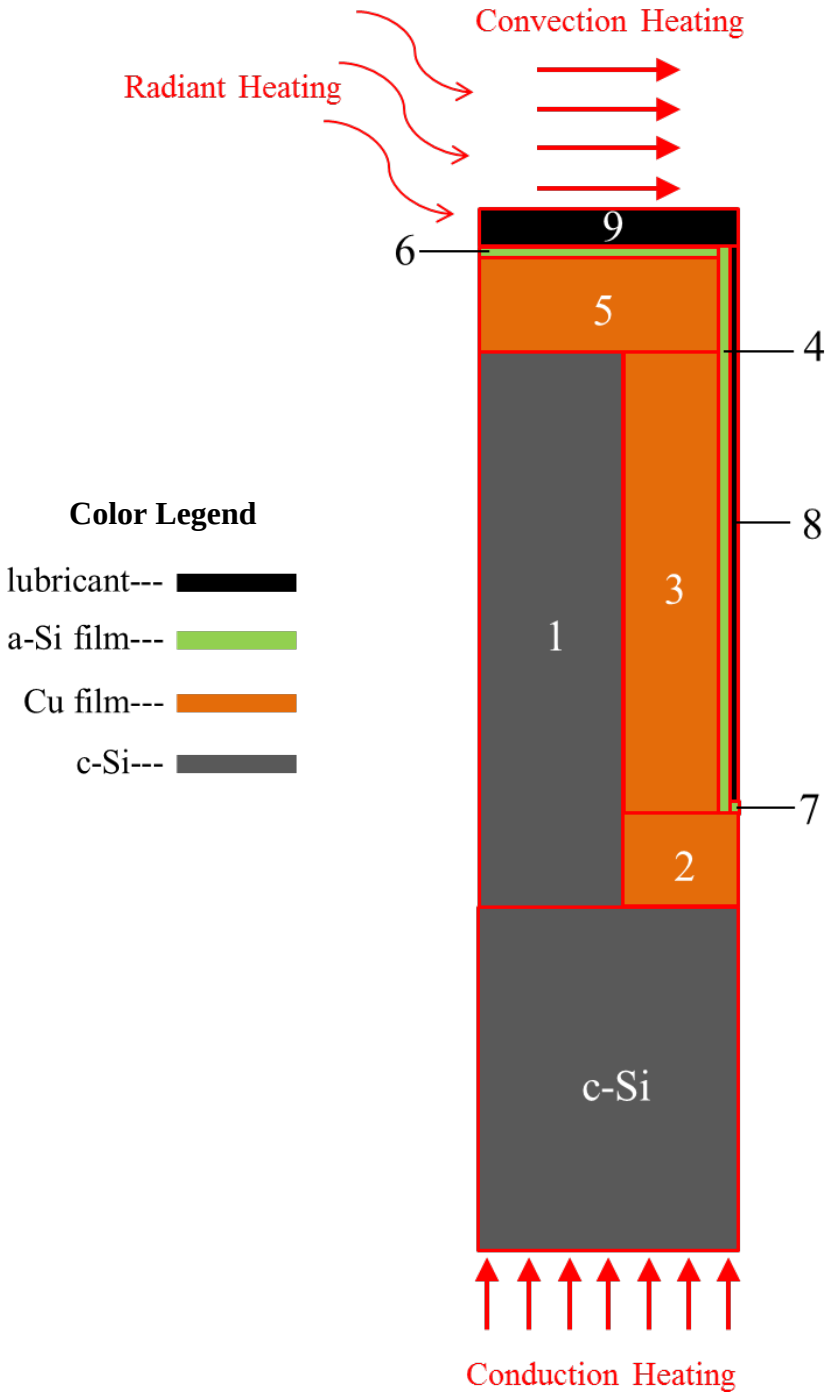

Figure 5.1. Illustration of a nano-pore partitioned and numbered for determining the required heat to evaporate lubricant. The ≈70 nm thick Pd-Sn seed layer applied during fabrication is not included in the model or R_T calculations for the nano-pores because of its negligible effect on thermal resistance and required heat (*Image from the author*).

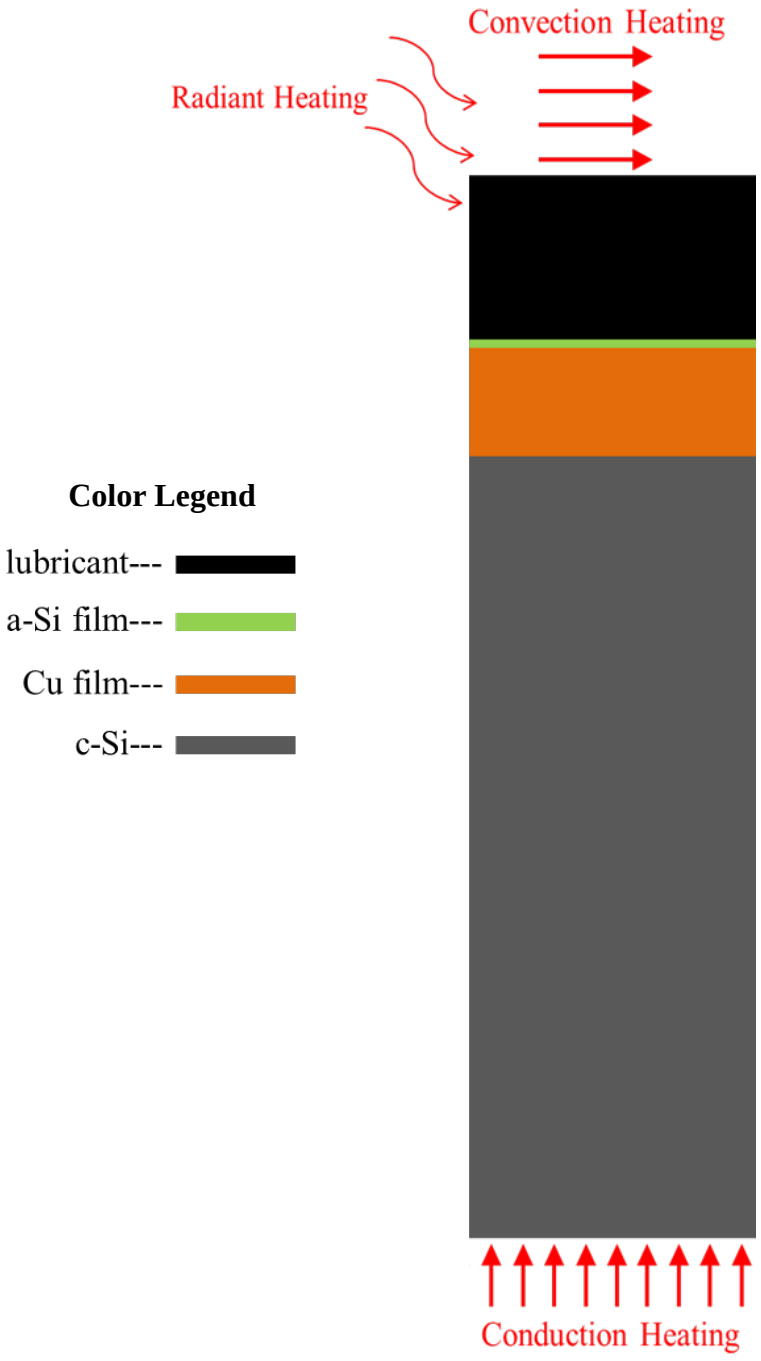

Figure 5.2. Illustration of a smooth topography created to determine the heat transferred in comparison to a nano-porous topography. The 50 nm thick Ti adhesion/barrier film applied during fabrication is not included in the model or R_T calculations for the smooth topographies because of its negligible effect on thermal resistance and heat transfer (*Image from the author*).

It should be pointed out that the topographies shown in Figures 5.1 and 5.2 included the layer of a-Si:H film as a surface chemistry modification to test its enhancement of lubricant retention. A series-parallel combination of resistors, shown in Figure 5.3a, represents the nano-pore resistance network having a-Si:H film. The network for smooth composites is shown in Figure 5.3b as 4 resistors in series. The networks are analogous to the resistance of electric circuits and are analyzed using Kirchhoff's loop circuit analysis methods (in the case of nano-pores) and Ohm's law for smooth topographies. The evaporation testing scheme will consider both topographies before and after modification.

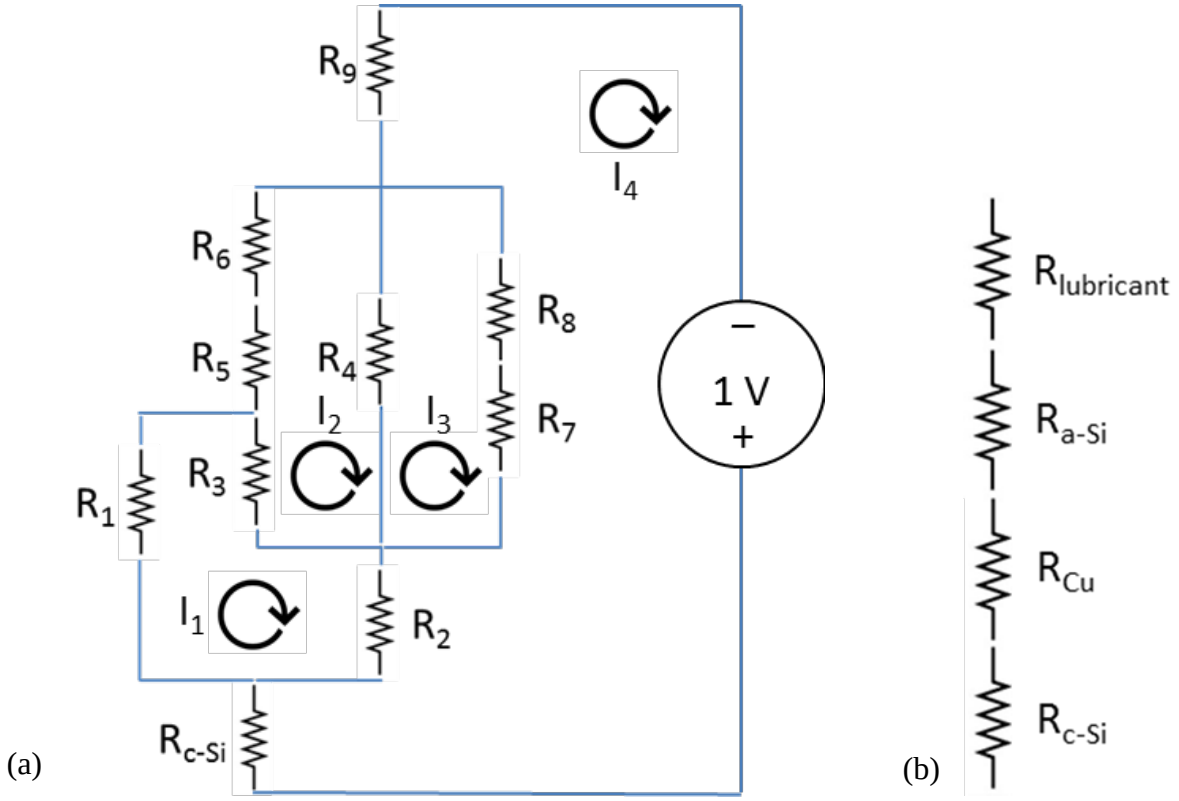

Figures 5.3a and b. Thermal resistance networks were created for (a) nano-porous and (b) smooth topographies illustrated in Figures 5.1 and 5.2 that included the resistance due to a-Si:H surface chemistry modification (*Images from the author*).

Separate networks were developed that deleted segments *4*, *6*, and *7* associated with a-Si:H film in the nano-porous resistance network (R_4, R_6, and R_7 in Figure 5.3a) and $R_{a\text{-}Si}$ from the smooth topography resistance network in Figure 5.3b. The modified networks are shown in Figures 5.4a and b.

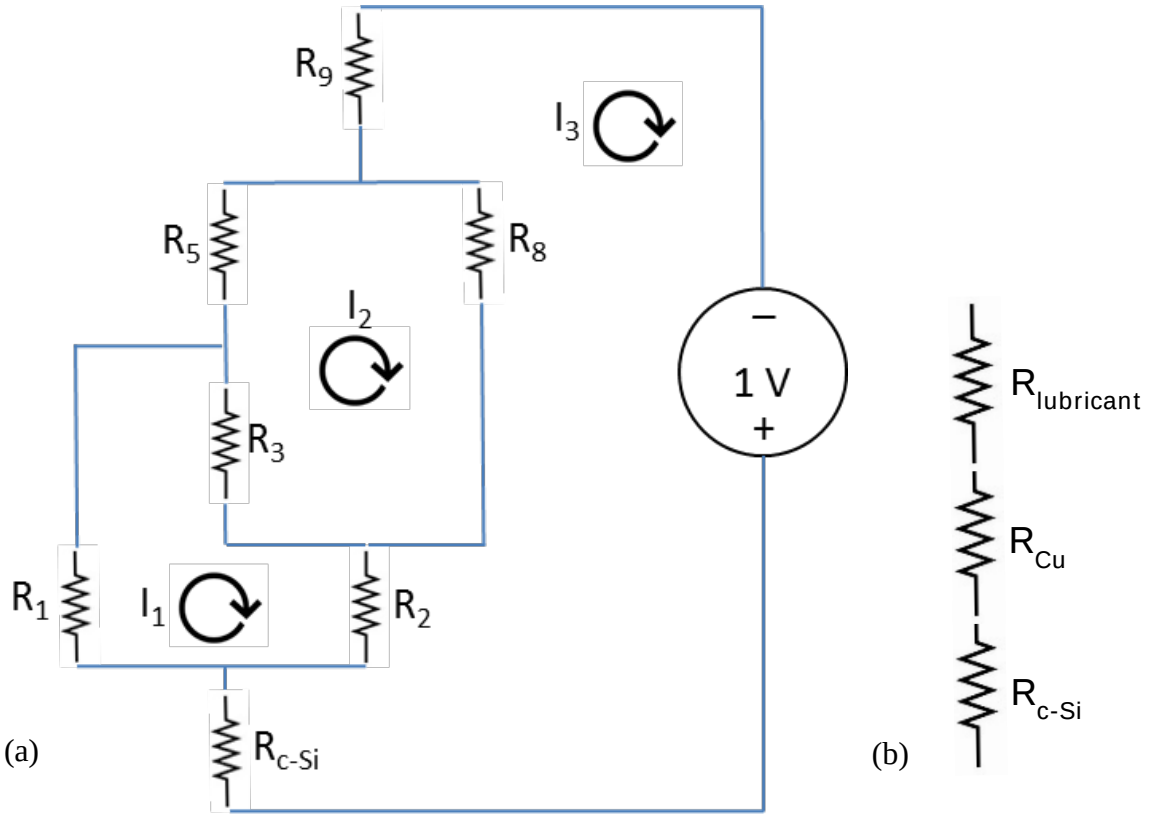

Figures 5.4a and b. Thermal resistance networks were created for (a) nano-porous and (b) smooth topographies that excluded the resistance due to a-Si:H surface chemistry modification (*Images from the author*).

In order to calculate R_T, the *k* value of each constituent material of the composite was needed. The *k* values are essentially constants which only varied marginally over the range of testing temperatures. The values were obtained from thermodynamics textbooks as well as other sources. The values are listed in Table 5.1.

Table 5.1. Thermal conductivities, k (W/μm·°C), of the materials used in the composite samples.

Oil	**a-Si:H**	**Cu**	**c-Si**
1.347 E-07	2.6 E-06	4 E-04	1.56 E-04

The other variables needed for calculating R_T were the thickness, t, of the Cu and a-Si:H films, the pore depth, and the cross-sectional area of the segments. The film thicknesses were tools used to adjust the pore diameters to desired values. However, they were inextricably linked to the pore depth because changing the depth altered the value of the vertical (thickness) dimension of some segments shown in Figure 5.1. Using a pore dimension fabricated in this research as an example, consider that the fabrication process began with pores etched in c-Si substrate which were 6 μm wide and a depth of 50 μm, and the c-Si pores were overlaid with a Cu film sputtered 2.5 μm thick followed by a-Si:H film deposited 250 nm thick. These values would produce a nano-pore with a diameter of 0.5 μm. The distance from the top to the bottom of the pore would remain 50 μm because the surface surrounding the pore opening would be deposited to the same film thickness as the bottom of the pore.

Let us now consider how a change in the pore depth can affect the segment dimensions. If the c-Si pore's depth which began as 50 μm was then reduced to 25 μm, and the original Cu and a-Si:H film thicknesses were retained, and the pore diameter remained 0.5 μm, the vertical dimensions of segments *1, 3, 4,* and *8* would be 25 μm less than the original ones, while *c-Si* would gain 25 μm. In a similar manner, the thermal resistance values were affected by the pore dimensions.

Thermal resistances were calculated for pores etched into c-Si substrate having initial diameters of 6 and 6.5 μm and depths of 25, 50, and 75 μm. The c-Si pores were overlaid with Cu film sputtered 2.5 μm thick along with a-Si:H film deposited to 250 nm thick. A thicker Cu film,

2.75 µm, was used to compensate for the thickness reduction in the models of pores where the a-Si:H film was omitted. The films overlaid on c-Si resulted in final pore diameters of 0.5 and 1 µm which were illustrated as filled with oil in Figure 5.1.

The remaining variable affecting R_T was the cross-sectional area of the pore. Recall that partitioning the pores into segments was done to retain a constant cross-sectional area from the top to the bottom of the segment, even though as demonstrated in Figure 5.1, this meant the constituent materials of the composite might be partitioned multiple times to achieve the desired result. All of the dimensions for the etched pores, cross-sections, film thicknesses, and other relevant information for the tested topographies are presented in their final form in chapter 7, Tables 7.1 - 7.6.

To envision how the cross-sectional areas of the pore's segments were determined, Figure 5.5 shows the top-down view of a cell containing a pore and its surrounding area. In principle, this was the same approach used when isolating a single pore for numerical analysis. The dimensions for the surrounding area was obtained from the pitch or center-to-center distance between adjacent pores as created using the photolithography mask discussed in section 4.2.2. The quantity that results from comparing the cross-sectional area of the pore opening to the cross-sectional area surrounding it is referred to as the area ratio. Area ratio is an especially useful quantity that describes the performance of the pore as related to the amount of hydrodynamic pressure it generates. For informational purposes, the area ratio for the 0.5 µm and 1 µm final diameter nano-pores were 0.001 and 0.004, respectively. Hydrodynamic pressure effect studies will be undertaken in future work.

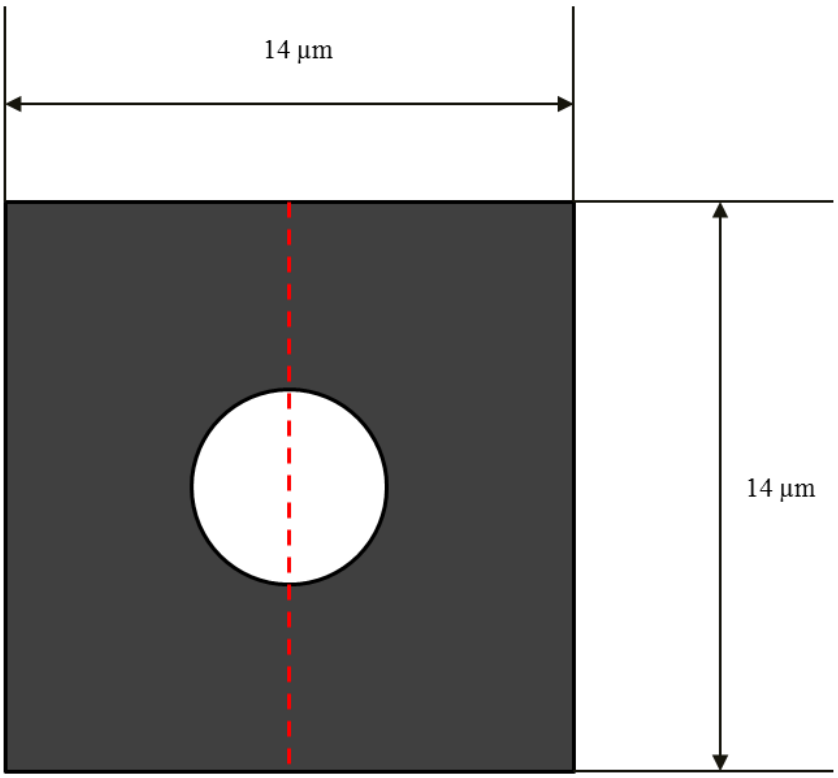

Figure 5.5. The top-down view of a cell containing a pore and its surrounding area (*Image from the author*).

Shown in Figure 5.5 is the image of the pore and surrounding area that was divided along the center to illustrate the partitioning done to take advantage of symmetry for mathematical analysis of the pore cross-sections. Looking from the top-down perspective of a half pore, four distinct cross-sectional shapes emerged. These are shown in Figure 5.6 as generic shapes having no dimensions; they serve as illustrations of the appearance of the segment cross-sections. The numbers below the shapes are coordinated with the segment numbers assigned in Figure 5.1 to indicate their association with that particular cross-section shape. Tables were created to organize the calculation's and sample information denoting the segment identity, material type, thickness, cross-sectional area, and R_T values for the 10 segments. The tables are shown later in section 7.1.1.

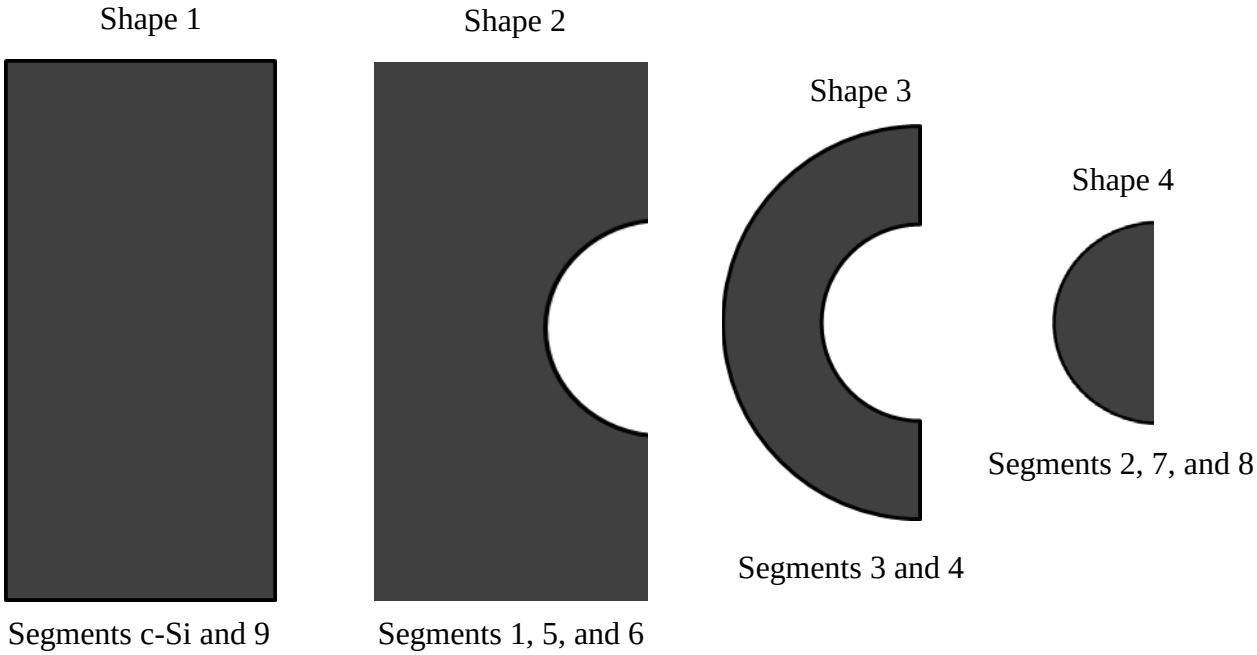

Figure 5.6. These cross-section shapes were formed during partitioning of the nano-pores into segments. The images illustrate the shapes for one half of a pore (*Images from the author*).

Keeping in mind that the shapes represented only one half of a pore, well-known mathematical formulas and strategies for calculating the surface areas of the shapes in Figure 5.6 were employed, namely,

$$\text{Surface Area}_{\text{ rectangle}} = \text{Length x Width} \qquad \text{Equation (5.4)}$$

and,

$$\text{Cross Sectional Area}_{\text{ circle}} = \frac{\pi * \text{Diameter}^2}{4} \qquad \text{Equation (5.5)}$$

Once the R_T values were found, Kirchhoff's node law was used in conjunction with the resistance network to calculate the current values. The node law says the algebraic sum of the currents flowing into a node must equal the sum of the currents flowing out of the node. The current quantities in electric circuit analysis are used analogously to represent the required

conduction heat to induce lubricant evaporation. Figure 5.3a is shown with current loops labeled I_1 through I_4 that correspond with thermal circuits 1 - 4, and Figure 5.4a has loops labeled I_1 through I_3 that correspond with thermal circuits 1 - 3. Circuits 3 and 4 of the figures have voltage sources rated for 1 v to complete the circuits. Notice that each voltage source was connected to the first resistor, $R_{c\text{-}Si}$, and to the last one, R_9. The voltage potential, therefore, represented the value for the temperature difference between the lower interior of the sample and upper interior of the lubricant. The temperature of the lubricant was assumed to be 25°C room temperature at the start of heating. The 1 v value was chosen purposely to represent 1°C so that the lower interior temperature of the sample (i.e., the testing temperature) minus the room temperature could be used as a multiplier to calculate the values for the current (i.e., required conduction heat) of the loops.

Having all of the necessary variables in hand, the equations for the loops were derived. The R_T of the segments, loop currents, and voltage source values were rearranged into matrices using Ohm's law expressed as,

$$[\mathrm{R}][\mathrm{I}] = [\mathrm{V}] \qquad \text{Equation (5.6)}$$

Inserting the components in the matrix expression of equation (5.6) produced the generalized matrices template of equation (5.7) which included the R_T values R_4, R_6, and R_7 for the a-Si:H segments,

$$\begin{bmatrix} (\mathrm{R_1}+\mathrm{R_2}+\mathrm{R_3}) & -\mathrm{R_3} & 0 & -\mathrm{R_2} \\ -\mathrm{R_3} & (\mathrm{R_3}+\mathrm{R_4}+\mathrm{R_5}+\mathrm{R_6}) & -\mathrm{R_4} & 0 \\ 0 & -\mathrm{R_4} & (\mathrm{R_4}+\mathrm{R_7}+\mathrm{R_8}) & -(\mathrm{R_7}+\mathrm{R_8}) \\ -\mathrm{R_2} & 0 & -(\mathrm{R_7}+\mathrm{R_8}) & (\mathrm{R_{c-si}}+\mathrm{R_2}+\mathrm{R_7}+\mathrm{R_8}+\mathrm{R_9}) \end{bmatrix} * \begin{bmatrix} \mathrm{I_1} \\ \mathrm{I_2} \\ \mathrm{I_3} \\ \mathrm{I_4} \end{bmatrix} = \begin{bmatrix} 0 \\ 0 \\ 0 \\ 1 \end{bmatrix} \qquad \text{Equation (5.7)}$$

The modified, generalized matrices template which excluded the a-Si:H segments was determined as,

$$\begin{bmatrix} R_1 + R_2 + R_3) & -R_3 & -R_2 \\ -R_3 & (R_3 + R_5 + R_8) & -R_8 \\ -R_2 & -R_8 & (R_{c-Si} + R_2 + R_8 + R_9) \end{bmatrix} * \begin{bmatrix} I_1 \\ I_2 \\ I_3 \end{bmatrix} = \begin{bmatrix} 0 \\ 0 \\ 1 \end{bmatrix} \quad \text{Equation (5.8)}$$

The solution matrices, [I], in equations (5.7) and (5.8) were solved by inverting the coefficient matrices, [R], and multiplying them by the constants matrices, [V], to yield the values of *I* for each loop. The required heat calculations for the modified topographies were performed as a comparison to the required heat for the topographies excluding a-Si:H segments.

The photolithographic mask design discussed in section 4.2.2 shows four different diameters available for creating nano-pores. Two of the diameters were used in conjunction with the 3 depths of nano-pores for lubricant retention modeling and testing. Examining the different combinations of diameters and depths helped to determine the most effective geometries for enhancing lubricant retention. Having established the methodology for calculating the required heat of nano-porous topographies and heat transfer of smooth topographies via conduction, the equations were set up in a Microsoft Excel™ spreadsheet for automatic calculation of the required variables representing all geometric variations of the nano-pores. The Texas Instruments TI-84™ calculator matrix solver was used to determine the required heat values. The calculations and results for the nano-porous samples are discussed in section 7.1.1. The calculations and results for smooth samples are discussed in section 7.1.1.1.

5.1.2 Convection Heating of Smooth and Nano-Porous Si-Cu Topographies

Forced convection heat transfer is defined as the transfer of heat through a fluid due to the bulk movement of fluid. The fluid motion in this research was produced by an air compression pump

which sent metered air through the test apparatus as indicated in Figure 4.32. Although the air moved inside of the apparatus, the flow was considered as external because it moved over the surface of standing lubricant that was deposited on the tested samples.

Forced convection heat transfer is based on Newton's law of cooling given by the equation,

$$Q_{convection} = h_{air}\, A_{lubricant\ surface}(T_{convection} - T_{lubricant\ surface}) \quad \text{Equation (5.9)}$$

in which h (W/μm^2·°C) is the convection heat transfer coefficient, A (μm^2) is the surface area of the lubricant in contact with the air, $T_{convection}$ (°C) is the selected evaporation testing temperature, and $T_{lubricant\ surface}$ (°C) is the temperature of the lubricant surface, assumed to be at room temperature of 25°C at the initiation of testing. The heat transfer coefficient was the most difficult parameter to determine because it depended on several factors, including air velocity, density, dynamic viscosity, thermal conductivity of air, and the flow characteristics. Of course when discussing the flow characteristics, deliberations must be given to the laminar and turbulent flow regimes, film temperature, the surface's shape, orientation, and roughness, and a number of dimensionless parameters such as Reynolds number (*Re*), Nusselt number (*Nu*), and Prandtl number (*Pr*) that combine to determine the heat transferred via convection. The *Re* number is the ratio of the inertial forces to the viscous forces of a fluid in motion. The *Pr* number is the ratio of the molecular diffusivity of momentum to the diffusivity of heat in a fluid. The *Nu* number is a non-dimensionalized convection heat transfer coefficient. The paragraphs that follow explain the rationale for using these parameters and the flow regime used.

The non-dimensionalized heat transfer coefficient was determined using the knowledge that there existed a no-temperature jump condition because of the no-slip region at the interface of the solid (the standing lubricant) and the air in contact with the lubricant surface. Because of the motionless lubricant surface and the flowing air, the heat transfer mechanisms were

simultaneously conduction and convection. Equating the two modes of heat transfer yielded the expression,

$$Q_{conduction} = \frac{k\Delta T}{L} = h\Delta T = Q_{convection} \qquad \text{Equation (5.10)}$$

Canceling terms and combining the equations gave the dimensionless parameter, *Nu*,

$$Nu = \frac{hL}{k} \qquad \text{Equation (5.11)}$$

Since finding *h* was the objective, the *Nu* equation was rearranged into,

$$h = \frac{Nuk}{L} \qquad \text{Equation (5.12)}$$

A considerable amount of empirical data had been compiled to derive *Nu* numbers for various shapes, fluid types, and flow regimes beforehand, so the secondary objective was to determine which one(s) might be applicable for the purpose of finding the convection heat transfer coefficient, and subsequently, the convection heat transfer. A physical correlation was evident between the topographies fabricated in this research and flat plates. An interesting fit seemed to exist with the *Nu* relation proposed by Churchill and Ozoe for parallel flow across flat plates [79] which did not depend upon a specific fluid type or a predetermined range of *Pr* numbers,

$$Nu_L = \frac{0.3387 Re_L^{\frac{1}{2}} Pr^{\frac{1}{3}}}{\left[1 + \left(\frac{0.0468}{Pr}\right)^{\frac{2}{3}}\right]^{\frac{1}{4}}} \qquad \text{Equation (5.13)}$$

As shown in equation (5.13), the *Nu* correlation was dependent on the *Re* and *Pr* numbers only, provided that the flow was laminar. A laminar flow along parallel plates was determined by evaluating the critical length, X_{cr}, associated with the widely accepted critical *Re* number value of $5x10^5$,

$$\mathrm{Re_{cr}} = \frac{\rho \mathrm{X_{cr}} \mathrm{U_\infty}}{\mu} = 5\mathrm{x}10^5 \qquad \text{Equation (5.14)}$$

where ρ (kg/m^3) is the density of the air, U_∞ (m/s) is the free stream air velocity, and μ (kg/m·s) represents the dynamic viscosity of air.

Density and dynamic viscosity were temperature dependent. A sample calculation for X_{cr} was done using the properties of air at 300°C and 1 atm. The basis for this particular temperature was the value represented the minimum evaporation testing temperature. Also, the μ/ρ (kinematic viscosity) quantity was the smallest value for the whole range of testing temperatures, therefore allowing the calculation of the least airflow length permitted before the airflow transitioned to the turbulent regime. If the X_{cr} value was greater than the length of travel of the airflow across the sample during testing, the flow remained laminar. It was convenient, too, that Re_{cr} numbers were available for flat plates which exhibited roughness, as was the case for nano-porous samples. The Re_{cr} value could vary as high as 3x10^6 to account for nano-porous surface roughness and free stream air turbulence [26].

The kinematic viscosity, ν (m^2/s), was given as 4.765x10^{-5} m^2/s at atmospheric pressure and air temperature of 300°C. The U_∞ was calculated using the 120.1 l/h volumetric flow rate of air through the evaporation apparatus divided by the cross-sectional area of the 6.35 mm air exit tubing. The value was 1.053 m/s. Plugging the values into the Re_{cr} expression and solving for X_{cr} yielded,

$$\mathrm{X_{cr}} = \frac{5\mathrm{x}10^5 \cdot 4.765\mathrm{x}10^{-5}}{1.053} = 22.6\ \mathrm{m} \qquad \text{Equation (5.15)}$$

Having determined the X_{cr} value for smooth topographies, it was clear that even the largest sample dimension of 25.4 mm was well short of the 22.6 m critical length. The lengthwise or

widthwise orientation of the sample was irrelevant as far as significantly affecting the *Nu* number. A similar calculation was done for nano-porous samples to determine its X_{cr}. Using the extreme value of Re_{cr}, the calculated X_{cr} value was,

$$\mathrm{X_{cr}} = \frac{3\mathrm{x}10^{6} \cdot 4.765\mathrm{x}10^{-5}}{1.053} = 135.8\ \mathrm{m} \qquad \text{Equation (5.16)}$$

The evidence was clear that both sample topographies could be modeled as flat plates having a laminar flow regime. The Churchill and Ozoe equation was an appropriate application for determining the *Nu* number and, consequently, the *h* of smooth and patterned Si-Cu topographies.

The *Nu* number was calculated using the expression for *Re* number,

$$\mathrm{Re_L} = \frac{\mathrm{U_\infty L}}{\nu} \qquad \text{Equation (5.17)}$$

in which *L* is the sample dimension oriented in the direction of air flow (0.0127 m for smooth and nano-porous topographies), U_∞ of 1.053 m/s, and *v* equal to $4.765\mathrm{x}10^{-5}$ m^2/s for air at 1 atm and 300°C. The value of *v* for 400°C temperature is $6.219\mathrm{x}10^{-5}$ m^2/s. Using equation (5.17), the range of *Re* values for evaporation testing was between 280.7 and 215, which were well below values denoting laminar flow. The *Pr* values for the range of testing temperatures were between 0.6935 (300°C) and 0.6948 (400°C) at 1 atm [26].

The range of *Re* and *Pr* values were used in the Churchill-Ozoe relation in equation (5.13) to determine the range of the *Nu* number values. The *Nu* values were between 4.835 (300°C) and 4.234 (400°C). It was noted that the *Re* number decreased as the temperature of the air increased. The *Re* number is dependent on *v* which increases with the temperature of air, whereas the *Pr* number has higher molecular momentum diffusivity as the temperature of air

increases in this particular temperature range. The result was a decrease in the *Nu* values as the temperature increased, as long as the same U_∞ and *L* values are used in the calculations. The results and discussion of the calculation for *h* used in this research is found in section 7.1.2.

5.1.3 Radiation Heating of Smooth and Nano-Porous Si-Cu Topographies

Radiation is heat transfer that occurs between objects separated by distance, without the influence of conduction or convection. It is thermal energy transmitted via the propagation of electromagnetic waves which result from the energy transitions of molecules, atoms, and electrons of matter. The wavelength of thermal radiation ranges between 100 μm and 0.1 μm of the electromagnetic wave spectrum and encompasses infrared, visible, and a portion of UV radiation.

Due to the design of the evaporation apparatus shown in Figure 4.31b, consideration was given to the role that thermal radiation had in contributing to the evaporation of lubricant. Cylindrically-shaped ovens having surfaces that were maintained at specific temperatures such as the test apparatus were a popular type of device analyzed in heat transfer texts to examine the effects of radiation heat transfer. A closer look at the apparatus' evaporation compartment is provided in Figures 5.7a and b.

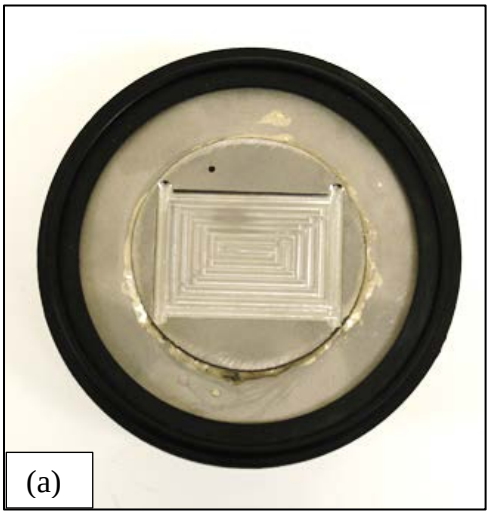

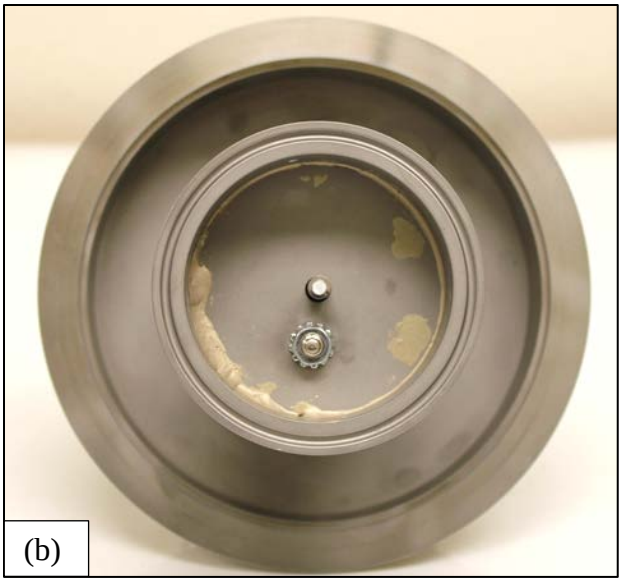

Figures 5.7a and b. The evaporation testing compartment which comprised (a) the mounting stage with a milled location for 3 samples, and (b) its enclosing cylinder (*Images from the author*).

The compartment created for evaporation consisted of a stage area on which a total of 3 samples could be placed. The area above the stage was totally-enclosed by a 7.62 cm diameter x 1.9 cm high cylinder composed of 3.18 mm thick stainless steel. This is the inner cylinder shown in Figure 5.7b. Also shown in the Figure 5.7b is the temperature sensing tip of the thermocouple and the inlet to the eduction tube referred to in section 4.5.

A number of different approaches existed to calculate the radiation heat transfer. The one chosen for this research involved modeling the chamber design using view factors and radiation energies. View factors use the effect of the physical orientation of surfaces to account for the fraction of direct radiation between those surfaces. The analysis technique works for surfaces that are uniform, isothermal, independent of wavelength (gray), non-transparent (opaque), and diffuse emitters and diffuse reflectors like the evaporation compartment. The technique is appropriate for situations where the space between the surfaces is occupied by vacuum or air.

Real surfaces have emissive power, εE_b (W/m^2) that is some proportion of an ideal emitter such as a blackbody. The proportionality constant, ε, describes a surface's emissivity relative to the blackbody, b, at the same temperature. A portion of the incident or irradiated energy, G (W/m^2), arriving from an adjacent surface is absorbed, leaving the balance to be reflected. The reflected amount is denoted by ρG. The proportionality constant, ρ, is the ratio of the reflected radiation to the amount of incident radiation. Both ε and ρ have values between 0 and 1, with 1 denoting the highest possible ε value obtained by the surface of a blackbody, whereas 0 is the lowest attainable ρ value signifying a black body surface. The radiosities, J (W/m^2), are the sums of εE_b and ρG radiation energies of each surface of the inner chamber regardless of the origin. Outside of the evaporation compartment are the locations of the cartridge heaters that provided an additional source of thermal radiation which heated the compartment walls on all sides as shown in Figure 5.8.

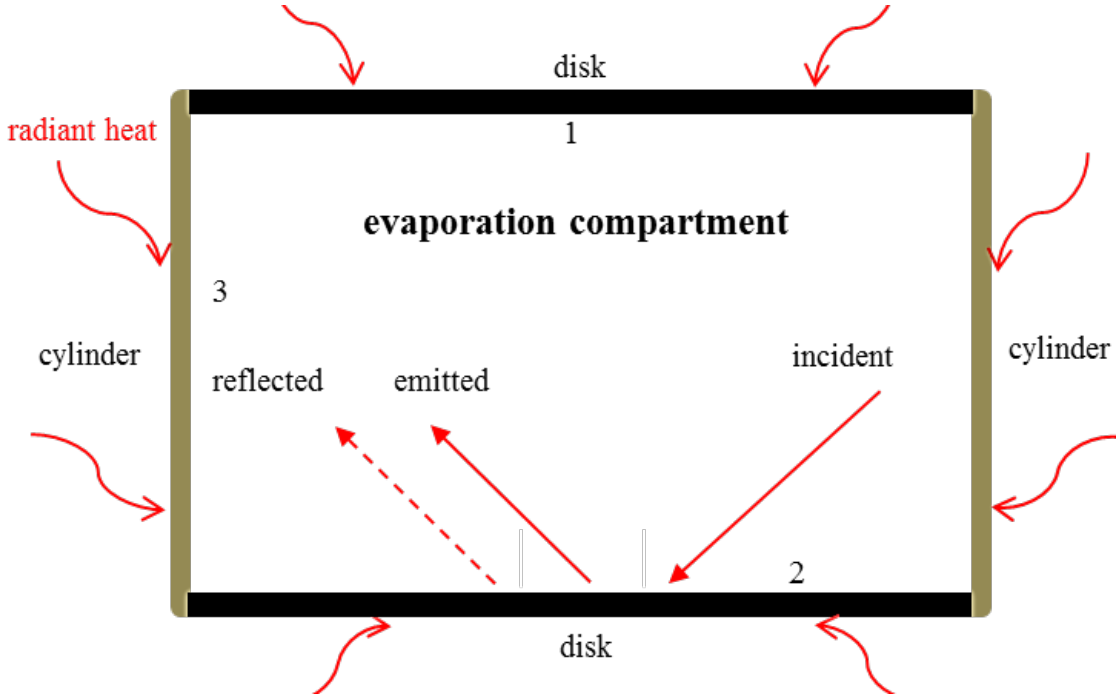

Figure 5.8. Radiant heat penetrated chamber walls 1 - 3 to produce incident, reflected, and emitted radiation from each wall interior (*Image from the author*).

The chamber walls of the compartment permitted the transmission of thermal energy from the cartridge heaters and through the material for producing radiant heat contributing to lubricant evaporation. The transmitted energy was counted as part of the emitted amount leaving the chamber's inner surfaces to serve as incident radiation between adjacent surfaces.

An obstacle to computing the radiation heat transfer, $Q_{radiation}$, was the determination of J for the surfaces. The dilemma was solved by noting that the approach used to determine $Q_{conduction}$ for nano-porous samples, namely Kirchoff's node law, had a parallel in $Q_{radiation}$. As was done for $Q_{conduction}$, analogies were made between the current and $Q_{radiation}$, and between voltage and J, with resistance, R, remaining unchanged. A resistance network was drawn that connected the resistances of each surface of the testing compartment with the resistances of the space between the surfaces. The network is shown in Figure 5.9.

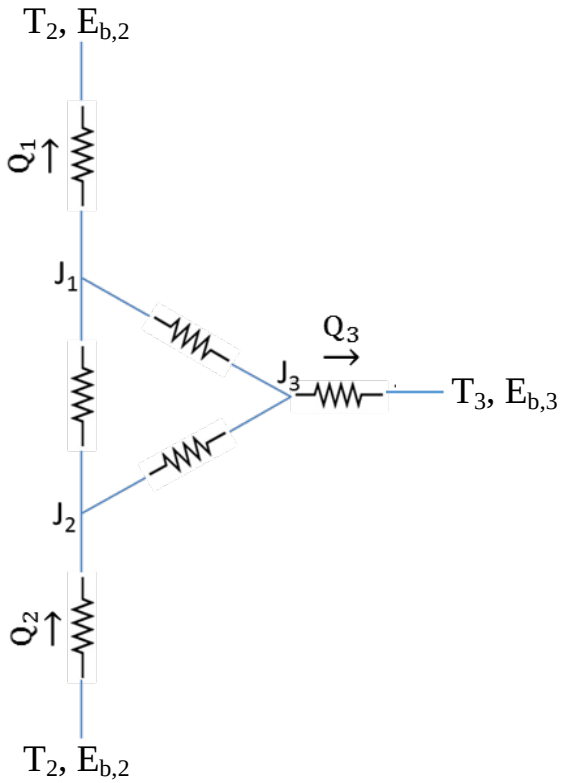

Figure 5.9. Model of the testing chamber's thermal radiation network (*Image from the author*).

Subscript numbering as well as letter indexing was used to reduce confusion when calculating the components of the heat transfer equations. In agreement with Figure 5.8, the top surface of the compartment is denoted by subscript number *1*, the bottom surface of the compartment (the sample stage) is *2*, and the vertical (side) surface of the chamber is number *3*. Since view factors are related to the space resistances, indexing using the letters *i* and *j* was helpful for noting the vantage point from which the view factor components, F_{ij}, were being calculated— whether $i \rightarrow j$ or $j \rightarrow i$. The index and subscript numbering schemes were carried forward as the discussion moved toward the calculation of $Q_{radiation}$.

The view factor and radiation energy approach was used to calculate $Q_{radiation}$. A requirement for the approach was to find the view factors for the evaporation chamber design. The view factors needed were: F_{12}, F_{13}, F_{21}, F_{23}, F_{31}, and F_{32}. The strategies employed for determining the view factors were the summation, symmetry, and reciprocity rules. To begin the calculations, a view factor chart for coaxially-aligned parallel disks was used to find the value of F_{12} which was 0.62. Then, the summation rule was used to find F_{13},

$$\mathrm{F_{11} + F_{12} + F_{13} = 1} \qquad \text{Equation (5.18)}$$

View factors F_{11}, F_{22}, and F_{33} values equaled zero. Solving equation (5.18) for F_{13} gave the value of 0.38. The symmetry rule was applied to F_{12} and F_{13}, respectively, to yield values of 0.62 for F_{21} and 0.38 for F_{23}. However, the calculation of F_{31} required the use of the reciprocity rule in equation (5.19) which was given as,

$$\mathrm{A_3 F_{31} = A_1 F_{13}} \qquad \text{Equation (5.19)}$$

The values for A_1 disk and A_3 cylinder surface areas were found to be 0.00419 m^2 and 0.004735 m^2, respectively. The reciprocity expression of (5.19) was solved for F_{31} to yield the value of

0.34. Once again employing the symmetry rule, the value of F_{32} was equal to F_{31}. A summary of the view factors is provided in Table 5.2.

Table 5.2. View factors for the calculation of $Q_{radiation}$.

	View Factors					
	$\mathbf{F_{12}}$	$\mathbf{F_{13}}$	$\mathbf{F_{21}}$	$\mathbf{F_{23}}$	$\mathbf{F_{31}}$	$\mathbf{F_{32}}$
Values	0.62	0.38	0.62	0.38	0.34	0.34

A number of derivations and substitutions were performed to arrive at generalized expressions for $Q_{radiation}$. The first expression, equation (5.20), was given as,

$$Q_{radiation} = \sum_{j=1}^{N} \frac{J_i - J_j}{R_{i\to j}} = \frac{E_{bi} - J_i}{R_i} \qquad \text{Equation (5.20)}$$

Equation (5.20) is an energy balance equation which says that the heat transfer via radiation that passes through the material and onto a surface is equivalent to the sum of the radiation heat transferred between that surface and the adjacent surfaces within the compartment. Substitutions into equation (5.20) were performed using three equations,

$$R_{i\to j} = \frac{1}{A_i F_{i\to j}}, \qquad R_i = \frac{1-\varepsilon_i}{A_i \varepsilon_i}, \qquad E_{bi} = \sigma T_i^4 \qquad \text{Equations (5.21), (5.22), (5.23)}$$

to arrive at the emissive power equation, E_{bi}, expressed as,

$$\sigma T_i^{\,4} = J_i + \frac{1-\varepsilon_i}{\varepsilon_i} \sum_{j=1}^{N} F_{i\to j}\left(J_i - J_j\right) \qquad \text{Equation (5.24)}$$

and the $Q_{radiation}$ equation for each surface of the compartment given as,

$$Q_i = A_i \sum_{j=1}^{N} F_{i\to j}\left(J_i - J_j\right) \qquad \text{Equation (5.25)}$$

Equation (5.24), which is necessary for the calculation of J, allows the emissive power to be expressed in terms of the surface temperatures of the evaporation compartment. The discovery

of the surface temperatures was done by programming the evaporation apparatus' PID heater controllers to achieve several temperature values spanning a wide range of the apparatus' capability. Once the apparatus' temperature stabilized, the actual temperature of each surface was recorded using an infrared thermometer. There were three surfaces, so three temperatures were recorded. These values were included in the temperature coefficient calculations in equation (7.1).

The constants in equation (5.24) were $\varepsilon_1 = \varepsilon_2 = \varepsilon_3 \approx 0.42$ for heated, lightly oxidized 304 stainless steel and the Stephan-Boltzman constant, σ =5.6704 E -08 W/m^2·K^4. The three equations derived from equation (5.24) are,

$$\sigma T_1^4 = J_1 + \frac{1-\varepsilon_1}{\varepsilon_1}[F_{12}(J_1 - J_2) + F_{13}(J_1 - J_3)] \qquad \text{Equation (5.26)}$$

$$\sigma T_2^4 = J_2 + \frac{1-\varepsilon_2}{\varepsilon_2}[F_{21}(J_2 - J_1) + F_{23}(J_2 - J_3)] \qquad \text{Equation (5.27)}$$

$$\sigma T_3^4 = J_3 + \frac{1-\varepsilon_3}{\varepsilon_3}[F_{31}(J_3 - J_1) + F_{32}(J_3 - J_2)] \qquad \text{Equation (5.28)}$$

Equations (5.26), (5.27), and (5.28) provided solutions for the 3 unknowns J_1, J_2, and J_3 after inputting the coefficient-adjusted T_1, T_2, and T_3 values. The table that shows the adjusted T_1, T_2, and T_3 values calculated for the range of evaporation temperatures is presented in section 7.1.3.

5.1.4 Combined Heat Transfer on Smooth and Nano-Porous Si-Cu Topographies

The chief objective of the research was the characterization of Si-Cu composites to enhance lubricant retention impacting the tribological properties of sliding surfaces. In so doing, a necessary task was the modeling of smooth and nano-porous surfaces to quantify the effects of the material properties and geometric dimensions on the evaporation of lubricant from the

surface of the samples. The major milestones up until this point were generated models of the three modes of heat transfer—conduction, convection, and radiation—which affected lubricant evaporation. These results were brought together to define the net heat transfer, Q_{net},

$$Q_{net} = Q_{conduction} + Q_{convection} + Q_{radiation} \qquad \text{Equation (5.29)}$$

The results can be found throughout section 7.1.4.

5.2 Fourier Transform Infrared Spectroscopy for a-Si:H Film Characterization

Fourier-transform infrared (FTIR) spectroscopy is a non-intrusive analytical technique that measures absorption, emission, photoconductivity, and Raman scattering using the infrared spectra of solids, liquids, and gases. The resulting infrared spectra are based on the interference between two radiation beams. In short, the radiation leaving the source in the spectrometer was passed through a beamsplitter, onto mirrors, and to the sample before reaching a detector. The detected radiation was used to create an interferogram. An interferogram is a plot generated from a signal that was produced whenever a change occurred in the path length between the two mirror's beams. After amplification of the signal and using attenuating filters to eliminate the high-frequency contributions, the signal was converted to digital form by an analog-to-digital converter and the data was transferred to a computer for Fourier transformation.

Figure 5.10 is a basic schematic of a Michelson interferometer that consists of two plane mirrors, one of which can travel in a direction perpendicular to the plane of the other mirror. A beamsplitter bisects the planes of the two mirrors. The beamsplitter material is chosen according to the IR region of interest. Thin organic films, such as polyethylene terephthalate, are used as beamsplitters in the far-IR region where the spectrum wavenumbers are 10 to 400 cm^{-1}. The mid-IR region covers the electromagnetic spectrum from 400 to 4000 cm^{-1} and the near IR

spectrum is 4000 to 14000 cm^{-1}. Materials such as germanium or iron oxide are coated onto IR-transparent substrates like KBr or CsI to produce beamsplitters for the mid- or near-IR regions.

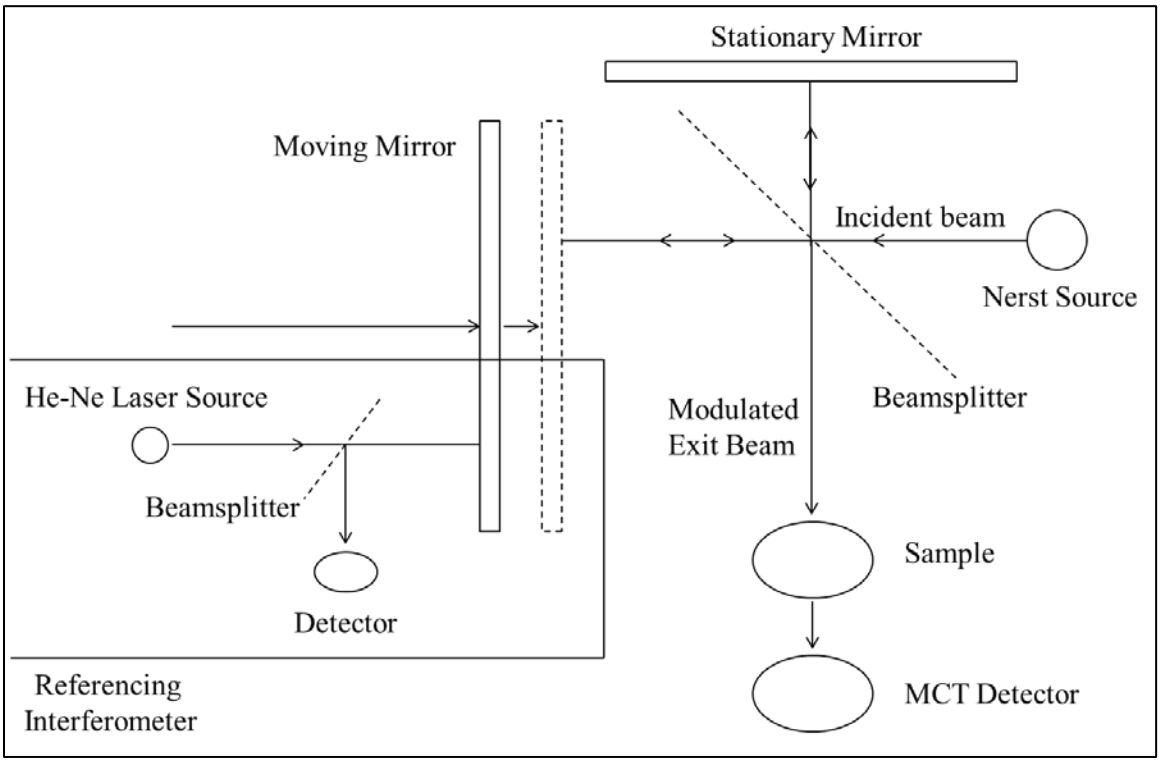

Figure 5.10. Illustration of the Michelson interferometer used in the FTIR experiments. (*Image from the author*).

In theory, if a collimated beam of monochromatic radiation of wavelength λ is passed into an ideal beamsplitter, half of the incident radiation is reflected to the fixed mirror while the other half is transmitted to the moving mirror. Fifty percent of the beam reflected from the fixed mirror is then transmitted through the beamsplitter while the other half is reflected back toward the source. The moving mirror's beam returns to the beamsplitter also. The combined beams interfere constructively or destructively, depending on the wavelength (or frequency expressed in wavenumbers) of the light and the optical path difference produced by the moving mirror. The beam that leaves the interferometer at 90° to the input beam is the modulated exit (transmitted)

beam and this is the one detected in FTIR spectrometry. The interferogram's data points are digitized at the zero crossings of a helium-neon (He-Ne) laser beam as depicted in Figure 5.12. A He-Ne laser serves as a referencing interferometer and ensures that the modulated exit beam's intensity is measured at precisely equal intervals of mirror positions, thereby providing an internal wavelength calibration for every scan.

FTIR spectrometers incorporate a Globar or Nernst source for examining the mid-IR region. If the far-IR region is to be studied, then a high-pressure mercury lamp can be used. For the near-IR region, tungsten–halogen lamps are used as sources. There are two commonly used detectors for the mid-IR region. The standard detector is a pyroelectric detection device containing deuterium triglycine sulfate (DTGS) housed in a temperature-resistant alkali halide window. For more sensitive spectra collection requirements, mercury cadmium telluride (MCT) can be used, but this approach requires cooling the detector to the temperature of liquid nitrogen. In the far-IR region, Ge or InSb detectors are employed which require operation at liquid helium temperatures. For the near-IR region, the detectors are generally PbS photoconductors.

The FTIR spectrometer was favorable for the analysis of thin films such as a-Si:H because the techniques were neither invasive nor destructive to the film's molecular structure. The energy of the IR photons was not powerful enough to cause electron excitation, but it was strong enough to cause rotation and vibration of the molecular structure which produced various changes in the dipole moment of the a-Si:H molecules. The dipole is the molecule's electric field due to positive and negative ends of the molecule whose strength (moment) is determined by the magnitude of the charge and the physical separation between poles. The material must have a dipole moment in order to absorb IR radiation. The absorbed radiation increases the vibration amplitude and/or rotation frequency of the molecules through the interaction of the photon's

electric field and the electric field (dipole) of the molecules. The vibration/rotation strength is related to the strength of the bond and mass of the atoms, so it provides unique identification for atomic and molecular structures. FTIR techniques are successful because the absorption of radiation occurs at the resonant frequency which matches the transition energy of the particular group or band that vibrates. An image of the FTIR apparatus, the Nicolet 8700 (Thermo Fisher Scientific, Madison, WI), that has full IR spectral analysis capabilities is shown in Figure 5.11.

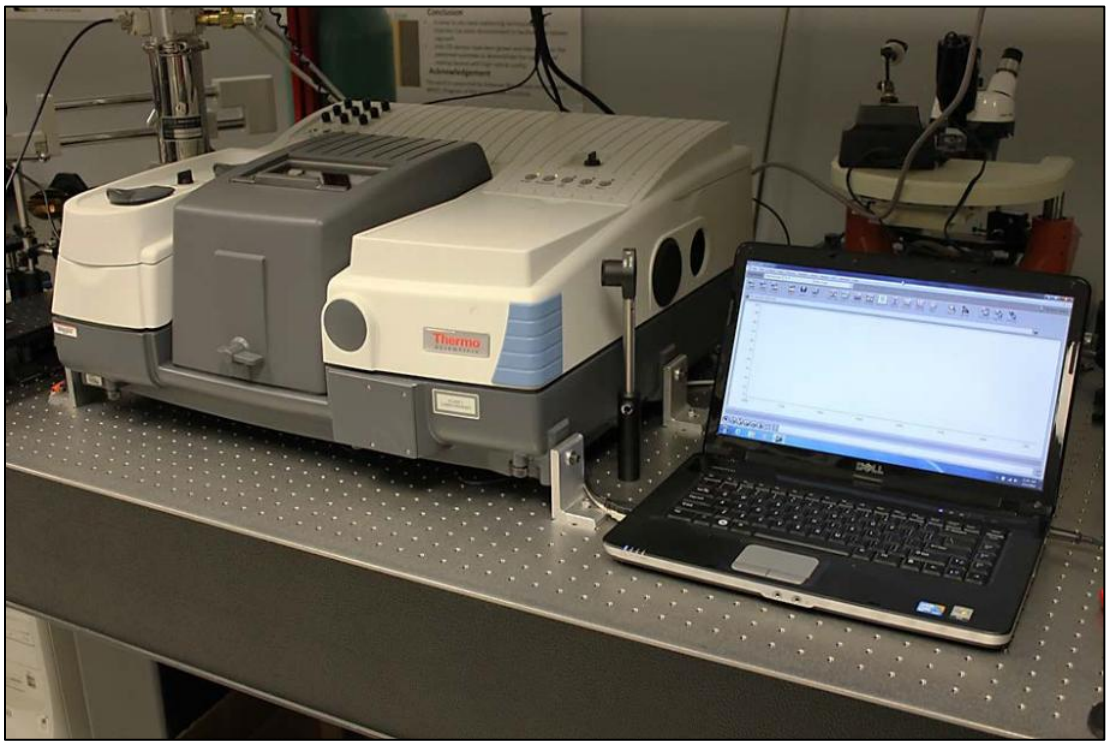

Figure 5.11. The FTIR spectrometer was used to assess a-Si:H film properties (*Image from the author*).

Section 5.2.1 discusses the preliminary considerations, materials, and machine settings needed to collect the spectra. Section 5.2.1.1 elaborates on the wavenumbers of certain compounds and functional groups found in a-Si:H film and hydrocarbon-based lubricants. Beer-Lambert's law is explained and related absorption formulae are derived. The rationale for using FTIR to calculate the number density of SiH_x bonds is explained, and a plan is presented to use the H number

density (concentration) to relate the effect of surface chemistry and geometric changes of the topography to the retention of lubricant.

5.2.1 Fourier Transform Infrared Spectrometry Set-Up

The first task to be performed when analyzing a sample containing an unknown composition of matter was to obtain a baseline interferogram or background IR spectra to subtract the effects of the machine and the room's contribution to the spectra of interest that would otherwise distort the data collected from the samples. If the intent is to investigate the changes to matter as variables in the experiment change, it is critical to collect spectra on the control and altered samples as closely as possible to the same environment because, over time, fluctuations in the room conditions such as its lighting and humidity can significantly affect the results. Only in this way can the baseline (the control sample's spectra) be subtracted from the subsequent spectra of the altered samples to differentiate the effects of the test variables. Not to be overlooked is the importance of choosing the proper type of substrate that is as IR-transparent as possible. For the author's research, this required producing samples using intrinsic (undoped), double-side polished, prime wafers (product number 4INT>80DSP) purchased from WRS Materials (wrsmaterials.com). The c-Si's wafer's properties are listed in Table 5.3.

Table 5.3. The c-Si wafer properties used in the FTIR experiments.

Diameter	Thickness	Orientation	Resistivity
100 mm	475 - 525 μm	(1-0-0)	> 80 Ω-cm

The spectrum of IR radiation necessary for examining the atomic and molecular structures of a-Si:H and lubricant films was the mid-IR range. The FTIR machine's settings were: % transmittance as the data collection type, 64 scans per wavenumber for accuracy, 6 cm^{-1} resolution, auto gain set to 1, aperture set to 75, detector type chosen as MCT, beam source was

IR, mirror velocity set to 1.2659, screen wheel set to 20 %, and data output selected as comma separated values.

5.2.1.1 FTIR Spectra Collection and Analysis for a-Si:H Film Characterization

The modes of vibration and rotation are classified by their effect on the bonds of the material. For example, stretching modes may be described as either asymmetric or symmetric if the bond lengths between atoms extend and retract telescopically. Bending modes may be defined by a change in bond angle, scissoring, wagging, rocking, and twisting/torsion actions. Though not considered in the author's research at this time, a few wavenumbers that are encountered in evaporated lubricant chemistry analysis are carbonyls (C=O) that exhibit stretching behavior at IR wavenumbers between 1650 cm^{-1} and 1830 cm^{-1}, and hydroxyl groups (-OH) and C-H bonds that stretch when absorbing IR spectra between 2500 cm^{-1} and 4000 cm^{-1}. Amorphous Si has a wagging mode at 640 cm^{-1} and stretching modes at 2000 cm^{-1} and 2100 cm^{-1} which correspond, respectively, to the presence of mono-hydride and poly-hydride atoms bonded with Si atoms [80]. The knowledge gained from the FTIR spectra could serve as a powerful quantitative tool to determine the number density, N_x (cm^{-3}), or concentration of sites available for bonding between hydrocarbon lubricants and a-Si:H film when it is used as a surface chemistry modification. The "*x*" term is a placeholder allowing for the substitution of an element of interest in the number density expression.

As mentioned in section 5.2.1, the data output chosen in the FTIR apparatus was % transmittance. The mathematical relationship of transmittance to IR absorption is provided by the Beer-Lambert law, stated as,

$$\text{Absorbance}_i = -\log(\text{Transmittance}_i) \qquad \text{Equation (5.30)}$$

where *Absorbance*$_i$ (typically reported in absorbance units, AU) is the absorbance value for a specific wavenumber of the mid-IR spectrum.

Transmittance is simply the ratio of the IR light's power that was transmitted through a-Si:H film to the original power level, or,

$$\text{Transmittance}_\text{i} = \left(\frac{\text{I}_\text{i}}{\text{I}_0}\right) \qquad \text{Equation (5.31)}$$

in which *I* (W) represents the power as intensity. The subscript "0" defines the state of the intensity before permeation into the material and "i" is the post-permeation intensity value encountered by a-Si:H film at the respective wavenumber.

Since the Beer-Lambert expression uses transmittance and it was provided by the apparatus as a percentage, % transmittance was substituted into equation (5.30) and divided by 100 to yield the appropriate values for absorbance, namely,

$$\text{Absorbance}_\text{i} = -\frac{\log\left(\frac{\text{I}_\text{i}}{\text{I}_0}\right)}{100} \qquad \text{Equation (5.32)}$$

When homogenous, thin film materials such as the a-Si:H produced in this research are analyzed, *Absorbance*$_i$ can be assumed to be linear with N_x and the thickness of the material. Doing so allows *Absorbance*$_i$ to be expressed in terms of an absorption coefficient, α_i (cm^{-1}). The absorption coefficient is the measure of how strongly a chemical species absorbs light of a given wavelength. A transparent material has a smaller α than an opaque one. Assuming the thickness of the a-Si:H film to be the path length (in cm) of the light, the equation for α_i becomes,

$$\alpha_\text{i} = \frac{\text{Absorbance}_\text{i}}{\text{path length}} = \frac{-\log\left(\frac{\text{I}_\text{i}}{\text{I}_0}\right)/100}{\text{film thickness}} \qquad \text{Equation (5.33)}$$

To restate, the ultimate goal was to determine the N_x of available bonding sites with Si atoms in the a-Si:H surface chemistry so that the N_x could be correlated to the changes in the geometry of the topographies. In essence, it is proposed that as more surface area is created by changing the geometry of the pores, more bonding sites will be formed, thus contributing to enhanced lubricant retention. For a-Si:H films, infrared absorption and the H concentration are related through the oscillation strength of the Si and H bond's stretching vibration [80]. By assigning a proportionality constant, A_ω, (cm^{-2}), that is the inverse of the oscillation strength and relating the H concentration to the integrated absorbance, δ (cm^{-1}), a simple relationship for N_H (cm^{-3}) can be expressed in the form of,

$$N_H = A_\omega \delta \qquad \text{Equation (5.34)}$$

where the subscript "ω" indicates the wavenumber associated with a particular proportionality constant and "H" indicates the appropriate mono- or poly-hydride bond type under consideration. Proportionality constants have been reported extensively for the wagging and stretching modes of a-Si:H films [81]. Though there were many researchers who investigated the constants for a variety of a-Si:H films, the values chosen for use in the calculation of N_H were uniquely applicable to film thicknesses less than 1 µm. The proportionality constant for the wagging mode was $A_{640} = 2.1 \times 10^{19}$ cm^{-2}, and the two stretching modes were $A_{2000} = 9.0 \times 10^{19}$ cm^{-2} and $A_{2100} = 2.2 \times 10^{20}$ cm^{-2} [82]. The value for A_{2000} was attributed to isolated mono-hydrides (SiH bonds) and the value for A_{2100} was for both clustered mono-hydrides and poly-hydrides (SiH_2 and SiH_3 bonds). A diagram and in-depth discussion of the various bond types are provided in section 7.2.1.

Efforts thus far have been focused on obtaining the value of α_i for its inclusion in equation (5.35) to determine δ. Once equation (5.35) was solved, it could be substituted in equation (5.34) to

determine N_H. Notice, however, that the division of equation (5.33) by ω_i is all that is required to arrive at the integrand of equation (5.35),

$$\delta = \int (\alpha_i/\omega_i)d\omega \qquad \text{Equation (5.35)}$$

The final substitution of equation (5.33) into the integrand makes the integral become,

$$\delta = \int \left(\frac{-\log\left(\frac{I_i}{I_0}\right)/100}{\text{film thickness} * \omega_i} \right) d\omega \qquad \text{Equation (5.36)}$$

To perform the integration, the FTIR data and film thickness comprising the integrand and variable of integration were plotted using a Microsoft Excel™ spreadsheet. An appropriate numerical integration scheme was employed to approximate the area under the curve. An example of a α/ω plot generated from 175 nm thick a-Si:H film is shown in Figure 5.12.

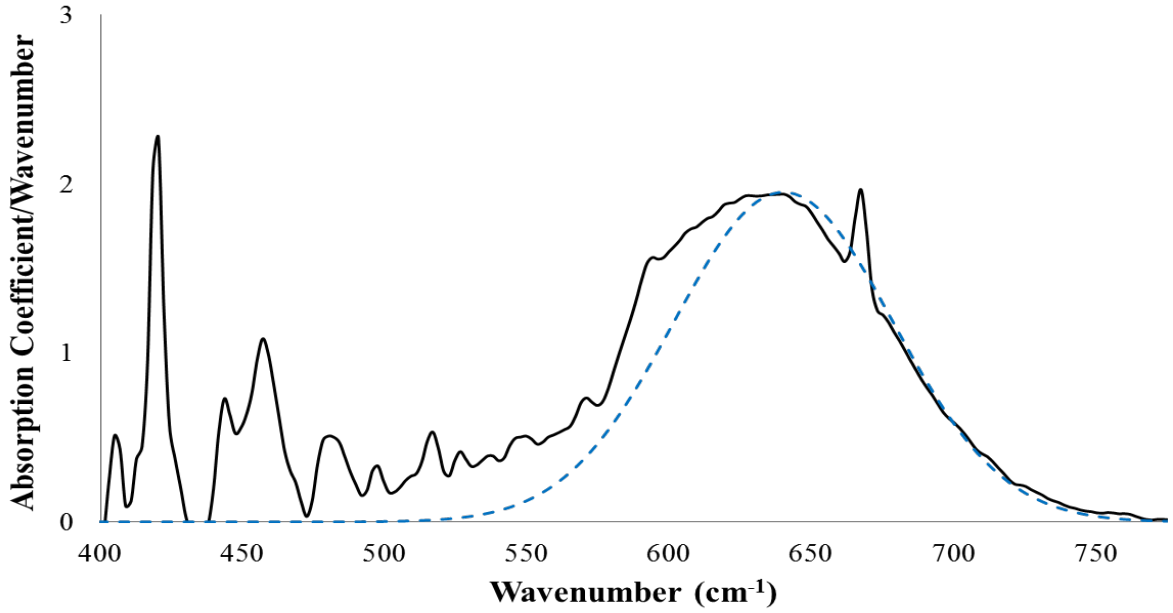

Figure 5.12. An α/ω plot was produced from a-Si:H film deposited 175 nm thick (*Image from the author*).

The solid line in Figure 5.12 was obtained by plotting the data for the integrand, α_i/ω_i, as the ordinate values and the variable of integration, ω_i, as the abscissa values. Integration of the α/ω plot was facilitated by the Gaussian curve. The Gaussian curve is represented by the dotted line in the figure. Manual manipulation of the Gaussian curve function, *G*, was desired to produce the best-fit to the α/ω plot. The function for the curve was developed as,

$$\mathrm{G} = \mathrm{height} * \exp\left(-\frac{((\omega_\mathrm{i} - \mathrm{position})^2)}{(2 * \mathrm{width}^2)}\right) \qquad \text{Equation (5.37)}$$

Three adjustable variables were incorporated into the Gaussian mathematical function: *position*, *height*, and *width*. The geometric illustration of the controllable variables of the Gaussian curve is shown in Figure 5.13.

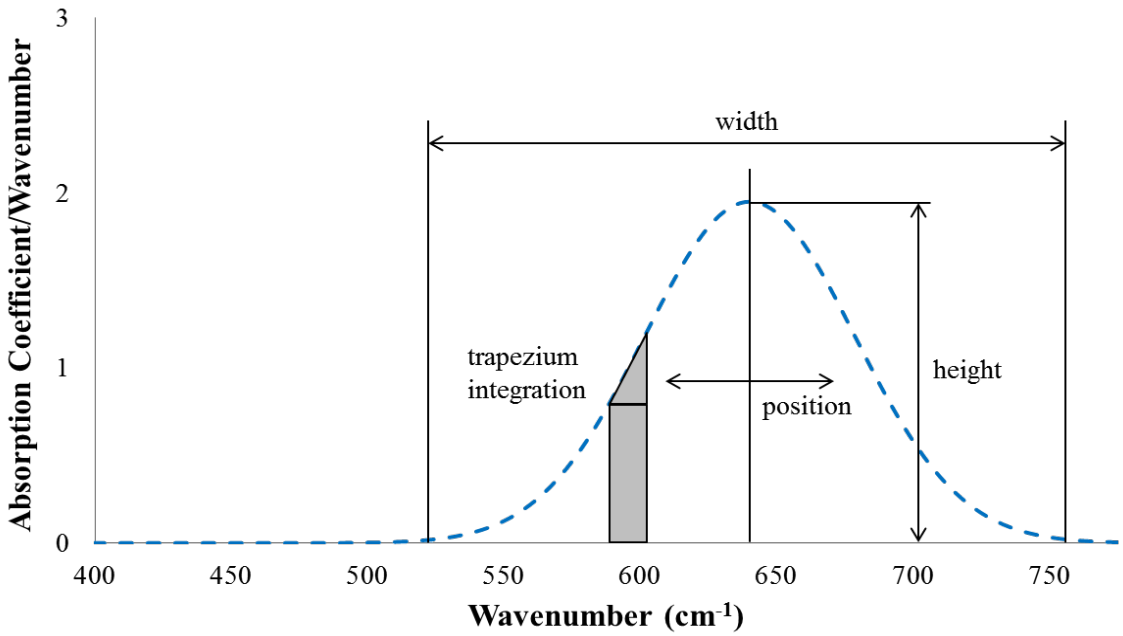

Figure 5.13. The adjustable variables of the Gaussian curve function permitted close fitting to the α/ω curve. Trapezium integration provided a suitable measurement of the area under the Gaussian curve (*Image from the author*).

The *position* variable controlled the left/right location of the center (peak) of the Gaussian curve. It is denoted by ω_i values on the *x*-axis. In Figure 5.12, the Gaussian curve was centered on 640 cm^{-1} and it was relatively congruent with the α/ω plot on which it was being fitted. This position, ω_{640}, was primarily for positive identification of a-Si:H film and was not included in any calculations. The ω_{2000} and ω_{2100} peak positions were used for determining the respective concentrations of mono- and poly-hydride bonds in a-Si:H film. The *height* variable manipulated the vertical distance of the peak as measured from the *x*-axis and along the center line of the Gaussian curve. *Height*, therefore, corresponded to the α_i/ω_i values shown on the *y*-axis. The peak of the Gaussian curve should visually align with the height of the peak of the α/ω plot. The *width* variable manipulated the base of the Gaussian curve. The change in *width* altered the slope of the curve while still allowing the distance between the curve and *x*-axis to approach zero as customary for asymptotic functions.

Having constructed the Gaussian curve to provide a best-fit to the α/ω plot, an integration scheme utilizing the trapezoid rule was employed for numerical integration of the Gaussian curve. An equation was formulated for the conjoined rectangle and triangle shown in Figure 5.12. Using the α/ω and ω values associated with the Gaussian curve, such that for $i \neq j$, the equation was,

$$\text{Trapezium Integration} = (\omega_j - \omega_i)\,\alpha_i/\omega_i + 0.5\left|(\alpha_j/\omega_j - \alpha_i/\omega_i)\right|(\omega_j - \omega_i) \quad \text{Equation (5.38)}$$

To conserve computation time and resources, the symmetry of the Gaussian curve was used to advantage which meant multiplying one half of the computed integral by two to attain the total area under the curve. For the example given in Figure 5.13, ω = 640 cm^{-1} (the center of the curve) was the starting ω value, and the differential change, $d\omega$, was chosen as 2 cm^{-1} to obtain the subsequent values for ω. Corresponding values of α/ω were chosen from the Gaussian

curve for those ω's to become inputs to equation (5.38) for arriving at the cumulative values of δ. Once again, the 640 cm^{-1} wavenumber was not the focus, but those of 2000 cm^{-1} and ≈2100 cm^{-1} were for observing the stretching bond behavior that characterized mono- and poly-hydride bonds in a-Si film. After determining the cumulative δ of the Gaussians centered on these wavenumbers, they were substituted into equation (5.34) for the calculation of total N_H, the concentration of H. The comprehensive discussion of the α/ω plot and Gaussian curves is provided in section 7.2.2.

An accounting of N_H and N_{Si} was required to determine the mole fraction of H atoms. The mole fraction of H was investigated in this work as a matter of interest to compare the results of this research with those reported in other literature. Crystalline Si concentration has been investigated and reported as $N_{Si} \approx 5 \times 10^{22}$ cm^{-3} [82]. The equation for the mole fraction is given by,

$$\text{mole fraction of H} = \frac{\mathrm{N_H}}{(\mathrm{N_H} + \mathrm{N_{Si}})} \qquad \text{Equation (5.39)}$$

The mole fraction of mono-hydrides and poly-hydrides can be determined separately by substituting the appropriate N_H expression into the equation, as was done during the determination of H concentrations of a-Si:H film. The atomic percentage is also commonly reported in literature. The atomic percentage is simply the mole fraction multiplied by 100, namely,

$$\text{atomic percentage} = \text{mole fraction} * 100 \qquad \text{Equation (5.40)}$$

CHAPTER 6

CHARACTERIZATIONS OF MATERIALS

6.1 Overview of the Materials Characterization

The fabrication of smooth topographies was discussed in sections 4.3 and 4.3.1. Some discussion of the fabrication of nano-porous topographies concerning electroless Cu was done in section 4.3.2. Arguably, that discussion could have been included in this chapter because it delved into the characterization of the materials. Ultimately, it was decided to leave the information in that section to preserve the continuity of the discussion regarding the nano-porous sample fabrication process. This chapter principally addresses the characterization of the materials in nano-porous topographies as it relates to their geometric and chemical characteristics.

It should be explained there were several sample configurations that fit within the description of nano-porous topographies. The nano-porous samples' fabrication parameters involved 2 pore diameters, 3 pore depths, Cu film, and a-Si:H film if the sample had its surface chemistry modified. Then these nano-porous topographies were chemically modified further after the testing lubricant was applied and evaporated. All of these structural and chemical components offered copious opportunities for imaging and spectroscopy. However, the characterization of these components individually would have been excessive and expensive. Instead, the decision was made to use characterization where needed to demonstrate core achievements in the fabrication of these topographies.

Where possible, multiple achievements may be demonstrated in a single image or spectroscopy. For instance, it was not necessary to capture images of the 3 depths that were etched in c-Si for

both pore diameters or to show the penetration of electroless Cu into the pores of every sample configuration. Rather, select images and spectroscopies were included in this chapter to show the penetration of Cu into the narrowest and the deepest pores, with the assumption that Cu penetrated the wider and shallower pores easily due to their lower resistance to the plating process. This simplified imaging approach was used for demonstrating the penetration of a-Si:H film and testing lubricant inside the pores. The imaging was done using scanning electron microscopy. The technique is discussed in section 6.2.

6.2 Material Characterization Using SEM

Scanning electron microscopy (SEM) is a nonintrusive imaging technique that captures high-resolution images of materials on the nano-scale. The main SEM system used in this work, the FEI/Philips environmental SEM (XL30, Hillsboro, Oregon, USA) is shown in Figure 6.1.

Figure 6.1. The ESEM system shown here was used to capture images of the nano-topographies [46] (*Image from the author*).

There were other SEM systems used in the characterization of the samples: The FEI Nanolab 200 and JEOL 6335. Each system offered its own advantages to the research that was accomplished.

6.2.1 C-Si Pore Characterization by SEM

Pores were used as a comparison to smooth samples during lubricant retention testing. The 616,080 pores were patterned as rectangular arrays and etched at specified depths into 640 µm thick c-Si wafers using DRIE discussed in section 4.2.4. The arrays had a fixed pitch of ≈14 µm for both pore diameters. An image of a partial array is shown in Figure 6.2.

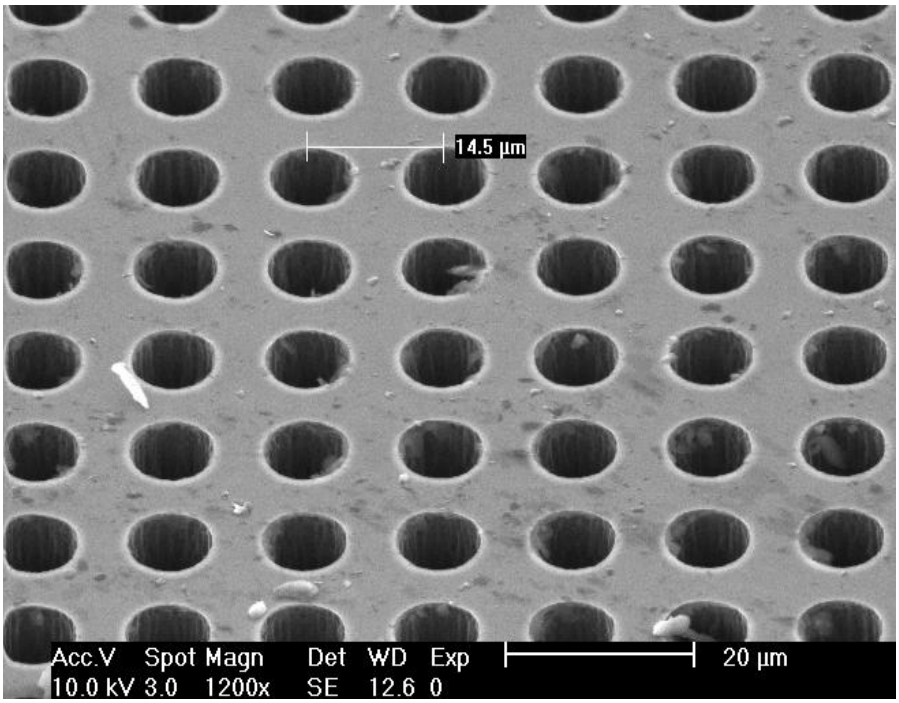

Figure 6.2. A SEM image of a partial array of pores created in c-Si wafers for lubricant retention testing (*Image from the author*).

The pores shown in figure 6.1 exhibited uniform geometry in terms of the circular shape, pitch, and diameter. The array-to-array appearance was consistent throughout the whole etched wafer. This outcome was the result of the quality of the chrome mask used during the photolithographic

process and the attention to quality control during the c-Si etching steps. The choice to use (1-0-0) c-Si prime wafers for this project was vindicated by the smooth surface they afforded. This was important in that the wafers did not add difficulty to the task of producing topographies that reflected the actual results of lubricant retention of the pores without interference from the surface's texture. The smoothness of the pore's horizontal surface was observed to occur at the various etch depths encountered during pore etching trials. This meant the bottom of the pores, no matter the depth, would have smooth, flat surfaces. The uniformity of depth was maintained from pore-to-pore for both pore diameters. Undoubtedly, this feature of c-Si contributes to the consistency of the data to be collected during lubricant retention testing.

The final pores used for retention testing had 2 diameters, 0.5 and 1 µm. These diameters, though, were achieved from larger pores which began as 6 and 6.5 µm, respectively. Figures 6.3a and b show the results that were obtained from photolithography and DRIE processes used on c-Si wafers. SEM images were used to capture the dimensional information annotated on the pore openings.

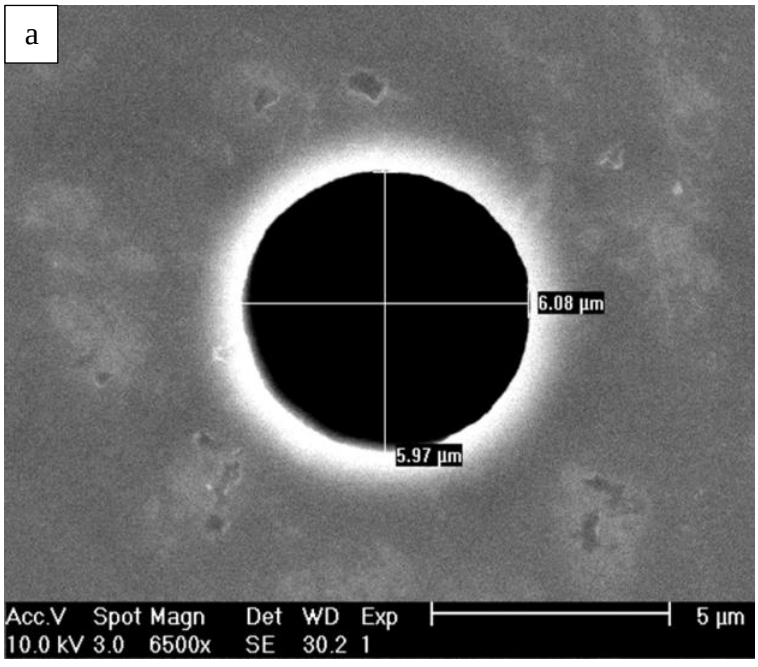

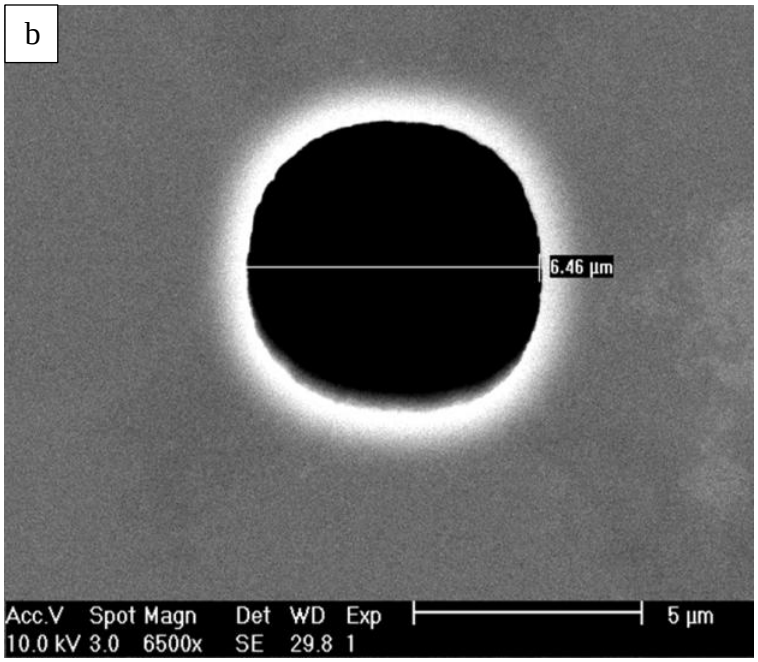

Figures 6.3a and b. SEM imaging was used to verify the intended pore diameters: (a) the 6 µm and (b) the 6.5 µm pore diameters. These eventually became nano-pore diameters of 0.5 and 1 µm, respectively (*Images from the author*).

The pore diameters shown in Figures 6.3a and b were typical of the pores created for lubricant retention testing. The glow observed around the pore circumference in the figures was characteristic of edge charging because of the build-up of electrons during SEM imaging. Charging occurred due to the low electrical conductivity of Si. This was not a lasting anomaly which affected subsequent processes on the wafers. Despite some appearance of rippling around the pore opening as a result of DRIE, the pores exhibited good uniformity in their shape and diameter, no matter their location on c-Si wafers.

Verification of the final pore depth was important for assuring the samples had achieved the intended depth during the etch process. The profile of the pores was desired to obtain this information. To obtain the profiles, the patterned c-Si wafers were diced into samples and the samples were cleaved. Cleaving is the process of creating a fracture that runs along (1-1-0)

plane, in the case of (1-0-0) wafers. This was the best method for creating profiles of the pores. Care was taken to cleave the samples so that the pores were dissected at the proper location to reveal the objective views. There were 3 pore depths etched in c-Si: 25, 50, and 75 µm. Examples of 25 µm depth pores are shown in Figure 6.4.

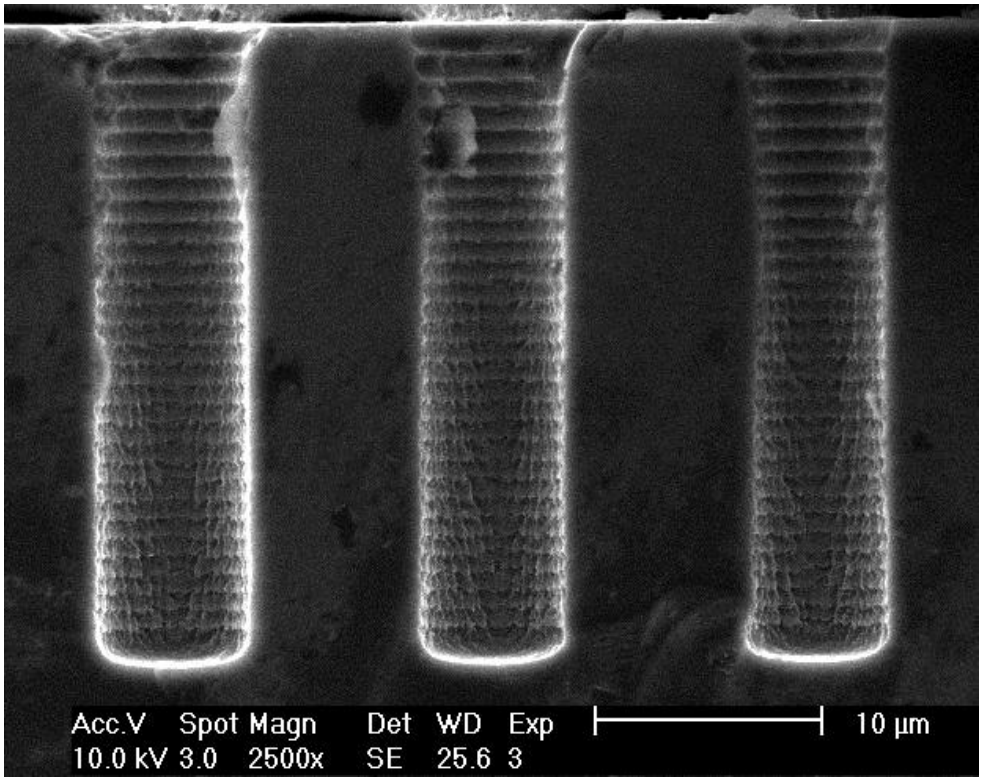

Figure 6.4. Pores were etched into c-Si using DRIE. These pores had a 6 µm diameter and a 25 µm depth (*Image from the author*).

The pores shown in Figure 6.4 had a 6 µm diameter. Pores were also etched to this depth for the 6.5 µm diameter. A characteristic of pores etched to this depth was the ripples that formed along the pore walls. The ripples are referred to as corrugations and they formed during the alternating etch and passivation steps of the Bosch process while etching the pores in c-Si [75]. The corrugation peaks were taller initially, but became less protruded as the objective depth was approached. The other depths did not exhibit these as prominently as the 25 µm depth. They

had their own peculiarities along their walls, however. Despite this outcome, the pore geometry for the 25 µm depth was remarkably uniform and there was no concern the imperfections would be an impediment to achieving the objective of lubricant retention testing.

The next depth etched into c-Si was 50 µm. The reason for the 25 µm increments was to provide sufficient disparity in the depths tested in order to clearly differentiate trends in the lubricant retention behavior of the respective depths. Pores that were etched to the 50 µm depth in c-Si are shown in Figures 6.5a and b.

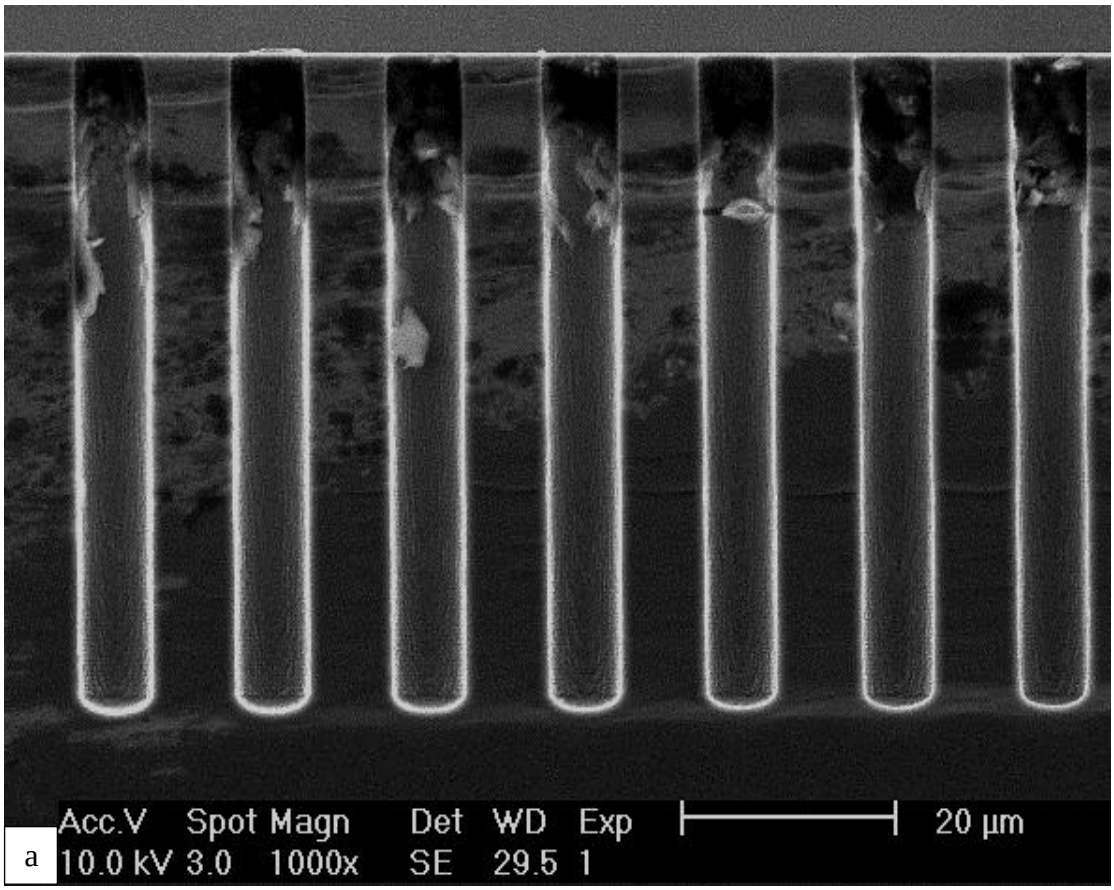

Figure 6.5a. The pores in this figure were ones having the 6 µm diameter and 50 µm depth. (*Image from the author*).

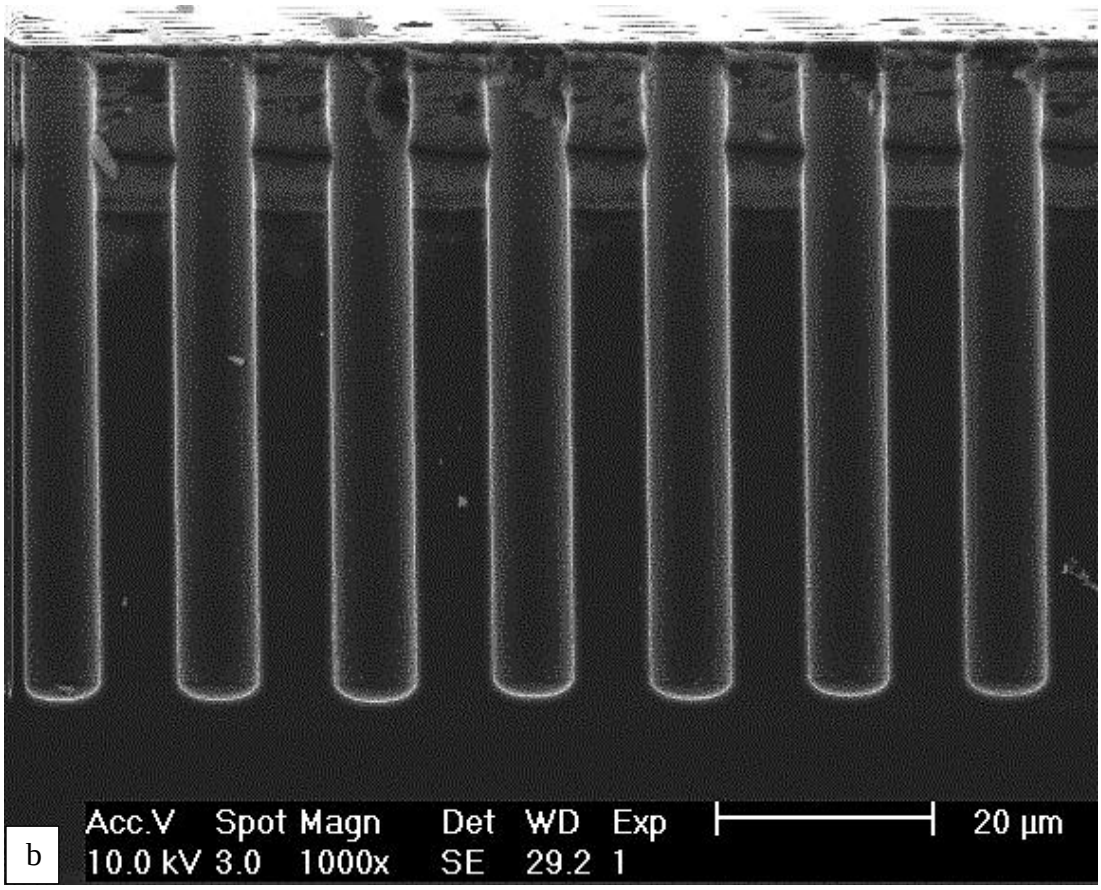

Figure 6.5b. The pores in this figure were ones having the 6.5 µm diameter and 50 µm depth (*Image from the author*).

Both SEM images provided good examples of the 50 µm depth pores that composed the arrays. Normally, it was very difficult to obtain clear images such as these, even if one were to attempt to dice the samples using a saw. It was noticed, though, that the images showed some debris that was lodged inside of the pores. This was the product of the cleaving process which could be quite explosive in nature as the fracture opened along the rows of pores and left behind stray pieces of c-Si. In spite of the presence of the debris, the images show the walls of the 50 µm depth pores of both diameters were the smoothest of the 3 depths etched. At this point, the presentation of pores etched in c-Si ends because a fair amount of attention will be given in later

figures to the 75 µm depth pores having a 6 µm outside pore diameter. Certain features of these c-Si based pores will be pointed out as the opportunity is afforded.

6.2.2 SEM Imaging and Spectroscopy of Cu Film

The deposition of Cu film on c-Si was important for producing patterned Si-Cu composites for lubricant retention testing. A departure from the discussion regarding patterned c-Si wafer is done to discuss the characterization of Cu film on smooth topographies. The deposition was performed using the sputtering technique described in section 4.3.1. There were 2 film thicknesses deposited: 2.5 and 2.75 µm. The Dektak 3030 profilometer was used to verify the thicknesses were achieved. The result for the 2.5 µm Cu thickness is shown in Figure 6.6.

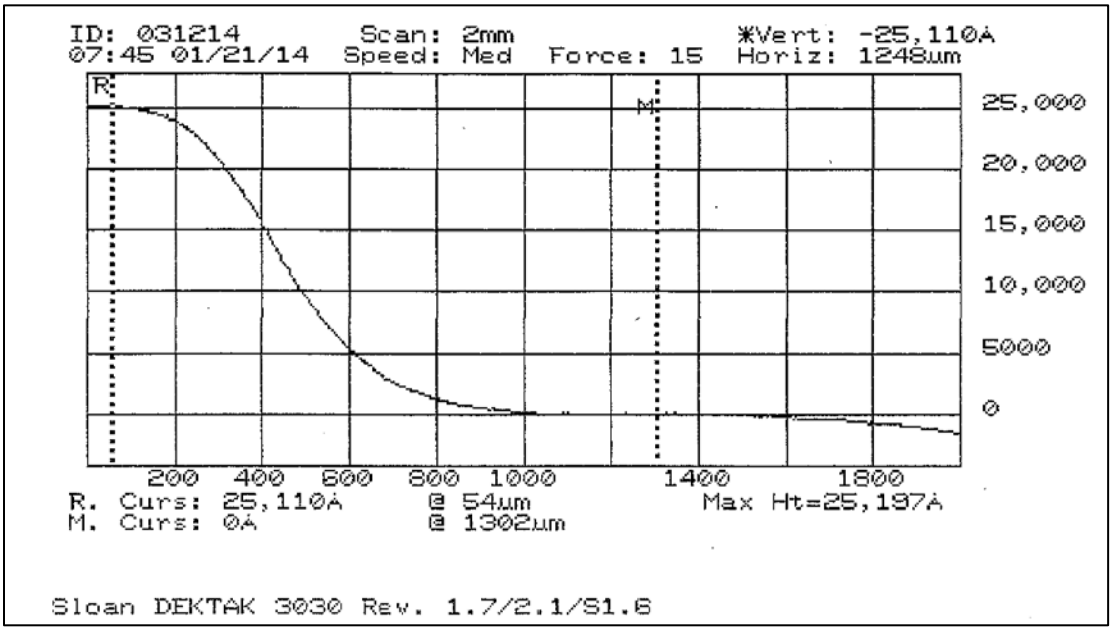

Figure 6.6. Cu film was deposited to 2.51 µm thickness on the surface of smooth c-Si wafers using the sputtering technique. The vertical measurement was recorded in units of Angstroms (*Image from the author*).

The sputtering technique covered the wafer with Cu film except at 4 locations where the wafer was mechanically clamped to the wafer transporting assembly in the sputtering machine. It was at these locations where there was exposed c-Si wafer surface that allowed the Dektak

profilometer to obtain measurements of the Cu film thickness. The Dektak's measuring stylus was maneuvered to these locations that included the edges that bordered the Cu film and c-Si wafer surface. A 2 mm length scan, a 15 mg stylus force, and stepped profile were used to perform the measurements. After obtaining the results of the scans, the reference and measurement bars, represented in Figure 6.6 by *R* and *M*, respectively, were positioned on the instrument's screen. The maximum height reading was selected on the front panel and the information was printed out as shown in the figure.

Returning attention to the patterned Si-Cu samples, the Cu film was deposited using the electroless deposition technique described in section 4.3.2 followed by electrolytic deposition techniques. An example of the Cu film that was produced using the combined techniques is shown in Figure 6.7.

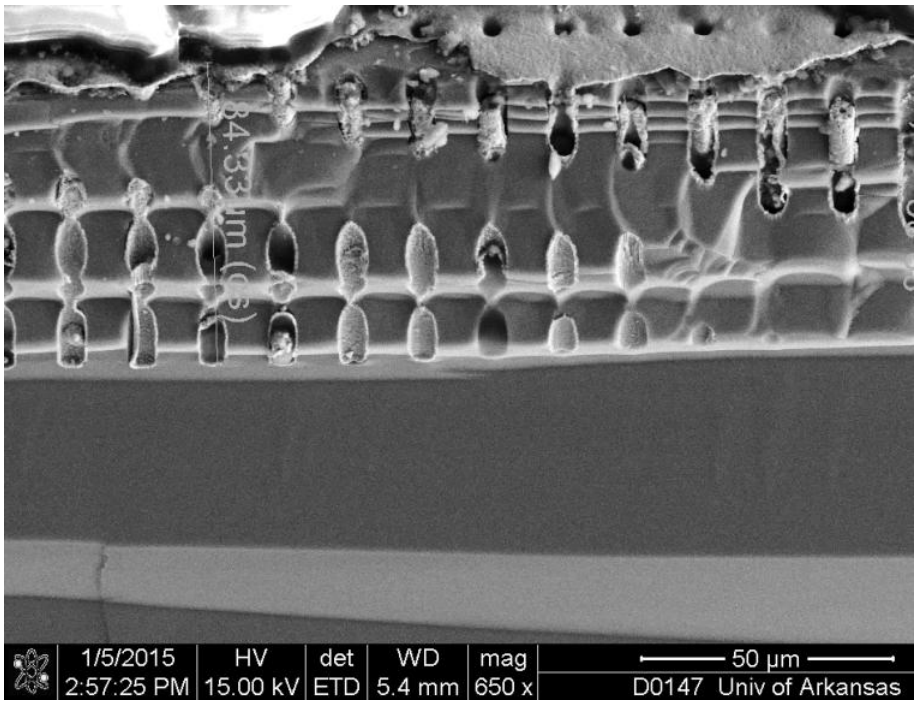

Figure 6.7. A Novalab 200 SEM micrograph of a patterned Si-Cu sample tilted 45° from vertical. The sample had a 6 µm outer pore diameter, 2.5 µm thick Cu, and lubricant deposited on the Cu film. The electroless Cu deposition penetrated to the depth of 84.3 µm (*Image from the author*).

Imaging using the Novalab 200 SEM was performed on a sample that had Cu film deposited approximately 2.5 µm thick. The sample also had lubricant applied and baked at 300°C on the Cu film to determine whether the lubricant had penetrated the depth of the pores during one of the trials. Sample cleaving was necessary for viewing the pore profiles. During cleaving, some of the pore's film structures were unavoidably destroyed. The sample had a pore depth of 84.3 µm and outer pore diameter of 6 µm. The depth reading is shown in the image of Figure 6.7. Closer examination of the image revealed the reduction of the inner pore diameter toward the 0.5 µm diameter which was the ultimate objective of the film deposition in 6 µm diameter pores. The main objective of this image, however, was to show the success achieved in depositing Cu film into the narrowest and deepest pores where the sputtering technique had failed. A question to be answered is, "How does one confirm the presence of Cu other than visually"?

A patterned Si-Cu sample was selected to perform SEM imaging and energy dispersive X-ray (EDX) spectroscopy. To stimulate the emission of X-rays from the sample, an incident, high-energy beam of charged electrons was focused onto the sample. Atoms at rest within the sample contained a ground state of electrons in discrete electron shells bound to the nucleus. The incident beam excited an electron in an inner shell and ejected it from the shell, thus creating an electron hole where that electron was located. An electron from a higher-energy outer shell then filled the hole. The difference in energy between the higher-energy shell and the lower energy shell was released in the form of an X-ray. The energy of the emitted X-rays was measured by a spectrometer. Because the energy of the X-rays was the difference in energy between the two shells and the atomic structure of the element from which they were initially emitted, this allowed the elemental composition of the sample to be determined.

The Cu film was overlaid by testing lubricant and baked dry because liquids were not allowed in the SEM. The SEM and EDX images are shown in Figures 6.8a and b.

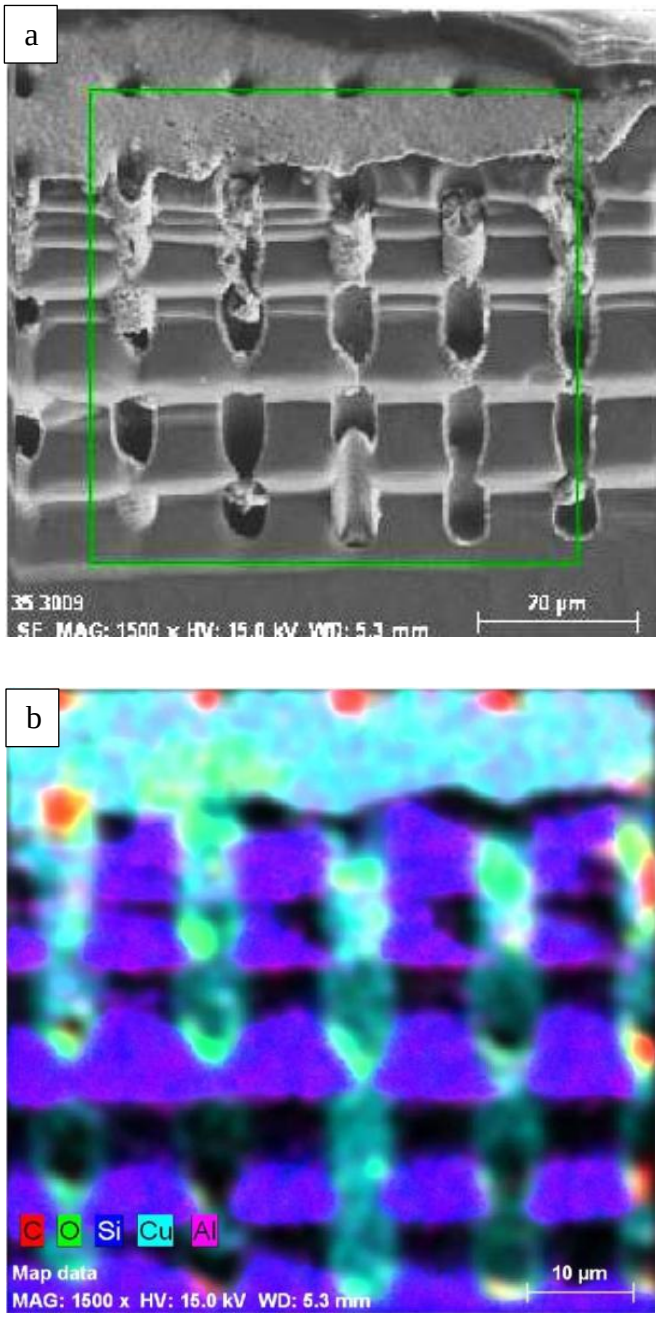

Figures 6.8a and b. (a) Energy dispersive X-ray spectroscopy was employed using the Novalab 200 SEM to determine (b) the elemental composition of the pore cross-sections (*Images from the author*).

The SEM image of Figure 6.8a was used to create the EDX image in Figure 6.8b. Note the green rectangle in Figure 6.7a. It encompassed the region of interest (ROI) and defined the border of the image in Figure 6.8b. The elements that composed the sample are shown in Figure 6.8b. They are C (carbon), O (oxygen), Si (silicon), Cu (copper), and Al (aluminum), and each element is color-coded to aid in its identification.

There was no Al used in the composition of the Si-Cu composites. It was determined that the detected Al came from the sample mounting stage which was constructed from it. According to the elemental composition of the sample, Cu film was present along the full depth of the pores and was prominent on the surface surrounding the pore openings. Si was present around the profile of the pores. There was also some C detected in the pore openings. The C indicated the presence of baked lubricant. The O element was deemed to be present everywhere in our atmosphere and so it was not of any consequence in the composition of the samples.

Having positively identified Cu film, the task now was to show it deposited in the 25, 50, and 75 μm pore depths. The straightness of the pores was on full display with the addition of Cu film. In a way, the straightness made the application of the Cu film more difficult because of the potential adhesion issues, but it made the physical structures and modeling of them accurate in the research. Since the structural complexity of the pores was still low, the opportunity to collect SEM images of Cu film in the pores was the best accomplished now. Fortunately, the sample cleaving process did not destroy the pore structures completely. The SEM images of the 3 pore depths are shown in Figures 6.9 – 6.11. Figure 6.9 is an image of the 25 μm pore depth that included Cu film.

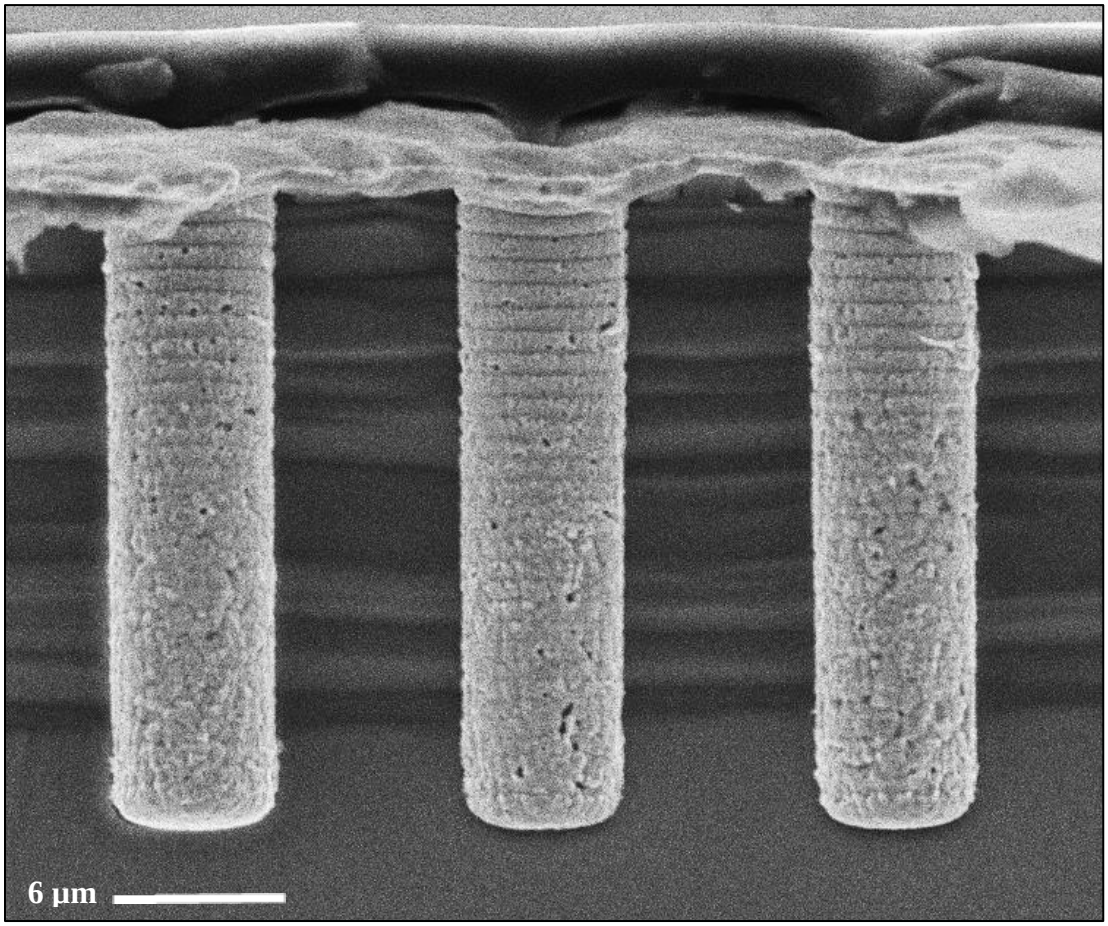

Figure 6.9. A JEOL SEM micrograph of Cu film deposited inside of c-Si pores having a 6 µm outer diameter and 25 µm depth (*Image from the author*).

The appearance of the Cu film is uniform. As proof of this, notice that the Cu film covered the corrugations along the outer side wall well, indicating a conformal film was achieved. The conformity aids in the transfer of heat to the testing lubricant. Section 4.3.2 also provided a few SEM images of the results of the electroless Cu process and they also corroborate the close fitment of Cu film to the c-Si pore walls.

Figure 6.10 is a SEM image of Cu film deposited in pores 50 µm deep. These pores proved to be the ideal pores in terms of the uniformity of the physical structure.

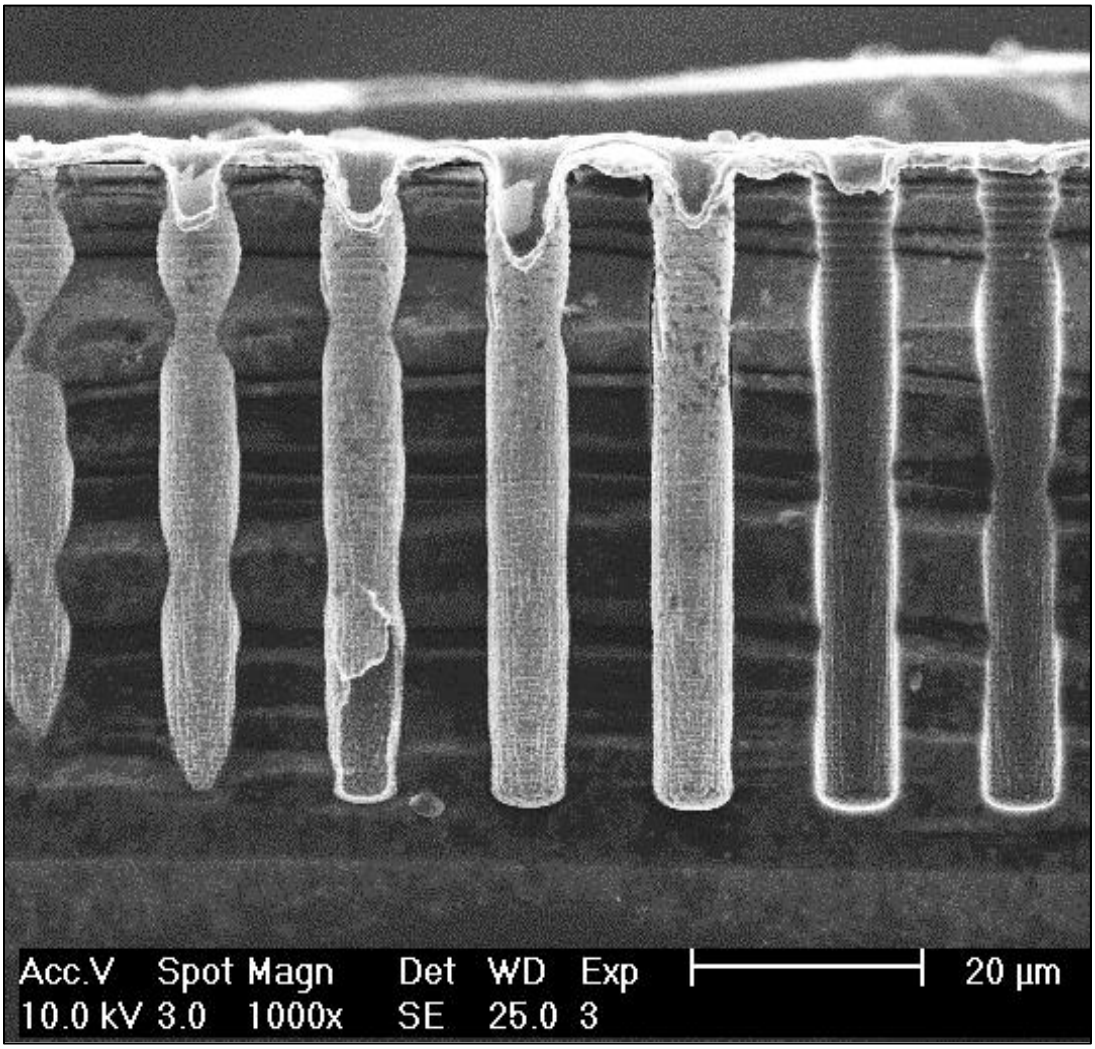

Figure 6.10. A SEM micrograph of Cu film deposited inside of c-Si pores having a 6 µm outer diameter and 50 µm pore depth (*Image from the author*).

As the pore depth increased, the ability to capture images of Cu film that penetrated the full pore depth became difficult to achieve. This was because cleaving the samples to obtain the profiles typically resulted in partial removal of the film. The missing film provided good opportunities, however, to demonstrate the difference in Cu film and the c-Si pores it filled. The Cu film was conformal to the c-Si pore wall as demonstrated by the corrugations in the SEM image.

Figure 6.11 is a SEM image of Cu deposited in a 75 µm deep pore.

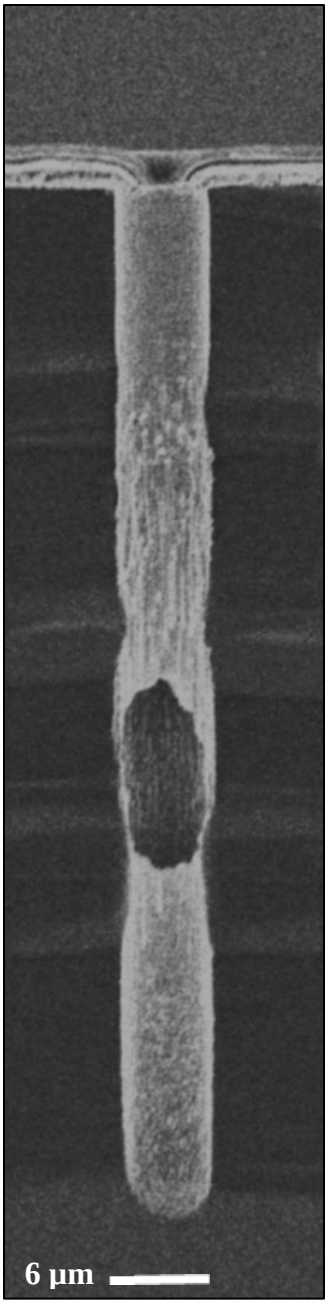

Figure 6.11. A JEOL SEM micrograph of Cu film deposited in a 6 µm outer diameter pore having 75 µm depth (*Image from the author*).

The image in Figure 6.11 was captured using the JEOL 6335 SEM. This pore depth was the most difficult to deposit Cu film inside of them. It was rare to find contiguous film along this

pore depth. Other examples of Cu film inside the 75 µm pore depth are provided later in section 6.2.3.

6.2.3 SEM Imaging of a-Si:H Film

The deposition of a-Si:H film was done to provide a surface chemistry modification to Cu film. The interest in a-Si:H film was to use it as a material that enhanced the attraction of lubricant. The a-Si:H film is shown in 25 µm deep pores in Figures 6.12a.

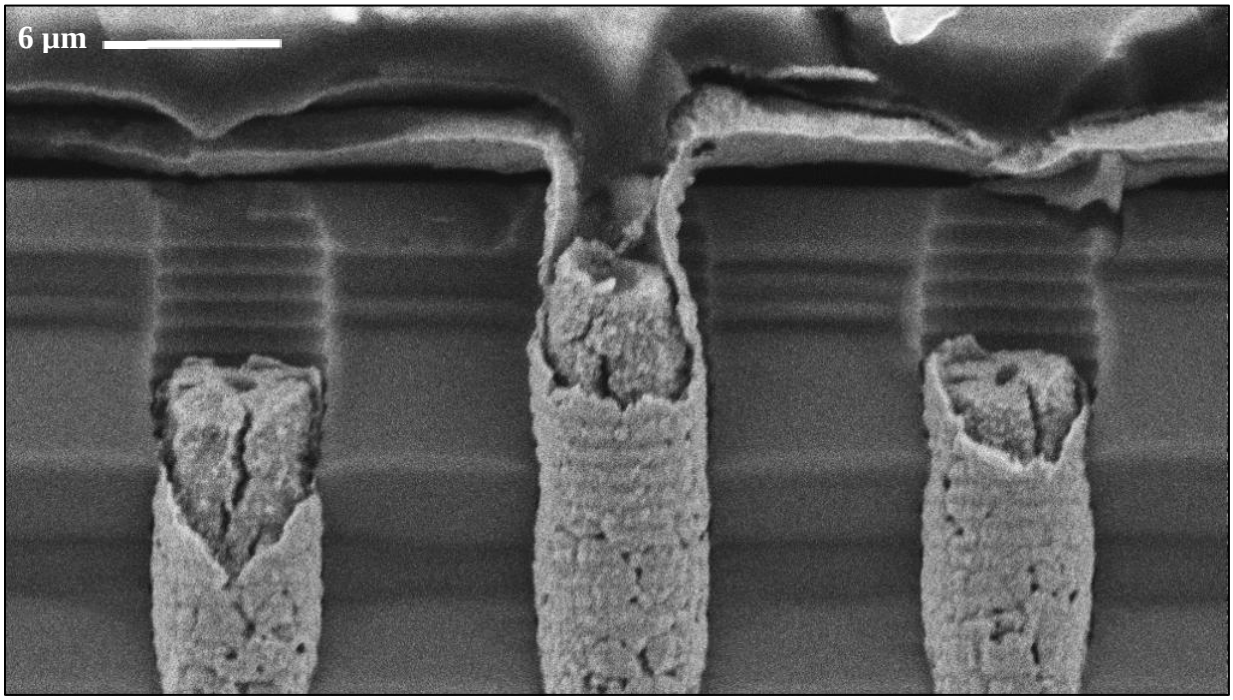

Figure 6.12a. The pores shown here had a-Si:H film inside of them. The pore diameter is 0.875 µm and the pore depth is 25 µm (*Image from the author*).

The a-Si:H film decreased the diameter of the pores toward the 0.5 µm final pore diameter. It was found that the pore diameter, after including a-Si:H film, was approximately 0.875 µm in this SEM image. This image represented the top half of 25 µm deep pores. Figure 6.11b shows the bottom portion of a pore having a-Si:H film.

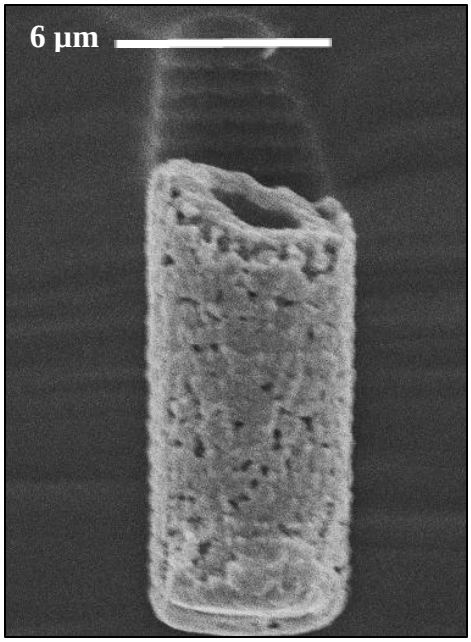

Figure 6.12b. Bottom portion of a pore having 2.5 µm thick Cu film, 250 nm thick a-Si:H film, and 25 µm depth (*Image from the author*).

Figures 6.13a and b and Figures 6.14a and b show the results of depositing a-Si:H film in the 50 and 75 µm pore depths, respectively. The samples having a-Si:H film were generally identified by the thin annular film deposited on Cu film. The a-Si:H film exhibited a darker color that distinguished it from the Cu film upon which it was deposited. The inner pore diameter was not reduced, according to these SEM images, as effectively as those of 25 µm pore depths. The cause of this was the thinning of the Cu film as the pores became deeper. The a-Si:H film thickness was fairly consistent regardless of the pore depth, however. The a-Si:H film did not appear to have issues reaching the full depth of the narrowest and deepest pores. This was because the deposition process for a-Si:H film was chemical vapor-based. The ability of the chemical vapor deposition process to penetrate locations having various dimensions and orientations was well known from previous work related to AIC of a-Si:H done by the author [46].

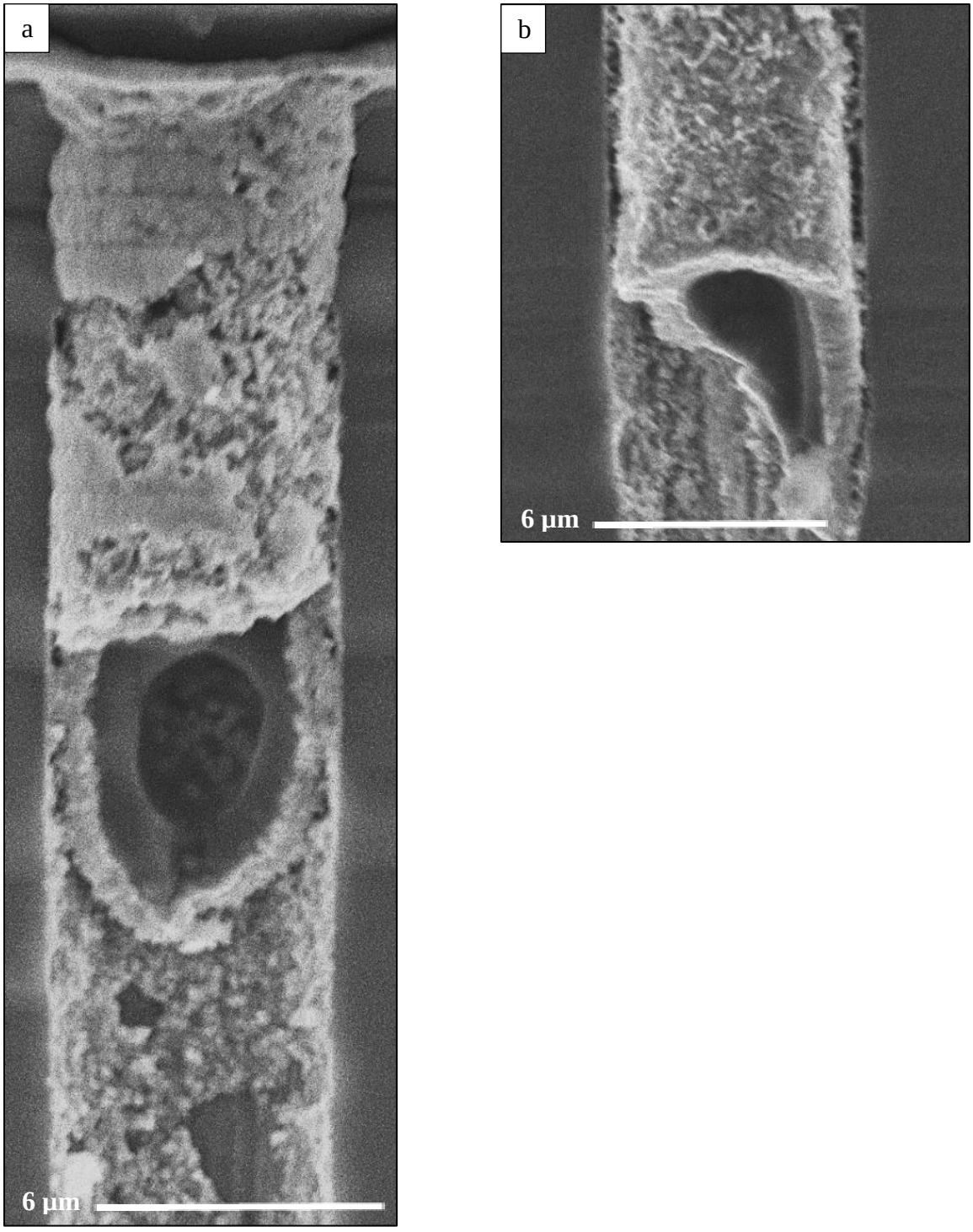

Figures 6.13a and b. Pores shown in this figure had a 6 µm outer diameter, 50 µm depth, Cu film, and 250 nm thick a-Si:H film. The a-Si:H film is identified by the dark, annular material on the inside of Cu film (*Images from the author*).

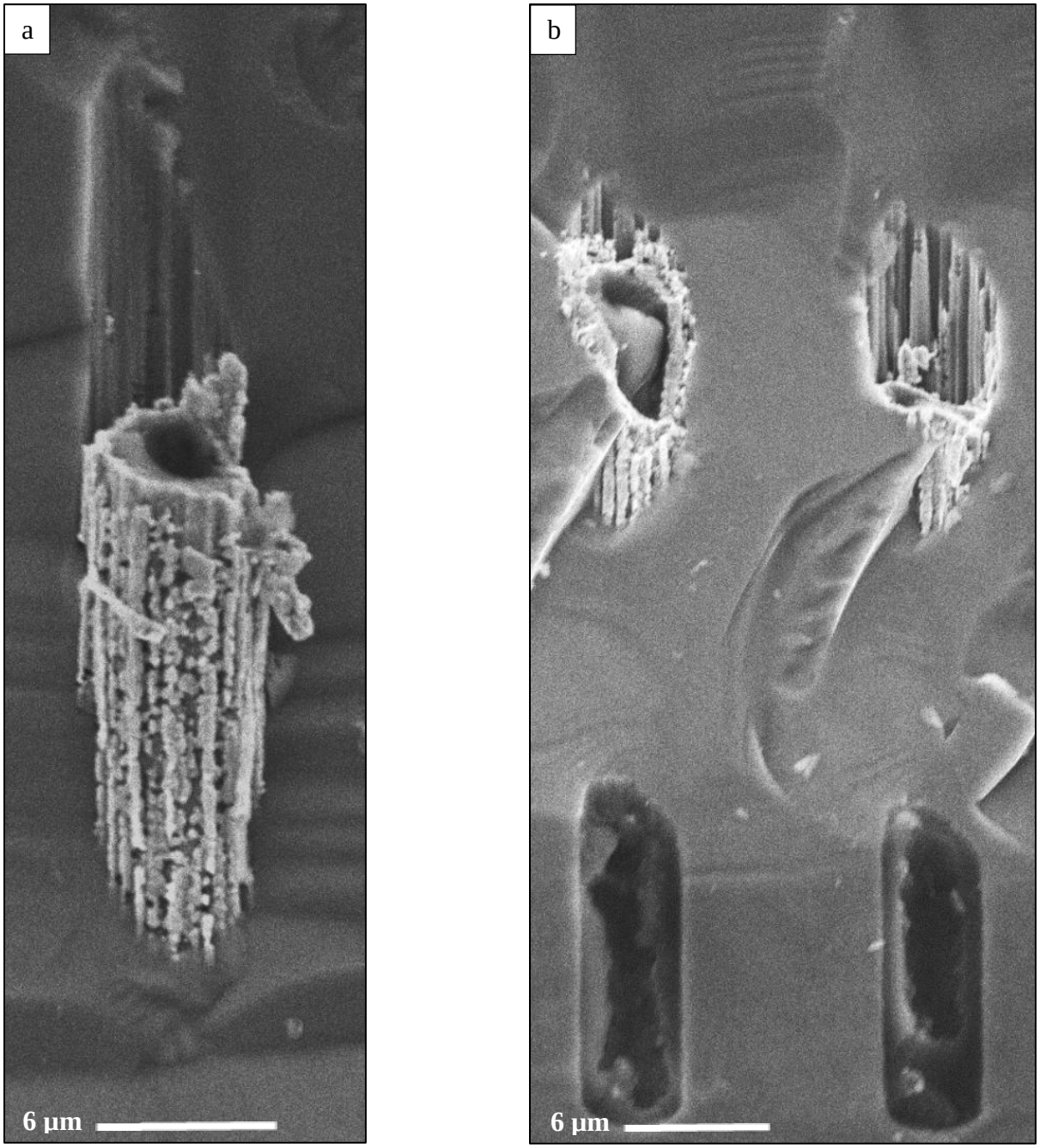

Figures 6.14a and b. Both (a) and (b) show 6 µm outer diameter, 75 µm depth pores featuring Cu film and 250 nm thick a-Si:H film. The grass-like features on the pore walls in (b) were unique to this pore depth due to the difficulty of removing the DRIE etching by-products as the pores became deeper. The Cu film filled the irregularities well to form a conformal surface to c-Si (*Images from the author*).

More proof is provided for the penetration of a-Si:H film in the 75 µm pores. Figure 6.15a shows a pore having Cu film beside a pore with Cu and a-Si:H films. Figure 6.15b illustrates thin Cu film around the pore opening and a-Si:H film inside of them. Cleaving the sample removed some of the films.

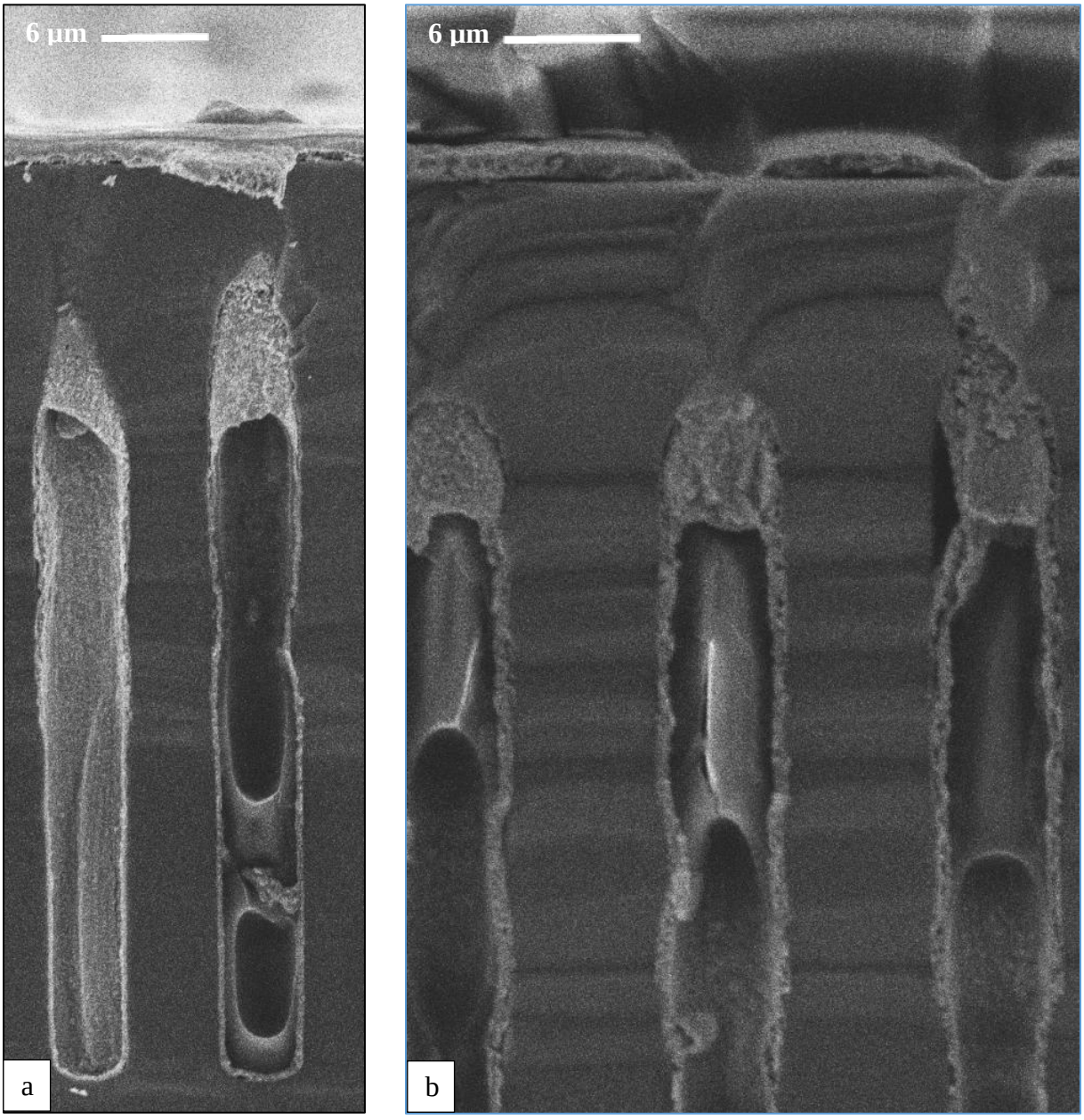

Figures 6.15a and b. Both (a) and (b): The pores had a 6 µm outer diameter, 75 µm depth, Cu film, and 250 nm thick a-Si:H film deposited in them (*Images from the author*).

The a-Si:H film was deposited on the surface of patterned Si-Cu samples having the 3 depths created for lubricant retention testing. Some of the pore opening achieved the 0.5 µm pore diameter while were others closed. The results are shown in Figure 6.16.

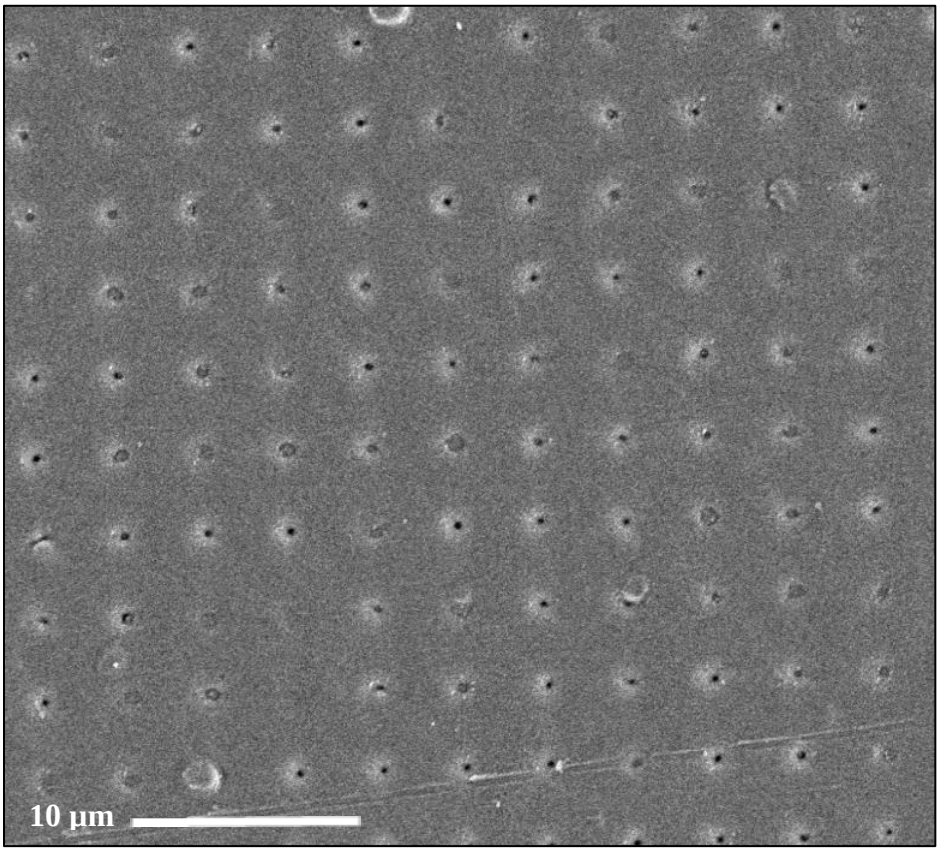

Figure 6.16. The 250 nm thick a-Si:H film was deposited on patterned Si-Cu samples (*Image from the author*).

6.2.4 SEM Imaging and Spectroscopy of Lubricant

Lubricant penetration into the pores was an important achievement for lubricant retention testing. The difficulty was primarily with the 50 and 75 µm pore depths. Various techniques such as heating the lubricant and allowing it to soak into the pores were investigated. EDX spectroscopy was used to verify the presence of lubricant in patterned Si-Cu samples. The results are shown in Figures 6.17a and b.

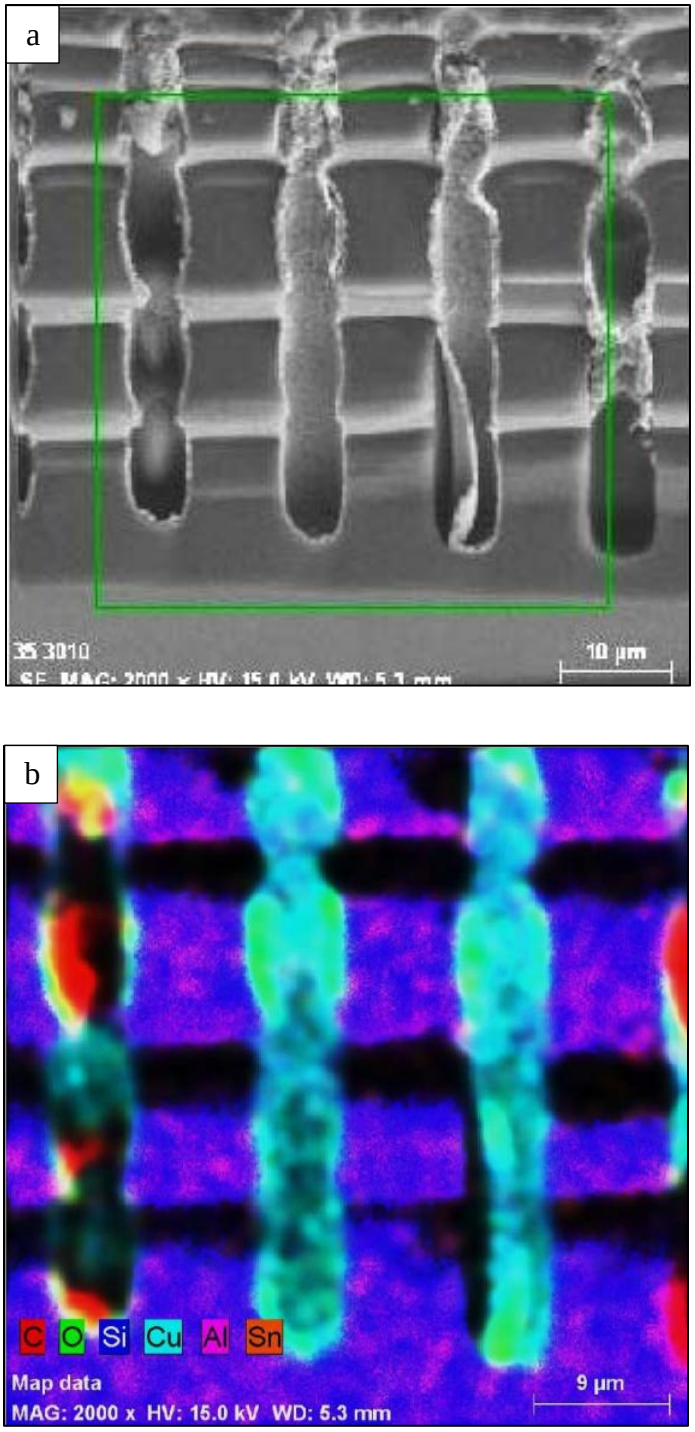

Figures 6.17a and b. Pores that featured lubricant and those that did not are demonstrated simultaneously. (a) Energy dispersive X-ray spectroscopy was employed using the Novalab 200 SEM to determine (b) the elemental composition of the pore cross-sections (*Images from the author*).

The green rectangle shows pores in the ROI in Figure 6.17a. EDX shows evidence of C along the pore depth by the red color in Figure 6.17b, whereas those pores having Cu exclusively were bluish green. The penetration of lubricant into the 75 µm depth pores is confirmed visually in Figure 6.18.

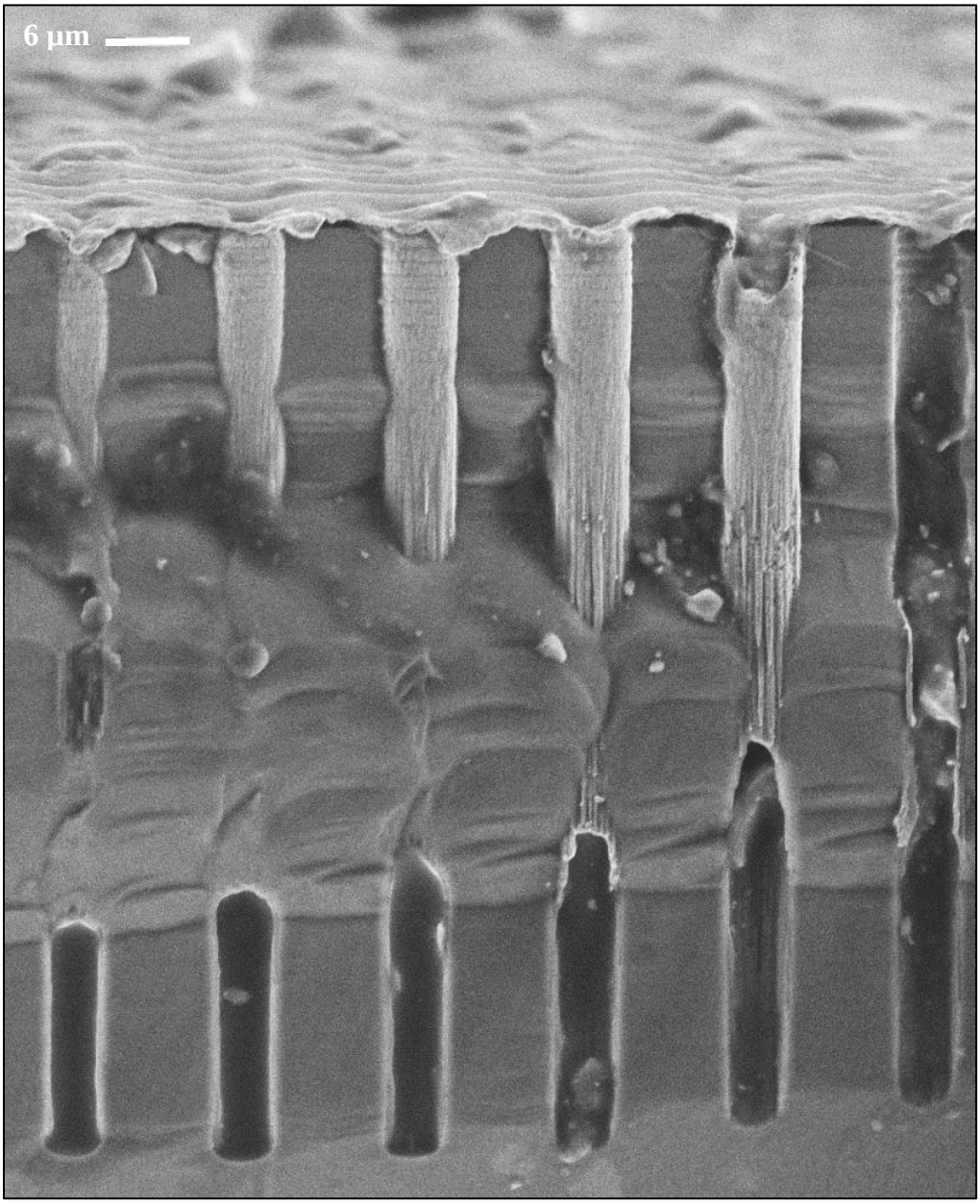

Figure 6.18. Pores having a 6 µm outer diameter, 75 µm depth, Cu film, and 3-n-One™ penetrating oil in them (*Image from the author*).

A closer look at the lubricant inside of the pores is provided in Figure 6.19.

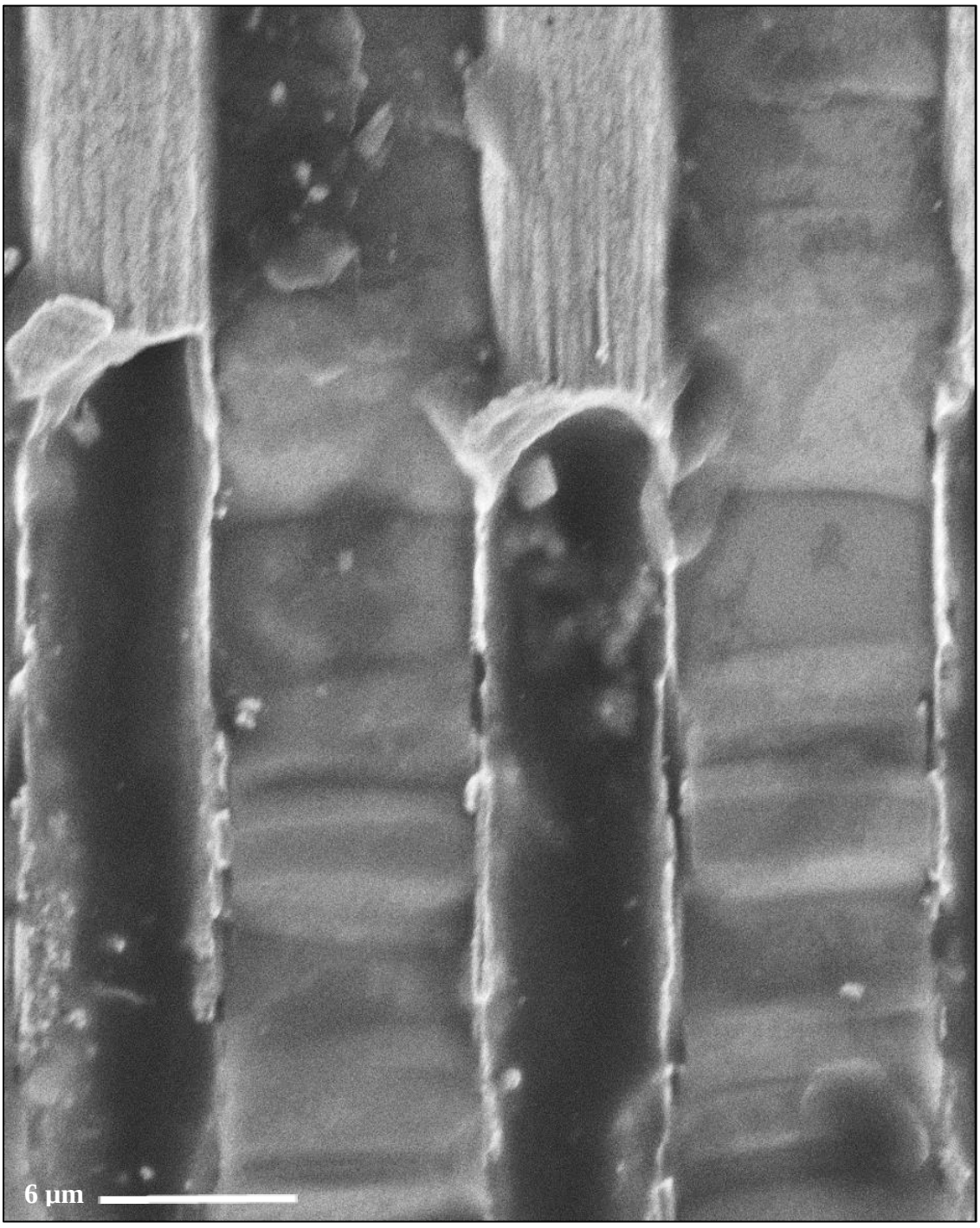

Figure 6.19. Pores having a 6 µm outer diameter, 75 µm depth, Cu film, and 3-IN-ONE™ penetrating oil along the wall (*Image from the author*).

The pores shown in Figure 6.20 are ones that have a-Si:H film and lubricant deposited in them. The opportunity to obtain comprehensive images that differentiated the Cu and a-Si:H films in addition to the baked lubricant was difficult due to the destructive nature of sample cleaving.

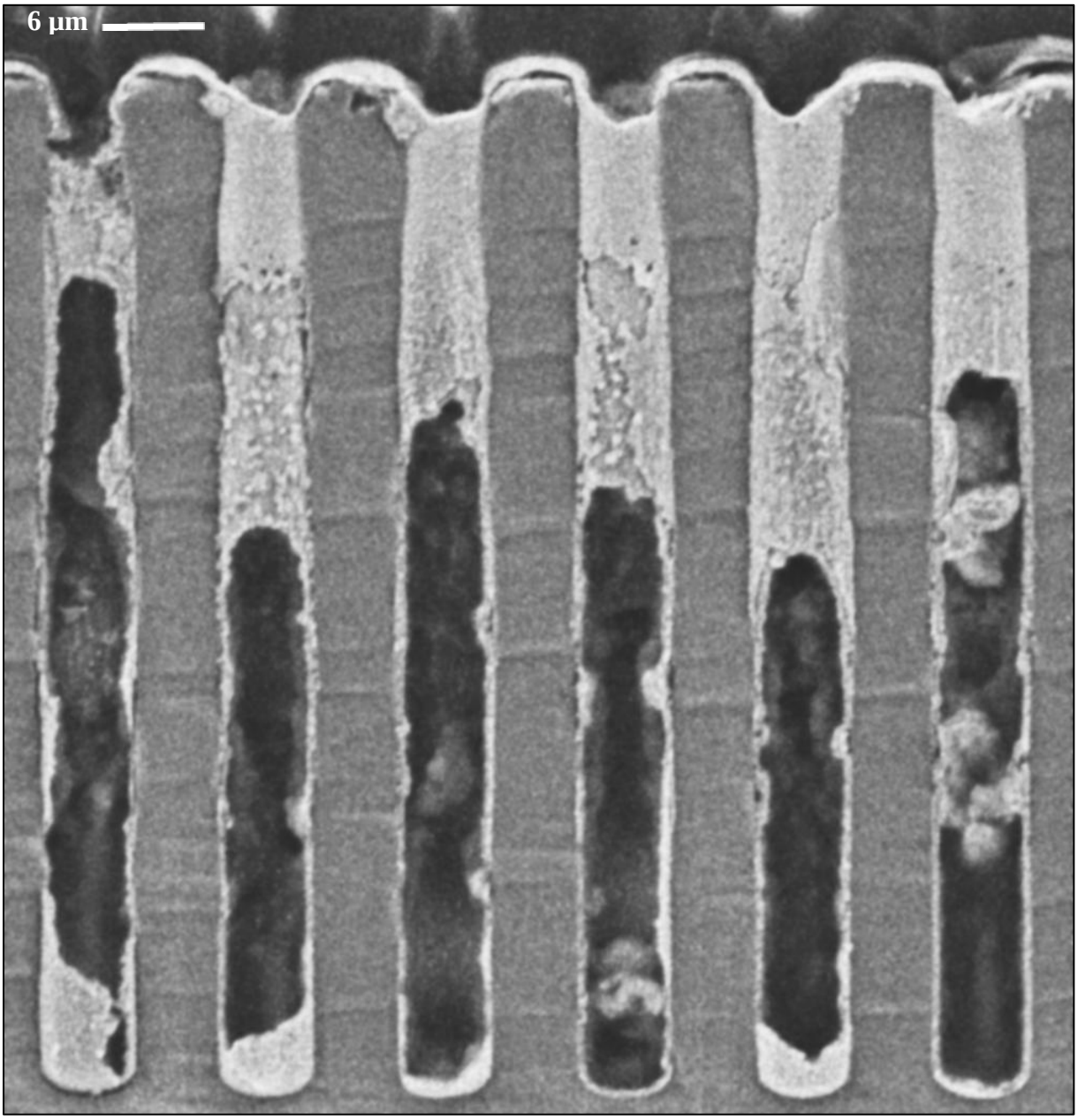

Figure 6.20. Pores having 6 µm diameter, 75 µm depth, Cu film, 250 nm thick a-Si:H, and 3-IN-ONE™ penetrating oil. The a-Si:H film and lubricant were difficult to differentiate during imaging (*Image from the author*).

In summary, electroless Cu was a solution to the problem of Cu deposition in the deepest pores. Cu film was deposited to a depth of 84.3 μm during a trial for determining the penetration of electroless Cu. The intended thickness of ≈2.5 μm was achieved in some instances. The majority of the objectives regarding Cu film were achieved for the shallowest depth. It was noticed that as the pore depth increased, the Cu film became thinner. This had an effect on the final pore diameters. To be fair, the thickness was not able to be determined in-situ (as the deposition was occurring) which made achieving the ideal thickness difficult. In addition, the electroless Cu deposition was outsourced to a service that may not have had the strict quality controls in place to ensure the thickness was reached for both pore diameters. Nonetheless, the process produced smooth pore structures and diameters that could provide information concerning the trends of lubricant retention behavior of patterned Si-Cu samples.

The a-Si:H film, on the other hand, was consistent for the 2 pore diameters and 3 pore depths. Chemical vapor deposition of the film benefited its uniform presence on the vertical pore walls. The film was for the creation of patterned Si-Cu/a-Si:H samples. Several figures were provided in this chapter that demonstrated the presence of a-Si:H film in the narrowest diameter and deepest pores. The expectation was the films (Cu and a-Si:H) were the most difficult to deposit in these sample geometries. The same challenge was faced in the goal to have lubricant penetrate the deepest pore depths. These challenges were overcome and lubricant retention testing was able to proceed.

CHAPTER 7

RESULTS AND DISCUSSION OF EVAPORATION MODELS AND TESTS

7.1 Overview of Results and Discussion

Physical, chemical, and thermodynamic changes occurring simultaneously during evaporation made precise characterization of the process too difficult. However thermodynamics-based numerical modeling of steady state conditions support a means to predict trends related to the thermal behavior of Si-Cu composite samples and indicates the potential of various topographies to enhance lubricant retention. Numerical models for the 3 modes of heat transfer encountered in this research were proposed in sections 5.1.1 - 5.1.3 to describe the thermodynamic behavior of the composites. The results of the models as well as their predictions regarding the retention of lubricant are presented in sections 7.1.1 - 7.1.4.

In addition to the fabrication of various smooth and nano-porous sample configurations, a-Si:H surface chemistry modification was proposed as a way to affect the retention of lubricant on Si-Cu composites. An FTIR-based characterization of smooth topographies having a-Si:H film was outlined in section 5.2.1.1 for examining the number of available bonding sites between the lubricant and surface. Tests related to the bonding theory were conducted. The results are presented throughout section 7.2. Finally, as a comparative tool to test the predictions of the numerical modeling on lubricant evaporation, extensive testing of the smooth and nano-porous Si-Cu composites was performed. The results are presented and discussed in section 7.3.

7.1.1 Conduction Heat Transfer Modeling Results

Conduction heat transfer modeling was the most complicated of the three modes of heat transfer. This was true because there were two final pore diameters of 0.5 and 1 μm, 3 pore depths of 25,

50, and 75 μm, and those porous topographies featured surfaces with and without a-Si:H chemistry modification. The porous topographies created without the a-Si:H surface chemistry had a 0.25 μm thicker Cu film to compensate for the exclusion of a-Si:H film for favorable comparison to the topographies having a-Si:H film. As a consequence, the segments shown in section 5.1.1 comprising the nano-pores had significant dimensional changes to consider. Then, there were 3 testing temperatures. Considering that 3 samples were created for testing each type of nano-porous topography, this brought the total sample count to 108.

For the smooth topographies, there were 2 types of samples produced for testing: samples that had c-Si overlaid by a Cu film 2.75 μm thick to account for the omission of a-Si:H film, and samples having c-Si overlaid by 2.5 μm Cu film which was then overlaid with a-Si:H film 0.25 μm thick as a surface chemistry modifier. Each type of smooth Si-Cu sample accommodated 3 equivalent lubricant depths that accounted for the amount of lubricant inside of the pores plus a thickness of 1 μm above the pore array. There were 2 pore diameters to consider for the equivalent lubricant calculations. As was done for the nano-porous topographies, 3 samples were used for each test and there were 3 testing temperatures, which brought the total smooth sample count to 108.

The thermal resistance, R_T, and heat transfer tables for smooth and nano-porous topographies appearing throughout this section were included to facilitate easier comparison of the topographies as the discussion moved toward determining the total required heat, *I*, and heat transferred, *Q*, via conduction. The sample calculations provided in this section are helpful to explain the methodology for determining *I* of an entire pore array and *Q* for smooth topographies. Actual values were used in *I* and *Q* calculations. Some of the values in the tables, however, were rounded to conserve table space. The references to the particular segments in the

tables were taken from their numerical designations in Figure 5.1. The captions for Tables 7.1 - 7.6 provide brief explanatory information identifying the sample geometries under consideration. A discussion of the table results is provided after presentation of the tables.

Table 7.1. Calculations for the thermal resistances of the segments of topographies having 0.5 and 1 μm final pore diameters, 25 μm depth, and including a-Si:H surface chemistry modification.

0.5 μm pore diameter, 25 μm depth with a-Si:H surface chemistry modification										
Segments	**c-Si**	**1**	**2**	**3**	**4**	**5**	**6**	**7**	**8**	**9**
Material Type	Si	Si	Cu	Cu	a-Si:H	Cu	a-Si:H	a-Si:H	Oil	Oil
Thickness (μm)	615	25	2.5	22.5	25.25	2.5	0.25	0.25	25	1
Cross-Section Area (μm^2)	98	83.9	14.14	13.74	0.295	97.6	97.6	0.0982	0.0982	98
R_T (°C/W)	40227	1910	442.1	4094	3.29 E+07	64.03	985.1	9.79 E+05	1.89 E+09	7.58 E+04
1 μm pore diameter, 25 μm depth with a-Si:H surface chemistry modification										
Segments	**c-Si**	**1**	**2**	**3**	**4**	**5**	**6**	**7**	**8**	**9**
Material Type	Si	Si	Cu	Cu	a-Si:H	Cu	a-Si:H	a-Si:H	Oil	Oil
Thickness (μm)	615	25	2.5	22.5	25.25	2.5	0.25	0.25	25	1
Cross-Section Area (μm^2)	98	81.4	16.59	15.71	0.491	97.1	97.1	0.393	0.393	98
R_T (°C/W)	40227	1969	376.7	3581	1.98 E+07	64.36	990.1	2.45 E+05	4.72 E+08	7.58 E+04

Table 7.2. Calculations for the thermal resistances of the segments of topographies having 0.5 and 1 μm final pore diameters, 25 μm depth, without a-Si:H surface chemistry modification.

0.5 μm pore diameter, 25 μm depth without a-Si:H surface chemistry modification							
Segments	**c-Si**	**1**	**2**	**3**	**5**	**8**	**9**
Material Type	Si	Si	Cu	Cu	Cu	Oil	Oil
Thickness (μm)	615	25	2.75	22.25	2.75	25	1
Cross-Section Area (μm^2)	98	83.9	14.14	14.04	97.9	0.0982	98
R_T (°C/W)	40227	1910	486.3	3962	70.22	1.98 E+09	7.58 E+04
1 μm pore diameter, 25 μm depth without a-Si:H surface chemistry modification							
Segments	**c-Si**	**1**	**2**	**3**	**5**	**8**	**9**
Material Type	Si	Si	Cu	Cu	Cu	Oil	Oil
Thickness (μm)	615	25	2.75	22.25	2.75	25	1
Cross-Section Area (μm^2)	98	81.4	16.59	16.2	97.6	0.393	98
R_T (°C/W)	40227	1969	414.4	3434	70.44	4.72 E+08	7.58 E+04

Table 7.3. Calculations for the thermal resistances of the segments of topographies having 0.5 and 1 μm final pore diameters, 50 μm depth, and including a-Si:H surface chemistry modification.

0.5 μm pore diameter, 50 μm depth with a-Si:H surface chemistry modification										
Segments	**c-Si**	**1**	**2**	**3**	**4**	**5**	**6**	**7**	**8**	**9**
Material Type	Si	Si	Cu	Cu	a-Si:H	Cu	a-Si:H	a-Si:H	Oil	Oil
Thickness (μm)	590	50	2.5	47.5	50.25	2.5	0.25	0.25	50	1
Cross-Section Area (μm^2)	98	83.9	14.14	13.74	0.295	97.6	97.6	0.0982	0.0982	98
R_T (°C/W)	38592	3820	442.1	8643	6.55 E+07	64.03	985.1	9.79 E+05	3.78 E+09	7.58 E+04
1 μm pore diameter, 50 μm depth with a-Si:H surface chemistry modification										
Segments	**c-Si**	**1**	**2**	**3**	**4**	**5**	**6**	**7**	**8**	**9**
Material Type	Si	Si	Cu	Cu	a-Si:H	Cu	a-Si:H	a-Si:H	Oil	Oil
Thickness (μm)	590	50	2.5	47.5	50.25	2.5	0.25	0.25	50	1
Cross-Section Area (μm^2)	98	81.4	16.59	15.71	0.491	97.1	97.1	0.393	0.393	98
R_T (°C/W)	38592	3938	376.7	7559	3.94 E+07	64.36	990.1	2.45 E+05	9.45 E+08	7.58 E+04

Table 7.4. Calculations for the thermal resistances of the segments of topographies having 0.5 and 1 µm final pore diameters, 50 µm depth, without a-Si:H surface chemistry modification.

0.5 µm pore diameter, 50 µm depth without a-Si:H surface chemistry modification							
Segments	**c-Si**	**1**	**2**	**3**	**5**	**8**	**9**
Material Type	Si	Si	Cu	Cu	Cu	Oil	Oil
Thickness (µm)	590	50	2.75	47.25	2.75	50	1
Cross-Section Area (μm^2)	98	83.9	14.14	14.04	97.9	0.0982	98
R_T (°C/W)	38592	3820	486.3	8413	70.22	3.78 E+09	7.58 E+04
1 µm pore diameter, 50 µm depth without a-Si:H surface chemistry modification							
Segments	**c-Si**	**1**	**2**	**3**	**5**	**8**	**9**
Material Type	Si	Si	Cu	Cu	Cu	Oil	Oil
Thickness (µm)	590	50	2.75	47.25	2.75	50	1
Cross-Section Area (μm^2)	98	81.4	16.59	16.2	97.6	0.393	98
R_T (°C/W)	38592	3938	414.4	7292	70.43	9.45 E+08	7.58 E+04

Table 7.5. Calculations for the thermal resistances of the segments of topographies having 0.5 and 1 μm final pore diameters, 75 μm depth, and including a-Si:H surface chemistry modification.

0.5 μm pore diameter, 75 μm depth with a-Si:H surface chemistry modification

Segments	**c-Si**	**1**	**2**	**3**	**4**	**5**	**6**	**7**	**8**	**9**
Material Type	Si	Si	Cu	Cu	a-Si:H	Cu	a-Si:H	a-Si:H	Oil	Oil
Thickness (μm)	565	75	2.5	72.5	75.25	2.5	0.25	0.25	75	1
Cross-Section Area (μm^2)	98	83.9	14.14	13.74	0.295	97.6	97.6	0.0982	0.0982	98
R_T (°C/W)	36957	5730	442.1	13191	9.81 E+07	64.03	985.1	9.79 E+05	5.67 E+09	7.58 E+04

1 μm pore diameter, 75 μm depth with a-Si:H surface chemistry modification

Segments	**c-Si**	**1**	**2**	**3**	**4**	**5**	**6**	**7**	**8**	**9**
Material Type	Si	Si	Cu	Cu	a-Si:H	Cu	a-Si:H	a-Si:H	Oil	Oil
Thickness (μm)	565	75	2.5	72.5	75.25	2.5	0.25	0.25	75	1
Cross-Section Area (μm^2)	98	81.4	16.59	15.71	0.491	97.1	97.1	0.393	0.393	98
R_T (°C/W)	36957	5906	376.7	11537	5.89 E+07	64.36	990.1	2.45 E+05	1.417 E+09	7.58 E+04

Table 7.6. Calculations for the thermal resistances of the segments of topographies having 0.5 and 1 µm final pore diameters, 75 µm depth, without a-Si:H surface chemistry modification.

0.5 µm pore diameter, 75 µm depth without a-Si:H surface chemistry modification							
Segments	**c-Si**	**1**	**2**	**3**	**5**	**8**	**9**
Material Type	Si	Si	Cu	Cu	Cu	Oil	Oil
Thickness (µm)	565	75	2.75	72.25	2.75	75	1
Cross-Section Area (μm^2)	98	83.9	14.14	14.04	97.9	0.0982	98
R_T (°C/W)	36957	5730	486.3	12865	70.22	5.67 E+09	7.58 E+04
1 µm pore diameter, 75 µm depth without a-Si:H surface chemistry modification							
Segments	**c-Si**	**1**	**2**	**3**	**5**	**8**	**9**
Material Type	Si	Si	Cu	Cu	Cu	Oil	Oil
Thickness (µm)	565	75	2.75	72.25	2.75	75	1
Cross-Section Area (μm^2)	98	81.4	16.59	16.2	97.6	0.393	98
R_T (°C/W)	36957	5906	414.4	11150	70.43	1.417 E+09	7.58 E+04

An analysis of the R_T values in Tables 7.1, 7.3, and 7.5 revealed some noteworthy trends. First, it should be explained that segment *9* was excluded from the discussion regarding the change in R_T values because the lubricant cross-sectional area of this segment remained constant regardless of the geometric changes that occurred when forming the pores. Segment *9*'s cross-section was the 7 μm x 14 μm area located above the half pore. During evaporation testing, segment *9*'s cross-sectional area was assumed to remain uniform in association with the geometric symmetry of the 6.35 mm x 19.05 mm testing area's cross-section and even distribution of the heat fluxes in the segment. The actual thickness of this segment undoubtedly changed as the excess lubricant's volatile constituents were driven off via thermal evaporation. The change in thickness was addressed by accounting for the loss in lubricant mass during evaporation testing. After the excess lubricant was driven away, however, there remained an oil film on the surface that was approximated as 1 μm thick. In addition to this observation, one can make the assumption that the amount of lubricant (typically 1 μm between sliding surfaces) will be replenished during the normal operation of machinery. Therefore, the thickness value of 1 μm was considered to remain constant for modeling purposes.

Other noteworthy trends were observed. For example when the pore depth was constant and there was a change in pore diameter, the thickness (height) of the segments of nano-porous topographies remained unchanged. The changes in R_T were apparent when examining the values of segments *1*, *3*, *4*, and *8* as the pore depth changed and the diameter was held to a constant value. The pore segment thickness only changed if the depth was altered such as when the etch depth into *c-Si* increased from 25 μm to either of the other depths of 50 or 75 μm. The *c-Si* R_T value varied indirectly to the change in thickness and not the diameter. As the pore depth increased, more material was removed from the *c-Si* segment, effectively reducing the thickness

of the segment. Less thickness translated to lower resistance to heat transfer as was demonstrated by the lower R_T values for the *c-Si* segment in Tables 7.1, 7.3, and 7.5. Although the change in thickness was an important variable affecting R_T, one must also consider the other variable affecting R_T, the pore diameter, to fully understand how the geometry affected R_T.

If the pore diameter changed from 0.5 to 1 μm, there was a direct change in R_T for some segments. The R_T values of all segments except *c-Si* and *9* were affected when the diameter was allowed to change and the depth was held to a constant value. Excluding segments *c-Si* and *9*, the other segment's cross-sectional areas had a dependent relationship on the diameter of the pore, whether it was the increase in the annulus cross-sectional area as happened with segments *3* and *4*, or the increase in the diameter (and cross-sectional area) that occurred with segments *2*, *7*, and *8*, or even the decrease in the cross-sectional area of segments *1*, *5*, and *6*—again, these changes occurred as the final pore diameter increased from 0.5 to 1 μm. Segments *c-Si* and *9*, as partitioned in Figure 5.1, lie below and above the pore array, respectively, so their cross-sectional areas and R_T values were not impacted by the diameter change in the same manner as other segments.

The R_T values of segments *2*, *7*, and *8* on the other hand, were adversely affected by the increase in diameter. As the diameter increases and the depth remains constant, these segments should distribute the same amount of heat as the smaller diameter pore but through pore segments having larger cross-sectional areas. The segments having larger cross-sectional areas had a reduction in their R_T values. This same reasoning applied to the annuli of segments *3* and *4*, resulting in their R_T decreases. Conversely, segments *1*, *5*, and *6* had more material removed from their cross-sections when the diameter increased, and this resulted in decreases to their cross-sectional areas. The same amount of heat that initially flowed through larger cross-

sectional areas was now constrained to smaller cross-sectional areas due to the larger pore diameter. The decreased cross-sectional areas caused the R_T values to increase.

The discussion now turns to the observations of R_T referred to in Tables 7.1, 7.3, and 7.5 concerning the nano-porous topographies without a-Si:H surface chemistry modification. Removing a-Si:H film eliminated segments *4*, *6*, and *7* from the nano-pore structures. To compensate for the change and retain the same pore sizes as the pore structures having a-Si:H segments, the thickness of the Cu segments, *2* and *5*, were increased from 2.5 to 2.75 μm, while segment *3*'s thickness was decreased by 0.25 μm. The cross-sectional areas of segments *3* and *5* were increased as well to preserve the pore geometry.

The choice of increasing the Cu film thickness was due to its easier manipulation in the nano-pore fabrication process, and of all of the materials used for Si-Cu composite formation, Cu had the highest thermal conductivity value which makes it the material least likely to negatively affect the transfer of heat through the sample. The compromise was made because it was important to preserve the ultimate objective of observing the effect of pore geometry on the retention of lubricant. Overall, the 0.25 μm increase in Cu film thickness created larger R_T values for segments *2* and *5* and smaller R_T values for segment *3*—all valid statements when comparing these segments to their counterparts having the same pore diameter and a-Si:H film included in their pore structure. The effect for the pore structures without a-Si:H film should be a heat transfer decrease for segments *2* and *5* and an increase for segment *3*. This outcome does not change the trends observed in the model already and the results anticipated for excluding the a-Si:H segments, namely, that the pore structures without a-Si:H film should require less heat per °C to produce lubricant evaporation than their counterparts having a-Si:H film.

Otherwise, the nano-pore structures without a-Si:H segments behaved similarly to those with the segments in terms of the effect of the change in geometry on the R_T values in Tables 7.1, 7.3, and 7.5. When the diameter was constant and the pore depth increased from 25 to 50 or 75 μm, the thickness of segments *1*, *3*, and *8* became greater and the change produced larger R_T values. Segments *2*, *5*, and *9* thickness values remained unchanged for a constant pore diameter, so their R_T values correspondingly did not change as the depth changed. Segment *5*'s R_T value, however, increased as the pore diameter increased (and the depth was held to a constant value) because the larger diameter removed surface area from the cross-section, therefore resulting in a R_T increase. Segments *2* and *8* cross-sectional areas increased as the pore diameter increased for a constant depth. As a consequence of the change, their R_T values decreased.

Segments *3* and *5* cross-sections were increased initially to compensate for removing the a-Si:H segments. However, increasing the pore diameter and holding the depth constant resulted in a further increase in segment *3*'s annulus cross-sectional area and a decrease in segment *5*'s cross-sectional area. Subsequently, segment *3* had a decrease in its R_T value and the value of segment *5* increased. If using a constant pore depth, the R_T value of the *c-Si* segment remained unchanged as the diameter increased from 0.5 to 1 μm. Its R_T values do respond to changes in the depth, though. Increasing the pore depth decreased the thickness of the material, resulting in smaller R_T values which decreased the *c-Si* segment resistance to heat flow.

In summary, whenever there were changes in the pore geometry, one should consider the effects that increasing or decreasing the thickness and cross-sectional area have on the segments because both can contribute to lower or higher R_T values in accordance with the segment's dependence on these variables.

Sample calculations are done using Table 7.3 R_T values from the nano-topography having a final pore diameter of 0.5 µm and depth of 50 µm to determine the R_T values as entries in the coefficient matrix [R]. Using the generalized matrices templates derived from equation (5.6), the values of each entry in the coefficient matrix [R] and constants matrix [V] of equation (5.7), are,

$$\begin{bmatrix} 12905.1 & -8643 & 0 & -442.1 \\ -8643 & 65524685.6 & -65514993.5 & 0 \\ 0 & -65514993.5 & 3846486506 & -3780971512 \\ -442.1 & 0 & -3780971512 & 3781086301 \end{bmatrix} * \begin{bmatrix} I_1 \\ I_2 \\ I_3 \\ I_4 \end{bmatrix} = \begin{bmatrix} 0 \\ 0 \\ 0 \\ 1 \end{bmatrix}$$

The *I* values were calculated to determine the amount of heat required per °C change in temperature for one half of a pore belonging to topographies having a 0.5 µm diameter, 50 µm depth, and including the a-Si:H segments. Since the conservation of energy was valid for *I* quantities, their amounts were summed for the 4 loops shown in Figure 5.3a. The results are shown in Table 7.7.

Table 7.7. The values of heat required per °C, *I* (W/°C), for loops 1 - 4 calculated for one half of a nano-pore structure with a-Si:H surface chemistry modification.

I_1 =	5.961402336E -06
I_2 =	8.467962221E -06
I_3 =	8.468428495E -06
I_4 =	8.468436576E -06
$I_1+I_2+I_3+I_4$ =	3.136622963E -05

Calculations without a-Si:H segments were simpler because of fewer segments and loops. Sample calculations were done using Table 7.3 R_T values from the nano-topography having a final pore diameter of 0.5 µm and depth of 50 µm to find the R_T values for one half of a nano-

pore. Using the generalized matrices templates derived from equation (5.6), the values of each entry in the coefficient matrix [R] and constants matrix [V] of equation (5.8), are,

$$\begin{bmatrix} 12719 & -8413 & -486.3 \\ -8413 & 3780000833 & -3779992349 \\ -486.3 & -3779992349 & 3780107227 \end{bmatrix} * \begin{bmatrix} I_1 \\ I_2 \\ I_3 \end{bmatrix} = \begin{bmatrix} 0 \\ 0 \\ 1 \end{bmatrix}$$

The *I* values determined by solving the matrix were used for calculating the amount of heat required per °C for one half of a pore belonging to topographies having a 0.5 μm diameter, 50 μm depth, and excluding the a-Si:H segments. The conservation of energy was valid for these quantities, so their amounts were summed for the 3 loops shown in Figure 5.4a. The results are shown in Table 7.8.

Table 7.8. The values of heat required per °C, *I* (W/°C), for loops 1 - 3 calculated for one half of a nano-pore structure excluding a-Si:H surface chemistry modification.

$\mathbf{I_1}$ =	5.973158839E -06
$\mathbf{I_2}$ =	8.537120489E -06
$\mathbf{I_3}$ =	8.537126356E -06
$\mathbf{I_1+I_2+I_3}$ =	2.304740568E -05

Using as a guide the methodology which determined the sample calculations, *I* values for the remaining nano-topographies were determined. The results are shown in Table 7.9.

Table 7.9. The values of heat required per °C, *I* (W/°C), calculated for one half of a nano-pore having the final diameters and depths indicated.

	Diameters Including a-Si:H		**Diameters Excluding a-Si:H**	
	0.5 µm	**1 µm**	**0.5 µm**	**1 µm**
Depth	**I (W/°C)**	**I (W/°C)**	**I (W/°C)**	**I (W/°C)**
25 µm	3.128672078E -05	3.098904029E -05	2.299748199E -05	2.267947625E -05
50 µm	3.136622963E -05	3.107783052E -05	2.304740568E -05	2.27460753E -05
75 µm	3.14442318E -05	3.116385569E -05	2.311588783E -05	2.281184962E -05

The quantities in Table 7.9 were multiplied by two to arrive at the amount of heat required by one nano-pore. The total number of nano-pores in the test area of each sample is 616,080, as calculated in section 4.2.2. Multiplying the number of nano-pores by the amount of heat required for each one gives the amount of conduction heat required for all pores per °C. Table 7.10 denotes the total heat required for each type of sample according to the evaporation testing temperature minus the room temperature.

Table 7.10. The values for total conduction heat required, *I* (W), by nano-porous topographies calculated using the 300, 350, and 400°C evaporation testing temperatures minus the room temperature.

	Evaporation Testing Temperature of 300°C			
	Diameters Including a-Si:H		**Diameters Excluding a-Si:H**	
	0.5 µm	**1 µm**	**0.5 µm**	**1 µm**
Depth	**I (W)**	**I (W)**	**I (W)**	**I (W)**
25 µm	10601.32	10500.46	7792.56	7684.8
50 µm	10628.26	10530.54	7809.48	7707.56
75 µm	10654.7	10559.69	7832.68	7729.66
	Evaporation Testing Temperature of 350°C			
	Diameters Including a-Si:H		**Diameters Excluding a-Si:H**	
	0.5 µm	**1 µm**	**0.5 µm**	**1 µm**
Depth	**I (W)**	**I (W)**	**I (W)**	**I (W)**
25 µm	12528.82	12409.62	9209.39	9082.04
50 µm	12560.67	12445.18	9229.38	9108.71
75 µm	12591.9	12479.63	9256.81	9135.05
	Evaporation Testing Temperature of 400°C			
	Diameters Including a-Si:H		**Diameters Excluding a-Si:H**	
	0.5 µm	**1 µm**	**0.5 µm**	**1 µm**
Depth	**I (W)**	**I (W)**	**I (W)**	**I (W)**
25 µm	14456.34	14318.79	10626.22	10479.28
50 µm	14493.08	14359.82	10649.29	10510.05
75 µm	14529.12	14399.57	10680.93	10540.44

There were noticeable trends associated with the calculations for each testing temperature. The nano-porous structures that included a-Si:H segments required more heat than the structures without the segments. This characteristic was observed for each testing temperature. This outcome was expected, considering that a-Si:H film had the lowest thermal conductivity of the materials used in Si-Cu composites. Its inclusion in the nano-pore structure should impede the transfer of heat. Another trend observed in the data of Table 7.10 as the temperature was held constant was the *I* for both sample types (including and excluding a-Si:H film) increased as the depth of the nano-pore increased. The reasons are segments *1* and *3* calculated in Tables 7.1 - 7.6 had R_T values that increased because of the increase in pore depth. If the topography included segment *4*, its R_T value also increased as the depth increased. The increasing resistances of segments *1*, *3*, and *4* were able to overcome any advantage had by decreasing the *c-Si* segment thickness (and its R_T) as the pore depth increased.

A trend toward decreased *I* was observed as the diameter increased from 0.5 to 1 μm. This is shown in Table 7.10 when examining the data for *I* while maintaining a constant depth and temperature. Thermal resistance decreased because the larger diameter created segments in the nano-pore structure whose cross-sectional area increased as the pore diameter increased. Segments *2* and *3* in Tables 7.1 - 7.6 are examples of such R_T increases for pore structures that both include and exclude a-Si:H film. Larger surface areas created smaller R_T values that, in turn, lead to less *I* to induce evaporation.

Observe that as the pore depth increased for a fixed 0.5 μm diameter, *I* differential values were less in magnitude than the corresponding differential values of the 1 μm pore diameter. Also, note that the differential decreased non-linearly when comparing the values of 25 μm and 50 μm depths versus the 50 μm and 75 μm depths, regardless of the diameter under consideration**.** The

depth change was linear, but *I* differential was not. The non-linearity was attributed to the squared term in the equations for the cross-sectional areas of certain segments used in the calculation of R_T. As the diameter increased, some of the segment's R_T values increased non-linearly while others decreased. The conclusion is there is more value in reducing the depth from 50 µm to 25 µm than going from 75 µm to 50 µm to reduce *I*. This trend implies there will be significantly less *I* when increasing the diameter and decreasing the depth; but, as the depth approaches zero there exists a limit to the reduction in *I*. The total *I* values were combined with the values from the other modes of heat transfer occurring at the same temperature to determine the net value reported in section 7.4.

7.1.1.1 Conduction Heat Transfer Modeling Results on Smooth Topographies

The thin film thicknesses of 2.5 and 2.75 µm for Cu and 0.25 µm for a-Si:H were retained for a sample calculation of *Q* through smooth samples. The thickness of the c-Si wafers used to produce the samples was 640 µm. Recall that the surface area used in the calculation of R_T for the smooth samples was the same as the cross-sectional area of the space located above the pores as shown in section 4.3.3. Using the *c-Si* and *Cu* thickness values which produced smooth Si-Cu topographies, the results for R_T are shown in Table 7.11.

Table 7.11. Calculation of thermal resistance, R_T (°C/W), for smooth Si-Cu topographies that excluded a-Si:H film and lubricant.

Segment Properties	**c-Si**	**Cu**
Thickness (µm)	640	2.75
Surface Area (µm^2)	120967500	120967500
R_T (°C/W)	0.033914598	5.6833447E -05

A layer of 0.25 μm thick a-Si:H film was deposited on smooth Si-Cu composites to investigate the effect of modifying the surface chemistry to enhance lubricant retention. The R_T values for this topography are shown in Table 7.12

Table 7.12. Calculation of thermal resistance, R_T (°C/W), for smooth Si-Cu topographies that included a-Si:H film but excluded the lubricant.

Segment Properties	**c-Si**	**Cu**	**a-Si:H**
Thickness (μm)	640	2.5	0.25
Surface Area (μm^2)	120967500	120967500	120967500
R_T (°C/W)	0.033914598	5.166677E -05	7.9487339E -04

The next task was to determine the volume of lubricant to deposit on smooth samples. Using the dimensions of the testing area illustrated in section 4.4.3 and the dimensions of the final pore geometries, the quantity for the total volume of lubricant in the pores plus the 1 μm depth above the pores was calculated to obtain the total volume to deposit on the surface of smooth samples. Then, the total volume was divided by the surface area of the test location which left the total thickness of the lubricant. The total thickness values were used in the calculation of the lubricant's R_T. The R_T calculations for smooth topographies are listed in Table 7.13.

Table 7.13. Thermal resistance, R_T (°C/W), values for equivalent lubricant on smooth topographies comparable to pore diameters of 0.5 and 1 μm, pore depths of 25, 50, and 75 μm, and excluding a-Si:H film.

	Pore Depths w/Final Pore Diameter of 0.5 μm		
	25 μm	**50 μm**	**75 μm**
Equivalent Lubricant Thickness+1 (μm)	1.025	1.05	1.075
Test Surface Area (μm^2)	120967500	120967500	120967500
Lubricant R_T (°C/W)	0.064439624	0.067508178	0.070576731

	Pore Depths w/Final Pore Diameter of 1 µm		
	25 µm	**50 µm**	**75 µm**
Equivalent Lubricant Thickness+1 (µm)	1.1	1.2	1.3
Test Surface Area (μm^2)	120967500	120967500	120967500
Lubricant R_T (°C/W)	0.073645285	0.085919499	0.098193713

The thickness value for the lubricant revealed an interesting outcome for 616,080 nano-pores having a 0.5 µm diameter and 25 µm depth, namely that the total amount of lubricant in the nano-pores would cover the testing area of the sample to a depth of only 25 nm. The largest value was 300 nm for the 1 µm diameter and 75 µm depth topographies. Ohm's law stipulated summing the R_T values of Table 7.11 together since they were in series. The resulting value represented the resistance encountered by smooth Si-Cu topographies excluding a-Si:H film. The R_T value for the Si-Cu composite in Table 7.11 is 0.0344829325°C/W.

The same R_T summation rule applies to Table 7.12 which represents smooth Si-Cu topographies having a-Si:H film as a surface chemistry modification. The R_T value for the Si/Cu/a-Si:H composite topography is 0.0347611379°C/W. Adding the equivalent lubricant thickness + 1 µm values from Table 7.13 was done to account for the amount of lubricant required by the respective pore diameters and depths. The combined thermal resistances of the smooth substrate and lubricant are shown in Table 7.14. Although the values were specifically for smooth topographies, the pore designations were retained for clarity to identify the amount of lubricant placed on the smooth topographies and to facilitate their comparison to the respective true nano-porous topographies during analysis.

Table 7.14. The combined values of thermal resistance, R_T (°C/W), calculated for 12 types of smooth samples using Tables 7.11 - 7.13.

Combined R_T of Smooth Si-Cu Composite and Equivalent Lubricant + 1 µm				
	Diameters Including a-Si:H		**Diameters Excluding a-Si:H**	
	0.5 µm	**1 µm**	**0.5 µm**	**1 µm**
Depth	**R_T (°C/W)**	**R_T (°C/W)**	**R_T (°C/W)**	**R_T (°C/W)**
25 µm	0.0992007619	0.1084064229	0.098922557	0.108128218
50 µm	0.1022693159	0.1206806369	0.101991111	0.120402432
75 µm	0.1053378689	0.1329548509	0.105059664	0.132676646

The values in Table 7.14 represent the R_T values of smooth substrates deposited with an equivalent thickness plus 1 µm of lubricant. Note that the R_T values increased as the so-called "diameter" increased from 0.5 to 1 µm. This was different behavior from porous topographies whose R_T values decreased as diameter increased. It must be remembered that the smooth topographies were deposited with an equivalent amount of lubricant as the porous topographies, so the amount of lubricant on smooth topographies was supposed to increase as the diameter increased. The same behavior, increased R_T, was observed for the so-called increase in "depth". Finally, as expected, the topographies that excluded a-Si:H film had lower R_T values (and higher heat transferred) than their counterparts with a-Si:H film.

Having the combined thermal resistances in hand, each testing temperature (minus the room temperature) was divided by the R_T values in Table 7.14 to determine the total conduction heat transferred, $Q_{conduction}$. For modeling purposes, T_2 was chosen as 25°C room temperature and T_1 became the specific testing temperature indicated in the table. The temperature values were input into equation (5.2) expressed previously. The results are shown in Table 7.15.

Table 7.15. Total conduction heat transfer, $Q_{conduction}$ (W), for the substrate and lubricant on smooth samples calculated for the evaporation testing temperatures of 300, 350, and 400°C minus the room temperature.

Total Conduction Heat Transfer of Smooth Si-Cu Composite and Lubricant at 300°C

	Diameters Including a-Si:H		Diameters Excluding a-Si:H	
	0.5 µm	**1 µm**	**0.5 µm**	**1 µm**
Depth	**Q (W)**	**Q (W)**	**Q (W)**	**Q (W)**
25 µm	2772.16	2536.75	2794.55	2555.48
50 µm	2688.98	2278.74	2710.04	2293.85
75 µm	2610.65	2068.38	2630.49	2080.82

Total Conduction Heat Transfer of Smooth Si-Cu Composite and Lubricant at 350°C

	Diameters Including a-Si:H		Diameters Excluding a-Si:H	
	0.5 µm	**1 µm**	**0.5 µm**	**1 µm**
Depth	**Q (W)**	**Q (W)**	**Q (W)**	**Q (W)**
25 µm	3276.19	2995.19	3302.65	3020.12
50 µm	3177.89	2693.06	3201.62	2710.91
75 µm	3085.31	2444.45	3110.31	2459.15

Total Conduction Heat Transfer of Smooth Si-Cu Composite and Lubricant at 400°C

	Diameters Including a-Si:H		Diameters Excluding a-Si:H	
	0.5 µm	**1 µm**	**0.5 µm**	**1 µm**
Depth	**Q (W)**	**Q (W)**	**Q (W)**	**Q (W)**
25 µm	3780.22	3459.21	3810.75	3484.75
50 µm	3666.79	3073.62	3695.51	3127.98
75 µm	3559.98	2820.52	3587.04	2837.47

The results in Table 7.15 initially have what may seem like contradictions to conventional thinking about the way heat transfer is supposed to proceed. Recall, however, that higher thermal resistance caused less heat transfer. The trends for total heat transfer via conduction that were noted for nano-porous topographies were also observed here on smooth topographies; specifically, as the temperature and "diameter" were held to constant values and "depth" increased, the heat transfer ability decreased accordingly. This occurred because the greater amount of lubricant associated with the deeper pores meant more oil was placed on the surface of the smooth samples as an equivalent amount, and this lead to higher resistance and lower heat transfer values. In the same manner, if the temperature and depth were held constant while the diameter changed, the heat transfer decreased. Again, the increase in diameter caused an increase in R_T which impeded heat transfer.

7.1.2 Results of Convection Heat Transfer Modeling

An obstacle to finding the convection heat transfer was the determination of *h*. The convection heat transfer coefficient, *h*, is directly proportional to *Nu*. To calculate *h*, the thermal conductivities (*k*) of air must be found for the range of testing temperatures. The *k* values were 0.04418 W/m·°C for 300°C and 0.05015 W/m·°C for 400°C temperatures. Inserting the corresponding *Nu* calculated in section 5.1.2 and *k* values into equation (5.12) and solving for *h* gave values of 16.82 and 16.72 W/m^2·°C, respectively. Table 7.16 summarizes the values of the parameters calculated thus far.

Table 7.16. Summary of variables for determining convection heat transfer of air.

Temperature (°C)	**ν (m^2/s)**	**Pr**	**Re**	**k (W/m·°C)**	**Nu**	**h (W/m^2·°C)**
300	4.765 E -05	0.6935	280.7	0.04418	4.835	16.82
400	6.219 E -05	0.6948	215	0.05015	4.234	16.72

The variables in Table 7.16 are represented by their minimum and maximum values for 300 and 400°C. This allowed the intermediate values for 350°C to be found using interpolation techniques. The values of *h* did not change significantly over the range of temperatures for lubricant evaporation testing. Having found the range of values for *h*, the amount of heat transferred by convection could be determined. The values for the surface area of the lubricant and the chosen evaporation testing temperature (minus the room temperature) were all that remained to calculate the heat transfer, $Q_{convection}$. As explained in section 4.4.3, the area above the pores served as the cross-sectional area. Defining this value as the surface area of the lubricant, the heat transfer due to convection was calculated using equation (5.9). The results are shown in Table 7.17.

Table 7.17. The convection heat transfer, $Q_{convection}$ (W), for the selected evaporation testing temperatures.

Temperature (°C)	$Q_{convection}$ (W)
300	0.61040201
350	0.71001874
400	0.80903064

Overall, the analysis of the $Q_{convection}$ quantities in Table 7.17 revealed that the contribution of convection to the total heat transfer was not significant. This occurred for a few reasons. The first was the flow of air modeled through the testing apparatus had a slow velocity of 1.053 m/s. Convection heat transfer is enhanced as the velocity increases because of its contribution to *h*. Other reasons can be gleaned from Table 7.16 which lists the *k* values and *Re* numbers of air. Air is a poor conductor of heat. The *k* values of air were small compared to the other phases of matter but typical of gases in general. The laminar flow regime, as indicated by the small *Re* number values, also contributed to the menial transfer of heat. Yet another reason was the small

testing surface area (121 mm^2) of the sample over which the air flowed. Larger surface areas increase $Q_{convection}$. The combination of small surface area, low flow velocity, *Re*, and *k*, and laminar flow regime resulted in negligible heat transfer. Nonetheless, the quantities were combined with the conductance and radiation heat transfers to yield the net value contributing to the evaporation of lubricant from the surface of Si-Cu and Si-Cu/a-Si:H composites.

7.1.3 Results of Radiation Heat Transfer Modeling

Figure 5.8 showed an illustration of the evaporation compartment located inside the testing apparatus. As anticipated, the surface temperatures were different depending on the surface location within the chamber. For example, when the chamber was operated at 315°C, surface *1* was actually 230°C, surface *2* was 305°C, and surface 3 was 300°C. The other testing temperatures yielded results relative to these because of the apparatus' linear temperature profile.

The fact that surface *2* had the highest temperature, followed by surface *3* and lastly, surface *1* the lowest was not completely surprising because the resultant surface temperatures were influenced by the conduction and convection heat transfer modes in addition to the proximity and orientation of the surfaces to the cartridge heater sources. Using relative temperatures formed by dividing the actual temperatures, $T_{actual,i}$, to the programmed one, $T_{test,}$= 315°C, three coefficients were found which simplified the automatic calculation of the actual surface temperatures and, consequently, J_1, J_2, and J_3. The equation formulated for determination of the actual temperature of each surface was,

$$T_{actual,i} = T_{coefficient\ i} * T_{test} \qquad \text{Equation (7.1)}$$

The coefficients were: $T_{coefficient\ 1}$ = 0.73, $T_{coefficient\ 2}$ = 0.99, and $T_{coefficient\ 3}$ = 0.97. Having the temperature coefficients in hand, the calculation of T_{actual} for each surface of the compartment at each testing temperature could proceed. These are shown in Table 7.18.

Table 7.18. Actual surface temperature, $T_{actual,i}$ (K), values of the evaporation testing compartment.

$T_{Testing}$ (K)	$T_{actual,1}$ (K)	$T_{actual,2}$ (K)	$T_{actual,3}$ (K)
573	418.29	567.27	555.81
623	454.79	617.77	604.31
673	491.29	666.27	652.81

Equations (7.2), (7.3), and (7.4) were derived from equations (5.26), (5.27) and (5.28) after substituting the σ and ε quantities into them and rearranging the values, so that,

$$(5.6704\ \mathrm{E}-08)\mathrm{T}_1^4 = 2.3809524\mathrm{J}_1 - 0.8561905\mathrm{J}_2 - 0.5247619\mathrm{J}_3 \quad \text{Equation (7.2)}$$

$$(5.6704\ \mathrm{E}-08)\mathrm{T}_2^4 = -0.8561905\mathrm{J}_1 + 2.3809524\mathrm{J}_2 - 0.5247619\mathrm{J}_3 \quad \text{Equation (7.3)}$$

$$(5.6704\ \mathrm{E}-08)\mathrm{T}_3^4 = -0.4695238\mathrm{J}_1 - 0.4695238\mathrm{J}_2 + 1.9390476\mathrm{J}_3 \quad \text{Equation (7.4)}$$

which are shown in generalized matrix form as,

$$\begin{bmatrix} 2.3809524 & -0.8561905 & -0.5247619 \\ -0.8561905 & 2.3809524 & -0.5247619 \\ -0.4695238 & -0.4695238 & 1.93904762 \end{bmatrix} * \begin{bmatrix} \mathrm{J}_1 \\ \mathrm{J}_2 \\ \mathrm{J}_3 \end{bmatrix} = \begin{bmatrix} (5.6704\ \mathrm{E}-08)\ \mathrm{T}_1^4 \\ (5.6704\ \mathrm{E}-08)\ \mathrm{T}_2^4 \\ (5.6704\ \mathrm{E}-08)\ \mathrm{T}_3^4 \end{bmatrix} \quad \text{Equation (7.5)}$$

After inputting the appropriate T_{actual} values from Table 7.18 for T_1, T_2, and T_3 in equation (7.5), the variables of the solution matrix [J_1, J_2, J_3] were determined by inverting the coefficient matrix and multiplying it by the constants matrix. These are shown in Table 7.19.

Table 7.19. The radiosities, J (W/m^2), of the surfaces in the evaporation testing compartment.

$T_{Testing}$(K)	J_1 (W/m^2)	J_2 (W/m^2)	J_3 (W/m^2)
573	3507.447808	4785.095202	4798.780792
623	4914.205897	6716.122991	6716.182332
673	6674.718772	9106.098574	9132.142447

Equations (7.6), (7.7), and (7.8) were derived from equation (5.25). The values for J_1, J_2, and J_3 were used in them. The $Q_{radiation}$ of the respective compartment surfaces are expressed as,

$$Q_1 = A_1[F_{12}(J_1 - J_2) + F_{13}(J_1 - J_3)] \qquad \text{Equation (7.6)}$$

$$Q_2 = A_2[F_{21}(J_2 - J_1) + F_{23}(J_2 - J_3)] \qquad \text{Equation (7.7)}$$

$$Q_3 = A_3[F_{31}(J_3 - J_1) + F_{32}(J_3 - J_2)] \qquad \text{Equation (7.8)}$$

where the disk surface areas, $A_1 = A_2 = 0.0045$ m^2 and $A_2 = 0.0087$ m^2. Table 7.20 shows the tabulated values of the heat transfers from the respective surfaces and testing temperatures.

Table 7.20. Calculated values of the radiation heat transfer, $Q_{radiation}$ (W) of each evaporation compartment surface for the three testing temperatures.

$T_{Testing}$ (K)	Q_1 (W)	Q_2 (W)	Q_3 (W)
573	-5.978338567	3.522062181	2.456276368
623	-8.391781385	5.000030485	3.3917509
673	-11.37685699	6.702530648	4.674326339

It is important to note the direction of the radiation heat transfers Q_1, Q_2, and Q_3. These were first indicated in the illustration of Figure 5.9. Recall that surface *2* had the highest temperature of the three compartment surfaces which suggested the transfer of heat flowed from surface *2* and it exited through the other surfaces that had lower temperatures. An initial assumption was made that some of the heat transferred from surface *2* would flow out of surface *3*. Table 7.20 positive values, however, plainly indicate the radiation heat was transferred into surfaces *2* (59% of total) and *3* (41% of total), and surface *1* incurred all of the radiation heat loss. The total $Q_{radiation}$ was the amount of Q_2 and Q_3. Their values were summed with the conduction and convection quantities for the net required heat I_{net} (W) and net heat transfer Q_{net} (W) calculations. The net values for the sample types are shown in Tables 7.21 and 7.22 in section 7.1.4.

7.1.4 Net Required Heat and Net Heat Transfer Modeling Results

Table 7.21. The net required heat, I_{net} (W), of nano-porous surfaces related to testing temperature, pore depths, pore diameters, and including and excluding a-Si:H film.

	Required Heat for Si-Cu Nano-Porous Topographies at 300°C			
	Diameters Including a-Si:H		**Diameters Excluding a-Si:H**	
	0.5 µm	**1 µm**	**0.5 µm**	**1 µm**
Depth	**I_{net} (W)**	**I_{net} (W)**	**I_{net} (W)**	**I_{net} (W)**
25 µm	10607.91	10507.05	7799.15	7691.39
50 µm	10634.85	10537.13	7816.07	7714.15
75 µm	10661.29	10566.28	7839.27	7736.25
	Required Heat for Si-Cu Nano-Porous Topographies at 350°C			
	Diameters Including a-Si:H		**Diameters Excluding a-Si:H**	
	0.5 µm	**1 µm**	**0.5 µm**	**1 µm**
Depth	**I_{net} (W)**	**I_{net} (W)**	**I_{net} (W)**	**I_{net} (W)**
25 µm	12537.92	12418.72	9218.49	9091.14
50 µm	12569.77	12454.28	9238.48	9117.81
75 µm	12601	12488.73	9265.91	9144.15
	Required Heat for Si-Cu Nano-Porous Topographies at 400°C			
	Diameters Including a-Si:H		**Diameters Excluding a-Si:H**	
	0.5 µm	**1 µm**	**0.5 µm**	**1 µm**
Depth	**I_{net} (W)**	**I_{net} (W)**	**I_{net} (W)**	**I_{net} (W)**
25µm	14468.53	14330.98	10638.41	10491.47
50 µm	14505.27	14372	10661.48	10522.24
75 µm	14541.31	14411.76	10693.12	10552.63

Table 7.22. The net heat transferred, Q_{net} (W), of smooth surfaces related to the testing temperature and equivalent lubricant thickness associated with nano-pore depths and diameters and including and excluding a-Si:H film.

	Net Heat Transfer for Smooth Si-Cu Topographies at 300°C			
	Diameters Including a-Si:H		**Diameters Excluding a-Si:H**	
	0.5 µm	**1 µm**	**0.5 µm**	**1 µm**
Depth	**Q_{net} (W)**	**Q_{net} (W)**	**Q_{net} (W)**	**Q_{net} (W)**
25 µm	2778.75	2543.34	2801.14	2562.07
50 µm	2695.57	2285.33	2716.63	2300.44
75 µm	2617.24	2074.97	2637.08	2087.41
	Net Heat Transfer for Smooth Topographies Si-Cu at 350°C			
	Diameters Including a-Si:H		**Diameters Excluding a-Si:H**	
	0.5 µm	**1 µm**	**0.5 µm**	**1 µm**
Depth	**Q_{net} (W)**	**Q_{net} (W)**	**Q_{net} (W)**	**Q_{net} (W)**
25 µm	3285.29	3004.29	3311.75	3029.22
50 µm	3186.99	2702.16	3210.72	2720.01
75 µm	3094.41	2453.55	3119.41	2468.25
	Net Heat Transfer for Smooth Topographies Si-Cu at 400°C			
	Diameters Including a-Si:H		**Diameters Excluding a-Si:H**	
	0.5 µm	**1 µm**	**0.5 µm**	**1 µm**
Depth	**Q_{net} (W)**	**Q_{net} (W)**	**Q_{net} (W)**	**Q_{net} (W)**
25 µm	3792.41	3471.4	3822.94	3496.94
50 µm	3678.98	3085.81	3707.7	3140.17
75 µm	3572.17	2832.71	3599.23	2849.66

Tables 7.21 and 7.22 show the tabulated values of net heat required for nano-porous topographies and net heat transfer for smooth topographies, respectively. An analysis of the tables revealed some noteworthy findings. For example, the values in Table 7.21 showed a pattern of requiring greater heat to evaporate lubricant (at a constant testing temperature and diameter) as the pore depth increased. This trend was consistent with the heat encountering greater R_T as the segments comprising the pores increased in thickness. Also, the I_{net} decreased as the diameter increased because changing the diameter increased the *Cu* segment's cross-sectional area. The larger cross-sectional area caused the R_T values to decrease, therefore lowering the I_{net} to produce evaporation of the lubricant.

On the bases outlined in the previous paragraph, the minimum I_{net} in Table 7.21 should be affiliated with samples having a 1 μm pore diameter and 25 μm pore depth. The highest I_{net} should be those having a 0.5 μm pore diameter and 75 μm pore depth. These findings are true for pore structures that include and exclude a-Si:H surface modification. The validity of these statements relies upon the assumption of a constant temperature. Also, the samples without a-Si:H modification have the lowest I_{net} values for achieving lubricant evaporation than their a-Si:H modified counterparts. The prediction, across the board, is the amount of evaporated lubricant should be higher for the samples that exclude a-Si:H film. Specifically, the highest evaporated amount should occur for samples having a 1 μm pore diameter and 25 μm pore depth that exclude a-Si:H film and the lowest evaporated amount should be associated with a 0.5 μm pore diameter and 75 μm pore depth having a-Si:H film—if the samples are compared at the same temperature.

Finally, according to the I_{net} calculations that resulted from an imposed 1 v source in the resistance network, increasing the testing temperature should cause greater I_{net} and therefore

reduce the evaporation of lubricant from the surface of the samples. As the testing temperature in Table 7.21 increases from 300 to 400°C, the model predicts the greatest I_{net} amounts will occur for samples tested at 400°C. Attempting to compare the results of samples tested at 300°C to those tested at 400°C would mean that the samples tested at 300°C are expected to evaporate more lubricant than the ones tested at 400°C, regardless of whether the samples have a-Si:H film deposited on them or not.. This outcome is contradictory to the physics of heat transfer. The caveat to this model, then, is one must apply the I_{net} predictions to all nano-porous sample configurations using a fixed temperature.

Table 7.22 shows values tabulated for Q_{net} through smooth samples. For good reason, the values in this table are much lower than those of Table 7.21. The predictions for these topographies undergoing heat transfer are as follows. When using a constant temperature and "depth" while allowing the "diameter" to change, the Q_{net} values should decrease because more oil would be deposited on the smooth samples to match the amount present in the larger 1 μm pore diameter. The additional lubricant should increase the R_T value and impede heat flow, therefore causing greater lubricant retention.

Examining the relationship in Table 7.22 between the depth and Q_{net} while the diameter and temperature were held constant showed that the Q_{net} values decreased as the depth increased. As stated previously, the equivalent amount of lubricant deposited on the smooth samples increased with the pore depth and resulted in increased R_T values. Increased R_T values lead to lower heat flow through the sample. Also, the Q_{net} through the topographies in which a-Si:H film was excluded was higher than the corresponding topographies with a-Si:H film, assuming the comparison is done using a constant temperature. In summary, the smooth sample topography having the equivalent lubricant amount associated with a 0.5 μm pore diameter and 25 μm pore

depth that excluded a-Si:H film should retain the least lubricant. The sample topography that retained the most lubricant should be the one having a 1 μm pore diameter and 75 μm pore depth and includes a-Si:H film. The predictions are based on maintaining a constant temperature and recalling that the "depths" and "diameters" terms are relative to equivalent lubricant on nano-porous Si-Cu topographies.

7.2 Formation Theory of a-Si:H Film and Hydrogen Concentration Modeling Results

Amorphous Si is a non-crystalline allotrope of Si. Its structure differs from single crystal Si in that a-Si:H film has a variety of short range crystalline lattices whereas single crystal Si only possesses a long range crystalline lattice. Hydrogenation during the deposition of a-Si:H film was important for producing films with low electronic defects so that it might find applicability in solar cells and other photovoltaic uses. In this author's research, the lubricant retention performance of surfaces without a-Si:H films were used as a comparison for whether improvement occurred as a result of a-Si:H surface chemistry modification. Investigating the formation of a-Si:H film was done to understand the availability of bonding sites that could be used to enhance the retention of a hydrocarbon-based lubricant. The theory is knowledge of the number of hydrogen atoms in the film could be used as a basis for determining the number of available bonds between the lubricant's atoms and dangling Si atoms. These bonds were created after a-Si:H film had been applied but before the application of the testing lubricant.

7.2.1 Formation Theory of a-Si:H Film

An illustration of the network of atoms that form a-Si:H film is shown in Figure 7.1. The formation consists of Si (black dots) and H atoms in a covalent bond arrangement. Neutral Si atoms have 4 valence electrons which allow it to bond with adjacent Si atoms, or alternatively, with as many as 4 H atoms, each sharing its lone electron to complete Si's outer electron shell.

This is the “perfect world” scenario. The reality is quite a bit more complicated as can be seen from the 5 different chemical reaction equations listed below. They represent only a few of the possibilities that explain the formation of a-Si:H film using a plasma source.

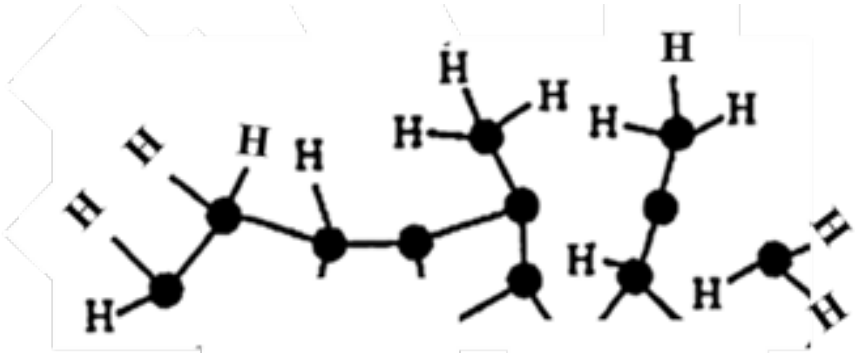

Figure 7.1. An illustration of the possible chemical reactions leading to the formation of a-Si:H film. The illustration shows SiH, SiH_2, and SiH_3 bonds produced on the surface of a-Si:H film. The black dots represent Si atoms (*Image from the author*).

The primary reactions are,

$$SiH_4 \rightarrow SiH_2 + H_2 \qquad \text{Equation (7.9)}$$

$$SiH_4 \rightarrow SiH_3 + H \qquad \text{Equation (7.10)}$$

$$SiH_4 \rightarrow Si + 2H_2 \qquad \text{Equation (7.11)}$$

and the secondary reactions are,

$$SiH_4 + SiH_2 \rightarrow Si_2H_6 \qquad \text{Equation (7.12)}$$

$$Si_2H_6 + SiH_2 \rightarrow Si_3H_8 \qquad \text{Equation (7.13)}$$

The primary reactions are important because they form the radicals within the plasma which could be the precursors for the surface chemical reactions that produce a-Si:H film. Concrete evidence of the exact nature of the chemical reactions at the surface is lacking, but it is strongly believed that only the reaction in equation (7.10) results in the formation of a-Si:H film. The reasons are the reactions in equations (7.9) and (7.11) that form SiH_2 and Si products are more

chemically reactive than SiH_3 produced in the reaction in equation (7.10), they are produced in low concentrations, and they have short diffusion lengths. The reactions in equations (7.9) and (7.11) high reactivity with other species in the plasma, low concentrations, and short diffusion lengths means the likelihood of arriving at the surface of the c-Si wafer to react with the adsorbed precursors is poor. The SiH_3 molecules, on the other hand, have relatively low reactivity with other species in the plasma and are produced in a large concentration (estimated to be 80% of all radicals produced), therefore increasing the probability that they are the precursors that survive the collisions to arrive at the surface to form a-Si:H film. The role of the products formed in the reactions in equations (7.12) and (7.13) is thought to be the by-products of the reactions in the plasma which modify the mix of radicals in some manner so as to moderate the film growth.

The growth of the film occurs at the surface of the wafer if the chamber conditions are such that the precursors arriving at the plasma's edge are not prevented from leaving it. Otherwise the growth takes place in the plasma. After arriving at the wafer surface, SiH_3 radicals will bond with un-terminated, adsorbed SiH_x, that is to say, the Si atoms that have vacancies in their outer shell. The vacancies can also occur as adsorbed SiH_3 molecules are located adjacent to other adsorbed molecules, and the weakly bonded monatomic H atoms of each molecule dissociates to form H_2, thereafter creating dangling Si bonds. The scavenging and formation of H_2 between molecules frees the H_2 from the adsorbed molecules, subsequently allowing bonds to form between the Si atoms as illustrated in Figure 7.1. The adsorbed Si molecules become absorbed in the film which then facilitates the bonding of other incoming molecules of SiH_3. The substitutions occur until the deposition process is completed. The final a-Si:H film surface configuration has bonds terminated with H_x atoms. It is anticipated that the mono- and poly-

hydride species can be driven away during thermal annealing of the samples to create the dangling bonds. This approach could possibly establish a correlation between the changes in pore geometry, the change in the number of available bonds with Si atoms, and the subsequent amount of lubricant retained.

7.2.2 Hydrogen Concentration Modeling Results

Chamber conditions, process gas recipe, and chemical vapor deposition plasma have significant impact on the percentage of H content and quality of a-Si:H film obtained for testing. Because of this reality, the results obtained by researchers are unique to their deposition systems. Therefore it is essential to perform analyses using widely accepted methods that allow comparison between these system's results. The total H content in a-Si:H film is routinely determined using FTIR spectroscopy. Table 7.23 is a partial listing of 1870 total data points of IR spectra collected from 250 nm thick a-Si:H film deposited on a double-sided polished c-Si wafer. The complete spreadsheet necessary to perform the calculations was too complex to include in its entirety in this work. The values of the dominant parameters and a few integration values are shown in the table.

Table 7.23. Partial spreadsheet values for the plotting of IR absorption data to calculate N_H.

Wave Number (cm^{-1})	% Transmittance	Absorp. Coef./Wave No.	2000 Gaussian Integration	2080 Gaussian Integration
1.77E+03	1.02E+02	7.84E-02	8.20822E-11	3.81005E-20
1.77E+03	1.05E+02	-1.92E-01	1.19913E-10	6.56371E-20
1.77E+03	1.06E+02	-3.37E-01	1.74803E-10	1.12815E-19
•	•	•	•	•
•	•	•	•	•
2.32E+03	1.01E+02	1.35E-01	6.43661E-20	2.15281E-12
2.32E+03	1.00E+02	1.64E-01	3.78598E-20	1.41219E-12
2.32E+03	1.01E+02	1.34E-01	2.21652E-20	9.21925E-13

In the spreadsheet, the full IR spectrum's data was obtained from 400 cm^{-1} to 4000 cm^{-1}. However, the region of interest was between 1800 cm^{-1} and 2250 cm^{-1} due to the presence of mono- and poly-hydride stretching mode wavenumbers. Within this region, the data for absorption/wavenumber, (α/ω), versus wavenumber, ω, was plotted. The 2000 and 2080 Gaussian curves were plotted with the α/ω plot. A combined Gaussians curve was created by adding the numerical variables of the 2000 and 2080 curves described as *position*, *height*, and *width*. The variables were explained in section 5.2.1.1. Note that the variables used to construct the α/ω plot are distinct from the α/ω values used to construct the Gaussian curves and perform their integrations.

The purpose of the combined Gaussians curve was to confirm whether or not there was close fitment with the α/ω plot. It served as an interactive tool that was separately manipulated by the 2000 and 2080 curves until good fitment was achieved. The plots are shown in Figure 7.2.

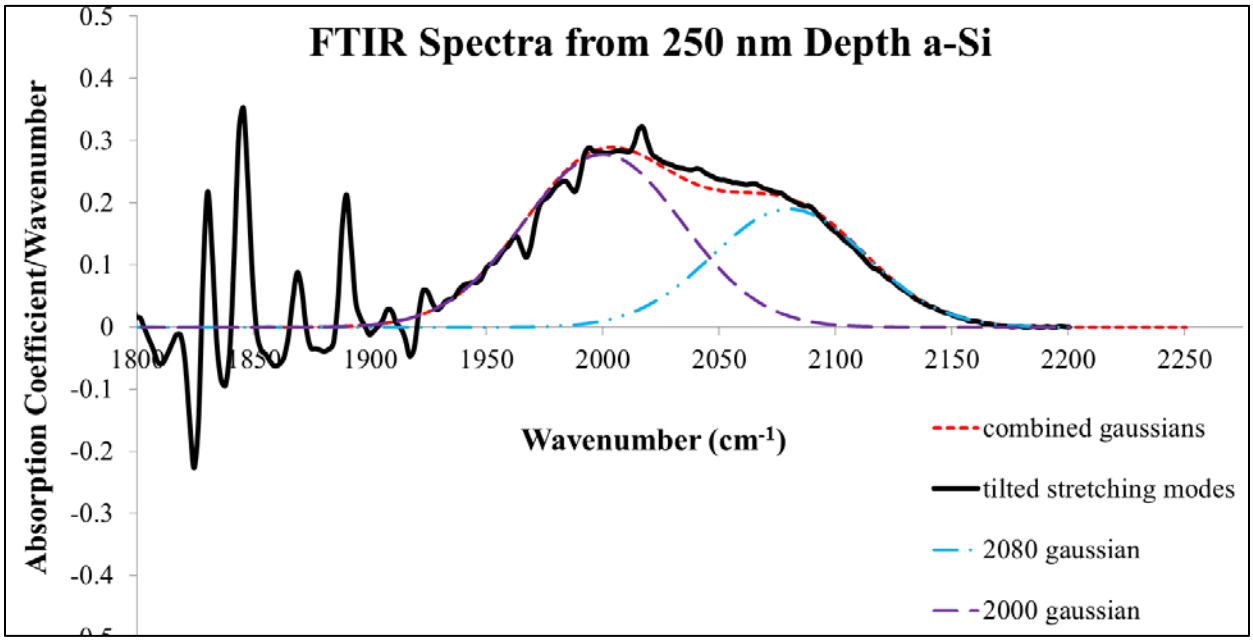

Figure 7.2. A comprehensive plot illustrating the FTIR spectra collected for estimating the concentration of H atoms occuring in 250 nm thick a-Si:H film on a smooth c-Si wafer (*Image from the author*).

Using equation (5.38), trapezium integration was implemented on the 2000 and 2080 Gaussian curves to find integrated absorbance, δ, and, consequently H concentration, N_H. A few numerical integration calculations were given in Table 7.23. The particular values in the table (note the small magnitudes) are associated with the tails of the Gaussian curves. To perform the calculations, it was necessary to visually-align the combined Gaussians curve and the α/ω plot. Once aligned, the individual integration values of the 2000 and 2080 curves were handled cumulatively to attain the total δ results. The value of the curve variables and cumulative integrated absorbance are provided in Table 7.24.

Table 7.24. The 2000 and 2080 Gaussians placement values used to form the curves and determine integrated absorbance.

Gaussian Curve Variables and Cumulative Integrated Absorbance

position	height	width	δ (cm^{-1})
2000	0.278	34	24.2
2080	0.190	33	16.08

Since a-Si:H film stretching modes consist of two peaks located at 2000 and ≈2100 cm^{-1}, proportionality constants were acquired for a-Si:H films less than 1 μm thick. These were combined with their respective cumulative δ to determine the concentration of H atoms. The proportionality constants are A_{2000} = 9.0 x 10^{19} cm^{-2} and A_{2100} = 2.2 x 10^{20} cm^{-2}. The equation for concentration, equation (5.34) is,

$$N_H \cong A_\omega \delta$$

Mono-hydride concentration was estimated as 2.18×10^{21} cm^{-3} and poly-hydride concentration was 1.0×10^{22} cm^{-3}. The total number of mono- and poly-hydride atoms was found by adding

the N_H quantities [83]. The total is 1.218×10^{22} cm^{-3}. The concentration of Si atoms was estimated as 5.0×10^{22} cm^{-3}. The mole fraction was determined from equation (5.39),

$$\text{mole fraction of H} = \frac{\text{N}_\text{H}}{(\text{N}_\text{H} + \text{N}_\text{Si})}$$

Inputting the respective concentration values into the equation, the mole fraction of mono-hydrides was 0.041789 and poly-hydrides was 0.066078. Multiplying the mole fraction amounts by 100 gave the atomic percentages. The percentages are shown in Table 7.25.

Table 7.25. The estimated atomic percentages of mono- and poly-hydrides that exist in 250 nm thick a-Si:H film deposited using the PECVD system at HiDEC.

% mono-H	% poly-H	% relative poly-H
4.1789	6.6078	61.2586

The total atomic percentage of mono- and poly-hydrides was estimated to be 10.8%. Clustered mono-hydrides and poly-hydride species in the a-Si:H film constitute approximately 61.3% of the types of H atoms as shown by the relative poly-hydride percentage.

7.2.2.1 Effect of a-Si:H Film Dehydrogenation on Lubricant Retention

The purpose of determining the concentration of H atoms was to estimate the number of bonding sites for lubricant that can be created when H atoms were released from the surface of a-Si:H film. In addition, during the heating of a hydrocarbon-based lubricant, C-H bonds will be broken therefore relocating H from the lubricant. As heat-induced lubricant degradation becomes progressively worse, the concentration of by-products such as hydroxyls (OH-), carbonyls (C=0), and carboxylic acid (C=O-OH) will increase [84].

Observe that the by-products all contained O in their formulations. The creation of lubricant degradation by-products resulted in the preferential oxidation of H atoms from the lubricant.

This left C atoms in place after they released their H atoms to these by-products. In essence, the dangling Si atoms in dehydrogenated a-Si film and the remaining C atoms in the lubricant could provide an opportunity for bonding [85]. Therefore, Si-C bonds may contribute to enhanced lubricant retention.

Hydrogen atoms can be eliminated using an annealing step to investigate the molecular interaction between the dehydrogenated a-Si film surface and hydrocarbon-based lubricant. To achieve dehydrogenation, the samples having a-Si:H film would need to be baked in an oven at 350°C for 60 min. The oven, the Lindberg Blue M (Thermo Scientific, Waltham, MA USA), shown in Figure 7.3, was used to dehydrogenate samples for preliminary lubricant retention testing.

Figure 7.3. The Lindberg Blue oven was used to dehydrogenate a-Si:H film before evaporation testing (*Image from the author*).

The physical appearance of the preliminary samples after dehydrogenation remained unchanged from the hydrogenated film's appearance. As a consequence, a method was needed to determine the success of the dehydrogenation technique. Sheet resistance has been used extensively as confirmation of dehydrogenation [86]. Sheet resistance is the electrical resistance along the plane of the thin film, not across its thickness. The instrument used to measure the resistance is the 4-point probe. The instrument also measures resistivity. Resistivity measurements incorporate the film's thickness in addition to its sheet resistance. The 4-point probe used in this research, model FPP5000 (Veeco Instruments, Inc., Plainview, NY), is shown in Figure 7.4.

Figure 7.4. The 4-point probe instrument was used to measure sheet resistance and resistivity of hydrogenated and dehydrogenated a-Si films (*Image from the author*).

As the name implied, 4 probe tips inside the instrument made contact with the material being measured. Current was passed through the outer probes and they, in turn, induced voltage on the inner probes. From these values, the resistance was calculated. Three sample types were tested:

polished c-Si wafer, a-Si:H film deposited to 250 nm thickness on c-Si, and the same sample type after dehydrogenation. The proof of dehydrogenation was a decrease in sheet resistance. Table 7.26 shows the results of the tests.

Table 7.26. Results of the 4 point probe measurements from smooth Si samples deposited with 250 nm thick hydrogenated and dehydrogenated a-Si films.

	Polished c-Si	**a-Si:H**	**a-Si:Dehydrogenated**
Sheet Resistance (Ω/square)	--	1171	316
Resistivity (Ω-cm)	5-30	0.0293	0.0079

The baseline values for c-Si were very small in comparison with the other samples. This indicated the other acquired readings were those solely belonging to the a-Si:H and dehydrogenated a-Si films. The sheet resistance and the resistivity values shown in the figure indicated that they were reduced 73% from the original hydrogenated values. Now, the theory put forth for the dehydrogenation of a-Si:H film could be tested using lubricated samples.

The effect of dehydrogenation on the evaporation of lubricant was determined by performing an evaporation experiment using smooth samples comprised from Si-Cu, Si-Cu/a-Si:H, and Si-Cu/a-Si:Dehydrogenated. Smooth Si-Cu samples were the baseline for comparison with the other sample types. Two samples were used for each type to demonstrate the test's repeatability. The mass of each sample was recorded before and after lubricant was applied. The amount of lubricant deposited on the samples was 0.0452 g. This amount of lubricant was chosen to ensure the samples were sufficiently covered. The testing temperature was 350°C for a total duration of 30 min. This temperature was the median of the three to be employed during lubricant retention testing of all of the samples. The change in mass (*Δmass*) of the samples was recorded every 5 min. An average value for the each sample type was compiled to observe trends occurring during lubricant evaporation. The results are presented in Table 7.27.

Table 7.27. Evaporation results compiled from samples pre- and post-dehydrogenation.

Sample ID	Tare Mass (g)	Mass (g) 5 min	Δmass (mg) 5 min	Mass (g) 10 min	Δmass (mg) 10 min	Mass (g) 15 min	Δmass (mg) 15 min	Mass (g) 20 min	Δmass (mg) 20 min	Mass (g) 25 min	Δmass (mg) 25 min	Mass (mg) 30 min	Δmass (mg) 30 min
Si-Cu	0.4748	0.4749	0.10	0.4748	0.00	0.4748	0.00	0.4748	0.00	0.4748	0.00	0.4748	0.00
Si-Cu	0.4750	0.4751	0.10	0.4750	0.00	0.4750	0.00	0.4750	0.00	0.4750	0.00	0.4750	0.00
Si-Cu	0.4749	0.4750	0.10	0.4749	0.00	0.4749	0.00	0.4749	0.00	0.4749	0.00	0.4749	0.00
Si-Cu/a-Si:H	0.4745	0.4748	0.30	0.4748	0.30	0.4748	0.30	0.4745	0.00	0.4745	0.00	0.4745	0.00
Si-Cu/a-Si:H	0.4753	0.4756	0.30	0.4756	0.30	0.4756	0.30	0.4753	0.00	0.4753	0.00	0.4753	0.00
Si-Cu/a-Si:H	0.4749	0.4752	0.30	0.4752	0.30	0.4752	0.30	0.4749	0.00	0.4749	0.00	0.4749	0.00
Si-Cu/a-Si:D	0.4750	0.4753	0.30	0.4753	0.30	0.4753	0.30	0.4753	0.30	0.4752	0.20	0.4752	0.20
Si-Cu/a-Si:D	0.4754	0.4757	0.30	0.4757	0.30	0.4757	0.30	0.4757	0.30	0.4757	0.30	0.4756	0.20
Si-Cu/a-Si:D	0.4752	0.4755	0.30	0.4755	0.30	0.4755	0.30	0.4755	0.30	0.4755	0.25	0.4754	0.20

The *Δmass* values in Table 7.27 indicated the amount of lubricant lost every 5 min and therefore were cumulative. They were calculated by subtracting the remaining mass of the sample and lubricant at the conclusion of each test from the tare mass of the sample recorded before lubricant was applied. The *Δmass* strategy was chosen purposely to minimize the effects of varying sample mass that occurred from small differences in size created when dicing the wafers into samples.

Giving attention to the averaged values (the pink-colored cells) for the three sample types in Table 7.27, clear trends emerged. Within the first 5 min of testing, all of the samples lost a significant portion of the 0.0452 g lubricant initially deposited on the surface. This occurred because excess lubricant was not in contact with the sample's surface, so it was easily evaporated. Si-Cu samples retained 0.1 mg, while an improvement was observed for a-Si:H and a-Si:Dehydrogenated samples which retained 0.3 mg. This represented a 0.2 mg savings. The seemingly miniscule amounts saved by the addition of a-Si:H and a-Si:Dehydrogenated films was significant in that each 0.1 mg conserved constituted 91% of the 1 μm oil thickness residing

on the sample testing area. Stated differently, the savings represented nearly twice the oil thickness residing between conformal, sliding surfaces of mechanical bearings and seals.

Further evaluation of the average values of the samples revealed that the Si-Cu samples lost all of their lubricant after 10 min, but the a-Si:H and a-Si:Dehydrogenated ones maintained identical amounts of 0.3 mg throughout 15 min of testing. The conclusion thus far is the addition of a-Si:H film had immediate and sustained benefits toward lubricant retention. After 20 min however, the dehydrogenated samples showed clear evidence of their superiority for retaining lubricant. The a-Si:H samples lost all of their deposited lubricant. Yet, the dehydrogenated ones held 0.3 mg more oil than the Si-Cu and Si-Cu/a-Si:H samples. Only after 25 min duration did the dehydrogenated samples begin to lose oil. Finally, after 30 min of testing, the dehydrogenated a-Si samples retained 0.2 mg more oil than the others. Clearly, greater retention of lubricant occurred on smooth samples as a result of dehydrogenation. This outcome gave justification for performing dehydrogenation on all of the samples deposited with a-Si:H film before lubricant retention testing began.

The Si-C bond hypothesis for enhancing lubricant retention was proven true. The non-polar, physisorbed interaction of unheated lubricant and a-Si:H film was based on weak van der Waal [48] or London dispersion forces [87][88]. Though concrete evidence of the exact nature of the chemical reactions at the surface is lacking, a stronger chemisorbed bond formation was created during heating of the lubricant that resulted in greater retention of lubricant. Bond dissociation energies may help explain the results. The bond dissociation energy values are 451 kJ/mol for Si-C bonds, 413 kJ/mol for C-H bonds, and 318 kJ/mol for Si-H bonds. Clearly, Si-C bonds had greater bond strength than Si-H_x of a-Si:H film or C-H bonds of the lubricant.

In addition to the strong Si-C bonds which enhanced lubricant retention, the inclusion of dehydrogenated a-Si film on the samples was believed to have contributed to the reduction of conduction heat transferred to the lubricant. To test of this hypothesis, smooth Si-Cu and Si-Cu/a-Si:Dehydrogenated samples were placed on a hotplate set to 350°C. Surface temperature measurements were taken from the hotplate and samples using an infrared thermometer. The samples remained on the hotplate for 5 min duration before recording the final temperature. The result was the top surface temperature of the Si-Cu samples having dehydrogenated a-Si film were 15°C lower than Si-Cu samples without the film which indicated the film retarded the transfer of heat to the surface. Undoubtedly, the reduction of the sample's surface temperature was an important factor in retaining more lubricant on smooth samples.

Attention now turned to developing a correlation between the number available bonding sites on the different topographies and their potential to enhance lubricant retention. All samples (including the smooth ones discussed here) have a test area size of 0.01905 cm long x 0.00635 cm wide. The 0.00025 cm dehydrogenated a-Si film thickness was multiplied by the sample test area size. This produced a dehydrogenated a-Si film volume equaling 3.0241875×10^{-8} cm^3. Multiplying the total N_H value of 1.218×10^{22} cm^{-3} times 3.0241875×10^{-8} cm^3 equals $3.683460375 \times 10^{14}$ available sites for C bonding with Si atoms on the smooth topographies' test area. The number of Si dangling bonds was estimated as 10^{15} cm^{-3} in [77] and 10^{15} - 10^{17} cm^{-3} in [82].

The calculations for the number of available bonding sites in nano-porous topographies were more complicated. This type of topography required an accounting for the volume of dehydrogenated a-Si film inside of the pores as well as the volume located on the testing area. The logic is there should be a greater number of bonds due to the presence of dehydrogenated a-

Si film in the nano-pores, and increasing the depth of the nano-pores should have a multiplying effect on the number of bonds. Increasing the number of bonds should, in response, lead to greater lubricant retention than nano-porous topographies that omit dehydrogenated a-Si film and smooth topographies having the film.

The volume of dehydrogenated film inside the nano-pores (V_{Pores}) plus the volume of film located on the testing area became the total volume (V_{Total}). Multiplying the V_{Total} amount times N_H allowed the calculation of the total number of available bonding sites (S_{Total}). The 0.5 and 1 µm pore diameters were used in the calculations. Truncated V_{Pores}, V_{Total}, and S_{Total} values for each configuration of nano-porous samples are shown in Table 7.28. All values in the table were truncated to conserve table space.

Table 7.28. Estimated number of the available bonding sites, (S_{Total}), on each sample type.

Oil Amt	**0.5 µm dia, 25 µm D**	**0.5 µm dia, 50 µm D**	**0.5 µm dia, 75 µm D**	**1 µm dia, 25 µm D**	**1 µm dia, 50 µm D**	**1 µm dia, 75 µm D**
V_{Pores} $(cm)^3$	6.136E -09	1.227E -08	1.841E -08	1.104E -08	2.209E -08	3.313E -08
V_{Total} $(cm)^3$	3.638E -08	4.251E -08	4.865E -08	4.129E -08	5.233E -08	6.338E -08
S_{Total}	4.431E +14	5.178E +14	5.926E +14	5.029E +14	6.374E +14	7.719E +14

The results presented in Table 7.28 indicate the changes in pore depth and diameter had an effect on S_{Total}. The S_{Total} values increased as the pore depth increased for both pore diameters. This outcome suggests deeper pores have greater potential to improve lubricant retention due to the higher S_{Total} values. It was proven from the thermodynamics standpoint that the inclusion of hydrogenated a-Si film enhanced lubricant retention more than surfaces that omitted it. It was also proven that smooth Si-Cu/a-Si:Dehydrogenated samples benefited from the Si-C bonding sites. Less obvious is whether the greater S_{Total} that occurred for the respective depths of the 1

μm diameter pores will improve lubricant retention above those of the 0.5 μm diameter pores. In other words, are the differences between the S_{Total} of the respective depths of the two diameters sufficient enough to significantly impact the mass of the lubricant so that it is detectable? Another question to be answered for the larger pores is whether the greater lubricant loss caused by the reduction in R_T will be offset by the greater S_{Total} which helps retain lubricant? Evaporation testing will resolve these questions as well as adjudicate the predictions made in section 7.1.4 concerning the thermal behavior of the various topographies.

7.3 Lubricant Retention Results from Evaporation Tests

This section discusses the lubricant retention results obtained during evaporation testing. Section 7.3.1 discusses the results for smooth samples and section 7.3.2 discusses the results obtained for nano-porous topographies. Also discussed in section 7.3.3 are the crossover situations encountered during testing. Crossovers are the points of diminishing returns discovered during data analysis where the benefits of the proposed improvements such as surface chemistry modification or pore depth or diameter changes were less attractive for enhancing lubricant retention.

The sample types tested were smooth Si-Cu, smooth Si-Cu/a-Si:Dehydrogenated, patterned Si-Cu, and patterned Si-Cu/a-Si:Dehydrogenated. There were 2 pore diameters and 3 pore depths tested for the nano-porous topographies. The evaporation of lubricant was performed using 3 testing temperatures on a total of 216 samples. As demonstrated in Table 7.27, there were 6 data points per sample which brought the total data set to 1296 points. Each point represented the amount of lubricant that remained on a sample after a 5 min testing increment. The tare mass of the sample was subtracted from the amount of lubricant retained after each testing increment to

arrive at the *Δmass* value for that duration. Consequently, the data values were used in the forthcoming charts detailing the results of lubricant retention.

Including in a chart every permutation of the data collected during testing would mean scores of charts would have to be plotted, and that would make the analysis of them cumbersome. The charts included in this work were selected to represent the behaviors of the various topographies as they were exposed to changes in pore diameter, pore depth, and testing temperature, in addition to surface chemistry modification (before-and-after). These parameters are presented in various combinations to reduce the number of required charts. After paring the available choices, 4 charts are presented throughout this section in Figures 7.5 - 7.8.

There were some commonalities in the charts that should be discussed before the comprehensive analysis of them begins. Each of the charts compared the retained lubricant mass versus the testing duration. Six samples were used in each chart to establish the trends associated with the effects under consideration. Every sample had 18 data points on display because the data represented the averages of retained lubricant mass compiled from 3 samples and the *Δmass* for 6 test durations from each of those samples. The *Δmass* values in all of the charts began at the 5 min test duration. The reasons for doing so are explained in the Appendix.

Observe also that none of the charts contained error bars on the data points. It must be kept in mind that the measurements were obtained using a digital scale whose accuracy was 0.1 ± 0.05 mg. It is not disputed that the scale's accuracy may have affected the readings. Any experimental testing results will have subjective outcomes that may be difficult to duplicate or quantify precisely. Perhaps shorter test durations or a scale with greater accuracy might have revealed minor differences in the retained lubricant mass between the samples. Instead of expecting NIST precision from the numerical quantities, what are being emphasized in this work

are trends that can be gleaned from the data. Other than the commonalities expressed in this and the previous paragraphs, the 4 charts provided a wide variety of information supporting the trends observed throughout the evaporation tests.

7.3.1 Lubricant Retention Results for Smooth Topographies

The first chart illustrates the effects of dehydrogenated a-Si film and temperature change on smooth topographies. The samples were tested at 300, 350, and 400°C temperatures. Comparisons and analyses were made for topographies having dehydrogenated a-Si film and those omitting the film for each of these temperatures. The plots are shown in Figure 7.5.

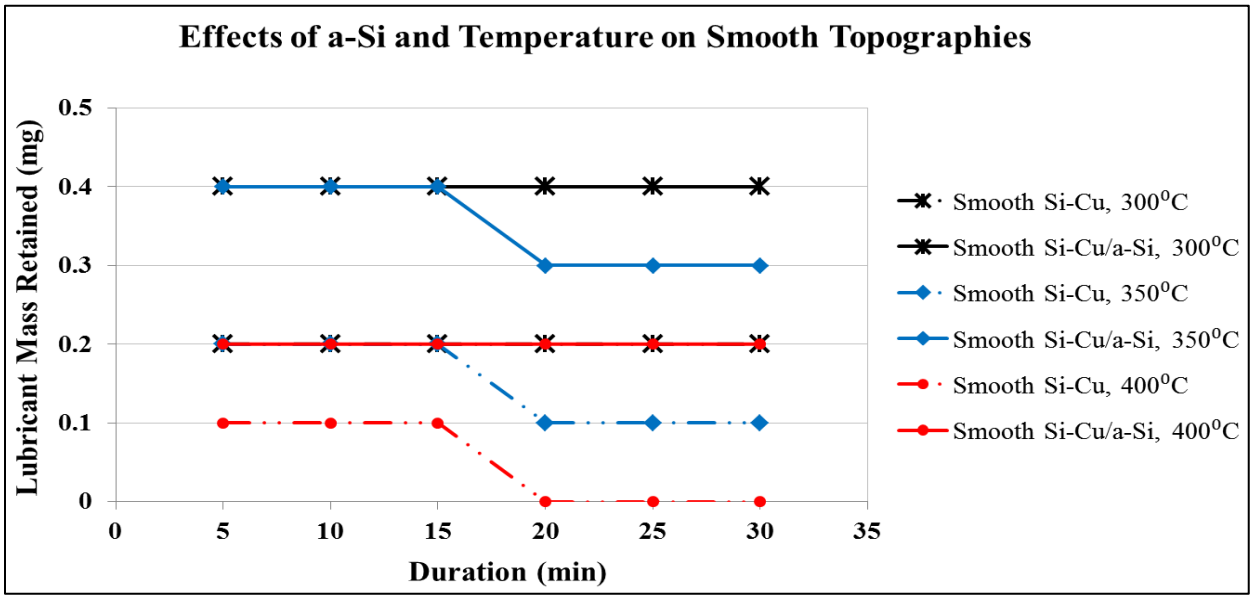

Figure 7.5. The chart demonstrates the effects of dehydrogenated a-Si film and temperature on smooth topographies (*Image from the author*).

It should be explained that an outcome which was rather surprising for smooth samples was the step taken to deposit equivalent lubricant on them was unnecessary. Recall that the equivalent lubricant solution for smooth samples was proposed and a way to favorably compare them with porous topographies having a change in pore diameter from 0.5 to 1 µm and to promote an equivalent amount on smooth samples that mirrored the 25, 50, and 75 µm depths of nano-

porous topographies. In reality, there was no retention difference for smooth topographies having equivalent lubricant when they were tested at a fixed temperature. This was because the equivalent lubricant amounts became excess lubricant that was easily evaporated away during the first 5 min of testing.

The contributors that had an impact on the amount of lubricant on smooth samples in Figure 7.5 were the testing temperature and duration and dehydrogenated a-Si film. Smooth Si-Cu samples that omitted dehydrogenated a-Si film were represented by plots having a dashed line style, while those having the film featured a solid line. Investigating the effect of temperature on the samples indicated the most lubricant was retained at the lowest temperature of 300°C. The least amount retained occurred for the samples tested at 400°C. The downward trend in the retention values of the respective plots was generally indicative of progressively higher temperatures but could also be due to longer testing durations. The effect of temperature is consistent with predictions based on Table 7.22 values for Q_{net}. Interestingly, the samples with dehydrogenated a-Si film that were tested at 400°C maintained the same amount of lubricant as the bare Si-Cu samples tested at 300°C. The 100°C temperature differential is significant. This affirms the benefit of using dehydrogenated a-Si film to enhance the retention of lubricant.

When comparing the results of the samples before and after the application of dehydrogenated a-Si film, the samples with the film retained more lubricant than its counterparts at the same temperature without the film. For the 300 and 350°C temperatures, the retained mass differential amounts were 0.2 mg throughout the entire duration of testing. As expected, the samples tested at the higher temperature, 350°C, lost more oil than ones tested at 300°C during the latter half of the testing duration's range but the differential held firm. The samples tested at 400°C had a retained mass differential of 0.1 mg during the first half of the testing duration's range. The

temperature increase initially had a greater effect on these samples, so the mass differential was not as significant as the ones for lower temperatures. However, the samples containing dehydrogenated a-Si film exerted their supremacy over the bare samples during the latter half of the testing duration's range by achieving a 0.2 mg savings. In summary, the results in Figure 7.5 showed dehydrogenated a-Si film gave the samples important advantages regarding lubricant retention, irrespective of the temperature, and the effect of testing duration was only evident during the latter half of the test duration's range for 350 and 400°C temperatures.

7.3.2 Lubricant Retention Results for Nano-Porous Topographies

It was important to observe the effects of depth and diameter on nano-porous Si-Cu samples. This was done using samples that had 0.5 and 1 µm pore diameters and 3 pore depths that were 25, 50, and 75 µm for each diameter. The evaporation testing temperature was maintained at 300°C for all samples. The plots are shown in Figure 7.6.

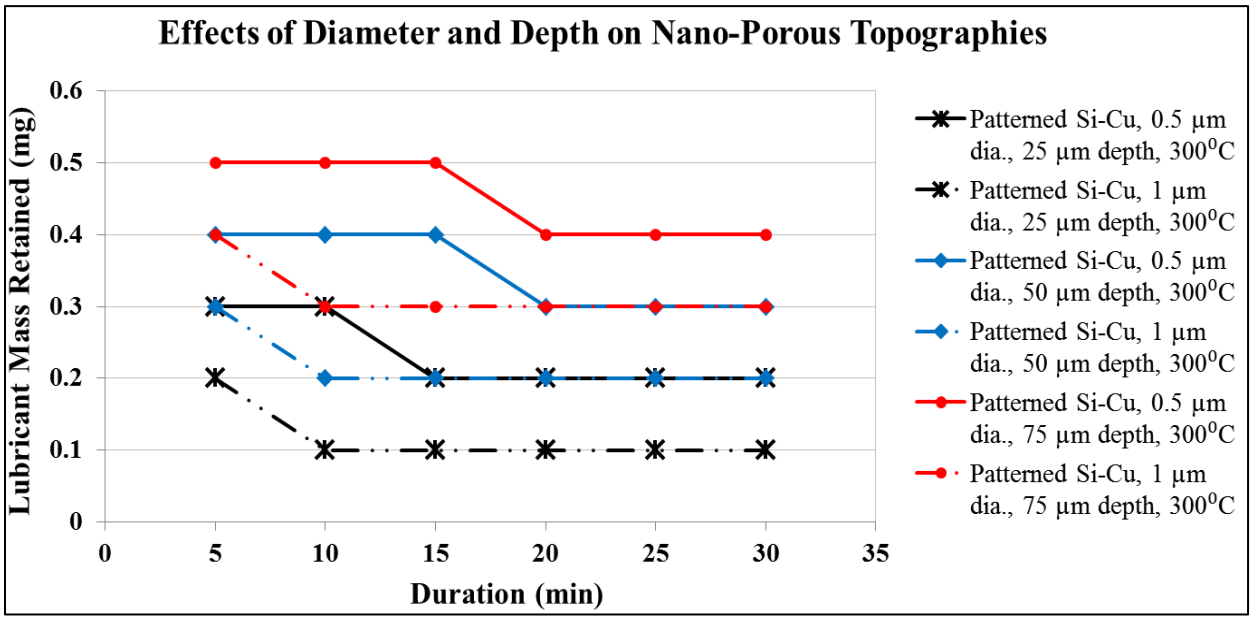

Figure 7.6. The chart demonstrates the effects of pore depth and diameter on the lubricant retention of nano-porous topographies (*Image from the author*).

Although the samples in Figure 7.6 omitted the dehydrogenated a-Si film, they compared favorably with those having the film in the sense that pore geometry affected the retention behavior of both similarly, though not equally. The depths could be held constant for allowing comparisons between patterned Si-Cu samples with different diameters. The result was the 1 μm pore diameter lost more oil than the samples having 0.5 μm diameter pores. The lubricant mass differential of samples having a 1 μm pore diameter was only 0.1 mg for the first 5 min of testing but the amount increased to 0.2 mg for the 10 min test duration. After the 15 min test duration, the amount of lubricant on these samples remained constant, but the 1 μm diameter samples were still lower than the 0.5 μm diameter ones for the remainder of the test duration.

The superior retention of the samples having a 0.5 μm diameter was displayed by their maintaining a 0.1 mg greater lubricant mass differential initially, but the differential grew to 0.2 mg for the 10 and test duration. Afterward, the lubricant mass differential dropped to 0.1 mg for the remainder of the test duration. To summarize, the retention behaviors in Figure 7.6 were related to the difference in the diameter of the pores. The prediction based on Table 7.21 was the smaller diameter pores caused higher R_T and therefore would require more heat to evaporate lubricant. All of the samples having 0.5 μm diameter pores retained more lubricant, so the prediction was proven true. This outcome was confirmed for all depths by their maintaining identical differentials throughout the entire range of testing.

In Figure 7.6, the pore depth affected the overall lubricant mass, with the 75 μm pores retaining the greatest amount of lubricant. The patterned Si-Cu samples with a 1 μm pore diameter and 25 μm pore depth had the lowest amount of retained lubricant. This patterned sample, curiously, did not hold more lubricant than the smooth Si-Cu samples tested at 300°C. In fact, the Si-Cu samples with 0.5 μm diameter pores and 25 μm depth was only better at retaining lubricant over

smooth Si-Cu samples for the first 5 min of testing before they were equal with the retention of smooth samples. The result here is the porous Si-Cu topographies had a threshold for the depth that required it to be greater than 25 µm in order to be a viable choice for enhancing lubricant retention. Additionally, samples having 1 µm diameter pores required deeper pores than the 0.5 µm diameter ones to overcome the tendency of wider pores to lose more lubricant mass.

The data for patterned Si-Cu samples that had dehydrogenated a-Si film reinforced the results obtained for those without the film, albeit the samples with the film retained more lubricant than their bare counterparts in Figure 7.6 that were tested at the same temperature and depth. Patterned Si-Cu and Si-Cu/a-Si:Dehydrogenated samples were tested to investigate the effects of a-Si:Dehydrogenated film and depth on nano-porous topographies. Three pore depths were tested while the pore diameter was held constant at 1 µm. The testing temperature was maintained at 300°C. The results are shown in Figure 7.7.

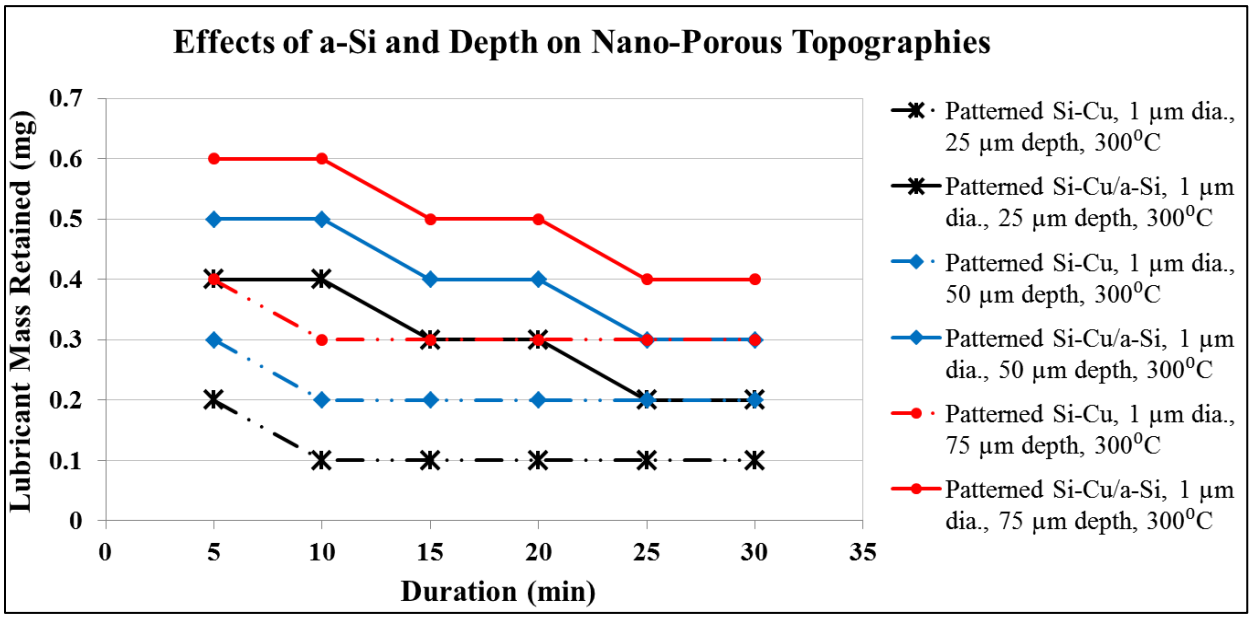

Figure 7.7. The chart demonstrates the effects of dehydrogenated a-Si film and pore depth on the lubricant retention of nano-porous topographies (*Image from the author*).

From the data plotted in Figure 7.7, clearly the depth of the samples was a key parameter for improving lubricant retention. A comparison between the patterned Si-Cu samples and Si-Cu/a-Si:Dehydrogenated samples with a 1 μm pore diameter and the 3 depths tested indicated the pore depth of patterned samples having dehydrogenated a-Si film provided a consistent 0.1 mg lubricant mass differential per 25 μm increase in the depth. This meant the 75 μm depth retained the most lubricant, followed by 50 μm, and lastly 25 μm. The patterned samples with dehydrogenated a-Si film performed better than patterned Si-Cu samples in that a larger lubricant mass differential occurred by decreasing the diameter rather than increasing the depth. The predictions alleged earlier in Table 7.21 that the pore depth increase and pore diameter decrease would increase the required heat to induce evaporation were proven true.

Overall, the prediction that the inclusion of dehydrogenated a-Si film on samples would enhance the retention of lubricant was also proven true. The lubricant mass differential between the patterned Si-Cu samples and Si-Cu/a-Si:Dehydrogenated ones in Figure 7.7 were characterized by 0.2 mg oil savings for dehydrogenated a-Si-deposited samples after the first 5 min of testing. The lubricant mass differential grew to 0.3 mg for the 10 min testing duration, but returned to 0.2 mg for the 15 and 20 min test durations. For the remainder of the tests, the lubricant mass differential dropped to 0.1 mg. The lubricant mass differential's pattern of behavior indicated the test duration was influential on the retained lubricant mass for the simple reasons that the lubricant mass differential of the samples remained consistent, regardless of the depth, and temperature and diameter changes were not factors in this case. If the temperature was allowed to increase, the effect on the curves in the figure would reflect a general collapsing of the respective curves toward lower lubricant mass differential values. This effect can be demonstrated by examining the next chart in Figure 7.8.

An investigation was done to determine the effects of dehydrogenated a-Si film and temperature on nano-porous topographies. The 0.5 µm pore diameter and 75 µm pore depth were chosen for testing. The testing temperatures were 300, 350, and 400°C. Patterned Si-Cu and Si-Cu/a-Si:Dehydrogenated samples were used in the tests to assess the benefit of dehydrogenated a-Si film. The results are shown in Figure 7.8.

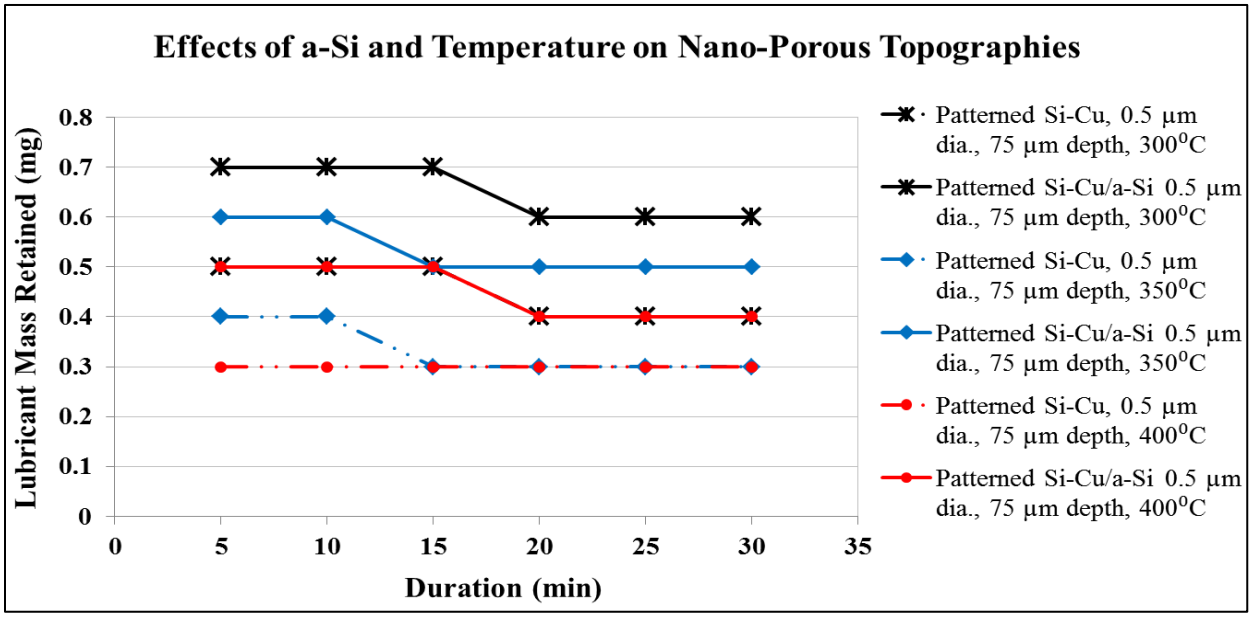

Figure 7.8. The chart demonstrates the effects of dehydrogenated a-Si film and temperature on the lubricant retention of nano-porous topographies (*Image from the author*).

The two sample types tested and plotted in Figure 7.8 were the most successful ones for improving lubricant retention. This was because the deepest pore and narrowest diameter have been proven to maximize retention. The difference was the samples having dehydrogenated a-Si film had higher retained oil mass due to the increased R_T of the pores. For example, the patterned Si-Cu/a-Si:Dehydrogenated samples retained 0.7 mg oil during the first half of the test duration's range for the 300°C testing temperature versus 0.5 mg retained by the patterned Si-Cu samples. This represented a lubricant mass differential of 0.2 mg, but when the patterned

samples containing dehydrogenated a-Si film were compared with the performance of smooth Si-Cu/a-Si:Dehydrogenated samples of Figure 7.5, the lubricant mass differential increased to 0.3 mg.

The mass differential of 0.2 mg was maintained for 300 and 350°C throughout the whole testing duration in Figure 7.8. This differential value was maintained at 400°C as well for the first half of the test duration's range before being reduced to 0.1 mg through the end. The combination of the higher temperature and longer test duration eventually affected the patterned Si-Cu/a-Si:Dehydrogenated samples, whereas the patterned Si-Cu samples obtained a 0.3 mg value from the beginning of testing and maintained it throughout the testing duration at 400°C. These behaviors typified many of the testing results that included dehydrogenated a-Si film—an extension of the test duration's range before the samples experienced a drop in the mass of retained lubricant. The dehydrogenated a-Si film undoubtedly had an extraordinary impact on the lubricant retention performances of all types of samples tested.

The lowest temperature had the highest retained lubricant mass as predicted by the I_{net} results in Table 7.21. The lubricant mass' downward shifting behavior that occurred for the 300 and 350°C in Figure 7.8 was characteristic of an increase in temperature. The mass shift for 300°C occurred at 20 min test duration and earlier at the 15 min duration for 350°C which demonstrated the influence of higher temperatures on the samples. An observation worth pointing out was the patterned Si-Cu/a-Si:Dehydrogenated samples that were tested at 400°C had the same retention behavior as the patterned Si-Cu samples tested at 300°C. This indicated dehydrogenated a-Si film was the major reason the patterned Si-Cu/a-Si:Dehydrogenated samples were able to compete against the 100°C temperature difference.

7.3.3 Crossover Conditions in the Lubricant Retention Data

The results shown in Figures 7.5 combined with those in Figure 7.8 made up the "best of all samples" for retaining lubricant. However, it was interesting to know how other samples having different depths fared in a comparison with smooth Si-Cu/a-Si:Dehydrogenated samples. The reason for this comparison was to illustrate the presence of crossover situations encountered during testing which identified the sample conditions where there were no gains in lubricant retention. These situations were few for the 216 samples that were tested because there was duplication of some of the crossover conditions for the 3 testing temperatures—but they were worth pointing out.

In a way, the nano-porous samples included in the crossover charts were data outliers. The perfect-world scenario would suggest that even the shallowest pore depth should surpass the lubricant retention performance of a smooth topography. This was not the case in a few instances. Despite being data outliers, these samples' data were useful because they supported several conclusions drawn earlier regarding lubricant retention behavior. To find the crossover points, the data was plotted for 300, 350, and 400°C temperatures. Three pore depths of 25, 50, and 75 μm were used in conjunction with 0.5 and 1 μm diameter pores. The sample types used in the comparison with the smooth Si-Cu/a-Si:Dehydrogenated topography were patterned Si-Cu and Si-Cu/a-Si:Dehydrogenated. The results are shown in Figures 7.9 - 7.11. An analysis of the figures follows their presentation. The crossover chart for the 300°C testing temperature is shown in Figure 7.9.

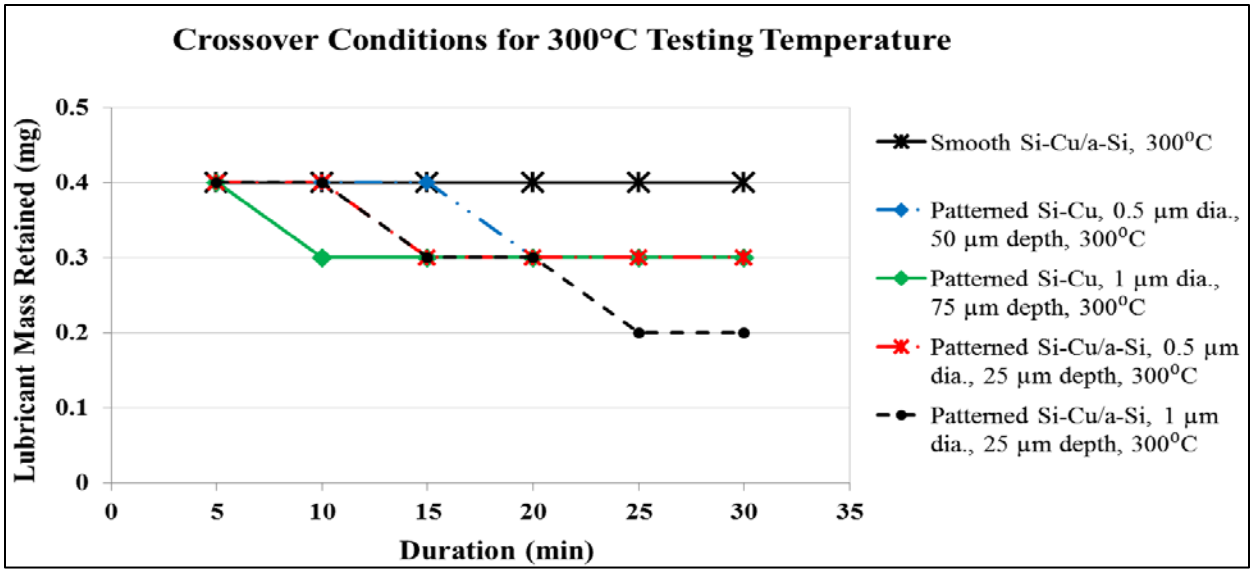

Figure 7.9. Sample types demonstrating the crossover conditions occurring at 300°C testing temperature (*Image from the author*).

The first item to note in Figure 7.9 was the retention performance of the smooth Si-Cu/a-Si:Dehydrogenated samples. This was the baseline for comparing the lubricant retention of the other sample types. The smooth samples maintained a constant 0.4 mg lubricant mass for the whole test duration. The advantage of having dehydrogenated a-Si film as a chemistry modifier was on display with these samples as evidenced by the constant retention value. What happened next when comparing the results of the smooth samples to the patterned Si-Cu samples that had a 0.5 µm diameter and 50 µm depth and the patterned Si-Cu samples that had a 1 µm diameter and 75 µm depth was remarkable in that this scenario provided a good opportunity to judge the retention predictions in Table 7.21. On one hand were patterned Si-Cu samples having a larger diameter (1 µm) and the deepest pores (75 µm). On the other hand were patterned Si-Cu samples that had the narrowest diameter (0.5 µm) and shallower pores (50 µm). Neither of the patterned samples outperformed the smooth samples, but they helped affirm which situation of the two was better to have for enhancing lubricant retention.

Recall that deeper pores could improve retention just as narrow pores could, though not equally. The patterned Si-Cu samples with the 0.5 µm pore diameter and 50 µm pore depth retained 0.4 mg of lubricant for the first half of the testing duration's range, just like the smooth samples, before the patterned samples' retention reduced to 0.3 mg for the remainder of the testing duration's range. The patterned Si-Cu samples with a 1 µm pore diameter and 75 µm pore depth retained 0.4 mg mass for the first 5 min of testing but dropped to 0.3 mg for the remainder of the test duration's range. The results show was it was better to have the narrower pore diameter on patterned Si-Cu samples. This was confirmed when comparing the respective I_{net} values in Table 7.21 for the patterned Si-Cu samples tested at 300°C. More heat was required to evaporate lubricant from the narrow pore even though it had the shallower depth.

Equally remarkable was the behavior of the patterned Si-Cu/a-Si:Dehydrogenated samples in Figure 7.9. Each sample type had a 25 µm pore depth. The only difference was the pore diameters. The retention hypothesis suggests the narrow pore should be superior. In terms of the retention results, both sample types retained identical lubricant amounts for the first 20 min test duration. Both samples types maintained 0.4 mg mass for 10 min before reducing to 0.3 mg for the next 10 min. From the 20 min duration until the end of testing, the lubricant mass differential was 0.1 mg, which meant the samples with a 1 µm pore diameter lost more lubricant during the latter testing duration than the ones having 0.5 µm diameter pores. The prediction for narrower pores ultimately was proven true, but the results have a caveat related to the predictions in Table 7.21; namely, that the table was based on steady state conditions and therefore cannot be used to predict every retention behavior such as that which occurred for the first 20 min test duration.

A further test of the predictions of Table 7.21 can be done by comparing the patterned Si-Cu samples that had a 1 µm diameter and 75 µm pore depth to the patterned Si-Cu/a-

Si:Dehydrogenated samples having a 1 µm diameter and 25 µm depth. Figure 7.9 comparisons gave an opportunity to test the retention limit of for dehydrogenated a-Si film in the shortest pores versus the retention of the deepest pores in Si-Cu samples that omitted dehydrogenated a-Si film. If there were patterned Si-Cu/a-Si:Dehydrogenated samples that did not perform better than smooth Si-Cu/a-Si:Dehydrogenated overall, it would be those having a 25 µm pore depth and 1 µm pore diameter. This is because the pore depth was not significant and I_{net} values were lower for this pore diameter. The patterned Si-Cu/a-Si:Dehydrogenated samples having a 1 µm pore diameter and 25 µm pore depth in Figure 7.9 were superior initially, in that they had a 0.1 mg lubricant mass differential over the patterned Si-Cu samples having a 1 µm pore diameter and 75 µm pore depth for the 10 min testing duration. That advantage was lost, however, for the 15 to 20 min test duration where the samples had an equal retained mass of 0.3 mg. The patterned samples having the 75 µm depth then maintained its 0.3 mg amount while the ones with a 25 µm depth and dehydrogenated a-Si film lost more oil which created a 0.1 mg mass differential for the 25-30 min test duration. Even though the samples having dehydrogenated a-Si film and 25 µm depth lost oil in the end, its ability to stay close to the retention values of the sample with 75 µm deep pores was impressive.

Other crossover conditions existed for the 350°C testing temperature. There were 4 crossover conditions encountered during testing as were for the 300°C testing temperature. The 4 sample types consisted of patterned Si-Cu having a 75 µm depth and patterned Si-Cu/a-Si:Dehydrogenated having a 25 µm depth. Both pore diameters were represented in each sample type. The lubricant retention of the patterned samples was compared to those of smooth Si-Cu/a-Si:Dehydrogenated samples. The results are shown in Figure 7.10.

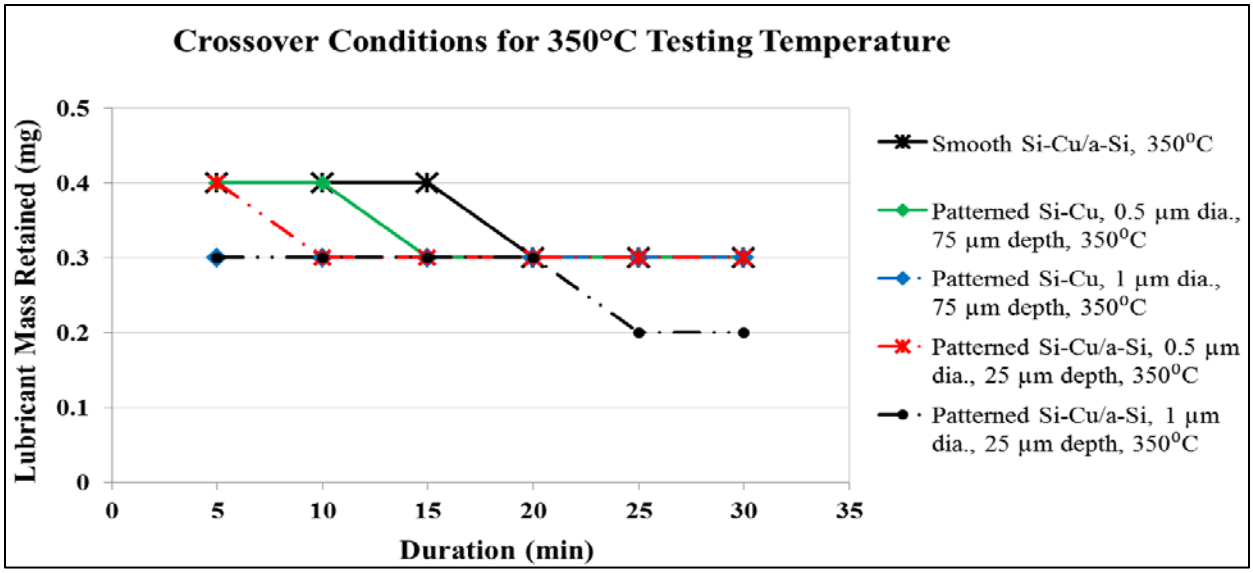

Figure 7.10. Sample types demonstrating the crossover conditions occurring at 350°C testing temperature (*Image from the author*).

The lubricant mass of the smooth Si-Cu/a-Si:Dehydrogenated samples continued to be the baseline for comparison to the patterned samples. The smooth samples maintained 0.4 mg lubricant mass for the first half of the testing duration's range and then reduced to 0.3 mg for the remainder of the range. Comparing the results which occurred for the smooth samples in Figure 7.9 to the ones here demonstrates the effect of the higher temperature where the familiar downward shift in retention occurred during the latter testing durations. If using the outcomes reported from the crossover samples tested thus far and predictions from Table 7.21, it should be no surprise that the patterned Si-Cu samples in Figure 7.10 having 0.5 µm diameter pores and 75 µm depth was competitive with the smooth Si-Cu/a-Si:Dehydrogenated samples. Though these were samples without a-Si:Dehydrogenated film, they had the advantages of a narrow pore diameter and the deepest pores. The patterned Si-Cu samples had a 0.4 mg lubricant mass for the first 10 min test duration's range and then reduced to 0.3 mg for the remainder of the range. The reduction created a 0.1 mg lubricant mass differential for the 15 min test duration only.

Comparing the results of patterned Si-Cu samples having a 0.5 μm diameter and 75 μm depth with the patterned Si-Cu/a-Si:Dehydrogenated samples having a 0.5 μm diameter and a 25 μm depth showed the positive influence of a-Si:Dehydrogenated film on lubricant retention, despite having the shallowest depth.

The patterned Si-Cu/a-Si:Dehydrogenated samples in Figure 7.10 with a 0.5 μm diameter and a 25 μm depth retained 0.4 mg of oil initially for the 5 min test duration and then reduced to 0.3 mg for the remainder of the test duration's range. The lubricant mass differential of these samples and smooth ones was 0.1 mg for the 10 and 15 min test durations, so these samples were highly competitive with the lubricant mass retention of patterned Si-Cu samples having the narrow diameter (0.5 μm) and deepest pores (75 μm). The deep pores on the patterned Si-Cu samples had a slight advantage over the patterned Si-Cu/a-Si:Dehydrogenated ones principally because of the extra depth.

An evaluation of patterned Si-Cu samples with a 1 μm pore diameter and 75 μm pore depth showed that they maintained 0.3 mg lubricant mass throughout the entire test duration's range. This produced a 0.1 mg lubricant mass differential for the first half of the testing duration's range when compared to smooth Si-Cu/a-Si:Dehydrogenated samples. The patterned Si-Cu samples retention behavior was the same as the smooth samples for the remainder of the testing duration's range. The patterned Si-Cu/a-Si:Dehydrogenated samples having a 1 μm pore diameter and 25 μm pore depth maintained 0.3 mg lubricant mass for the first 20 min of the test duration's range before reducing to 0.2 mg for the remainder of the range. They were only equal to smooth Si-Cu/a-Si:Dehydrogenated samples for the 20 min test duration; otherwise, there was a 0.1 mg lubricant mass differential for the rest of test duration's range. The 1 μm pore diameter coupled with the 25 μm depth resulted in these samples achieving the worst retention

performance against smooth Si-Cu/a-Si:Dehydrogenated samples. The results in Figure 7.10 proved there were limits to the ability to compare the thermal behavior in Table 7.21 of patterned Si-Cu/a-Si:Dehydrogenated samples having a 25 µm depth with patterned Si-Cu samples having a 75 µm depth at the 350°C test temperature.

The final crossover data was analyzed for the 400°C testing temperature. There were patterned Si-Cu and patterned Si-Cu/a-Si:Dehydrogenated sample types whose data was plotted alongside the baseline smooth Si-Cu/a-Si:Dehydrogenated samples. The results are shown in Figure 7.11.

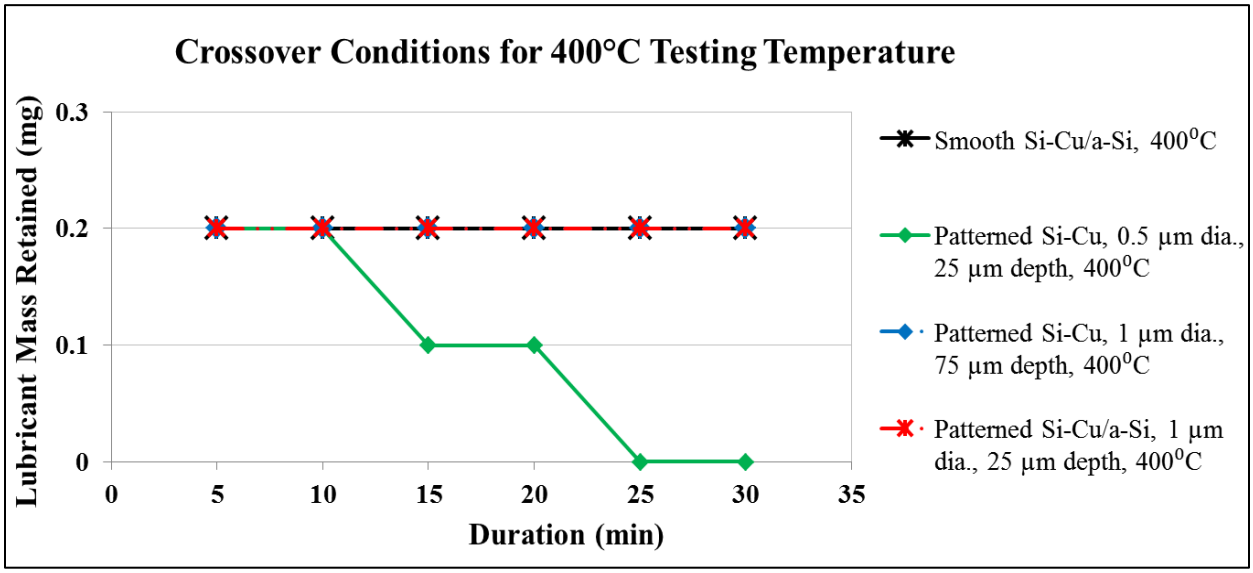

Figure 7.11. Sample types demonstrating the crossover conditions occurring at 400°C testing temperature (*Image from the author*).

This chart had fewer crossover conditions (3) than the other test temperatures. At the outset, it was noted that 3 of the 4 samples had identical lubricant retention amounts of 0.2 mg throughout the whole test duration's range. The effect of the high testing temperature on these samples was evident when comparing the results in this figure to Figures 7.9 and 7.10. The baseline smooth Si-Cu/a-Si:Dehydrogenated samples for the 400°C test temperature had a lubricant mass differential that was 0.2 mg throughout the entire test duration's range when compared to the

300°C testing temperature. The lubricant mass differential for the 350°C test temperature compared to the 400°C testing temperature for smooth Si-Cu/a-Si:Dehydrogenated samples was 0.2 mg for the first half of the test duration's range before reducing to 0.1 mg at the 20 min test duration. The retained masses were equal for the 25 and 30 min test durations.

Figure 7.11 revealed further corroboration of the lubricant retention enhancement capabilities of a-Si:H film. The patterned Si-Cu/a-Si:Dehydrogenated samples with a 1 μm pore diameter and 25 μm pore depth competed favorably with the patterned Si-Cu samples having the same diameter and 75 μm deep pores, with both sample types retaining 0.2 mg of lubricant throughout the entire test duration's range. There was equivalence to the 0.2 mg retention of smooth Si-Cu/a-Si:Dehydrogenated samples with the patterned Si-Cu samples having 0.5 μm diameter pores and a 25 μm depth for the 5 and 10 min test durations. The amount of retained lubricant on these samples reduced to 0.1 mg for the 15 and 20 min test durations before reducing to zero for the 25 and 30 min durations. The results showed that although these samples had the narrow pores, the other sample types had either dehydrogenated a-Si film or deep pores that overcame the lubricant-saving effect of narrow pores.

In summary, the crossover conditions were plotted and analyzed to determine the outliers that existed for 300, 350, and 400°C testing temperatures where there was diminished lubricant retention enhancement over the performance of smooth Si-Cu/a-Si:Dehydrogenated samples. A total of 11 crossover conditions existed for the data collected on 216 samples. In reality, though, several of these conditions were duplicated for the 3 testing temperatures. These conditions might have occurred because of errors in the photolithography and fabrication processes that produced inconsistences in the dimensions of the pores, inconsistencies in the Cu and dehydrogenated a-Si film thicknesses deposited on the samples, the wafer dicing process created

tare mass differences between samples of the same type, quantization errors associated with the digital scale used for mass measurements, or errors made while recording the data. Despite these errors, all of the patterned samples containing dehydrogenated a-Si film in the crossover charts were close to the lubricant mass retention of smooth samples, regardless of the temperature.

CHAPTER 8

SUMMARY

8.1 Overview of the Research Objectives

The purpose of this research was the characterization of nano-porous Si-Cu composites to enhance lubricant retention that impacted the tribological properties of sliding surfaces. An investigation of the capabilities of smooth and nano-porous Si-Cu composite samples was done to determine the topographies that were the most successful for improving the retention of lubricant by reducing its evaporation.

While simulation software such as Ansys™ might have told one the final outcome of the thermodynamic behavior encountered by the sample types, the knowledge of specific factors which caused the lubricant retention outcomes would not have been obvious, nor would an understanding and appreciation of the underlying engineering principles been demonstrated. Tables were created to organize the information concerning the physical properties of the materials to be used in the fabrication of the samples and to facilitate the calculation of R_T. The R_T values were included in the thermal resistance networks constructed for calculating the conduction heat transfer used in the determination of Q and I. The convection and radiation heat transfers were calculated also. The outcomes from the 3 heat transfer modes were brought together to produce Q_{net} and I_{net} tables for smooth and patterned samples, respectively. These tables served as thermodynamics-based numerical models for predicting the lubricant retention behavior of the various sample configurations. Comparison of the model predictions with the results from evaporation testing was done to test the validity of the models.

Si wafers were patterned using photolithographic techniques. Pores were etched into the patterned Si wafers to depths of 25, 50, and 75 μm using DRIE. There were two pore diameters, 6 and 6.5 μm, used for the samples. Various Cu deposition techniques were employed on smooth and patterned c-Si wafers to create Si-Cu composite samples having 0.5 and 1 μm final pore diameters. These smooth and patterned Si-Cu samples were used as control specimens.

Smooth and patterned Si-Cu samples were also deposited with a-Si:H film using PECVD to serve as a surface chemistry modification for investigating the thermal effect of the film on the retention of lubricant. This effect was accounted for in the thermodynamics-based numerical modeling. Another investigated effect of a-Si:H film was its ability to promote greater bonding opportunities than the normal physisorbed interaction of the film and lubricant. FTIR spectroscopy was implemented to create a model that estimated the H atom concentration in a-Si:H film. Knowledge of the H atom concentration provided an estimate for the number of available bonding sites, S_{Total}, between the lubricant and dangling Si atoms. These sites and C in the lubricant offered good opportunities for enhancing lubricant retention.

To expose the dangling Si bonds, dehydrogenation of a-Si film needed to be performed. Dehydrogenation occurred by subjecting the samples to an oven temperature of 350°C for 1 h. It was confirmed by the decreased sheet resistance of the film. The lubricant retention of smooth Si-Cu samples was tested in comparison with smooth Si-Cu/a-Si:H and smooth Si-Cu/a-Si:Dehydrogenated ones to determine which result—hydrogenation or dehydrogenation—would be most advantageous for enhancing lubricant retention of smooth Si-Cu and patterned Si-Cu samples. At the end of 30 min retention testing, the smooth Si-Cu/a-Si:Dehydrogenated samples retained 0.2 mg more oil than the other smooth samples. The dehydrogenation of the samples was the best method for enhancing lubricant retention due to the creation of chemisorbed Si-C

bonds that were stronger than Si-H_x bonds of a-Si:H film and C-H bonds of the lubricant. The increase in retained lubricant was due to the enhanced capillary attraction of the surface toward the lubricant. Based on this outcome, all of the samples containing a-Si:H film were dehydrogenated before lubricant retention testing began.

The success of the smooth Si-Cu/a-Si:Dehydrogenated samples to retain more lubricant spurred the investigation of S_{Total} occurring in patterned Si-Cu/a-Si:Dehydrogenated samples. If there were available bonding sites present on the smooth sample, there would certainly be bonding sites that could be taken advantage of by patterned samples having dehydrogenated a-Si film. The S_{Total} would be greater than the number found on smooth samples, and that number would depend on the pore's diameter and depth. Table 7.28 showed the pores having a 1 μm diameter had more S_{Total} than 0.5 μm pores having an equivalent pore depth. The question to be answered was, "How would this information about S_{Total} manifest itself?" Testing the samples by the evaporation of lubricant from the various topographies would help answer this question.

A lubricant retention testing scheme was devised for all of the sample configurations. The task included designing and employing a custom lubricant evaporation test apparatus. There were 216 samples to be tested in the apparatus. The samples were weighed before testing to obtain their tare mass and 3-N-One™ penetrating oil of a specified amount was deposited on each one. Three testing temperatures of 300, 350, and 400°C were used. Testing durations occurred in 5 min increments, with the total testing duration culminating in 30 min for each sample. The *Δmass* readings were obtained at each increment. The retention results of 3 samples were used to produce averaged *Δmass* readings. Although the duration of testing was not explicitly indicated in the models, most samples types that were tested lost lubricant as the testing proceeded toward

the end of its 30 min duration—if the sample's retention results were constrained to a fixed temperature.

The retention results were plotted in the charts shown in Figures 7.5 - 7.8 to demonstrate the effects of pore diameter, pore depth, dehydrogenated a-Si film, and temperature on the samples. The effects were arranged in strategic combinations to reduce the total number of charts. The crossover conditions in the data, or the situations where there was no point in introducing pores or a-Si film on the topographies to enhance lubricant retention, were also plotted to give information about the anomalies in the data. The crossover points also showed the conditions where the numerical models failed to fully anticipate the lubricant retention behavior of certain topographies when compared to others.

8.2 Similarities and Differences of the Thermodynamic Models

Numerical model results were used to predict the lubricant retention behavior of the various configurations of smooth and patterned Si-Cu samples. There were separate models, I_{net} and Q_{net}, shown in Tables 7.21 and 7.22 for smooth samples and patterned ones, respectively. Overall, both models were successful in their purpose.

Some similarities existed in the models. The models showed numerical results for the 3 testing temperatures. Also, the models incorporated the pore diameter and depth designations. The nano-porous topographies were patterned with different pore diameters and depths, so Table 7.21 was set up using the depth and diameter designations to reflect the required heat for the different configurations. In response, the heat transfer calculations in Table 7.22 were arranged using pore depth and diameter designations to indicate equivalent lubricant conditions on smooth samples for convenient heat transfer comparisons to its nano-porous counterparts.

The models were dissimilar in a few ways. For instance, the I_{net} model for nano-porous samples was not accurate when predicting that all sample types tested at progressively higher temperatures lost more lubricant than samples tested at lower temperatures. A fixed temperature must be used as explained on page 220. Table 7.21 results were used for comparing the I_{net} of patterned samples so that if a value in the table was smaller than others, it meant the sample type had a higher propensity toward evaporation.

The Q_{net} model for smooth samples was accurate when predicting that all sample types tested at progressively higher temperatures lost more lubricant than samples tested at lower temperatures. Table 7.22 results were used for comparing the Q_{net} of smooth samples so that if a value in the table was larger than others, the sample type had a higher propensity for evaporation than those with a smaller value. The samples with the most lubricant retained at the end of testing corresponded with the 300°C temperature, and the samples that lost the most corresponded with 400°C. Now that the peripheral matters of both tables have been discussed, the comparisons of the tables with the actual retention results are presented.

8.3 Summary of Smooth Topography Testing Results

An outcome from the Q_{net} model that was unexpected was the streamlined lubricant retention behavior of the smooth Si-Cu and smooth Si-Cu/as-Si samples. The model predicted that the equivalent amount of lubricant added to the surface would reduce Q_{net} in response to the increased thickness of lubricant on the surface. Efforts were made to ensure the smooth sample types had equivalent lubricant for favorable comparison to its nano-porous counterparts. In the end, there was no need to deposit extra lubricant on the smooth samples because it simply resulted in excess lubricant that was evaporated away during the initial moments of testing.

Adding the extra lubricant did not matter because it was located farther from the surface of the sample where capillary attraction could not aid in its retention.

The Q_{net} model for smooth sample types predicted the enhanced lubricant retention of Si-Cu/a-Si:Dehydrogenated samples over those without a-Si film. The model indicated that less heat was transferred through smooth Si-Cu/a-Si:Dehydrogenated samples, and this would translate to more lubricant retained on these sample types. Actual testing of smooth samples supported this prediction. Smooth Si-Cu samples were tested alongside smooth Si-Cu/a-Si:Dehydrogenated ones to determine the effect of dehydrogenated a-Si film and temperature on these sample types. Figure 7.5 showed the addition of the film to the samples resulted in 0.2 mg lubricant savings to the samples that included the film. This outcome was true for 300 and 350°C testing temperatures throughout the testing duration, and even for the 400°C one during the latter part of the testing duration's range.

The effect of temperature on smooth sample types was evident in the Q_{net} model and Figure 7.5 as well. The Q_{net} model predicted more heat was transferred as the testing temperatures increased from 300 to 400°C. For the actual testing at 300 and 350°C temperatures, the lubricant mass differential between smooth Si-Cu and Si-Cu/a-Si:Dehydrogenated samples was 0.2 mg throughout the entire testing duration's range. The 350°C temperature, however, experienced a downward mass shift half way through the testing duration's range. Although maintaining the 0.2 mg lubricant mass differential, the mass shift was indicative of the effect of higher testing temperatures. The 400°C testing temperature also had a lubricant mass differential, though less than the other temperatures at 0.1 mg. It experienced a mass shift that increased the lubricant mass differential to 0.2 mg. The increase occurred because the smooth Si-Cu samples lost all of their lubricant during the latter half of the testing duration's range while the Si-Cu/a-

Si:Dehydrogenated ones maintained the same lubricant mass throughout their entire testing duration. The result is the addition of dehydrogenated a-Si film caused smooth samples having the film to maintain their lubricant masses for longer testing durations, even as testing temperatures escalated. Downward mass shifts, if they occurred at all, tended to occur less frequently due to presence of the film.

8.4 Summary of Nano-Porous Topography Testing Results

The I_{net} model predicted the 0.5 µm diameter pores would retain more lubricant than 1 µm diameter pores. This prediction was applicable whether or not the nano-pores had dehydrogenated a-Si film deposited on them, and it was anticipated for all testing temperatures. Actual evaporation testing results supported this prediction well. The samples having 0.5 µm diameter pores performed better than the samples having 1 µm ones. Figure 7.6 was an example of the retention results obtained by comparing the pore diameters. The testing temperature was held constant at 300°C. In that experiment, the 0.5 µm diameter pores had as much as a 0.2 mg lubricant mass differential over the 1 µm diameter pores. This outcome was true for the 25, 50, and 75 µm pore depths.

The model for nano-porous topographies predicted higher I_{net} values as the testing temperatures increased. It must be remembered that the model was built on an imposed wattage for the I_{net} amounts. It must be accepted that higher testing temperatures produce greater evaporated lubricant amounts than lower temperatures. Therefore, for this model to be valid, the comparisons between sample types should be restricted to a fixed temperature. Looking at the combined effects of pore diameter and depth for a fixed temperature, the I_{net} model predicted the greatest lubricant loss should occur for samples having the 1 µm diameter and 25 µm depth pores. This should be true for samples without dehydrogenated a-Si film. The lubricant

retention results of Figure 7.6 affirmed this prediction. The samples were tested at 300°C, the pore diameter was 1 µm, the pore depth was 25 µm, and the sample type was patterned Si-Cu. This sample maintained the least lubricant at 0.1 mg for most of the duration of its testing. The I_{net} model also predicted the most lubricant should be retained on patterned Si-Cu/a-Si:Dehydrogenated samples having a 0.5 µm pore diameter and 75 µm pore depth. To test this prediction, patterned Si-Cu/a-Si:Dehydrogenated samples were used, the pore diameter and depth were the same as the predicted ones, and they were tested at 300°C testing temperature. The model's prediction was correct as confirmed in Figure 7.8. These samples held 0.7 mg for a portion of the testing duration before reducing to 0.6 mg for the rest of the testing duration, thus indicating their superior retention over all sample types. The results were based on a fixed temperature as cautioned earlier. To summarize, the model was effective for predicting the behavior of the best and worst patterned Si-Cu samples for retaining lubricant.

The I_{net} model was used to predict the effect of pore depth on the retention behavior of patterned Si-Cu samples, too. According to the model, the retention should improve with the increase in pore depth because of having larger I_{net} values. To examine this claim, patterned Si-Cu samples having a fixed 0.5 or 1 µm pore diameter were tested at 300°C testing temperature. The pore depth was changed from 25, to 50, and then to 75 µm. Figure 7.6 shows the results of actual testing. The 75 µm pore depth and 1 µm pore diameter held the most lubricant by maintaining a 0.2 mg lubricant mass differential over samples having a 25 µm depth and 1 µm pore diameter. The 50 µm pore depth and 1 µm pore diameter had a lubricant mass differential of 0.1 mg over the 25 µm pore depth and 1 µm pore diameter. The samples having a 0.5 µm pore diameter and 75 µm pore depth performed better than those having a 0.5 µm pore diameter and 25 µm pore depth. The 75 µm pore depth had as much as a 0.3 mg lubricant mass differential before

reducing to 0.2 mg later in the testing duration's range. The samples having a 0.5 µm pore diameter and 50 µm pore depth also performed better than those having a 0.5 µm pore diameter and 25 µm pore depth. The 50 µm pore depth had a 0.1 mg lubricant mass differential throughout the testing duration's range. The result is increasing the depth had a significant impact on lubricant retention enhancement regardless of the pore diameter.

The I_{net} model was used to predict the effect of dehydrogenated a-Si film by comparing the lubricant retention behavior of patterned Si-Cu samples and patterned Si-Cu/a-Si:Dehydrogenated ones. The prediction was the samples with dehydrognated a-Si film would have higher I_{net} than samples without it. Figure 7.7 features a chart of the results that were obtained from samples during lubricant evaporation. The samples had 1 µm diameter and pore depths of 25, 50, and 75 µm. The testing temperature was fixed at 300°C. Patterned Si-Cu samples that had dehydrogenated a-Si film retained more lubricant than the samples without it. Patterned Si-Cu/a-Si:Dehydrogenated samples had a 0.3 mg maximum lubricant mass differential that was reduced to 0.2 mg during the middle of the test duration range and finally to 0.1 mg toward the end of the testing range. The same mass differential behavior occurred for all pore depths. The 75 µm pore diameter's mass differential had the highest starting value, followed by the 50 µm, and lastly the 25 µm depth which supported the predictions of the model concerning the effects of depth and dehydrogenated a-Si film to enhance lubricant retention. The result is the higher I_{net} values that were calculated for dehydrogenated a-Si film in successively deeper pores translated to more lubricant retained, as the testing results demonstrated. The depth increase was important, but when it was coupled with dehydrogenated a-Si film, the lubricant retention results improved dramatically.

The caveats of using the I_{net} model for determining the effect of temperature on patterned Si-Cu sample types have been explained. The results of actual testing were presented in the chart in Figure 7.8. Patterned Si-Cu and Si-Cu/a-Si:Dehydrogenated samples having a 0.5 μm diameter and 75 μm depth were used to investigate the effect of temperature on lubricant retention testing. The testing temperatures were 300, 350, and 400°C. Just as the smooth samples in Figure 7.5 maintained a 0.2 mg lubricant mass differential during the 300 and 350°C testing temperatures, so did the patterned samples in figure 7.8. These patterned Si-Cu/a-Si:Dehydrogenated samples began at higher retained mass values than smooth Si-Cu/a-Si:Dehydrogenated ones. The effect of temperature was apparent by the occurrence of downward mass shifts in the lubricant retention results. The shifts occurred for 300 and 350°C testing temperatures, but it was noticed that the shift happened at an earlier testing duration for the 350°C testing temperature. This was indicative of the effect of higher temperatures. A downward mass shift occurred for the 400°C testing temperature, too, but the shift occurred in the latter half of the testing duration's range. The lubricant mass differential began at 0.2 mg during the first half of the duration's range but reduced to 0.1 mg for the latter half. This behavior occurred because the retained mass for the patterned samples having dehydrogenated a-Si film at the 400°C testing temperature began at 0.5 mg and reduced to 0.4 mg during the latter half of the testing duration's range, while the samples without the film maintained a constant 0.3 mg throughout the range. The result is the testing temperature had an effect on patterned Si-Cu samples with and without dehydrogenated a-Si film. The film helped the samples extend the duration in which they maintained their lubricant amounts. The mass shifts occurred less frequently for patterned Si-Cu/a-Si:Dehydrogenated samples than patterned Si-Cu ones, indicating temperature was less impactful on the lubricant retention of samples having the dehydrogenated a-Si film.

8.5 Summary of Crossover Condition Results

There were outliers in the data that was collected from smooth Si-Cu/a-Si:Dehydrogenated and patterned Si-Cu and Si-Cu/a-Si:Dehydrogenated sample types. These outliers are identified as crossover conditions. Crossover conditions were present in the data where the benefits of patterned surfaces and dehydrogenated a-Si film were not worthwhile to apply on smooth Si-Cu samples. These conditions were differentiated according to the testing temperatures at which they occurred. The results are shown in Figures 7.9 – 7.11.

The crossover conditions for the 300°C numbered 4. What are discussed in this paragraph are the conditions that must be met if the sample types will exceed the lubricant retention results of smooth Si-Cu/a-Si:Dehydrogenated samples. If the patterned Si-Cu samples had 0.5 µm diameter pores, the samples would need to have a pore depth greater than 50 µm. If the patterned Si-Cu samples had 1 µm diameter pores, they would need to reduce the pore diameter to 0.5 µm and have a pore depth greater than 75 µm. Depositing dehydrogenated a-Si film on patterned Si-Cu samples would aid the retention results of this sample type across the board. Patterned Si-Cu/a-Si:Dehydrogenated samples having a 0.5 µm pore diameter would need to have a pore depth greater than 25 µm. Patterned Si-Cu/a-Si:Dehydrogenated samples having a 1 µm pore diameter would need to have a pore diameter reduction and have a depth greater than 25 µm.

The crossover conditions for the 350°C numbered 4 also. What are discussed are the conditions that must be met if the sample types will exceed the lubricant retention results of smooth Si-Cu/a-Si:Dehydrogenated samples. If the patterned Si-Cu samples had 0.5 µm diameter pores, the samples would need to have a pore depth greater than 75 µm. If the patterned Si-Cu samples had 1 µm diameter pores, they would need to reduce the pore diameter to 0.5 µm and have a pore

depth greater than 75 µm. Depositing dehydrogenated a-Si film on patterned Si-Cu samples would aid the retention results of this sample type universally. The suggestion for patterned Si-Cu/a-Si:Dehydrogenated samples having a 0.5 µm pore diameter would be to incorporate a pore depth greater than 25 µm. Patterned Si-Cu/a-Si:Dehydrogenated samples having a 1 µm diameter pore would need to have a pore diameter reduction and a depth greater than 25 µm.

The crossover conditions for the 400°C numbered the fewest at 3. What are discussed are the conditions that must be met if the sample types can exceed the lubricant retention results of smooth Si-Cu/a-Si:Dehydrogenated samples. If the patterned Si-Cu samples had 0.5 µm diameter pores, the samples would need to have a pore depth greater than 25 µm. If the patterned Si-Cu samples had 1 µm diameter pores, it is suggested to reduce the pore diameter to 0.5 µm and have a pore depth greater than 75 µm. Depositing dehydrogenated a-Si film on patterned Si-Cu samples would aid the retention results of this sample type collectively. Patterned Si-Cu/a-Si:Dehydrogenated samples having a 1 µm pore diameter would need to have a pore diameter reduction and have a depth greater than 25 µm.

8.6 Summary of the Effects of Dehydrogenated a-Si Film

An investigation of H concentration in a-Si:H film was done to determine the number of available bonding sites for Si atoms in the film and C atoms from the lubricant. The film was deposited in patterned samples having 25, 50, and 75 µm pore depths and 0.5 and 1 µm pore diameters and on smooth Si-Cu samples. The expectation was porous topographies had more bonding sites due to their greater film volume than smooth samples. The results of the dehydrogenation experiments in Table 7.27 and those from smooth samples data in Figure 7.5 suggested the effect of Si-C bonds was felt during the longer durations of heating. The results of temperature testing done on patterned Si-Cu/a-Si:Dehydrogenated sample types in Figure 7.8

suggested that the presence of its Si-C bonds aided lubricant retention improvement, too. It was proven that the presence of the film reduced the conduction heat temperature on smooth Si-Cu/a-Si:Dehydrogenated samples by 15°C for the 350°C testing temperature. A reduction in temperature was assumed for patterned Si-Cu/a-Si:Dehydrogenated samples as well. The dehydrogenated a-Si film reduced the amount of heat that was transferred to the lubricant at all testing temperatures. The effects due to the film's thermal resistance and promotion of Si-C bonds were observed in the higher lubricant retention data values of the samples at higher testing temperatures and longer testing durations.

Was there a threshold for S_{Total} that had to be exceeded to affect retention? The results of the crossover data of patterned Si-Cu/a-Si:Dehydrogenated samples compared to smooth Si-Cu/a-Si:Dehydrogenated ones suggested that a limit existed for the enhancement of lubricant by both the thermal resistance and Si-C bonding of dehydrogenated a-Si film. When examining the actual lubricant retention data, there appeared to be a threshold that had to be exceeded to affect retention. The patterned samples could exceed the threshold by incorporating pores deeper than 25 µm, in the case of patterned Si-Cu/a-Si:Dehydrogenated samples having 0.5 µm diameter pores, and pores deeper than 75 µm when using patterned Si-Cu samples having a 1 µm pore diameter. Patterned Si-Cu sample types can include dehydrogenated a-Si film to enhance lubricant retention. The data also suggested the incorporation of smaller pore diameters improved lubricant retention for the crossover situations.

CHAPTER 9

CONCLUSIONS AND FUTURE WORK

9.1 Conclusions

It was proposed that geometric features in the form of nano-pores and the inclusion of a surface chemistry modifier had the potential to enhance the retention of lubricant over the performance of smooth samples. Using modeling and empirical-based approaches, the lubricant retention behavior of smooth and nano-porous samples were revealed. The core findings and conclusions derived from this research are enumerated in this section.

The dimensional aspects of the nano-pores were important. It was found that an optimal geometry was produced by incorporating 0.5 μm diameter pores having a 75 μm pore depth into the smooth sample's topography. The R_T was greatestfor the smallest diameter and deepest pores which resulted in the highest I_{net}. The highest I_{net}, in turn, caused the greatest lubricant retention to occur.

The inclusion of 250 nm thick dehydrogenated a-Si film was investigated a way to enhance the retention of lubricant on smooth and patterned samples types. The benefit of the film was its low thermal conductivity. As a consequence, the film's presence resulted in a lower surface temperature and less conduction heat transferred to the lubricant which was deposited on it. The heat retardation caused less lubricant to be evaporated, and thus the retention was enhanced.

Another benefit of dehydrogenated a-Si film was it permitted stronger bonds to exist between the lubricant and dangling Si atoms in the film. The a-Si:H film offered only a thermal retardation benefit whose effect was shown to diminish during the latter portion of the evaporation testing duration's range. The a-Si:H film, at best, provided only a physical bond in which the lubricant

simply lay next to the a-Si:H film without a chemical interaction between them. The dehydrogenated film, on the other hand, allowed a stronger chemical-based Si-C bond whose effect resulted in the improved capillarity of the surface. The higher capillary force produced by the creation of strong Si-C bonds, then, enhanced the retention of lubricant.

The results of the smallest pore diameter, the increase in pore depth, and the inclusion of dehydrogenated a-Si film were cited as contributors to the enhancement of lubricant retention. The question that naturally arises is which of these properties are most-to-least beneficial toward the retention of lubricant? It was found that a lubricant retention hierarchy existed that could be used to advantage in engineering the retention behavior of nano-porous topographies.

The most effective approach for retaining lubricant on the topography was depositing and dehydrogenating a-Si film. As much as a 0.3 mg lubricant mass differential was obtained when it was included on samples and the comparison was made to samples which omitted it. The next beneficial strategy was incorporating the smallest pore diameter of 0.5 μm. The higher I_{net} of this approach created as much as a 0.2 mg lubricant mass differential when compared to 1 μm diameter pores having the same depth. The least impactful action was increasing the pore depth. For every 25 μm increase in pore depth, the amount of lubricant mass differential increased by 0.1 mg.

The crossover conditions revealed interesting conclusions, too. Patterned Si-Cu samples need to have a depth greater than 75 μm to improve the lubricant retention results above that of smooth Si-Cu/a-Si samples. Patterned Si-Cu/a-Si samples need to have a depth greater than 25 μm to improve the lubricant retention results above that of smooth Si-Cu/a-Si samples. Unless the pore depths suggested here are incorporated for the respective sample types, the work invested in

creating the pores will yield no benefits. The use of the smallest pore diameter must be part of this solution, too.

9.2 Future Work

It was not possible in this work to distinguish the effect of Si-C bonds from the thermal resistance benefit of a-Si film for porous topographies. Another round of evaporation testing using a-Si:H film on patterned Si-Cu samples and comparing the results to dehydrogenated patterned Si-Cu/a-Si already tested will resolve the questions concerning the effect of Si-C bonds alone. Of interest, too, would be determining the effects of depositing thicker a-Si film layers on the lubricant retention behavior of the samples

There were other pore diameters present on the photolithographic mask that could have provided more insight into the behavior of patterned Si-Cu samples during evaporation testing. The 7.5 and 9.5 μm diameter pores were available to produce final pore diameters of 2 and 4 μm, respectively, if retaining the 2.5 μm Cu and 250 nm a-Si film thicknesses used in the current work. The incorporation of these pore diameters could have allowed some interesting tests such as examining the trends of surface capillarity for the 4 pore diameters as well as using a constant volume scenario to investigate the most effective geometry for lubricant retention. These investigations were undertaken to a limited extent in the current work, but the discovery of more lubricant retention trends might be possible using the additional pore diameters in evaporation testing. Furthermore, the number of pores on the samples was limited to 616,080. Retention tests that considered fewer or additional numbers of pores for the 4 diameters are other possibilities for future research. Finally, the opportunities to expand this research to specific engineering applications and mass manufacturing are other avenues that deserve attention in the future.

REFERENCES

1. Sibley, L., and Kennedy, F., "Achievements in Tribology", *American Society of Mechanical Engineers*, Vol. 1, 1991.

2. Feeny, B. et al., "A Historical Review on Dry Friction and Stick-Slip Phenomenon" *Applied Mechanics Reviews*, Vol. 53, No. 5, pp. 321 - 341, 1998.

3. Jost, H., "Tribology Micro & Macro Economics-A Road to Economic Savings", *Tribology and Lubrication Technology*, October issue, pp. 18 - 22, 2005.

4. Jost, H., "Tribology-Origin and Future", *Wear*, Vol. 136, No. 1, pp. 1 - 17, 1990.

5. Tinham, B., "Time for Tribology", *The Plant Engineer"* November/December, pp. 16 - 17, 2013.

6. Jost, H., "Energy Savings Through Tribology: A Techno-Economic Study", *Proceedings of the Institution of Mechanical Engineers*, Vol. 195, 1981.

7. Dowson, D., "History of Tribology in America" *Journal of Lubrication Technology*, Vol. 103, No. 3, pp. 323 - 333, 1981.

8. Ludema, K., "Seventy Years of Research on Wear", *Achievements in Tribology*, Vol. 1, p. 112, 1991.

9. Young, L., and Lebeck, A., "The Design and Testing of Moving Wave Mechanical Face Seals Under Variable Operating Conditions in Water", *American Society of Lubrication Engineers/American Society of Mechanical Engineers Tribology Conference, Atlanta, Georgia, USA, October 8 - 10, 1985*.

10. Wang, X., Kato, K., and Adachi, K., "The Lubrication Effect of Micro-Pits on Parallel Sliding Faces of Sic in Water," *Tribology Transactions*, Vol. 45, No. 3, pp. 294 - 301, 2002.

11. Wang, Y., et al., "Theoretical Analyses and Design Guidelines of Oil-Lubricated Mechanical Face Seals with Spiral Grooves", *Society of Lubrication Engineers' 59th Annual Meeting in Toronto, Ontario, Canada, May 17 - 20, 2004.*

12. Etsion, I., “Improving Performance of Mechanical Components by Laser Surface Texturing”, *Tribology Letters*, Vol. 17, No. 4, pp. 733 - 737, 2004.

13. Komvopoulos, K., “Adhesion and Friction Forces in Microelectromechanical Systems: Mechanisms, Measurement, Surface Modification Techniques, and Adhesion Theory”, *Journal of Adhesion Science and Technology*, Vol. 17, No. 4, pp. 477 - 517, 2003.

14. Burton, Z., and Bhushan, B., “Hydrophobicity, Adhesion, and Friction Properties of Nanopatterned Polymers and Scale Dependence for Micro- and Nano-Electromechanical Systems”, *Nano Letters*, Vol. 5, No. 8 1607 - 1613, 2005.

15. Law, K., Zhao, H., and Sambhy, V., “Effects of Surface Texture and Chemistry on Surface Hydrophobicity and Oleophobicity”, *NSTI - Nanotech 2009*, Vol. 3, pp. 177 - 179, 2009.

16. Ramos, S., et al., “Superoleophobic Behavior Induced by Nanofeatures on Oleophilic Surfaces”, *Langmuir*, Vol. 26, No. 7, pp. 5141 - 5146, 2010.

17. Taolei, S., et al., “Bioinspired Surfaces with Special Wettability”, *American Chemical Society*, Vol. 38, No. 8, pp. 644 - 652, 2005.

18. Yoona, E. - S., et al., “Tribological Properties of Bio-Mimetic Nano-Patterned Polymeric Surfaces on Silicon Wafer”, *Tribology Letters*, Vol. 21, No. 1, 2006.

19. Peterson, M., “Advancements in Tribological Materials 1937 - 1987 - 2002” *Tribology, Friction, Lubrication, and Wear Fifty Years On, International Conference, Queen Elizabeth II Conference Centre, London, England, UK, July 1 - 3, 1987*.

20. Bartz, W., “Tribology, Lubricants and Lubrication Engineering-A Review, *Wear*, Vol. 49, No. 1, pp. 1 - 18, 1978.

21. Roberts, W., “Surface Engineering”, *Transactions of the Institution of Engineers, Australia. Mechanical Engineering*, Vol. 14, No. 1, pp. 3 - 16, 1989.

22. Zhang, Y., et al., “Surface Texturing Technology by Laser Honing Based on Hydrodynamic Lubrication”, *Key Engineering Materials*, Vol. 359 - 360, pp. 340 - 343, 2008.

23. Booser, E., and Wilcock, D., “Hydrodynamic Lubrication”, *Lubrication Engineering*, Vol. 47, No. 8, pp. 645 - 647, 1991.

24. Woydt, M., “History of the Stribeck Curve and Ball Bearing Steels: The Role of Adolf Martens, *Wear*, Vol. 268, No. 11, pp. 1542 - 1546, 2010.

25. Reynolds, O., “On the Theory of Lubrication and Its Application to Mr. Beauchamp Tower’s Experiments Included an Experimental Determination of the Viscosity of Olive Oil” *Philosophical Transactions of the Royal Society*, Vol. 177, No. (i), pp. 157 - 234, 1886.

26. Cengel, Y., and Turner, R., *Fundamentals of Thermal-Fluid Sciences*, 2nd edition, McGraw-Hill, New York, NY, pp. 681, 789, 1113, 2005.

27. Ishii, T., Miyagawa, S., and Taguma, I., “Research and Development on the Hydrodynamic Pressure Generation Between Contacting Flat Surfaces”, *American Society of Lubrication Engineers*, Vol. 29, No. 3, pp. 339 - 346, 1986.

28. Bernd, L., “Survey of Theory of Mechanical Face Seals-1”, *Lubrication Engineering*, Vol. 24, No. 10, pp. 525 - 530, 1968.

29. Ludwig, L., and Greiner, H., “Designing Mechanical Face Seals for Improved Performance-1 Basic Configurations”, *Mechanical Engineering*, Vol. 100, No. 11, pp. 38 - 46, 1978.

30. Bernd, L., “Survey of Theory of Mechanical Face Seals-3”, *Lubrication Engineering*, Vol. 24, No. 10, pp. 597 - 604, 1968.

31. Etsion, I., Kligerman, Y., and Halperin, G., "Analytical and Experimental Investigation of Laser-Textured Mechanical Seal Faces," Tribology Transactions, Vol. 42, No. 3, pp. 511 - 516, 1999.

32. Bellosi, A., et al., "UV laser ablation of alumina ring faces for mechanical seal applications," *Applied Physics*, Vol. A, No. 69, pp. 539 - 42, 1999.

33. Allegretti, D., Daurelio, G., and Guerrini, F., "Laser surface micro-texturing on the mechanical seal rings for enhancing the tribological properties," *XIII International Symposium on Gas Flow and Chemical Lasers and High Power Laser Conference, Florence, Italy, September 18 - 22, 2000*.

34. Pride, S., Folkert, K., Guichelaar, P., "Effect of Micro-Surface Texturing on Breakaway Torque and Blister Formation on Carbon-Graphite Faces in a Mechanical Seal," *Lubrication Engineering*, Vol. 58**,** No. 10, pp. 16 - 21, 2002.

35. Guichelaar, P., Wilde, D., and Williams, M., “The Detection and Characterization of Blisters on Carbon-Graphite Mechanical Seal Faces”, *Tribology Transactions*, Vol. 43, No. 3, pp. 395 - 402, 2000.

36. Van Rensselar, J., “Trends in Industrial Gear Oils”, *Tribology and Lubrication Technology*, Vol. 69, No. 2, pp. 26 - 33, 2013.

37. Yang, S., Guo, F., and Wang, H., “Study of Orientation Effects of Grooves on the Film Thickness in Hydrodynamic Lubrication”, *Nanoscience and Nanotechnology Letters*, Vol. 4, No. 9, pp. 895 - 900, 2012.

38. Peng, X., et al., “Effects of Dimple Geometric Parameters on the Performance of a Laser-Textured Mechanical Seal”, *Key Engineering Materials*, Vol. 373, pp. 766 - 769, 2008.

39. Nosowicz, J., “Laser-Structured Faces Can Enhance Mechanical Seals”, *Chemical Engineering*, Vol. 110, No. 13, pp. 51 - 53, 2003.

40. Etsion, I., and Michael, O., “Enhancing Sealing and Dynamic Performance with Partially Porous Mechanical Face Seals”, *Tribology Transactions*, Vol. 37, No. 4, pp. 701 - 710, 1994.

41. Fowell, M., et al., “Entrainment and Inlet Suction: Two Mechanisms of Hydrodynamic Lubrication in Textured Bearings”, *Journal of Tribology*, Vol. 129, No. 2, pp. 336 - 347, 2007.

42. Cecil, R., “High Temperature Thickening of Motor Oils”, *Journal of the Institute of Petroleum*, vol. 59, No. 569, pp. 201 - 210, 1973.

43. Santos, J., et al., “Thermoanalytical and Rheological Characterization of Automotive Mineral Lubricants after Thermal Degradation”, *Fuel*, pp. 2393 - 2399, 2004.

44. Van Rensselar, J., “Used Oil Analysis for Predictive Maintenance”, *Tribology and Lubrication Technology*, Vol. 68, No. 1, pp. 34 - 45, 2012.

45. Van Rensselar, J., “Static Discharge”, *Tribology and Lubrication Technology*, Vol. 68, No. 9, pp. 46 - 53, 2012.

46. Morehead, J., *Surface Wetting and Friction Studies of Nano-Engineered Surfaces on Copper Substrate*, ProQuest/UMI 1500599, Ann Arbor, MI, pp. 42 - 71, 2011.

47. Kichkin, G., and Markov, A., “Relationship Between Lubricating Properties of Hydrocarbons of Oil Fractions and their Adsorption Properties on Metal”, *Petroleum Chemistry USSR*, Vol. 18, No. 1, pp. 25 - 30, 1978.

48. Vargas, F., and Chapman, W., “Application of the One-Third Rule in Hydrocarbon and Crude Oil Systems” *Fluid Phase Equilibria*, Vol. 290, Nos. 1 - 2, pp. 103 - 108, 2010.

49. Kennedy Jr., F., “Observation of Contact Conditions in Mechanical Face Seals” *American Society of Lubrication Engineers*, Vol. 27, No. 2, pp. 122 - 128, 1984.

50. Moshkovich, A., et al., “Stribeck Curve Under Friction of Copper Samples in the Steady Friction State” *Tribology Letters*, Vol. 37, No. 3, pp. 645 - 653, 2010.

51. Guo, Z., et al., “Fabrication of Superhydrophobic Copper by Wet Chemical Reaction”, *Thin Solid Films*, Vol. 515, pp. 7190 - 7194, 2007.

52. Xu, W., et al., “Fabrication of Superhydrophobic Surfaces with Hierarchical Structure through a Solution - Immersion Process on Copper and Galvanized Iron Substrates”, *Langmuir*, Vol. 24, No. 19, pp. 10895 - 10900, 2008.

53. Petzow, G., *Metallographic Etching - Metallographic and Ceramographic Methods for Revealing Microstructure*, American Society for Metals, 1976.

54. Etsion, I., Kligerman, Y., and Halperin, G., “Analytical and Experimental Investigation of Laser - Textured Mechanical Seal Faces” *Tribology Transactions*, Vol. 42, No. 3, pp. 511 - 516, 1999.

55. Gao, X., et al., “The Diffusion and Interfacial Reaction of Cu/Si (100) Systems” *Advanced Materials Research*, Vols. 287 - 290, pp. 2302 - 2307, 2011.

56. Sanjurjo, A., Wood, K., and Krishnan, G., “W - Si, Fe - Si, and Cu-Si Interfaces”, *Scripta Metallurgica et Materialia*, Vol. 31, No. 8, pp. 1019 - 1024, 1994.

57. Stolt, L., Heurle, F., and Harper, J., “On the Formation of Copper-Rich Copper Silicides” *Thin film Solids*, Vol. 200, pp. 147 - 156, 1991.

58. Kovacik, J., et al., “Effect of Composition on Friction Coefficient of Cu-Graphite Composites”, *Wear*, Vol. 265, pp. 417 - 421, 2008.

59. Zhan Y., and Zhang G., “Friction and Wear Behavior of Copper Matrix Composite Reinforced with SiC and Graphite Particles”, *Tribology Letters*, Vol. 17, pp. 91 - 98, 2004.

60. Rajkumar, K., and Aravindan, S., Tribological Performance of Microwave Sintered Copper-TiC-Graphite Hybrid Composites”, *Tribology International*, Vol. 44, pp. 347 - 358, 2011.

61. Shang J, Wenlin M, Lu J. “Formation of Laminar Structure under Unlubricated Friction of Cu-SiO_2 Composite”, *Tribology Letters*, Vol. 48, pp. 249 - 254, 2012.

62. Sugafuji, A., et al., “Effects of Silicon and Copper Contents on Sliding Properties of Al-Si-Cu-Mg Alloys in Boundary Lubrication” *Journal of Japan Institute of Light Metals*, Vol. 53, No. 3, pp. 93 - 97, 2003.

63. Yang, H., et al., “Evolution of the Morphology of Cu Films on Nanoporous Si Pillar Arrays”, *Materials Science in Semiconductor Processing*, Vol. 16, No. 3, pp. 747 - 751, 2013.

64. Ahmadi, A., Zhengchun, P., and Nair, S., “Wafer-Scale Process for Fabricating Arrays of Nanopore Devices” *Journal of Micro/Nanolithography MEMS MOEMS*, Vol. 9, No. 3, pp. 0330111 - 0330118, 2010.

65. Anupras, Sˇ. lancˇiauskas , R., Kalpokait, E., “Behaviour of a Heavy Fuel Oil Droplet on a Hot Surface”, *International Journal of Heat and Mass Transfer*, Vol. 49, pp. 1050 - 1057, 2006.

66. Wang, X., Adachi, K., Otsuka, K., 2006, "Optimization of the Surface Texture for Silicon Carbide Sliding in Water," *Applied Surface Science*, Vol. 253, No. 3, pp. 1282 - 6, 2006.

67. Wang, X., Kato, K., and Adachi, K., 2002, "The Lubrication Effect of Micro-Pits on Parallel Sliding Faces of Sic in Water," *Tribology Transactions*, Vol. 45, No. 3, pp. 294 - 301, 2002.

68. Kelly - Zion, P., et al., “Evaporation Rates of Pure Hydrocarbon Liquids under the Influence of Convection and Diffusion”, *International Journal of Heat and Mass Transfer*, vol. 52, pp. 3305 - 3313, 2009.

69. Sodtke, C., Ajaev, V., and Stephan, P., “Evaporation of Thin Liquid Droplets on Heated Surfaces”, *Heat Mass Transfer*, Vol. 43, pp. 649 - 657, 2007.

70. Sodtke, C., Ajaev, V., and Stephan, P., “Dynamics of Volatile Liquid Droplets on heated Surfaces: Theory versus Experiment”, *Journal of Fluid Mechanics*, Vol. 610, pp. 343 - 362, 2008.

71. Takashima, T., and Shiota, H., “Evaporation of an Oil-in-Water Type Emulsion Droplet on a Hot Surface”, *Heat transfer*, Vol. 34, No. 7, pp. 527 - 537, 2005.

72. Wang, H., Zou, M., and Wei, R., "Superhydrophilic Textured - Surfaces on Stainless Steel Substrates," *Thin Solid Films*, Vol. 518, No. 5, pp. 1571 - 1574, 2009.

73. Morehead, J., and Zou, M., “Superhydrophilic Surface on Cu Substrate to Enhance Lubricant Retention”, *Journal of Adhesion Science and Technology Special Issue: Superhydrophilic Surfaces*, Vol. 28, No. 8 - 9, pp. 833 - 842, 2014 (online 2012).

74. Fingas, M., “Studies on the Evaporation of Crude Oil and Petroleum Products: I. The Relationship between Evaporation Rate and Time”, *Journal of Hazardous Materials*, Vol. 56, pp. 227 - 236, 1997.

75. Laermer, F., and Schilp, A., *Method of Anisotropically Etching Silicon*, Robert Bosch GmbH, U.S. Patent 5,501,893; 1996.

76. Shikida, M., et al., “The Mechanism of Selective Corrugation Removal by KOH Anisotropic Wet Etching”, *Journal of Micromechanics and Microengineering*, Vol. 20; pp. 1 - 9, 2010.

77. Street, R., *Hydrogenated Amorphous Silicon*, Cambridge University Press, New York, NY, pp. 19, 25, 53, 59, 177, 185; 1991.

78. Madou, M., *Fundamentals of Microfabrication-The Science of Miniaturization*, 2nd edition, CRC Press, Boca Raton, FL, p. 149, 2002.

79. Churchill, S., and Ozoe, H., “Correlations for Laminar forced Convection in Flow over an Isothermal Flat Plate and in Developing and Fully Developed Flow in an Isothermal Tube” *Journal of Heat Transfer*, pp. 719 - 784, 1973.

80. Shanks, H., et. al, “Infrared Spectrum and Structure of Hydrogenated Amorphous Silicon”, *Physica Status Solidi (b)*, Vol. 100, No 1, pp. 43 - 56, 1980.

81. Maley, N., and Szafranek, I., *Amorphous Silicon Technology*, Materials Research Society Symposia Proceedings, Vol. 192, p. 663, 1990.

82. Langford, A., et al., "Infrared Absorption Strength and Hydrogen Content of Hydrogenated Amorphous Silicon", *Physical Review B*, Vol. 45, No. 23, pp. 13367 - 13377, 1992.

83. John, P., et. al, "Determination of the Hydrogen Content of a-Si Films by Infrared Spectroscopy and 25 MeV α-Particle Elastic Scattering", *Journal of Physics C: Solid State Physics*, Vol 14, pp. 309 - 318, 1981.

84. Rensselar, J., "Used-Oil Analysis for Predictive Maintenance" *Tribology and Lubrication Technology*, Vol. 68, No. 1, p. 42, 2012.

85. Akagi, K., and Tsuneyuki, S., "Unsaturated Cyclic-Hydrocarbon Molecules on a Si (001) Surface—A First-Principles Approach", *Surface Science*, Vol. 493, pp. 131 - 37, 2001.

86. Phuong,N., et. al, "Characterization of Photoconductive Amorphous Si:H Films for Photoconducting Sensor Applications", *Electrochemical and Solid-State Letters*, Vol. 10, No. 9, pp. 1 - 3, 2007.

87. Riazi, M., *Characterization and Properties of Petroleum Fractions*, 1st edition, American Society for Testing and Materials, West Conshohoken, PA, p. 45, 2005.

88. Kolasinsky, K., *Surface Science: Foundations of Catalysis and Nanoscience*, 2nd edition, John Wiley and Sons, Ltd, West Sussex, England, p. 29, 2008.

APPENDIX

EXPLANATIONS FOR THE AMOUNTS OF LUBRICANT DEPOSITED AND THE OMISSION OF SAMPLE TARE + OIL MASS VALUES IN THE PLOTS FOR LUBRICANT MASS RETAINED

Section 4.4.3 explained the methodology used to calculate the amount of lubricant that was deposited on the samples for evaporation testing. These values are reprised from Table 4.10.

Table 4.10. Values for M_{Total} calculated for oil deposition on smooth and nano-porous samples.

Oil Amt	**6 µm dia, 25 µm D**	**6 µm dia, 50 µm D**	**6 µm dia, 75 µm D**	**6.5 µm dia, 25 µm D**	**6.5 µm dia, 50 µm D**	**6.5 µm dia, 75 µm D**
V_{Pores} $(\mu m)^3$	435481290	870962581	130644387	511085681	102217136	153325704
V_{Total} $(\mu m)^3$	556448791	991930081	142741137	632053181	114313886	165422454
M_{Total} (mg)	0.50356949	0.89766697	1.29176447	0.57198917	1.03450638	1.49702359

After taking steps to remove the air from the lubricant and pores, the M_{Total} values calculated in Table 4.10 were used to adjust the mass of the penetrating oil applied on the samples. The amounts were chosen to ensure complete coverage of the testing area and pore diameters and depths encountered during evaporation. It was decided that allowing the large number of digits in the table values was essential to avoid truncation errors that occur from eliminating trailing digits too soon. This typically affects numbers involved in or derived from multiple computations. However, the amounts were rounded to the nearest 0.1 mg before the lubricant's deposition on the samples.

The tare mass of the samples, which was recorded after the deposition of Cu and dehydrogenated a-Si films, were paired with the appropriate lubricant amount from Table 4.10 to produce the

sample tare + oil mass amounts. As an example, the patterned samples that had the 6 µm outer pore diameter and 25 µm pore depth were deposited with 0.5 mg lubricant. If sample no. 181's *sample tare mass* of 0.4685 g was used as a basis, the *sample tare + oil mass* became 0.4690 g as shown in the partial worksheet below. The same deposition procedures were done for all sample types and configurations. The worksheet was composed to keep track of the descriptions, physical properties, and raw data related to the lubricant retention of the 216 samples undergoing evaporation testing.

Sample No.	Sample ID	Dia. (µm)	Depth (µm)	Test Temp (°C)	Sample Tare Mass (g)	Sample Tare + Oil Mass (g)	Mass 5 min (g)	ΔMass 5 min (mg)	Mass 10 min (g)	ΔMass 10 min (mg)	Mass 15 min (g)	ΔMass 15 min (mg)	Mass 20 min (g)	ΔMass 20 min (mg)	Mass 25 min (g)	ΔMass 25 min (mg)	Mass 30 min (g)	ΔMass 30 min (mg)
181	Patterned Si-Cu/a-Si	0.5	25	400	0.4685	0.4690	0.4688	0.3	0.4688	0.3	0.4688	0.3	0.4687	0.2	0.4687	0.2	0.4687	0.2
182	Patterned Si-Cu/a-Si	0.5	25	400	0.4701	0.4706	0.4704	0.3	0.4704	0.3	0.4704	0.3	0.4703	0.2	0.4703	0.2	0.4703	0.2
183	Patterned Si-Cu/a-Si	0.5	25	400	0.4680	0.4685	0.4683	0.3	0.4683	0.3	0.4683	0.3	0.4682	0.2	0.4682	0.2	0.4682	0.2
184	Patterned Si-Cu/a-Si	0.5	50	400	0.4702	0.4711	0.4706	0.4	0.4706	0.4	0.4705	0.3	0.4705	0.3	0.4705	0.3	0.4705	0.3
185	Patterned Si-Cu/a-Si	0.5	50	400	0.4682	0.4691	0.4686	0.4	0.4686	0.4	0.4685	0.3	0.4685	0.3	0.4685	0.3	0.4685	0.3
186	Patterned Si-Cu/a-Si	0.5	50	400	0.4700	0.4709	0.4704	0.4	0.4704	0.4	0.4703	0.3	0.4703	0.3	0.4703	0.3	0.4703	0.3
187	Patterned Si-Cu/a-Si	0.5	75	400	0.4610	0.4623	0.4615	0.5	0.4615	0.5	0.4615	0.5	0.4614	0.4	0.4614	0.4	0.4614	0.4
188	Patterned Si-Cu/a-Si	0.5	75	400	0.4609	0.4622	0.4614	0.5	0.4614	0.5	0.4614	0.5	0.4613	0.4	0.4613	0.4	0.4613	0.4
189	Patterned Si-Cu/a-Si	0.5	75	400	0.4620	0.4633	0.4625	0.5	0.4625	0.5	0.4625	0.5	0.4624	0.4	0.4624	0.4	0.4624	0.4

Regarding the plotting of lubricant retention data in Figures 7.5 – 7.11, it was determined that the inclusion of the *sample tare + oil mass* amounts in the charts were unnecessary. During testing, it was observed that the first 5 min was the occasion for the burn-off of excess lubricant resting on the surface of the testing area. Excess lubricant undergoing evaporation loses mass at a linear rate, so plotting it does not contribute to the mission of determining the trends of lubricant retention. Rather, its inclusion further complicates the analysis of the trends of the various topographies under consideration.

Furthermore, the objective was to focus on the change in lubricant mass on the samples. Calculating *Δmass* required subtracting the *sample tare mass* from the *sample tare + oil mass* amounts that remained after each 5 min testing increment. The samples, absent any lubricant, had variations in their mass due to dimensional irregularities created during their fabrication. An examination of the worksheet values for a fixed pore depth of one's choosing illustrates the point. Notice the variations in the *sample tare mass* and *sample tare + oil mass* values for the 3 samples. Considering that 3 samples were tested per configuration and there were 6 sample configurations plotted in each chart, attempting to use each *sample tare + oil mass* as a starting point could generate 18 plots having different starting masses. In the end, it was more sensible to utilize the averaged *Δmass* values that were independent of the *sample tare mass* and start each plot at the 5 min testing duration where the *Δmass* values were calculated.